N°d'ordre NNT : xxx

THESE de DOCTORAT DE L'UNIVERSITE DE LYON
opérée au sein de
l'Université Claude Bernard Lyon 1

Ecole Doctorale N° 52
Physique et Astrophysique

Spécialité de doctorat :chimie-physique

Soutenue publiquement/à huis clos le 20/10/2016, par :
Vojkovic Marin

Synthesis and reactivity of bare and ligated small metal complexes

---

Devant le jury composé de :

Bonacic-Koutecky, Vlasta, DR, ICAST	Rapporteure
Focsa, Christian, PR Laboratoire PhLAM	Rapporteur
Dossmann, Heloise, Maitre de conferences, IPCM	Examinatrice
O'Hair, Richard, PU, University of Melbourne	Examinateur
Dugourd, Philippe, DR, CNRS	Directeur de thèse
Rayane, Driss, PR, Université Lyon 1	Co-directeur de thèse

Table of contents

1. Introduction 9

1.1 Optical properties 10

1.2 Chemical properties 11

Bibliography 14

2 Experimental techniques and setup 17

2.1 Mass spectrometry 17

2.1.1 Ion traps 19

2.1.2 Detectors 25

2.2 Electrospray Ionisation 27

2.2.1 Electrospray mechanism 27

2.2.2 Sensitivity and use 31

2.3 Laser ablation 33

2.4 LAVESI experimental setup description 40

2.4.1 Laser Vaporization Electrospray Ionization (LAVESI) 41

2.4.3 Gas phase reaction setup 48

2.4.3 Conclusion 50

Bibliography 51

3. Wet chemistry synthesis 59

3.1 Synthesis in solution: $Au_{15}SG_{13}$ 59

3.2 Synthesis in electrospray: small clusters 60

3.3 Collision induced dissociation of small clusters 61

3.4 Conclusion 64

Bibliography 65

4. Synthesis and characterisation of bare and ligated-metal species by Laser Vaporization Electrospray Ionization (LAVESI) 67

4.1 Formation and properties of metal oxides 67

4.1.1. Analysis of results obtained in positive mode 69

4.1.2 Analysis of results obtained in negative mode 72

4.1.3 Conclusions on metal oxides 81
4.2 Ligated metal complexes 83
4.2.1 Ligated silver complexes 83
4.2.2 Ligated gold complexes 86
4.2.3 Ligated copper complexes 88
4.2.4 Ligated bimetallic complexes 91
4.2.5 Conclusions on ligated complexes 93
4.3 Conclusion 93
Bibliography 94
5. Gas phase reactions 97
5.1 Metals with CO 97
5.1.1 Reactions at low CO concentration 99
5.1.2 Reactions at high CO concentration 101
5.1.3 Hydrogen stabilised metallic dimers 108
5.2 Theory 113
5.2.1 Au^+ structures and reactions 113
5.2.2 Au_2^+ and Au_2H^+ structures and reactions 116
5.3 Conclusions 119
Bibliography 121
Appendix 1 125
Appendix 2 137

List of figures

Figure 1. 1 Real world examples of metallic nanoparticles. 9
Figure 1. 2 (Top left) Photofragmentation shows how the silver cluster modifies the optical properties of the peptide. (Top right) Microscopy imaging with nanoclusters (Bottom) Reaction pathway of CO oxidation mediated by the Au_6 cluster. 12

Figure 2. 1 General schematic of a mass spectrometer. 17
Figure 2. 2 Examples of application of mass spectrometery. 18
Figure 2. 3a) quadrupole potential b) cross section of a linear quadrupole ion trap with hyperbolic electrodes c) cross section of a linear quadrupole ion trap with circular electrodes d) x and y direction ion motion in the ion trap e) y direction ion motion comparison between circular and hyperbolic electrodes. 21
Figure 2. 4 (left) Regions of stability of ion trajectories for a given pair of values of a and q parameters. (right) Region I enlarged. 22
Figure 2. 5 a) Schematics and constituting parts of a 3D quadrupole ion trap. b) a-q plot of stability regions for ion trajectories. c) q-m/z dependence. By increasing RF voltage, the stability region moves to the left, sequentially ejecting the ions. 25
Figure 2. 6 a) Schematics of linear and curved channel electron multiplier. b) The operation of a conversion dynode. 26
Figure 2. 7 a) The macromolecular beam device used by Dole et al. b) The first ESI device used by Fenn, the design of which was inspired and based on Dole's device. 28
Figure 2. 8 Top row - modes of Taylor cone formation as a function of capillary voltage. Middle row – formation of droplets from the cone. Bottom row – illustration of IEM mechanism. 30
Figure 2. 9 Schematic of a coupled laser ablation – electrospray mass spectrometry source. 34
Figure 2. 10 Examples of different laser-ESI coupled ionisation methods. 35
Figure 2. 11 Examples of first MALDI mass spectra. 36
Figure 2. 12 Mass spectra obtained by Smalley group at Rice Univerisy by laser ablation of metal rods. a) Mass spectrum of Al clusters. b) Mass spectrum of Cu clusters. 37
Figure 2. 13 Variations of a laser ablation source. (left) Standard source. (middle) Cutaway source. Offset source. 39
Figure 2. 14 Ion source, ion optics and mass analyser schematics of the LTQ XL mass spectrometer. 40
Figure 2. 15 Schematic of the LAVESI source set-up. 42
Figure 2. 16 a) The LAVESI setup. b) A look inside the ESI source and the metal rod placed in front of the entrance to the ion transfer capillary. c) Metal rods used for ablation. 42
Figure 2. 17 Comparison of LAVESI mass spectrum a), ablating the silver rod and electrospraying thioglycolic acid, and standard ESI mass spectrum b) of thioglycolic acid. 43
Figure 2. 18 LAVESI mass spectra obtained with different concentrations of thioglycolic acid ranging from 0-2% (v/v). 44
Figure 2. 19 Power dependence of the species observed in the mass spectrum of the LAVESI source. 45

Figure 2. 20 Wavelength dependence of the species observed in the mass spectrum of the LAVESI source. The experiments were conducted with second (top) and fourth (bottom) harmonic of a Nd^{3+}:YAG laser. 46
Figure 2. 21 Examples of the CID mass spectra. a) MS^2 mass spectrum of a gold-water complex. b) MS^2 and MS^3 spectra of a copper-thioglycolic acid complex. 47
Figure 2. 22 Schematic of the experimental set-up for gas phase reactions. 48
Figure 2. 23 Example reactions inside the ion trap. a) With pure He buffer gas. b) With He/NO 5% mixture. ... 49

Figure 3. 1 ESI mass spectrum of $Au_{15}SG_{13}$ water solution. Inset: close-up of the isotopic distribution of $Au_{15}SG_{13}^{5-}$, and comparison with a simulated mass spectrum. 60
Figure 3. 2 ESI mass spectrum of small silver-thioglycolic acid complexes obtained through wet chemistry synthesis. 61
Figure 3. 3 CID fragmentation channels of selected small silver nanoclusters. Left – the peak at 502.7 Da corresponding to $\boldsymbol{Ag3(SR)2-2H-}$ (simplified notation) isolated with a m/z window of 10Th, with (bottom) and without (top) collisional activation energy (in arbitrary units). 62
Figure 3. 4 CID mas spectra of 4/4 singly (left) and doubly (right) charged. 63
Figure 3. 5 ESI mass spectrum of small gold-thioglycolic acid complexes, obtained through wet chemistry synthesis. 64

Figure 4. 1 Example of comparison of mass spectra obtained with different electrospray plume compositions, with electrospray syringe empty and turned off, and with pure water for gold monomer and dimer in negative mode. 68
Figure 4. 2 Example of comparison of mass spectra obtained with different electrospray plume compositions for water and heavy water for gold monomer and dimer in negative mode. 69
Figure 4. 3 Mass spectra obtained by vaporisation of silver rod, with different in-source activation energies, in positive mode. 70
Figure 4. 4 Total relative intensities of pure silver complexes and their products, as a function of activation energy in positive mode. 70
Figure 4. 5 MS^2 spectra of selected silver complexes in positive mode. 73
Figure 4. 6 Mass spectra obtained by vaporisation of gold rod, with different in-source activation energies, in positive mode. 74
Figure 4. 7 Relative intensities of bare metal and metal complexes obtained through ablation of the gold rod as a function of collisional activation energy in positive mode. 74
Figure 4. 8 MS^2 mass spectra of gold complexes in positive mode. Star symbols mark the centre of isolation interval. N.C.E. stands for normalised collision energy and is expressed in arbitrary units. 76
Figure 4. 9 Mass spectra obtained by vaporisation of silver rod, with different in-source activation energies, in negative mode. 77
Figure 4. 10 (left) Total relative intensities of pure silver complexes and their products, as a function of activation energy in negative mode. (right) Stoichiometries of the most intense group of products observed for a given number of silver atoms in full mass spectrum. 77

Figure 4. 11 MS^2 spectra of selected silver complexes in negative mode. 78
Figure 4. 12 Mass spectra obtained by vaporisation of gold rod, with different in-source activation energies, in negative mode. 80
Figure 4. 13 Relative intensities of bare metal and metal complexes obtained through ablation of the gold rod as a function of collisional activation energy in negative mode. 80
Figure 4. 14 MS^2 spectra of gold complexes in negative mode. 82
Figure 4. 15 a) Mass spectrum recorded using the thioglycolic acid solution without metal vaporisation. b) LAVESI mass spectrum obtained by vaporisation of a silver rod and spray of a thioglycolic acid solution c) LAVESI mass spectrum obtained by vaporisation of a silver rod and spray of a thioglycolic acid 84
Figure 4. 16 Example of isotopic distribution comparison of experimental and simulated species for silver-thioglycolic acid complexes. 84
Figure 4. 17 The MS^n spectra of selected LAVESI species. (left) MS^2 spectrum of $\boldsymbol{Ag4(SR)3-2H-}$, with and without the collisional activation. (right) MS^2 to MS^4 spectrum starting with $\boldsymbol{Ag8(SR)5-4H-}$. 85
Figure 4. 18 LAVESI mass spectrum obtained by vaporisation of a gold rod and spray of thioglycolic acid. (top) and high mass range (2000-4000 Da) (bottom) due to the technical constraints of the instrument. 87
Figure 4. 19 LAVESI mass spectrum obtained by vaporisation of a copper rod at a capillary temperature of 50°C. 88
Figure 4. 20 Isotopic distributions for several ligated copper complexes created by LAVESI. Coppers characteristic isotopic pattern helps us identify the observed signal in some cases as superposition of two species. 91
Figure 4. 21 LAVESI mass spectrum obtained through vaporisation of gold-silver alloy rod (1/1 ratio) and electrospraying thioglycolic acid. 92

Figure 5. 1 Reactions of small $\boldsymbol{Aun+, n=1-4}$ clusters with low concentration CO. 100
Figure 5. 2 Reaction with low concentration CO for $\boldsymbol{Aun+}$ where $\boldsymbol{5 \le n \le 9}$.. 100
Figure 5. 3 Reaction with low concentration CO for $\boldsymbol{Pt+}$, $\boldsymbol{Pt2+}$, $\boldsymbol{Pt3+}$ and $\boldsymbol{Pt4+}$. 102
Figure 5. 4 Reactions of silver at low CO concentrations. a) silver monomer in pure helium buffer gas. b) silver monomer in He/CO 0.1% mixture. 102
Figure 5. 5 (left) MS^2 spectrum of gold monomer with high concentration of CO in the ion trap. (right – top) Zoom in on $\boldsymbol{Au(CO)3+}$ peak. (right – bottom) Zoom in on $\boldsymbol{Au(CO)6+}$ peak.. 103
Figure 5. 6 (left)MS^2 spectrum of the gas phase reaction of $\boldsymbol{Au3+}$ with CO, for two different concentrations of CO. (right - top) Reaction kinetics for the $\boldsymbol{Au3+}$ for 5% He/CO. (right – bottom) Relative intensities as a function of collisional energy for 5% He/CO. 104
Figure 5. 7 (left) MS^2 spectrum of m/z 788 which corresponds to $\boldsymbol{Au4+}$ (marked with a red star) for two different concentrations of He/CO. 105
Figure 5. 8 Reaction with high concentration CO for a) $\boldsymbol{Pt+}$, b) $\boldsymbol{Pt2+}$, c) $\boldsymbol{Pt3+}$ and d) $\boldsymbol{Pt4+}$. 106
Figure 5. 9 Mass spectra of silver monomer reactions with CO. The red number above the peaks mark the number of CO molecules adsorbed to the cluster. The exact number of hydrogen atoms can only be resolved for the $\boldsymbol{Ag(CO)5H2,4+}$. 107

Figure 5. 10 Gas phase reactivity of gold dimer. (left) Mass spectrum of isolated gold dimer in pure He (top) and in He/CO mixture (bottom). (right) Reaction kinetics for 5% He/CO..... 108
Figure 5. 11 Gas phase reactivity of $\boldsymbol{Au2H+}$. (left) Mass spectrum of isolated gold dimer in pure He (top) and in He/CO mixture (bottom). (right) Reaction kinetics for 5% He/CO..... 109
Figure 5. 12 Mass spectrum of $\boldsymbol{Ag2+}$and $\boldsymbol{Ag2H+}$ in pure helium. Inset shows enlarged area in the rectangle. The peaks in between the $\boldsymbol{Ag2+}$ correspond to $\boldsymbol{Ag2H+}$..... 110
Figure 5. 13 Gas phase reactivity comparison of $\boldsymbol{Ag2+}$and $\boldsymbol{Ag2H+}$. a) Isotopic $MS^2$of selected peaks of both species and comparison with simulated mass spectrum. b) Mass spectra of reactions of each of the species with CO. 111
Figure 5. 14 Reactions spectra of palladium dimer. a) and b) monoisotopic peaks of $\boldsymbol{Pd2+}$and $\boldsymbol{Pd2H+}$respectively and c) comparison with simulated mass spectrum. d) mass spectrum of reactions of $\boldsymbol{Pd2+}$ with CO. The black square, triangle and circle represent $\boldsymbol{Pd2(CO)2+}$, $\boldsymbol{Pd2(CO)3+}$ and $\boldsymbol{Pd2(CO)4+}$ respectively. e) mass spectrum of reactions of $\boldsymbol{Pd2H+}$ with CO. T..... 112
Figure 5. 16 (top) DFT structures of $\boldsymbol{Au(CO)3+}$, $\boldsymbol{Au(CO)4+}$ and $\boldsymbol{Au(CO)5+}$. (bottom) Lowest energies of structures as a function of number of CO in the complex, for two different functionals. 114
Figure 5. 17 The chemical cycle of forming $\boldsymbol{Au(CO)3H6+}$. (top) a)-d) the stages in the production oh CHOH group on $\boldsymbol{Au(CO)2+}$. (bottom) the CHOH groups from 3 cycles combine with a gold atom to produce $\boldsymbol{Au(CO)3H6+}$. 115
Figure 5. 18 DFT structures of 1-4 molecules of CO coordinated to $\boldsymbol{Au2+}$ and $\boldsymbol{Au2H+}$. For $\boldsymbol{Au2+}$, the lowest energy structure and the structure with the biggest Au-Au distance is shown. 117
Figure 5. 19 Energy diagrams of a) $\boldsymbol{Au2(CO)n+}$ and b) $\boldsymbol{Au2H(CO)n+}$. The blue and red marks in a) represent the lowest energy structure and the structure with the greatest Au-Au distance..... 118

Figure 6. 1 a) Schematic of single-photon, two-photon and three-photon excitation. b) Fluorescing areas in single- and multi- photon excitation process used in microscopic imaging. 126
Figure 6. 2 General schematic representation of experimental setup used for measuring hyper-Rayleigh scattering.. 127

1. Introduction

Even though unknown, nanoparticles and nanoclusters have been in use throughout human history. This can be seen in objects like the stained glass, which was made by mixing of metal salts with molten glass during the glassmaking process. This would create a stable colloid of metallic particles which would modify the optical properties of glass to create the desired colouring[1,2]. The famous Damascus steel is another good example. Even though the exact technique of production is lost to history, modern analytical techniques reveal the existence of carbon nanotubes mixed in the crystal lattice of the steel giving it extraordinary mechanical properties that have earned its reputation[3].

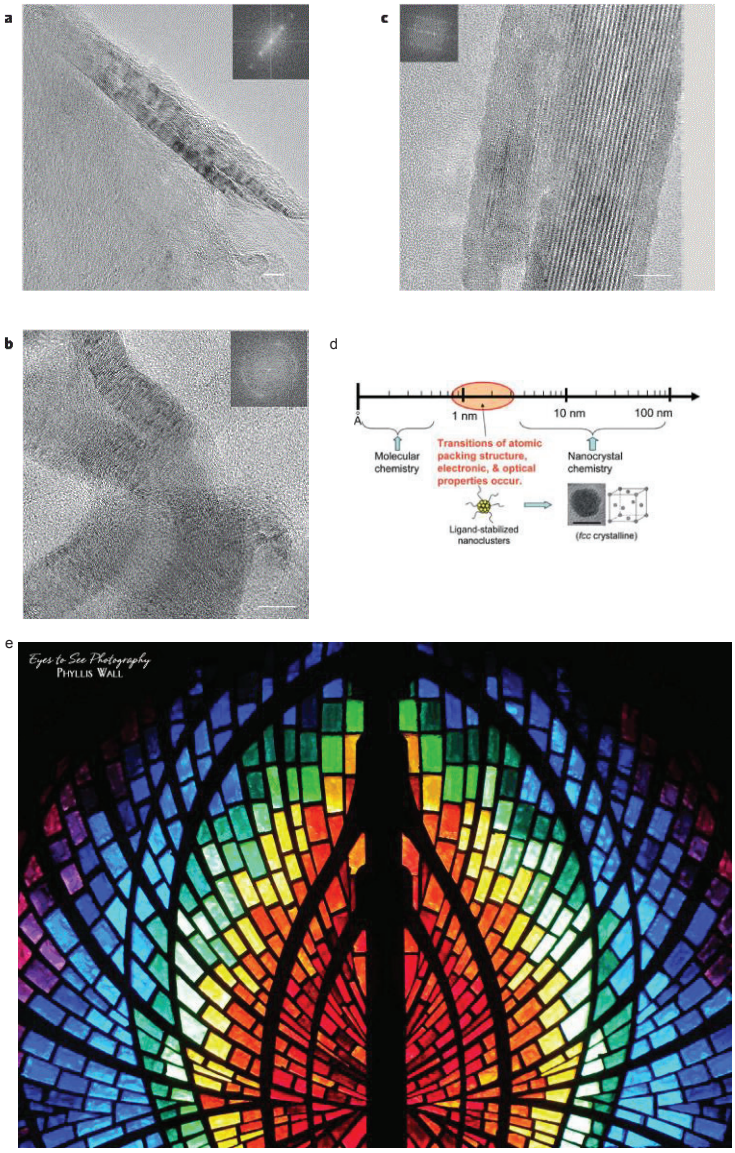

Figure 1. 1 a-c) TEM images of carbon nanotubes in an authentic Damascus sabre. Scale bars: 5nm, 10nm, 5 nm for a),b),c) respectively. d) Scale length of study for the metallic nanoclusters, between the nanocrystals and molecular chemistry. e)A multi-coloured stained glass motif. Different colouring was achieved by mixing of iron, manganese, chromium, vanadium and other transitional metal salts into the molten glass during the production process. a-c) reprinted with permission from reference [3] with permission from Nature Publishing Group. d) Reproduced from Ref. [4] with permission from the Centre National de la Recherche Scientifique (CNRS) and The Royal Society of Chemistry. e) Eyes to see, Phyllis Wall, Plainview, Texas.

Methodical scientific studies of small metallic particles start with Michael Faraday in 1857[5] and were continued by Gustov Mie in 1908[6]. The research of physical and chemical properties of metal clusters continued after that, but detailed understanding of their properties did not start until the 1960s and the development of the electron band theory[4]. Starting in the 1970s, the study of metal clusters has been rapidly increasing in popularity and attractiveness. It has also been supported by development of technology which provided new experimental techniques for producing and studying them. In recent decades, especially since the 1990s a tremendous advance has been achieved in nanoparticle research, both in regards to theoretical and experimental aspects. New techniques have been developed to synthesize nanoparticles of various sizes and composition, to study their structure and physical as well as chemical properties[1].

One of the main motivations to study small clusters is the interest in changing physical properties on small scales, from individual atoms to bulk material. These patterns did not come into focus until the early 80s with the work of the group of Walter Knight's which produced and studied the alkali metal clusters with up to 100 atoms[1,7]. This research uncovered the increasing stability of certain sizes of sodium clusters (8, 20, 40, 58 and 90), corresponding to shell closing of a one-electron shell model. For clusters of the simplest metals, the alkali and noble metals, the electronic structure is dominated by the number of valence electrons, and the ionic cores are of secondary importance. These electrons are delocalized, and the electronic system exhibits a shell structure that is closely related to the well-known nuclear shell structure[1,8]. The term nanoscale typically refers to a length scale of 1-100 nm, the domain between individual atoms and bulk solids. The term “nanocluster” is used to describe the smallest nanostructures of ~1-500 metal atoms. These can be free (or bare) metal clusters, or ligated i.e. protected and stabilised by certain molecules. These species have attracted significant attention because of their discrete electronic bands, and molecular like properties, which makes them and their properties fundamentally different than larger species whose properties are of plasmonic nature. Since in this regime the number of metal atoms influence the clusters properties significantly, the nomenclature M(n)L(n) is useful where M denotes the number of metal atoms and L is the number of ligand molecules.

1.1 Optical properties

Faradays studies of metallic nanoparticles were spurred by his fascinations with their optical properties. He was so intrigued by the ruby red colouring of gold colloid, so different from the colour of bulk gold, that he started studying the two phase system prepared by reduction of gold salt with white phosphorus[5]. This stimulated additional research in metal colloids. The research of optical properties was advanced by Gustov Mie who succeeded in describing the optical properties of gold nanoparticles by solving the Maxwell equations for a single gold particle[6]. The development of research of optical properties of nanoparticles today is driven by the numerous possibilities of application in biotechnology. It is of great interest for example to monitor particular biological processes. Various techniques are available for

doing this, but the standard organic dyes used suffer from a number of issues[9–12]. Metallic clusters have shown to modify the optical properties of chromophores[13,14]. As such they are good candidates for a new type of label free biosensors. For this purpose, peptide ligated small silver clusters systems in gas phase were studied, determining their stable structure, and shedding light on the mechanism of electronic excitations in such hybrid system, where, the addition of the silver cluster to the peptide significantly enhances its absorption, due to charge transfer from the metal cluster. This way the cluster can increase the ease of detection of the peptide, avoiding the chemical coupling seen in organic dyes. Therefore these small systems may present suitable building blocks for future applications[15]. Additionally, metallic clusters have shown to possess quite strong non-linear optical response, particularly two photon absorption (TPA) in the case of gold clusters, which makes them suitable candidates for biological imaging, particularly multi-photon microscopy. Due to transparency of biological tissues to near infra-red (NIR) light, contrast agents with strong absorption in the NIR region are of interest[16,17]. Some research on gold clusters capped with glutathione has shown them to possess strong one- and two-photon emission, which paired with their photostability and non-toxicity makes them very promising candidates for non-linear optics applications[18,19].

1.2 Chemical properties

Modern technology and industry rely a great deal on chemistry and chemical reactions in order to process the raw materials found in nature into usable technological components. It is therefore of continuous interest and importance to find ways to optimise the chemical reactions most often used in industry. At the same time there is an increasing need for environmental protection and preservation in the modern industrialised world. The need for higher efficiency in reactions and processes which minimise the production of useless or harmful by products has driven the search for new kinds of catalysts for years in order to find suitable materials capable of efficiently promoting the desired reactions, while inhibiting the unwanted ones. These principles are the main guidelines of what is today known as green chemistry. The reactions recognised as the most important for the chemical industry in the context of green chemistry are: the selective transformation of methane, aerobic oxidation of alcohols and selective oxidation of CO.

The chemical properties of metal clusters are very interesting for potential uses in industrial chemical reactions, namely as catalysts. This comes from their ability to act as active sites, in addition to drastic change of properties with even a small change in structure or number of atoms. This gives great possibilities in tuning the reactivity of the clusters or selectivity of the reaction. The initial investigations on clusters in the gas phase probed some of the important reactions like O_2 activation, C-H bond cleavage, C-C scission and hydrocarbons oxidation[20].

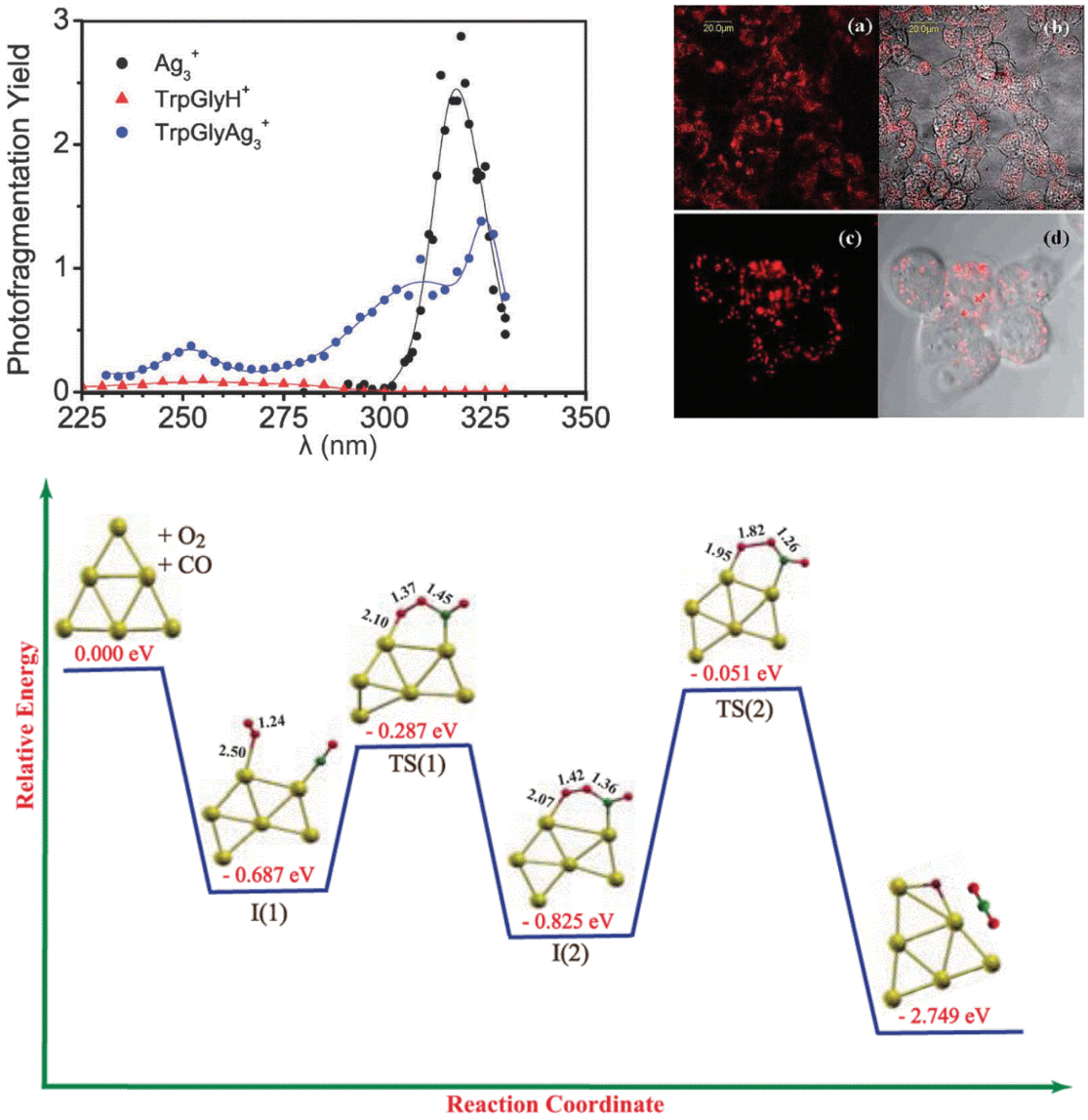

Figure 1. 2 (Top left) Photofragmentation yield fir bare Ag_3^+ cluster, peptide alone and metal-peptide hybrid, shows how the silver cluster modifies the optical properties of the peptide. (Top right) a) one-photon, c) two photon excitation fluorescence of neuroblastoma cells. b) and d) Fluorescence images overlaid with differential interference contrast images to show the outlines of cells. (Bottom) Reaction pathway of CO oxidation mediated by the Au_6 cluster. (Top left) Reproduced from Ref. [15] *with permission from the PCCP Owner Societies (Top right) Reproduced from Ref.* [18] *with permission from the Centre National de la Recherche Scientifique (CNRS) and The Royal Society of Chemistry. (Bottom) Reprinted with permission from Manzoor, D. Pal, S.; J. Phys. Chem. C, 2014, 118, 30057-30062 . Copyright 2014 American Chemical Society.*

They present the basis of knowledge today in regards to the chemical activity of the metal clusters. Detailed chemical studies of reactions mediated by the metal clusters encounter many difficulties in the condensed phase, such as influence from the solvent, and the fact that many catalytic processes are in fact heterogeneous. For this reason mass spectrometry, and the possibilities it offers in the study of metallic clusters in the gas phase is an invaluable tool in this branch of research. The coupling of electrospray ionization (ESI) with quadrupole ion trap (QIT) provides a "complete gas phase chemical laboratory"[21–23]. Ion traps make it easy to mass select individual species and test their reactivity. Furthermore because of the very high sensitivity of detection in mass spectrometry, reaction products can be detected even in cases of low reactivity reactants. In complement with computational methods it

is possible to study structure and size effects of the bare metal clusters and ligated clusters as well as their interactions in chemical reaction. On the way to realistic functional new catalysts still many obstacles remain. Even though some studies have been able to investigate clusters under realistic conditions[24–31], a lot of research is still carried out in well controlled environment, which, though suitable for study of basic properties does not give good representation of the suitability for real-world use. One of the problems as well is the scaling of production process, as the current methods of producing metallic nanoclusters are suitable only for very low quantities. New techniques are currently in development to address these issues as well.

In this thesis I present my work on small, bare and ligated clusters of noble metals, focusing on nickel and copper group. First, in Chapter 2 I give an overview and basic principles behind the methods used, and the detailed description of the experimental setup. During the development of the setup, influence of various parameters were tested. Chapter 3 focuses on wet chemistry synthesis of thiolated gold, silver and copper clusters and complexes, which were tested in the mass spectrometer and subsequently used for comparison with the species generated by the LAVESI setup. In Chapter 4 I describe the results with metal oxides, hydroxides and nitrides, where we investigate their stability and fragmentation channels. Also, the chapter deals with the complexes of gold, silver and copper ligated by thioglycolic acid. The results with ligated LAVESI species and small complexes obtained with wet chemistry have already been published. The paper in question can be found in Appendix 1. The gas phase reactions, mainly with CO, and some with NO are described in Chapter 5. Special attention is given to the difference in reactivity and stability of metallic M_2^+ and M_2H^+ species with CO. Some DFT calculations have been done in order to better understand this effect. Finally, Chapter 6 gives a short introduction to non-linear optics, the main principles and some application prospects. It is intended to give the reader a broader background of the subject presented in the paper in Appendix 2 which presents an investigation of non-linear properties of glutathione ligated gold clusters in solution.

Bibliography

1. De Heer, W. A. The physics of simple metal clusters: Experimental aspects and simple models. *Rev. Mod. Phys.* **65,** 611–676 (1993).

2. De Jong, B. H. W. S., Beerkens, R. G. C. & van Nijnatten, P. A. in *Ullmann's Encyclopedia of Industrial Chemistry* (Wile & Co., 2000).

3. Reibold, M. *et al.* Materials: Carbon nanotubes in an ancient Damascus sabre. *Nature* **444,** 286–286 (2006).

4. Jin, R. Quantum sized, thiolate-protected gold nanoclusters. *Nanoscale* **2,** 343–362 (2010).

5. Faraday, M. The Bakerian Lecture: Experimental Relations of Gold (and Other Metals) to Light. *Philos. Trans. R. Soc. London* **147,** 145–181 (1857).

6. Mie, G. Beiträge zur Optik trüber Medien, speziell kolloidaler Metallösungen. **330,** 377 (1908).

7. Knight, W. D. *et al.* Electronic shell structure and abundances of sodium clusters. *Phys. Rev. Lett.* **52,** 2141–2143 (1984).

8. Kappes, M. M., Kunz, R. W. & Schumacher, E. Production of large sodium clusters (Nax, x < 65) by seeded beam expansion. *Chem. Phys. Lett.* **91,** 413–418 (1982).

9. Eggeling, C., Widengren, J., Rigler, R. & Seidel, C. A. M. Photobleaching of Fluorescent Dyes under Conditions Used for Single-Molecule Detection: Evidence of Two-Step Photolysis. *Anal. Chem.* **70,** 2651–2659 (1998).

10. Schmidt, T., Kubitscheck, U., Rohler, D. & Nienhaus, U. Photostability Data for Fluorescent Dyes: An Update. *Single Mol.* **3,** 327–327 (2002).

11. Hoogenboom, J. P., Hernando, J., van Dijk, E. M. H. P., van Hulst, N. F. & García-Parajó, M. F. Power-Law Blinking in the Fluorescence of Single Organic Molecules. *ChemPhysChem* **8,** 823–833 (2007).

12. Lill, Y. & Hecht, B. Single dye molecules in an oxygen-depleted environment as photostable organic triggered single-photon sources. *Appl. Phys. Lett.* **84,** 1665 (2004).

13. Lakowicz, J. R. Radiative decay engineering 5: metal-enhanced fluorescence and plasmon emission. *Anal. Biochem.* **337,** 171–194 (2005).

14. Zhao, Jensen, L. & Schatz, G. C. Pyridine−Ag 20 Cluster: A Model System for Studying Surface-Enhanced Raman Scattering. *J. Am. Chem. Soc.* **128,** 2911–2919 (2006).

15. Bonačić-Koutecký, V. *et al.* Silver cluster–biomolecule hybrids: from basics towards sensors. *Phys. Chem. Chem. Phys.* **14,** 9282 (2012).

16. Escobedo, J. O., Rusin, O., Lim, S. & Strongin, R. M. NIR dyes for bioimaging applications. *Curr. Opin. Chem. Biol.* **14,** 64–70 (2010).

17. Hu, R. *et al.* Functionalized near-infrared quantum dots for in vivo tumor vasculature imaging. *Nanotechnology* **21,** 145105 (2010).

18. Polavarapu, L., Manna, M. & Xu, Q.-H. Biocompatible glutathione capped gold clusters as one- and two-photon excitation fluorescence contrast agents for live cells imaging. *Nanoscale* **3,** 429–434 (2011).

19. Ramakrishna, G., Varnavski, O., Kim, J., Lee, D. & Goodson, T. Quantum-sized gold clusters as efficient two-photon absorbers. *J. Am. Chem. Soc.* **130,** 5032–5033 (2008).

20. Tyo, E. C. & Vajda, S. Catalysis by clusters with precise numbers of atoms. *Nat. Nanotechnol.* **10,** 577–588 (2015).

21. Porter, C. J., Beynon, J. H. & Ast, T. The modern mass spectrometer—a complete chemical laboratory. *Org. Mass Spectrom.* **16,** 101–114 (1981).

22. Brunnée, C. The ideal mass analyzer: Fact or fiction? *Int. J. Mass Spectrom. Ion Process.* **76,** 125–237 (1987).

23. O'Hair, R. a J. The 3D quadrupole ion trap mass spectrometer as a complete chemical laboratory for fundamental gas-phase studies of metal mediated chemistry. *Chem. Commun. (Camb).* 1469–1481 (2006).

24. Lee, S. *et al.* Selective Propene Epoxidation on Immobilized Au 6-10 Clusters: The Effect of Hydrogen and Water on Activity and Selectivity. *Angew. Chemie Int. Ed.* **48,** 1467–1471 (2009).

25. Lei, Y. *et al.* Increased Silver Activity for Direct Propylene Epoxidation via Subnanometer Size Effects. *Science (80-.).* **328,** 224–228 (2010).

26. Vajda, S. *et al.* Subnanometre platinum clusters as highly active and selective catalysts for the oxidative dehydrogenation of propane. *Nat. Mater.* **8,** 213–216 (2009).

27. Yin, F., Lee, S., Abdela, A., Vajda, S. & Palmer, R. E. Communication: Suppression of sintering of size-selected Pd clusters under realistic reaction conditions for catalysis. *J. Chem. Phys.* **134,** 141101 (2011).

28. Deng, W. *et al.* Cleavage of the C–O–C bond on size-selected subnanometer cobalt catalysts and on ALD-cobalt coated nanoporous membranes. *Appl. Catal. A Gen.* **393,** 29–35 (2011).

29. Negishi, A. *et al.* Size-selective formation of tungsten cluster-containing silicon cages by the reactions of Wn+(n=1–5) with SiH4. *Chem. Phys. Lett.* **388,** 463–467 (2004).

30. Kwon, G. *et al.* Size-Dependent Subnanometer Pd Cluster (Pd 4 , Pd 6 , and Pd 17) Water Oxidation Electrocatalysis. *ACS Nano* **7,** 5808–5817 (2013).

31. Bonanni, S., Aït-Mansour, K., Harbich, W. & Brune, H. Effect of the TiO 2 Reduction State on the Catalytic CO Oxidation on Deposited Size-Selected Pt Clusters. *J. Am. Chem. Soc.* **134,** 3445–3450 (2012).

2 Experimental techniques and setup

2.1 Mass spectrometry

Mass spectrometry (MS) is an analytical technique widely used in physics, chemistry, biology, biochemistry, pharmacy and medicine. It is a way of "weighting" molecules and atoms, and it can provide us with the information about the molecular weight of the compound or compounds in the sample, structure, as well as elemental composition of molecule and its fragments, and relative isotopic abundancies if elements. The basic principle of MS is to generate ions from a sample we wish to analyse, separate them according to their mass to charge ratio (*m/z*) and detect them based on this separation principle. Therefore a typical mass spectrometer consists of an ion source, mass analyser and a detector, all connected to a data system which records the data, and (in case of modern systems) controls the whole device (Figure 2. 1).

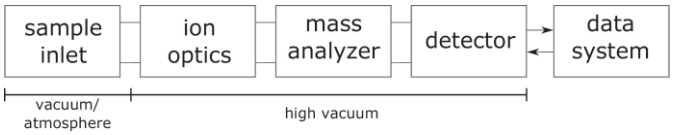

Figure 2. 1 General schematic of a mass spectrometer.

There are numerous methods for ionising the analyte, and the one most relevant to this work (Electrospray Ionisation - ESI) will be discussed in detail in the next chapter. Detected ions can be singly or multiply charged atoms, clusters, molecules or their fragments and aggregates. Due to this versatility, MS is used for various applications, such as analysis of combinatorial libraries[1], sequencing biomolecules, and determining protein structure, function, and interactions[2–4]. MS is also important in single cell exploration and drug exploration (both during the development phase as well as quality control). Coupled with techniques like High Performance Liquid Chromatography (HPLC) and Pipette Tip-matrix Solid Phase Dispersion (PT-MSPD) MS is used in food quality control, for example, to determine antibiotic sulphonamide levels in milk[5], fish[6] and other marine products[7]. Due to high sensitivity MS is also suitable for inorganic trace analysis, to determine the presence of inorganic impurities, in high-purity materials (alloys, semiconductors, chemical reagents, thin films, etc.)[8]. This is also important in environmental and geosciences for water and soil contamination control[8], and the analysis and understanding of atmospheric aerosols [9] which greatly influence visibility, Earth's energy balance, and hydrological cycle. It has even found application in modern astronomy and astrophysics where it is used for analysis of solar wind composition and determining chemical compositions of other hard bodies in the Solar system (planets, planetoids, comets). Through MS techniques we have obtained first information about atmospheric composition of Mars[10] and first evidence of existence of molecular oxygen on a comet[11]. In the world of professional sports, it is used for forbidden substance testing and control in athletes[12,13] (Figure 2. 2).

Principles of MS were established in the late 19th and early 20th century. First mass spectrometry experiments are attributed to J.J. Thomson, who, after the discovery of electron and winning the physics Nobel Prize in 1906 turned to the study of so called "rays of positive electricity", "anode rays" or "kanalstrahlen". He used the electric gas discharge device, with the parabolic slit, to record what is probably the first mass spectrum in history (Figure 2. 2). Over the next several decades this work was resumed and improved primarily by Francis William Aston and Arthur Jeffrey Dempster. At this time, due to low mass range and limited capabilities, mass spectrometry was used as a physics tool, to determine the masses and relative abundances of elements and their isotopes. While Thompson foresaw the analytical utility of MS in organic chemistry and biology as early as 1911, and tried to promote it [14,15], it wasn't until the 1930s that researchers outside of physics community decided to apply mass spectrometry to their fields. At this time, most of the mass spectrometers were still home-made in the labs, though, some commercial options have started to emerge. The first commercial mass spectrometer, called 21-101, was developed by Consolidated Engineering Corporation (CEC) in 1943 for Atlantic Refining Company[16].

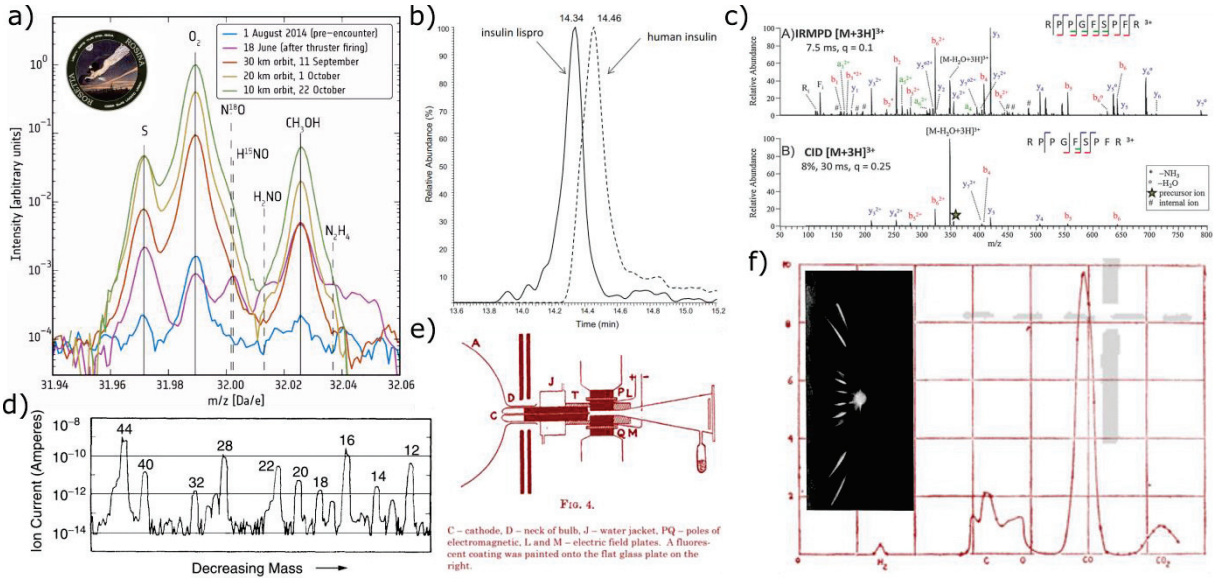

Figure 2. 2 a) Mass spectrum of 67-P/Churyumov-Geraschimenko comets coma, obtained by ROSINA-DEMS mass spectrometer device mounted on Rosetta spacecraft. b) Human insulin spiked with synthetic insulin lispro, obtained in MS analysis of an athlete's urin sample. c)(top) Infra-red photodissociation and (bottom) colli sion induced dissociation mass spectrum of bradykinin. d) First mass spectrum of Martian atmosphere recorded at 135km by Viking 1 spacecraft in 1976. Shows the presence of CO_2, Ar, N_2, O_2 as well as O and CO. e) Schematic of one of the first mass spectrometers, a parabola mass spectrometer which used photographic plates as detectors. f) Probably the first mass spectrum in history, recorded by Thompson in 1912. (inset) photograph of a parabola mass spectrum recorded on a photographic plate. a) Reprinted by permission from Macmillan Publishers Ltd: Nature, Bieler et. al, 526, 7575, 678-68, copyright 2015. b) Reprinted from J. Chromatogr. A, 1292, Thevis et. al, 1292, 50, 2013 2013, with permission from Elsevier. c) Reprinted from ref [4] with permission of The Royal Society of Chemistry. d) Reprinted from ref [10] with permission of John Wiley & Sons. e), f) Reprinted from ref [15] with permission of The Royal Society.

This also marks the advent of use of MS in organic chemistry, for understanding the interactions of organic ions in the gas phase. Development of this application led to first direct observation of the monomeric metaphosphate ion (PO_3^-) in 1979[17], and the detection of buckminsterfullerene by Kroto and Smalley in 1985[18] and its subsequent investigation[19].

While the first MS instruments were mostly magnetic sector type instruments, quickly the new experimental setups started to emerge. The Time of Flight Mass Spectrometry (TOF-MS) was introduced in 1943 by William Stephens[20], and by 1953 Wolfgang Paul has started his work on RF ion traps[21]. Another widely used type of ion trap, the Fourier Transform Ion Cyclotron Resonance (FT-ICR), was developed in 1974 by Marshall and Comisarow[22].

2.1.1 Ion traps

Ion traps are devices for storing ions in a gas phase, so that they can be studied experimentally. They use electric and magnetic fields to keep the ions in stable trajectories. Ion traps play a very important role in mass spectrometry, and in laser spectroscopy of ions as the spatial confinement makes the ion cloud and laser beam intersection suitable. Ion trapping pioneers Hans G. Dehmelt and Wolfgang Paul have been awarded 1989 Nobel Prize in physics for their work on the development of ion trapping techniques.

RF traps

Also known as Paul traps, in RF traps, the ion trapping is achieved without using any magnetic fields for confinement, and accomplishing it only with radiofrequency (RF) fields. In order to better understand their function, we shall derive some of the equations that govern their operation. The electric potential for this kind of trapping system will be considered first, and afterwards we will look at the ion trajectories in the trap.

With the assumptions of $\vec{B} = \vec{0}$ (from the definition of RF trap), and $\nabla \cdot \vec{E} = const.$ we get the expression for the electric field

$$\vec{E} = E_0(\lambda x\hat{\imath} + \sigma y\hat{\jmath} + \gamma z\hat{k}) \tag{2.1}$$

In the absence of charge, the Laplace equation for our case becomes:

$$\nabla \cdot \vec{E} = 0 \tag{2.2}$$

And therefore

$$\lambda + \sigma + \gamma = 0. \tag{2.3}$$

One of the possible solutions is the case when $\lambda = -\sigma$ and $\gamma = 0$, reducing the problem to two dimensions. This is the case of 2D quadrupole ion trap. Another example of RF trap is a 3D quadrupole ion trap, when $\lambda = \sigma$ and $\gamma = -2\sigma$.

The electric field $\vec{E}$ can be expressed as:

$$\vec{E} = \nabla\Phi \tag{2.4}$$

Which, written by components is:

$$E_x = -\frac{\partial\Phi}{\partial x} \tag{2.5}$$

$$E_y = -\frac{\partial\Phi}{\partial y} \tag{2.6}$$

$$E_z = -\frac{\partial\Phi}{\partial z} \tag{2.7}$$

Integration gives:

$$\Phi = -\frac{E_0}{2}(\lambda x^2 + \sigma y^2 + \gamma z^2) \tag{2.8}$$

Which is the general form of electric potential in the RF trap.

2D quadrupole ion trap

As was said before, one of the solutions to Laplace equation is obtained in case of $\lambda = -\sigma$ and $\gamma = 0$. This makes the electric potential become:

$$\Phi = -\frac{E_0\lambda}{2}(x^2 + y^2) \tag{2.9}$$

This type of field corresponds to the shape of a "saddle", or more precisely a hyperbolic paraboloid (Figure 2. 3), and can be achieved by four electrodes with hyperbolic cross sections (Figure 2. 3), when all electrodes are set to the potential of the same magnitude, but different polarity between adjacent electrodes. For ease of production sometimes electrodes of circular profile are used (Figure 2. 3). If the radius of the rods is $R = 1.1468$[23], the circular electrodes approximate the field of the hyperbolic ones. However, even slight mechanical imprecisions and deformations, as well as outside fields can perturb their performance. Repeated measurements, as well as calculations have investigated the difference in performance of the hyperbolical and circular electrodes (Figure 2. 3). If the distance between two opposite electrodes is defined as $2r_0$ (Figure 2. 3) and $\Phi_0 = -E_0\lambda$ we can rewrite the electric potential as:

$$\Phi = -\frac{\Phi_0}{r_0^2}(x^2 + y^2) \tag{2.10}$$

We can now write the equations of motion for an ion in the electric field. Starting from Newton's second law of motion and $\vec{F} = e\vec{E}$, and separating by components we get:

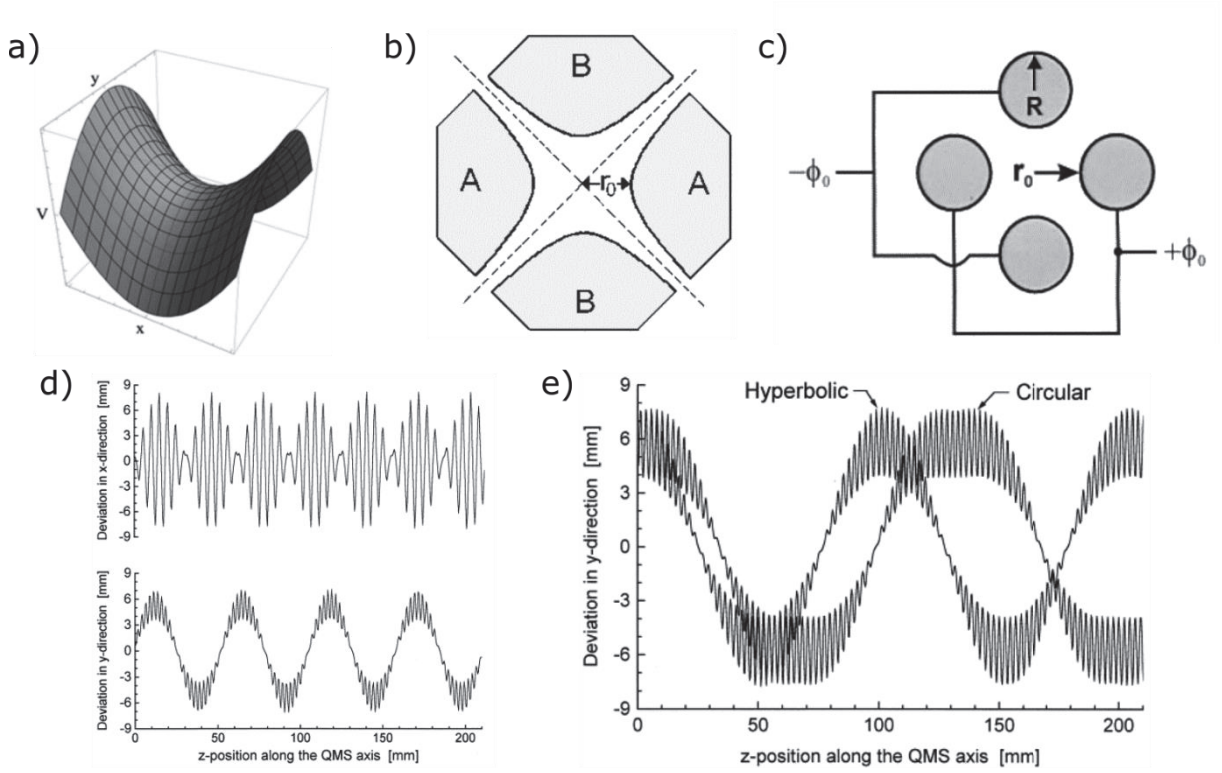

Figure 2. 3a) quadrupole potential b) cross section of a linear quadrupole ion trap with hyperbolic electrodes c) cross section of a linear quadrupole ion trap with circular electrodes d) x and y direction ion motion in the ion trap e) y direction ion motion comparison between circular and hyperbolic electrodes. b), d), e) Reprinted with permission of Springer, Mass spectrometry, Instrumentation, 2011, Jürgen H. Gross. a), c) Reprinted from "Laser Photodissiciation and Spectroscopy of Mass-separated Biomolecular Ions", chapter 3, volume 83, 2013, N. c; Polfer, P. Dugourd, With permission of Springer.

$$m\frac{d^2x}{dt^2} = eE_x \tag{2.11}$$

$$m\frac{d^2y}{dt^2} = eE_y \tag{2.12}$$

$$m\frac{d^2z}{dt^2} = eE_z \tag{2.12}$$

By inserting our potential we get:

$$\frac{d^2x}{dt^2} + \frac{2e}{mr_0^2}\Phi_0 x = 0 \tag{2.13}$$

$$\frac{d^2y}{dt^2} - \frac{2e}{mr_0^2}\Phi_0 y = 0 \tag{2.14}$$

$$\frac{d^2z}{dt^2} = 0 \tag{2.15}$$

In the case when Φ_0 is time independent, the ion motion becomes simple harmonic oscillations in *xz* plane ($x(t) = C_2 \sin\left(\sqrt{\frac{2e}{mr_0^2}\Phi_0 t}\right) + C_1\cos(\sqrt{\frac{2e}{mr_0^2}\Phi_0 t})$), and are therefore stable, but in *yz* plane the motion will be unstable ($y(t) = C_2 e^{\sqrt{\frac{2e}{mr_0^2}\Phi_0 t}} + C_1 e^{-\sqrt{\frac{2e}{mr_0^2}\Phi_0 t}}$).

Instead we can choose $\Phi_0 = U - Vcos\Omega t$, where U is a DC voltage on the electrodes, V is the amplitude of RF oscillating field, and Ω is the angular frequency of oscillations. The equations of motion then become:

$$\frac{d^2x}{dt^2} + \frac{2e}{mr_0^2}(U - Vcos\Omega t)x = 0 \tag{2.16}$$

$$\frac{d^2y}{dt^2} - \frac{2e}{mr_0^2}(U - Vcos\Omega t)y = 0 \tag{2.17}$$

By introducing the substitution

$$a_u = a_x = -a_y = \frac{8eU}{m\Omega^2 r_0^2} \tag{2.18}$$

$$q_u = q_x = -q_y = \frac{4eV}{m\Omega^2 r_0^2} \tag{2.19}$$

$$\xi = \frac{\Omega t}{2} \tag{2.20}$$

And simplifying the resulting expression, we get:

$$\frac{d^2u}{d\xi^2} + (a_u - 2q_u cos2\xi)u = 0 \tag{2.21}$$

Which is the canonical form of the Mathieu equation. The detailed discussion of the solutions of Mathieu equation and their determination (be it algebraic or numerical) is very complex[24], and will not be discussed here.

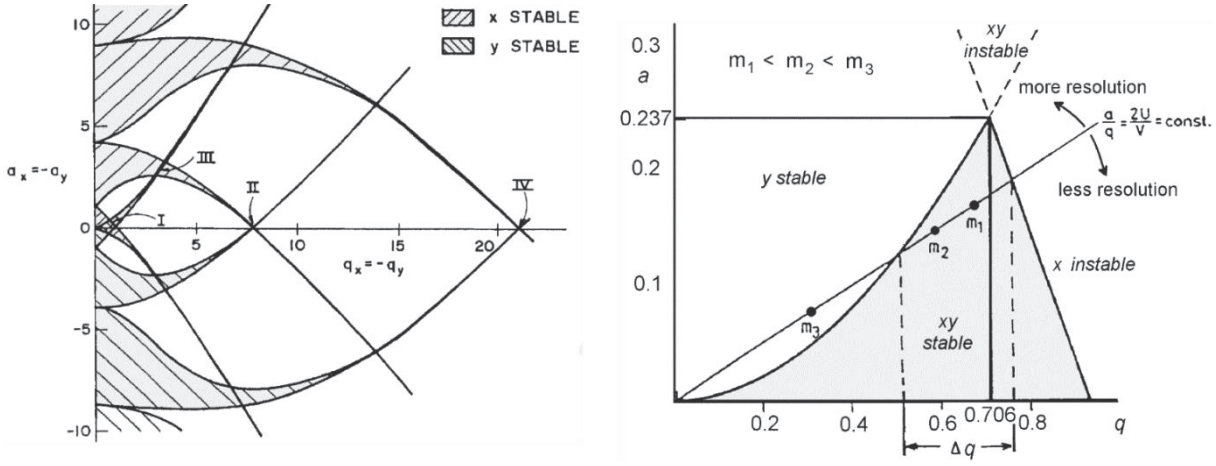

Figure 2. 4 (left) Regions of stability of ion trajectories for a given pair of values of a and q parameters. (right) Region I enlarged. The a/q line line traverses the ion stabilty region, showing how scanning the U and V values provides stability for different ion masses, enabling the use of quadrupole trap as a mass analyzer. Reprinted with permission of Springer, Mass spectrometry, Instrumentation, 2011, Jürgen H. Gross.

In the context of ion motion in a trap, we will divide the solutions into two groups[25]:

1. Stable motion – the particles oscillate in *xy* plane with finite amplitudes, and go through the quadrupole field without colliding with the electrodes (Figure 2. 3d).
2. Unstable motion – the amplitudes grow exponentially in *xy* plane, and the ions are lost.

We plot the parameter a_u versus parameter q_u, to obtain the stability diagram for a two-dimensional quadrupole field (Figure 2. 4). We can see that regions of stability emerge in either *x*, *y*, or both directions. There are four regions in the plot where both *x* and *y* trajectories are stable. Of special interest is the region I, shown in Figure 2. 4, for $a_u \in \langle 0,0.237 \rangle$ and $q_u \in \langle 0,0.908 \rangle$, as this is where the operations of an ion trap take place.

Linear quadrupole can also be used as a mass analyser. With a smart choice of RF and DC voltage ratios we can achieve a transmission of ions in a very narrow mass range. If the a/q ratio is chosen so that

$$a = 0.237, q = 0.706 \Rightarrow \frac{a}{q} = 0.336 \tag{2.22}$$

the stability region is reduced to a single point. By varying the values of a and q (which is achieved by varying U and V), we can get an increasingly wider m/z range to be transmitted through the trap (Figure 2. 4). Varying the U and V in time with a fixed ratio enables us to scan through the masses trapped, thus obtaining the mass spectrum. The steeper the a/q line selected, the higher the resolution will be, but at the cost of lower signal intensity, due to a lower number of ions being transmitted.

The analysis so far has been focused on the stability of motion in *xy* plane, while the motion along the z axis has been ignored. The trapping of the ions along the *z*-axis can be achieved by adding an additional electric field (induced by two additional electrodes added to the front and back ends of the trap), with a minimum in the centre of the trap. The potential at the entrance to the trap is set to be just below the kinetic energy of incoming ions, while the potential at the end is higher, so as to stop the ions from exiting the trap. In order to prevent the ions from rebounding from the back-end potential barrier and escaping the trap through the front entrance again, a so called buffer gas is added into the trap. Collisions with the gas particles reduce the kinetic energy of the ions below the entrance barrier, so that they remain confined. Through these collisions the ions are thermalized and successfully trapped in the minimum of the trapping potential. As a result, the ion cloud gradually shrinks, until the shrinking force of the trapping field is counteracted by the Coulomb repulsion force.

Since the motion of ions inside the trap is governed by RF fields, the total motion of the ion cloud is a superposition of several frequency modes. The lowest frequency is called the macromotion or secular frequency and can be written as

$$\omega_0 \approx \frac{q\Omega}{\sqrt{8}} \tag{2.23}$$

3D quadrupole ion trap

As stated above, another simple solution for electric potential with Laplace constraints exists, and is obtained by choosing $\lambda = \sigma$ and $\gamma = -2\sigma$ and substituting them into:

$$\Phi = -\frac{E_0}{2}(\lambda x^2 + \sigma y^2 + \gamma z^2) \tag{2.24}$$

Thus we obtain the electric potential inside the 3D quadrupole ion trap:

$$\Phi = -\frac{E_0}{2}(x^2 + y^2 - 2z^2) \tag{2.25}$$

3D quadrupole trap consists of three electrodes; two endcap electrodes, and one ring electrode, all of them with hyperbolical inner surfaces (Figure 2. 5).

Following the same procedure as for 2D traps, we can derive the equations for ion trajectories inside the trap, and by choosing the appropriate substitution

$$a_u = a_z = -2a_r = \frac{-16eU}{m\Omega^2(r_0^2+z_0^2)} \tag{2.26}$$

$$q_u = q_z = -2q_r = \frac{8eV}{m\Omega^2(r_0^2+z_0^2)} \tag{2.27}$$

We obtain, once again, the Mathieu equation.

As before, we will not concern ourselves with solving the Mathieu equation, but rather with the nature, i.e. the stability of the ion trajectories, these solutions represent. For this reason we introduce the parameter β_u as

$$\beta_u \approx \sqrt{a_u + \frac{q_u^2}{2}} \tag{2.28}$$

Ions achieve stable trajectories for $0 < \beta_u < 1$. In Figure 2. 5 the stability regions for z direction are shown. When using the 3D ion quadrupole trap as a mass analyser, there are two methods by which we can eject the ions from the trap. The first one, relies on the ejection of ions at the stability limit. If we apply the same DC voltage at both endcap electrodes, then $a_z = 0$, and therefore the stability of the ions in the trap depends solely on q_z. Since q_z is dependant on m/z value (Figure 2. 5), changing it, changes the stability limit for a particular ion. Therefore, by linearly increasing the RF voltage, we sequentially destabilise the trajectories of bigger and bigger ions, ejecting them from the trap and obtaining the mass spectrum. The second mass analysing method is based on secular frequency of ions for resonant ejection. This means resonantly exciting their periodic motions in the trap. In a 3D trap, ions oscillate in the parabolic potential wells in radial and axial directions, with the secular frequency

$$\omega_u = (n + \frac{2\beta_u}{2})\Omega \tag{2.29}$$

For resonant ejection, the lowest mode $(n = 0)$, in the axial direction is selected, and an RF voltage resonant with the secular frequency is applied to the endcaps, gradually increasing the ions amplitude. When the amplitude is big enough, the ion is ejected from the trap and onto the detector. This method is useful in tandem MS, as both ions with larger and smaller mass than the isolated one can be ejected from the trap (Figure 2. 5).

2.1.2 Detectors

There are many different types of detecting devices used in MS. The simplest type is a Faraday cup, normally used in atomic isotope ratio measurement, an electrode on which the incoming ions deposit their charge. For early mass spectrometers, and for some types of magnetic sector instruments, photographic plates have been used as detectors. For scanning types of instruments, detectors working on the principle of secondary electron emission are commonly used. These include secondary electron multipliers (SEM), channel electron multipliers (CEM), conversion dynodes etc. For some types of MS, for example high mass TOF-MS, special cryogenic detectors are in use.

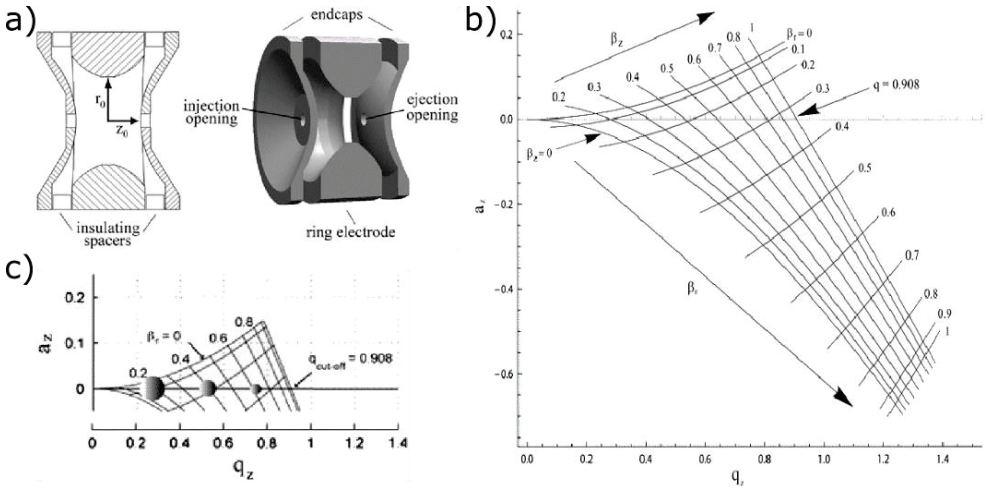

Figure 2. 5 a) Schematics and constituting parts of a 3D quadrupole ion trap. b) a-q plot of stability regions for ion trajectories. c) q-m/z dependence. By increasing RF voltage, the stability region moves to the left, sequentially ejecting the ions. Reprinted from "Laser Photodissiciation and Spectroscopy of Mass-separated Biomolecular Ions", chapter 3, volume 83, 2013, N. c; Polfer, P. Dugourd, With permission of Springer.

Channel electron multiplier

Electron multiplier detectors use secondary electron emission of materials to amplify the current caused by incident ions, enough so, that it can be detected. When a surface of a material is bombarded by a stream of electrons, some of the electrons in the surface are given enough energy to break off from the material. This process is governed by two main parameters: the electronic work function of the material

and the kinetic energy of incident electrons. The lower the former, and the higher the latter, the more electrons will be emitted from the surface. Thus, given enough energy, an incident electron can cause the emission of several secondary electrons.

Channel electron multiplier is essentially a glass tube coated with a material of suitably low electronic work function (lead oxide, silicone oxide, etc.), whose ends are held at electric potential difference, typically of 1-2kV. Primary electrons enter the tube at an angle and strike the tubes side, causing secondary electron emission. Due to the potential difference applied to the ends of the channel, the stream of secondary electrons is accelerated in the electric field, so that when they strike the opposite side of the tube, they cause the emission of more electrons (Figure 2. 6). The repetition of this process creates a cascade of electrons which is then collected by an electrode placed at the end of the tube. Sometimes, a modified, curved, design of the multiplier tube is used, because for gains greater then 10^4, random contributions to the signal may arise due to the ions of residual gas in the tube. Curved design shortens their flight paths, reducing the noise (Figure 2. 6).

Conversion dynode

The electron multiplier devices such as SEMs, CEMs and MCPs, show discrimination of slower ions compared to faster, and thus a reduction in sensitivity for ions below a certain velocity threshold. This translates to reduced sensitivity for high-mass ions. Thus, conversion dynodes were developed. A conversion dynode is a robust electrode, which uses high voltage of appropriate polarity to attract the ions coming out of the mass analyser. The ions impact on the dynode creates secondary electrons which are then used for detection, usually with a SEM or a CEM (Figure 2. 6). If the conversion dynode is placed perpendicular to the direction of the ion beam coming out of the mass analyser, the electrons and residual neutrals are prevented from reaching the detector.

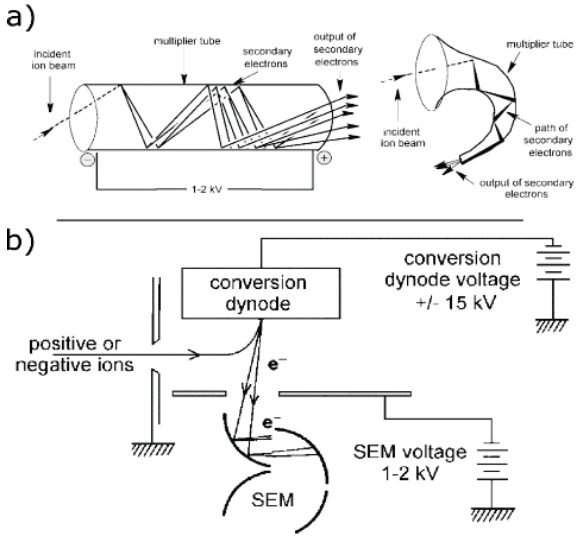

Figure 2. 6 a) Schematics of linear and curved channel electron multiplier. b) The operation of a conversion dynode. Reprinted with permission of Springer, Mass spectrometry, Instrumentation, 2011, Jürgen H. Gross.

2.2 Electrospray Ionisation

A very commonly used method for ionisation of analytes and their transfer to the gas phase is Electrospray Ionisation (ESI). It is a soft ionization technique where the solution is put under high voltage in order to spray the charged droplets toward a counter electrode. ESI is very widely used, owing to its versatility and ability to produce intact, multiply charged ions from large and rather fragile species[26]. It makes it an effective physical-chemistry tool. The electrospray technique is a member of a larger family of spray ionization techniques. The three important members of this family are the thermospray (TS), aerospray (AS) and the electrospray (ES). They all use the same basic mechanism of producing ions. The ES developed during 1960s through 1980s, from the free-jet experiments with molecular beams, through the work of Malcolm Dole[27], and building on his experiments, John B. Fenn[28] (Figure 2. 7). The principle of ESI revolves around pushing the analyte solution through a thin capillary and applying a high voltage onto it. This leads to the formation of a so called Taylor cone, from which under the influence of the electric field droplets break off. The droplets are sequentially reduced in size until we are left with ions in the gas phase.

The softness of ESI has made it a method of choice in MS characterisations of biological macromolecules. It is therefore understandable that some time has passed since the first ideas and applications of ESI-MS, to their use in studying the transitional metal complexes in 1990[29]. The use of ESI in study of these transition metal complexes is two-pronged. It can be used for mass spectrometric characterisation of solution based species, and also as a means of researching the transition metal intermediated in gas phase reaction, usually with the aid of collisional energy activation and/or dissociation to obtain structural information as well [30].

2.2.1 Electrospray mechanism

The ESI is a very complex technique, and as such its performance depends on many parameters such as type and molecular weight of the analyte, type of solvent and any additives used in the solution to aid the ionisation. Also important is the mass flow of the solution through the capillary, the voltage applied, the drying gasses, and the overall geometry of the ESI source employed. There are three stages in the electrospray process:

1. Droplet production
2. Shrinking of droplets
3. Production of the ions

Following these ambient processes, and preceding the vacuum area of the mass analyser is usually a transfer region consisting of a capillary and/or ion skimmer. Their purpose is the clean-up of the residue solvent molecules clustering on the ions, by thermal declustering and collisional activation respectively[31].

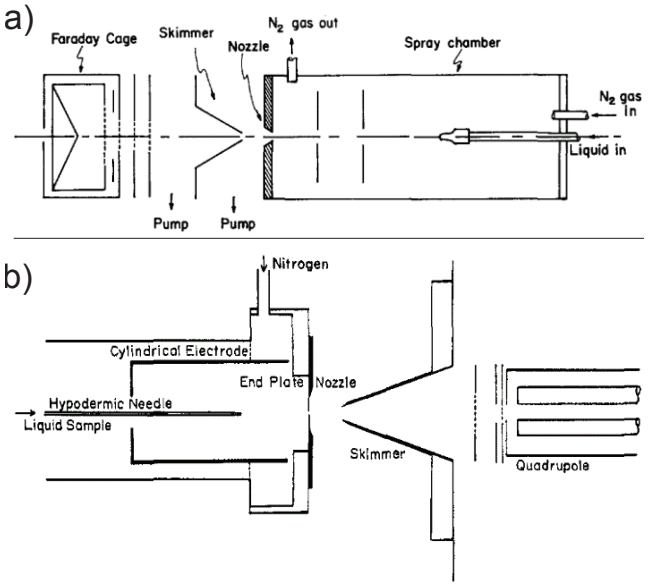

Figure 2. 7 a) The macromolecular beam device used by Dole et al. b) The first ESI device used by Fenn, the design of which was inspired and based on Dole's device. a) Reprinted with permission from M. Dole, et al., J Chem.Phys.,49,2240–2249, 1968. Copyright 1968 AIP Publishing LCC b) Reprinted with permission from M. Yamashita and J. B. Fenn, J Phys.Chem., 1984,88,4451–4459. Copyright 1984 American Chemical Society.

Droplet production

Typical solution used in ESI contains a polar solvent in which the analyte is solvable. Because of the high sensitivity of ESI and of MS, very low concentrations can be used. This also allows for use of solvents that don't have a great solubility. As shown in Figure 2. 8, the solution is pushed through the capillary. The voltage is applied on the tip of the capillary. This means that the electric field at the tip will be

$$E_c = \frac{2V_c}{r_c ln\frac{4d}{r_c}} \tag{2.30}$$

Where V_c is the applied voltage, the r_c the outer radius of the capillary, and d is the distance from capillary to electrode. When turned on, the field, which is highest at the capillary tip, penetrates the solution. This causes the polarization of the solution, leading to the charge build up on the surface. When we place a liquid under the influence of an electric field, the field distorts the shape of liquid surface, dependent of the size of fluid surface and field strength. The membrane shape varies, but some of those are similar to what is known as Taylor cone which is important for ESI. Following the work of Zeleny[32,33] and basing on the Lord Rayleigh[34] work about the instability of liquid droplets in the electric field, the study of droplets and surfaces under the influence of electric fields was continued by Taylor[35]. His study included the analysis of the works of Rayleigh and Zeleny, and concentrated on the disintegration of water droplets, focused on analysis of boundary and equilibrium conditions of spheroidal droplets under an electric potential. It is now understood that there exist several regimes of Taylor cones, but their

mechanics are so far poorly understood. The regime which is investigated in most detail and best understood is the simplest, and the most useful one, the cone-jet[36]. The experiment showed the soap film under the increasing electric potential forms a conical shape after certain voltage level. The tip of the cap forms into conical shape at the apex of the oscillations. The cone formation is achieved when balance is established, between the capillary and electrostatic stresses, at the surface of the equipotential cone[36]. This is true for non-conducting liquids. Taylors treatment can be applied for conducting liquids as well, where a different type of instability arises (also studied by Rayleigh), a so-called Plateau-Rayleigh instability, or varicose instability[37]. If the applied field is high enough, the tip of the cone becomes unstable, and a jet of droplets emerge from it. These droplets are charged due to an excess of charge from the cone surface. Further theoretical and experimental studies have determined that, because the size of the droplets from jet depends on its diameter, the majority of the droplets produced is monodisperse[38,39].

Due to the high potentials required for ESI, both for positive and negative mode, electric discharges sometimes occur in the ESI source. The onset of the discharge is somewhat lower for the negative mode (when the capillary electrode is negative), probably due to emission if electrons which initiate the discharge. This phenomenon is relevant because the presence of discharge is harmful to the ESI-MS, as the signal from the ions produced by the discharge can overshadow the signal of the studied sample. This also shows that the fact that ESI is an atmospheric pressure process is not only convenient for technical reasons. As the free electrons are accelerated by the high electric field, they can initiate the discharge. The oxygen in the air is a very efficient electron scavenger, and it actively contributes to the reduction of the free electron count in the electrospray region. There are other gases which have even higher electron affinity and electron capture cross section than oxygen, and they have been successfully used to prevent discharges in electrospray, but they also increase the risk of contaminating the mass spectrum with additional ions[31].

Shrinking of droplets

The charged droplets breaking off of the Taylor cone tip travel through ambient gas. During this time the gas provides thermal energy to the droplets, enabling solvent evaporation from the droplets. This causes droplets to shrink in size. Since there is no charge loss in this process, the coulombic repulsion between surface charges increases, until, at certain radius the droplet becomes unstable, as the repulsion overcomes the surface tension. This instability is governed by condition called the Rayleigh limit[34]

$$Q_R = 8\pi(\varepsilon_0 \gamma R^3)^{1/2} \tag{2.31}$$

where Q_R is the charge on the droplet, R is the radius of the droplet, γ is the surface tension of the solvent, and ε_0 is the electrical permittivity. The instability leads to the fission of the droplet, producing a daughter droplet, approximately 98-99% of the mass of parent droplet, but retaining only 60-85%

charge (highly depending on the solvent), and a host of small charged droplets. The repeated fission finally results in very small, highly charged droplets that are precursors of gas phase ions Figure 2. 8.

Production of the ions

There are two main mechanisms which explain the droplets size reduction and the transfer of ions into gas phase.The IEM (Ion Evaporation Mechanism) was developed by Iribarne and Thomson in 1976[40]. After the reduction in size the droplet went through due to Rayleigh instability and Coulombic fission, we are left with very small, charged droplets, who cannot achieve the Rayleigh instability. This happens for droplet radius of around 100Å (84Å for positively charged droplets and 134Å for negatively charged droplets[40]). At this point, the droplet size becomes small enough, so that the curvature of the surface is so high, that the electric field due to surface charge density is strong enough, so that the ions have enough energy to detach from the droplet and overcome the potential electrostatic barrier (Figure 2. 8). Charged Residue Model (CRM) was developed by Dole et al. in 1968[27]. It pertains to the formation of ions of macromolecules. As the name states, he charge residue model assumes the charge of the final ion is the residue charge from the droplet. The model states that as the droplets undergo the reduction in size, most of the very small charged droplets which are precursors to ions contain one molecule of

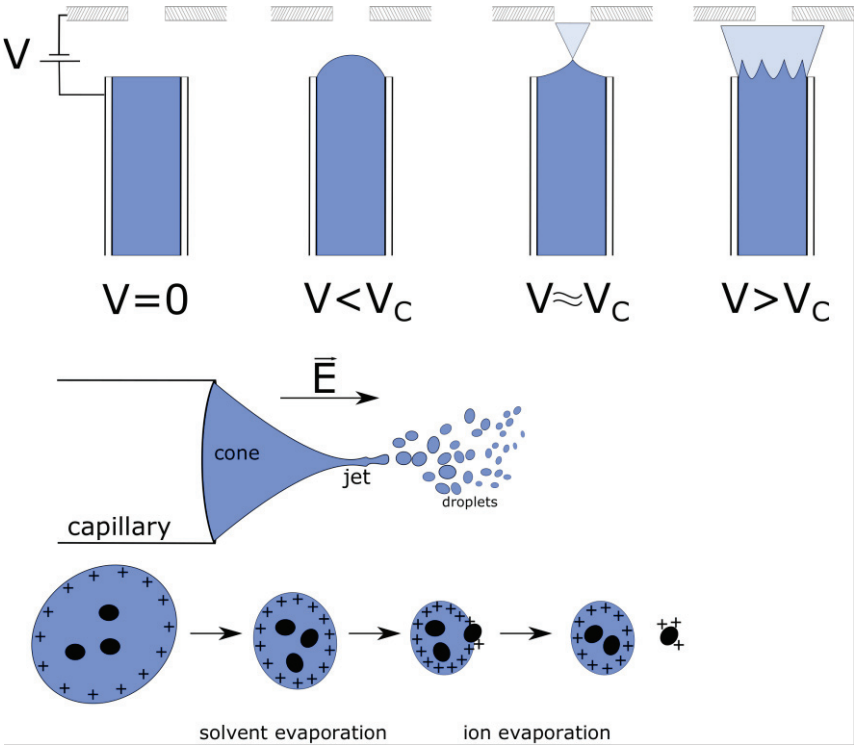

Figure 2. 8 Top row - modes of Taylor cone formation as a function of capillary voltage. The cone starts to form as the voltage approaches V_C, a critical value needed to establish a cone. Middle row – formation of droplets from the cone. The voltage causes the prolongation of the tip of the cone into a jet, which destabilises at its end, which causes droplets to break off. Bottom row – illustration of IEM mechanism. As the droplets reduce in size due to solvent evaporation, the surface field due to charge becomes very strong causing the ejection i.e. evaporation of ions from the droplet. Experiments have shown this model to explain very well the formation of ions of small molecules and compounds.

analyte. As all of the solvent evaporates from the droplet, the analyte molecule is left, and the charge it carries is the residual charge the droplet had on it.

Both models have been successfully applied to explain the ionisation of a wide variety of molecules. They present a distinctly different ways of separating the analyte molecule from the others. In general, CRM has been used more successfully to explain the gas phase formation of ions of higher masses, while IEM has had more successful application for small ions. Also, a combined model has been suggested for the mechanism of charging macromolecules, which is still under debate[41].

2.2.2 Sensitivity and use

Compared to other techniques, ESI has proven very good for determining equilibrium constants of reactions[31]. It can be used for reactions much slower than the droplet evaporation time.

The electrical field between the spraying and entrance capillary is responsible for droplet separation from the Taylor cone, but also in part for the droplet transfer between the two capillaries. Increase in voltage increases ion abundance, but favouring smaller and highly charged ones. This indicated the role of ion mobility in the process of electrospray. While the increase in voltage increases the total ion current (TIC), it changes the relative abundances of ions. The effect of ion mobility is not the only one in play though. Ion stability plays an important role too. Some charge states might be more or less energetically favourable than the others, so it might contribute to differences in their relative intensities[42]. Another effect which influences the intensities of analyte signal is the so-called "matrix effect". It refers to enhancement or suppression of the signal caused by different materials being present in the electrospray, especially volatile salts[43]. This effect is problematic as it can hinder the ESI ability of quantitative analysis. Quantitative determinations of concentration with ESI are possible but not easy. The method relies on the connection between analyte concentration and ion current in the spray[44].

In ESI-MS the analyte is present both in solution and in gas phase. The resulting mass spectrum can therefore reflect both conditions. The main difference in context of MS is that in water solutions, the separation of ionic pair such as Na^+Cl^- occurs very easily, while in the gas phase, the dissociation energy for them is quite high. The positive adducts in the gas phase (like Na^+ and K^+) can form rather strong bonds with the analyte, especially with polar or aromatic compounds. This can cause the adducts to not dissociate from the analyte molecule in the clean-up phase of the ESI[31].

As was mentioned before, ESI is a very god method for trace compound analysis. Paired with MS it is able to detect analyte even in very low concentrations. The limit of detection concentrations for several metal-APC (APC-Aminopolycarboxylate) complexes are shown in Table 2. 1.

In negative ion mode, it is very well suited for detection of organic analytes with acidic functional groups, such as carboxylates, sulphates, sulfonates and phosphates. They are easily ionised, and though the ESI does not offer very high sensitivity in these cases, its ease of use has caused it to be a widely

Table 2. 1 Limit of detection (LOD) for several metal-APC complexes in $[nmol/L]$*.The APCs used are: N-(2-hydroxyethyl)ethylelenediamine N,N',N'-triacetic acid (HEDTA), nitriloacetic acid (NTA), ethylenediaminetetraacetic acid (EDTA), trans-1,2-diaminocyclohexane-N,N,N'N'-tetraacetic acid (CyDTA) and diethylenetriamine-N,N,N',N'',N''-pentaacetic acid (DTPA). Reprinted with permission from Hotta, et al., Anal. Chem. 2009,81,6357. Copyright 2009 American Chemical Society.*

metal	HEDTA	NTA	EDTA	CyDTA	DTPA
$^{27}Al^{3+}$ (100%[a])	10	2500	11	21	29
$^{55}Mn^{2+}$ (100%)	61	6	81	16	33
$^{56}Fe^{3+}$ (92%)	2	110	5	10	4
$^{60}Ni^{2+}$ (26%)	29	360	31	25	57
$^{63}Cu^{2+}$ (69%)	4	100	6	3	13
$^{66}Zn^{2+}$ (28%)	15	25	10	9	10
$^{114}Cd^{2+}$ (29%)	71	11	37	59	3
$^{208}Pb^{2+}$ (52%)	7	15	93	7	10

[a] Isotope ratio. These were estimated as S/N = 3 values.

applied method in research. In environmental research it's been used to analyse haloacetic acid, perfluorocarboxylates, trace explosives and phenolic compounds[45].

New/alternative/complementary methods – paper spray, tissue spray, wooden tip ESI, direct probe and probe ESI. Also can be coupled with IMS for ES-DMI (Electrospray – differential mobility analysis).

Over time a host of variations and complementary spraying ionisation methods have emerged. One of the very widely used methods is nano electrospray (nano-ESI). The main difference from conventional ESI is in the amount of sample used, but it is also in the mechanism of droplet formation. While in conventional ESI the usual analyte flow is $> 1\mu L/min$, in nano-ESI it is $\sim 1 - 100nL/min$. This allows for a much greater sample efficiency. Usually in nano-ESI there is no back pressure being applied to the sample. The flow is achieved by the electric field propelling the particles, and all of the sample is contained in the spraying capillary. Due to very low flow rates, the nano-ESI is much less likely to produce a discharge. Also, the undesirable matrix effect is greatly reduced[31,46].

One very simple and versatile variation of ESI which has emerged is the "paper spray" method. A drop of substrate is placed on a triangular piece of paper, and voltage is applied between the paper and entrance of the instrument. Ions in gas phase are formed from the edge of the paper through the electrospray mechanism. Though called "paper spray", any porous material can be used for this method. The microdroplets travel through the material by numerous microchannels in paper, so the final result is equivalent to multiple nanosprays[47]. Efficiency of this method is very dependent on the geometry of the paper used. Research has shown that the strongest spray is achieved for spray tip angle of 30°. The increasing of this angle causes the spray to narrow down and loose intensity, and around 150° disappear completely. Narrowing of the spray increases its efficiency, as higher proportion of the ions are transferred to the analyser. Therefore, the optimal angle of the spray tip is 60°-90°[48]. Paper samples prepared with this technique are suitable for longer storage, and even distant shipping for reanalysis. So far, the dominant applications of paper spray have been in biomedical research[48]. With use of portable mass spectrometers, this method shows great promise for *in situ* analysis[49]. A spin-off of "paper spray"

ionisation method is the so called “tissue spray” or “leaf spray”. This method uses a piece of plant leaf, either cut to the desired shape or its natural sharp tip is used as a spraying tip. It is used for studying plant based sugars, amino acids and organic acids. As plant leafs are rich in electrolytes, this method does not require the use of solvent to obtain very good mass spectra, however, a solvent can be used for the process[50].

Electrospraying can also be achieved from wooden tips. They are very easily produced from ordinary, commercially available toothpicks with sharpened tips. The tip is then dipped into the sample and attached to a high voltage supply. Thus, the mass spectra of both small (amino acids) and large (proteins) molecules can be obtained[50].

A simple copper of platinum coil can be connected to a high voltage supply. By depositing the sample solution inside the probe, and applying the voltage we get the direct electrospray probe (DEP). Compared to conventional electrospray, this method has several advantages, such as, low sample consumption, immediate sample switching, it’s impossible to clog the probe, and it’s simple and cheap to produce and maintain[50]. This technique has already been applied to many biological samples such as urine, milk, mouse brain, mouse liver, salmon egg and various fruits[51]. Some of the drawbacks of this technique include the lack of ion stability, very hard reproducibility in case of pure aqueous solutions, and the fact that it’s only applicable to wet samples[50].

2.3 Laser ablation

Detailed investigations of metal clusters and complexes are particularly difficult. Bare metal clusters as well as any coordinatively unsaturated metal clusters are very reactive and can be easily influenced even by extremely inert supports. Because of this, the technique that would permit their study in controlled collisionless environment is extremely important[52]. The idea of use of optical energy for ionisation of molecules has also existed for a long time[53,54], and laser vaporisation and ionization techniques have been in increasing use since the invention of laser, and consequently the laser MS. It belongs to a group of so called energy sudden ionization methods, along with fast ion bombardment (FAB), plasma desorption (PD) and secondary ion mass spectrometry (SIMS). Among the energy sudden techniques laser desorption (LD) is one of the least catastrophic one in terms of sample degradation. The main principle of these techniques is achieving the almost instantaneous high energy density in the sample solution or matrix, thus avoiding the fragmentation of the sample. This approach was first proposed by Beuhler in 1974 by using rapid heating to ionize small peptides[55]. Since these methods have shown to be useful as a means of ionization and transfer of samples to the gas phase, in 1980s, rapid development of laser ablation and other techniques ensued, in the attempt to move the upper mass limit over the 1kDa barrier[56].

Due to the difference in mechanisms and physical processes involved, for transferring the molecules to gas phase for the atmospheric pressure mass spectrometry, both femtosecond and nanosecond lasers

have been investigated. Since the thermal processes dominate in the case of nanosecond laser pulses, they cause a degree of thermal damage and fragmentation to the sample. It was found that femtosecond laser pulses can generate gas phase ions while avoiding thermal damage, since their duration is much shorter than the molecular rearrangement time ($\sim 50 fs$). Nanosecond laser on the other hand can yield more ions than the femtosecond laser for the similar laser pulse energy[57,58]. Nanosecond laser pulses also produce an abundance of neutral molecules instead of ions, when employing the laser desorption without the matrix. There are multiple ambient pressure laser ablation methods in use today. We will first give a short overview of methods combining the laser ablation of the sample (with or without matrix support) with electrospray, in order to transfer the sample to the gas phase and ionize it (Figure 2. 9).

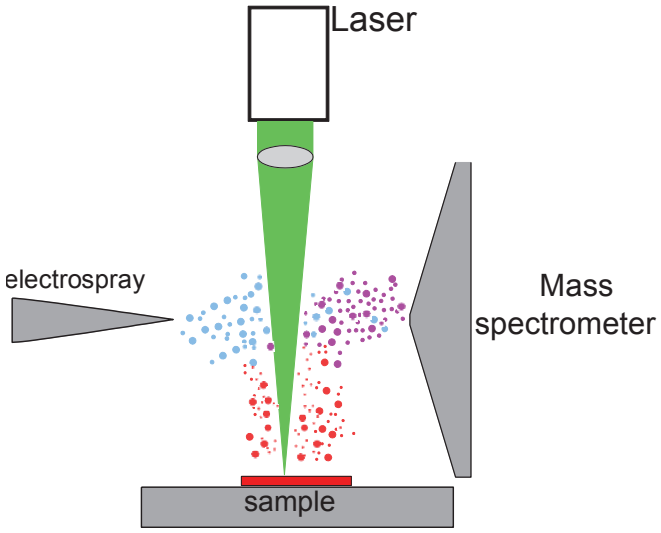

Figure 2. 9 Schematic of a coupled laser ablation – electrospray mass spectrometry source. Many variations of the same principle are in use today, involving laser power, pulse duration, angle of incidence of the laser beam, use and type of the matrix and use and type of the solvent.

After that, we will briefly discuss some other laser ablation methods, with focus on metal cluster generation, and a brief overview of physical processes involved in laser ablation.

Laser electrospray mass spectrometry (LEMS) is an analytical technique, coupling laser vaporisation and electrospray ionisation (Figure 2. 10b, c, d). It typically uses a femtosecond laser in the near infra-red wavelengths ($\sim 800 nm$). LEMS has successfully been used on a variety of different samples: liquid, dried, tissue, etc. This method does not require the use of matrix in the vaporisation process. The sample, which is deposited on a plate just in front of the entrance to the mass spectrometer, is vaporised with a laser pulse. After vaporisation it enters the electrospray plume of drying gas, just above the vaporisation region, where it is ionized and transferred into the analyser. Experiments have shown, that the termination of electrospray voltage and plume resulted in loss of signal, indicating the ionisation happens because of electrospray, not because of AP-MALDI-like process. LEMS method has so far been used to analyse many different samples such as protein, pharmaceuticals, lipids, blood, milk and various tissue samples[56].

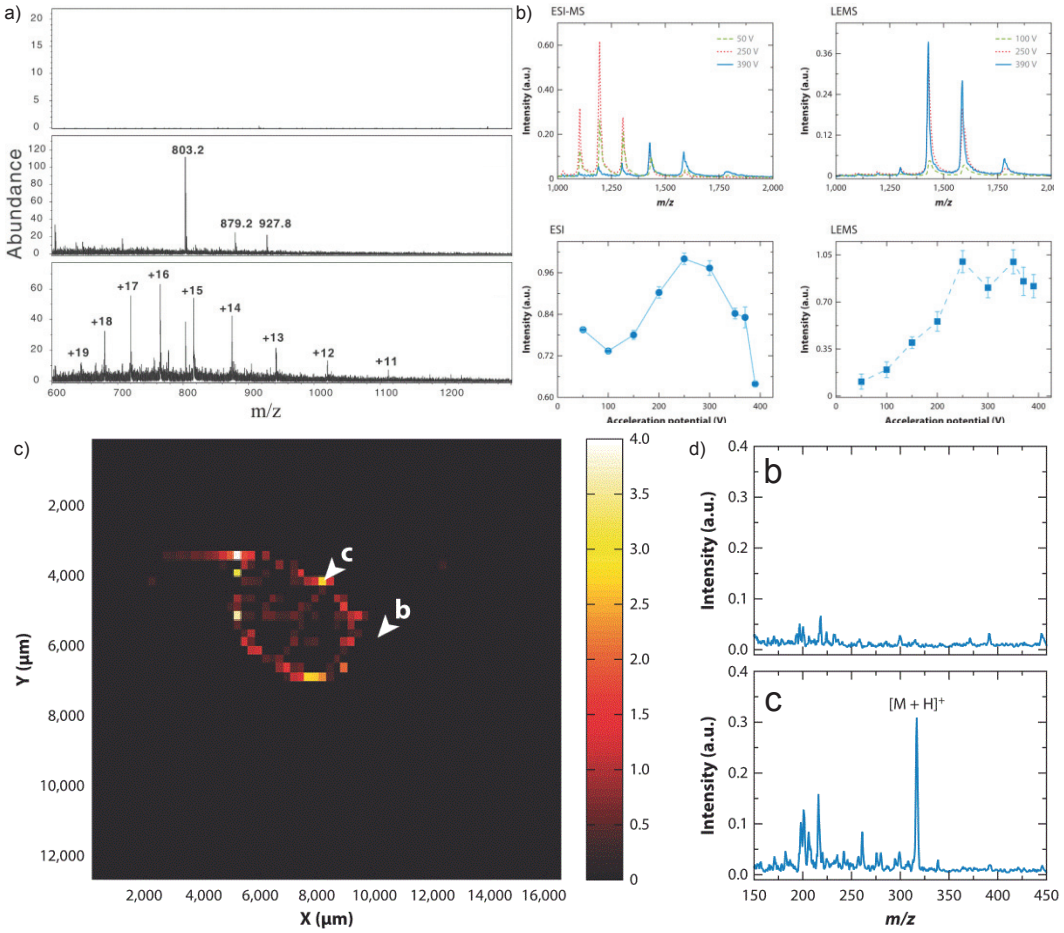

Figure 2. 10 Examples of different laser-ESI coupled ionisation methods. a) Mass spectrum of bovine cytochrome c obtained with only laser desorption, only ESI and both laser desorption and ESI (respectively top to bottom). b) Comparison of ESI-MS and LEMS, for lysozyme. The mass spectra shown were obtained with different in-source collision voltage. c) 2D map of oxycodone on a stainless steel slide obtained using LEMS and d) the mass spectra obtained in points b and c. the colour bar represents signal intensity given in arbitrary units. a) Reprinted from ref[59] with permission of John Wiley & Sons. b), c), d) Reprinted from ref[56]with permission of Annual Reviews.

When used in protein analysis, with LEMS, a condensed phase structure can be discerned from the charge state distribution in the mass spectrum. Studies performed on solution phase lysozyme have shown that the vaporisation with femtosecond pulses preserves the condensed phase structure of the protein in the gas phase.

Similar to LEMS, Electrospray-Assisted Laser Desorption/Ionisation (ELDI) and Laser Ablation Electrospray Ionisation (LAESI) are a combination of laser ablation and electrospray. They are all methods which utilise two stage process, the laser ablates the sample, and the electrospray ionises it. Both ELDI and LAESI use nanosecond laser pulses in the SW-IR region, and sometimes in N-IR and UV (ELDI). They are suitable for both solid and liquid types of samples. The ELDI method uses a standard electrospray conditions, while LAESI uses nanospray. The ELDI was successfully used in analysis of various, surface deposited molecules such as cytochrome c, lysozyme and myoglobin[59,60] (Figure 2. 10a). In these experiments, a nanosecond nitrogen laser of 337nm was used for desorption. This technique also allows the 2D mapping of biological samples such as fungal and animal tissue

samples with spatial resolution of up to $250\mu m$[61,62]. LAESI offers an even better spatial resolution of around $30-40\mu m$, allowing for mass spectral analysis of cells[63–65]. There are several variations of LAESI technique such as infrared laser assisted desorption electrospray mass spectrometry (IR-LADESI)[66], infrared desorption electrospray ionisation (IR-LDESI)[67] and laser ablation mass spectrometry (LAMS)[68].

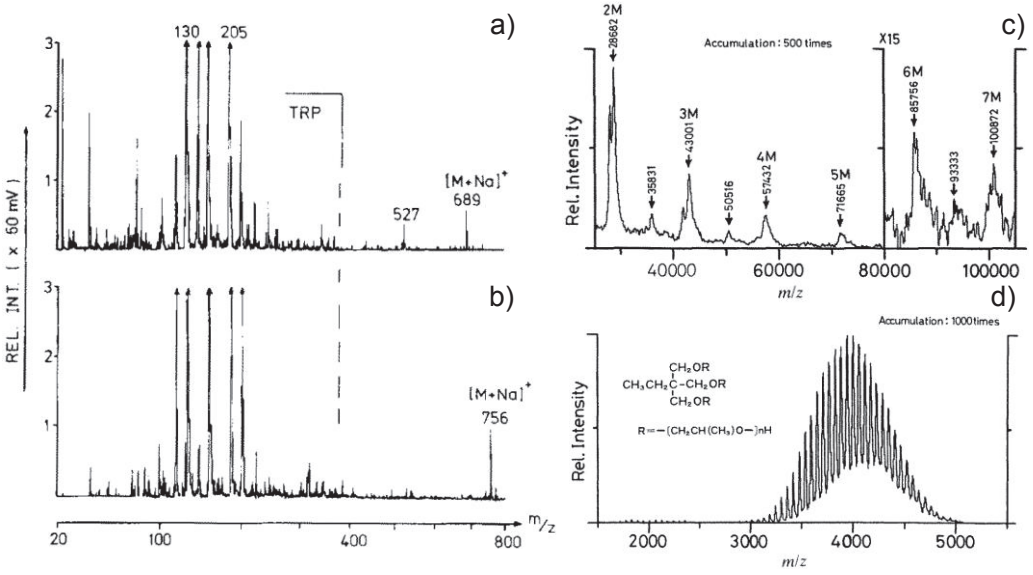

Figure 2. 11 Examples of first MALDI mass spectra. a) and b) mass spectra of stachyose and erythromycin respectively embedded in tryptophan matrix obtained by Hillenkamp et al[69] in 1987. MALDI mass spectra of c) and d) lysozyme and polypropylene glycol respectively obtained by Tanaka et al.[70] in 1988. a) and b) Reprinted from ref [69] with permission of Elsevier. c) and d) Reprinted from ref [70] with permission of John Wiley & Sons.

Today, together with ESI, Matrix Assisted Laser Desorption/Ionisation (MALDI) is the dominant method used in ionization for MS. This method was developed in late 80s by Koichi Tanaka[70]. A pulsed nitrogen laser was used to desorb several samples of proteins and polymers: lysozyme, (14306 Da), chymotrypsinogen (25717 Da), poly (propy1ene glycol) (PPG), (4 kDa), and PEG20K (20 kDa) (Figure 2. 11). The novelty of the method was in combining the two previously known techniques, the ultra-fine metal powder (UFMP) often used in metallurgy and glycerine matrix, commonly used in FAB ionisation. These aided the rapid heating desorption caused by the laser pulse, while aiding to avoid the fragmentation of the molecule of interest. In similar work, Franz Hillenkamp and his group demonstrated that molecules like tryptophane, nitric acid, sucrose, 3-nitrobenzyl alcohol and 2-nitrophenyl octyl ether in a matrix can be suitable for ionisation of proteins and peptides[69,71] (Figure 2. 11). Even though multiply charged species have been observed in AP-IR-MALDI experiments[72], typically MALDI produced species are singly charged. It is for this reason that the Matrix-Assisted Laser Desorption

Electrospray Ionization (MALDESI) was developed where ESI is used for postionisation of the sample[56].

First to apply the laser ablation to production of metal clusters was the group of Richard E. Smalley at Rice University, in 1981. They used a second harmonic of an Nd:YAG^{3+} laser to ablate a piece of aluminium and produce Al_x clusters which were characterised by TOF MS[52](Figure 2. 12). Eventually, in collaboration with Harold Kroto, their experiments led to discovery and study of fullerenes[18,19]. At roughly the same time as Smalley group, similar work was done by dr. Vladimir Bondybey at AT&T Bell Laboratories [73]. In the beginning these experiments were focused on producing the clusters of main group and transitional metals, but soon many variations emerged[74]. Experiments were being conducted on semiconductors (Si, Ge, GeAs)[75–77] as well as carbon[18,78–80]. Soon afterwards studies have also been extended from pure metal clusters to alloys and other mixtures[74,81–83], and metal compound clusters such as metal carbides[84–89], metal oxides[90–95] and metal silicon[96–98] clusters.

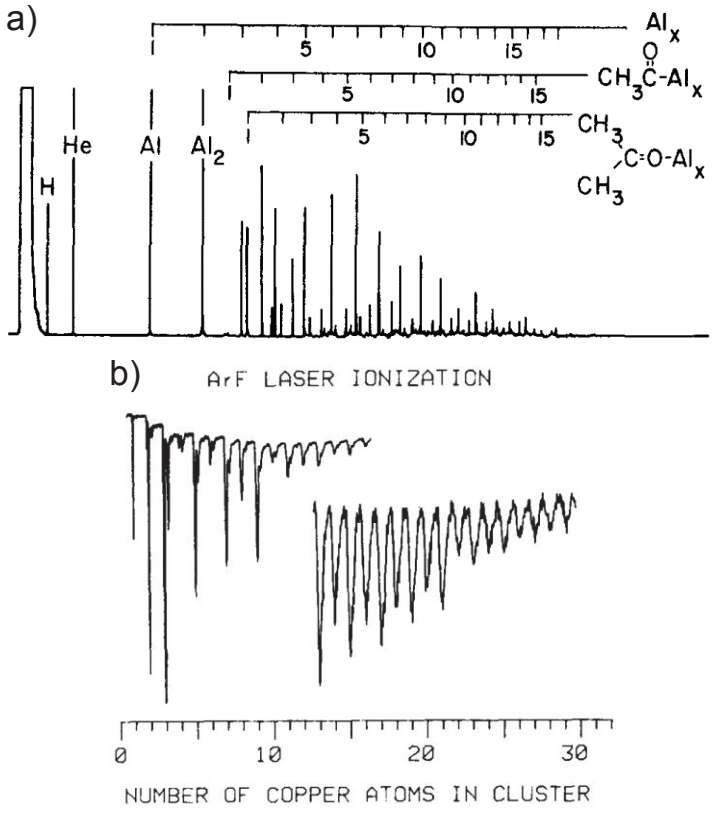

Figure 2. 12 Mass spectra obtained by Smalley group at Rice Univerisy by laser ablation of metal rods. a) Mass spectrum of Al clusters. b) Mass spectrum of Cu clusters. a) Reprinted from ref[52] with permission of AIP Publishing. b) Reprinted from ref[99] with permission of AIP Publishing.

Size and geometry of the sample are an important factor in production of metal clusters by laser ablation. Most commonly used samples are metal rods, as it allows for easy rotational and translational movement to ensure uniform ablation of the sample. In early versions of the experiment it was observed that with

immovable target, over time, the size of he detected clusters reduced. This was because, as the laser cut deeper and deeper into the target, the molten droplets and vapour could not escape into the pulsed gas region as efficiently. Therefore a rotating rod or a disc geometry ensures the fresh surface with each laser shot and avoids this problem. The optimal speed of rotation depends on the material, as some metals with low melting point (tin, lead, germanium, …)[74] need to rotate more quickly, and are ablated much faster than the more durable metals such as gold, silver, cobalt etc.[74] These issues are also influenced by the intensity and pulse duration of the laser used in the experiment. Since most metals are highly refractory materials, a high peak energy is required for their vaporisation. Therefore pulse lasers such as Nd:YAG^{3+}, excimer, copper vapour etc. are typically used for this purpose. Early studies into laser-metal interaction have shown high dependence of vaporisation to laser pulse duration. Longer pulses (millisecond range) penetrate deeper into the material and are less sensitive to effects of reflectivity and thermal conductivity and therefore they ablate more material. For the shorter pulses (nanosecond range) the vaporisation occurs rapidly, and is followed by formation of a plasma plume which interacts with the rest of the pulse[100,101]. Looking more closely, as the light hits the material it is absorbed by electrons. These electrons get excited and propagate the energy by interactions with lattice phonons. There are three time scales that need to be considered when talking about laser-solid interactions. They are: the electron cooling time, the lattice heating time and duration of the laser pulse. Most of the processes can be described by thermal processes especially for the nanosecond and longer laser pulses, as the time for energy transfer from electrons to the lattice in metals is $\sim 10^{-12} s$, we can assume the local thermal equilibrium, so the concepts of heat conduction can be applied[102]. There are different mechanisms that play a role in the process of ablation. The ejection of material can be in the form of liquid droplets caused by heating and melting effects, and broken off by surface instabilities caused by pressure gradients in the vapour plume and background gas. Solid particulates can also be ejected, which is caused when laser-induced stress exceeds the dynamic tensile strength of the material. The dominant mechanisms and their relative importance in the process of ablation depends on physical properties of the sample, as well as the microscopic structure and surface roughness. If we consider the interaction of a nanosecond laser pulse of around $10 ns\, FWHM$, on a metal surface in vacuum, the process can be divided into several steps for easier understanding. Since the absorption length of a metal is on the order of $10^{-8} m$, much smaller than the typical laser beam profile ($\sim 100 \mu m$), we can only consider the heat propagation inwards, i.e. deeper into the metal. As the heat propagates, the metal heats from surface inwards. When it reaches high enough temperature the metal melts, and starts to evaporate. This explains the existence of a power threshold below which no clusters can be observed, and also why after certain pulse power further increase is counterproductive[74]. As the vapour expands in the vacuum, and, since its formation happens on a timescale shorter than the duration of the laser pulse, it absorbs a part of the laser pulse. This causes the partial ionization of the vapour and the emergence of plasma, which consists of metal neutrals, metal ions and electrons. After the initial onset of vaporisation and

plasma, the plasma shielding effect causes a significant drop in the laser power available to the metal surface[100]. The absorption of light in the plasma plume happens by inverse Bremsstrahlung and photoionization. At the beginning, the photoionization (single and multiphoton) dominates the absorption process, to be taken over by inverse Bremsstrahlung at around $t = 9.5ns$. The inverse Bremsstrahlung absorption happens in two stages, first, the free electron absorbs a photon in the electric field of neutral, then electron-ion inverse Bremsstrahlung begins[103]. The modelling of the size, shape and dynamics of the plume can be done by pure hydrodynamic approach, by Monte Carlo simulations, or a combination of both. Some models focus more on expansion of evaporated material, some focus more on the early stage plasma caused by electron emission, as it interacts with the incoming laser light[100]. During this process neutral, and ionized metal particles are formed in the plume, as well as ejected electrons. Cluster growth is believed to occur by vaporisation of atoms, followed by three body collisions which form dimers, trimers and sequentially bigger polymers. This process requires the presence of a third body in order to remove the translational energy. This is why the type of gas nozzle and expansion gas used is also connected with the effect of laser pulse energy. Because the plasma created by the laser ablation is very hot, collisional cooling is required to facilitate cluster growth and supress the excited states and formation of various metastable species.

The presence of a collision gas increases the density of the third bodies available, and promotes cluster growth. The most efficient way to do that is with a supersonic nozzle source[74]. The details of the collisional energy transfer are very well known[115], and are applicable in this case. Through some of these considerations, we can get an idea of the suitability of individual gases for the use in cooling. For example, by simply considering the efficacy per collision, argon gas is more effective than helium in removing the translational energy. The configurations of different experiments differ from one another. Some general layouts are shown in Figure 2. 13.

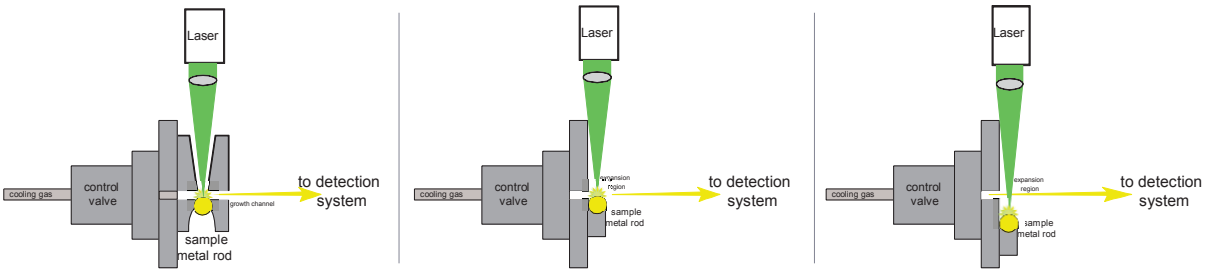

Figure 2. 13 Variations of a laser ablation source. (left) Standard source – the metal rod is mounted in a solid block with a channel running back to front, from the gas valve to the entrance of the detector. The part of the channel after the ablation region is called the growth channel and it keeps the cooling gas and the ablated material confined to ensure the continuation of cluster growth. The growth channel is usually at room temperature, but some experiments employ cooling as well [104–114]. (middle) Cutaway source – used to produce metal compounds, with molecular ligands or with rare gas atoms. This design allows for a free jet expansion which is needed to make weakly bound ligated complexes, as they require extremely cold supersonic expansion. (right) Offset source – for some ligated systems it proved to be beneficial to displace the laser ablation region and the plasma plume from the expansion region, to prevent the recombination effects that take place in the plasma plume [74].

Besides atmospheric pressure and vacuum laser ablation sources, laser ablation in solutions is also possible. This technique was pioneered in the early 1990s by Fojtik and Henglein[116], and has confirmed its versatility and utility in producing ligated metal clusters[117–122], nanocrystals[123] and nanodiamonds[124,125]. The main idea is that a piece of metal is placed in a vial of solution of a desired molecular ligand, and is then ablated with a laser. This approach has several benefits. Unlike the dry nanopowder they are non-inhalable and therefore much safer to handle. Also repeated experiments have shown that this synthesis provides high yields of products, which is especially beneficial in work with expensive substrates, and since it doesn't require any chemical precursors, resulting product is of high purity.

In conclusion, laser ablation is a good general technique for producing pure or ligated metal clusters. There are many variations of this technique in use today either for transfer of analytes into the gas phase with minimal damage, either for producing pure and ligated metal nanoclusters.

2.4 LAVESI experimental setup description

Laser Vaporization Electrospray Ionization (LAVESI) was developed as a means of synthesis of ligated and bare metal clusters and metal oxides. The main idea behind this experimental setup was coupling the well-known laser ablation synthesis of metal clusters[52] with electrospray ionisation method[28]. It is an ambient nanosecond laser desorption method of nanocluster synthesis, based on a LTQ XL linear ion trap from Thermo Fisher Scientific (San Jose, CA, USA). The LTQ XL is a typical linear ion trap mass spectrometer. It is equipped with an electrospray ionisation (ESI) source which allows us to transfer the

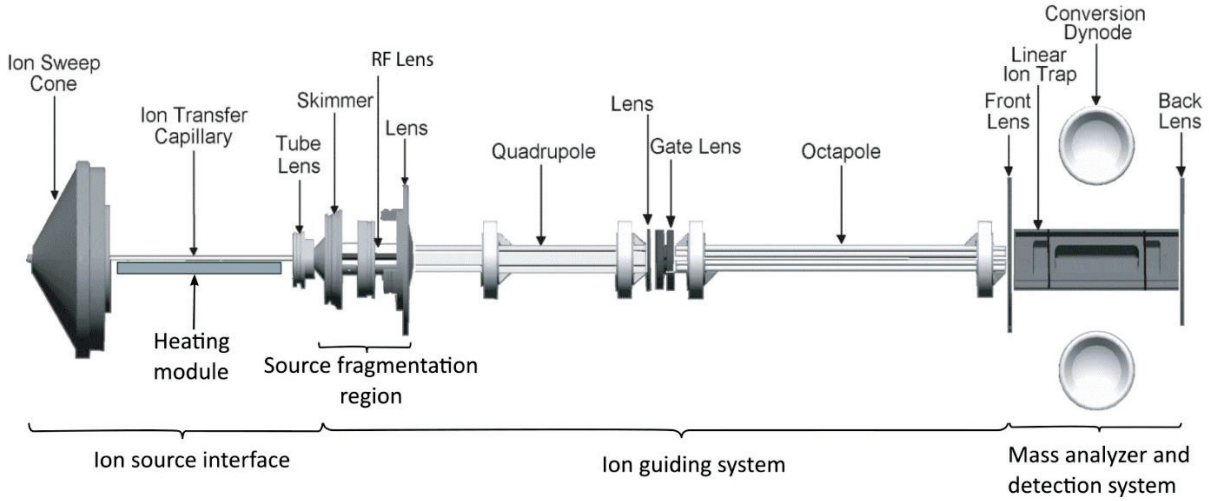

Figure 2. 14 Ion source, ion optics and mass analyser schematics of the LTQ XL mass spectrometer.

sample into the gas phase, ionize it and introduce it into the instrument. The ionised sample is guided by a series of multiplied and electromagnetic lenses and are led to the mass analyser (Figure 2. 14).

The entrance to the mass spectrometer is protected by an ion sweep cone. It acts as a physical barrier and increases the robustness of the device. It is followed by the ion transfer capillary which aids the

desolvation of ions. For this purpose, it can be heated up to 400°C[126]. After this, ions are transferred through tube lens and skimmer to the high vacuum part of the device. The skimmer acts as the barrier between the two regions. The ion optics part, consisting of RF lens and multipole ion guides serves to transfer the ions to the mass analyser. This is also the region where the source fragmentation occurs. As ions pass through the skimmer and into the ion optics region, they are accelerated by the difference in potential between the skimmer (at ground potential) and the first multipole. The multipole dc offset voltage is set such that it imparts enough kinetic energy to the ions so that, when they collide with solvent or air molecules (which acts as collision gas) present in the ion optics region, the ions dissociate to form product ions. This feature can be turned on and off at will, and in our experiments is used to probe the general stability of the species observed in the mass spectrum[127]. When discussed in experiments, we use the dc offset voltage $(0 - 100V)$ as a measure of this parameter.

After the ion optics region, the ions are injected into the mass analyser. This is where the storage, isolation, collision induced dissociation and scan-out is carried out. It consists of front and back lens and the linear ion trap. The front and back lens provide the confinement limits for the ions. Typically, the back lens is on ground potential, and -4V to -7V in case of positive ions is applied to the front lens [126]. Helium gas is introduced into the mass analyser that slows the motion of ions so that they can be trapped by the RF voltage fields. The partial pressure of helium damping gas is maintained at about 0.1 Pa[128]. Its presence in the mass analyser significantly enhances sensitivity and mass resolution. The helium also acts as a collision gas for collision induced dissociation (CID).

2.4.1 Laser Vaporization Electrospray Ionization (LAVESI)

The standard ESI source of the LTQ XL mass spectrometer was modified, by drilling a hole on its bottom surface to allow for a placement of a support mechanism for the ablation target. A 3 mm diameter metal rod is placed on the support, and is located between the capillary of the spray source and the entrance flange of the mass spectrometer as shown in Figure 2. 15 and Figure 2. 16. Step motors controlled by a home-made software allow *xyz* as well as rotational motions of the rod. The *x* and *y* motions are used to position the rod within the spray. *z* and rotational motions are actioned during experiments to provide a helicoidal motion of the rod so that the rod is uniformly irradiated by the laser. The distance between rod and ESI tip is typically 10 mm.

The laser used is a frequency doubled Nd^{3+}:YAG laser (532 nm). A lens with a focal length of 75 mm is used to focus the laser beam on the metal rod. The repetition rate of the laser is 20 Hz, typical energy per pulse was 10 mJ. The size of the spot on the rod is estimated to 0.44 mm^2.

The metal rods of 99.9% purity were purchased from Goodfellow (Lille, France). The rods are cylindrical in shape, of 3 mm diameter and 30 mm length, so that they can fit into the customised slot on the motor controlled metal rod support (Figure 2. 16).

First tests of the experimental setup provide the proof of concept (Figure 2. 17). The mass spectra obtained with and without the laser are completely different. In absence of laser ablation, the mass spectrum consists only of peaks corresponding to the thioglycolic acid aggregates (Figure 2. 17b). Upon turning on the laser the peaks corresponding to the thioglycolic acid disappear, and new peaks corresponding to the ligated silver thioglycolic acid complexes appear (Figure 2. 17a).

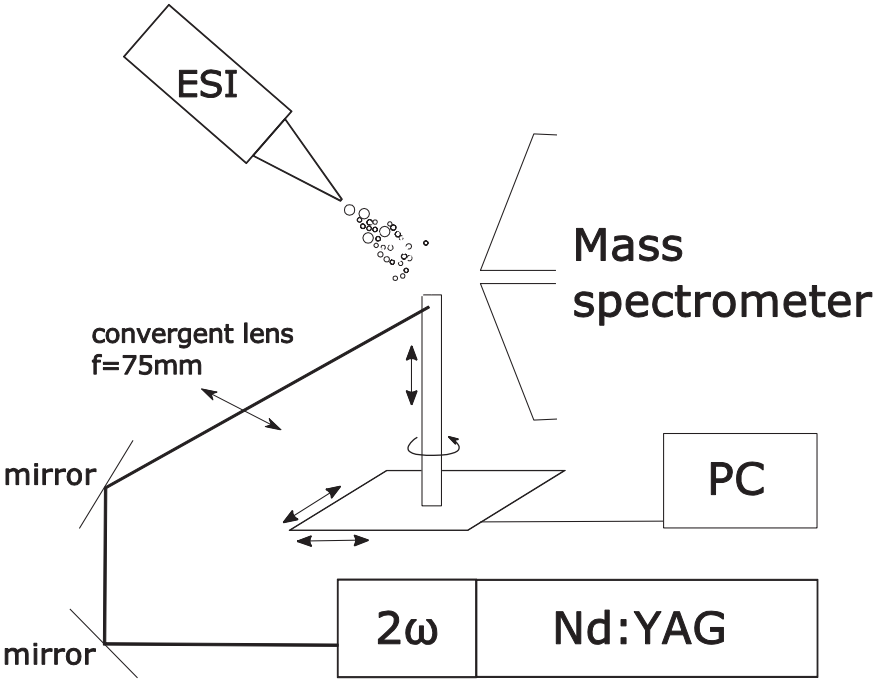

Figure 2. 15 Schematic of the LAVESI source set-up.

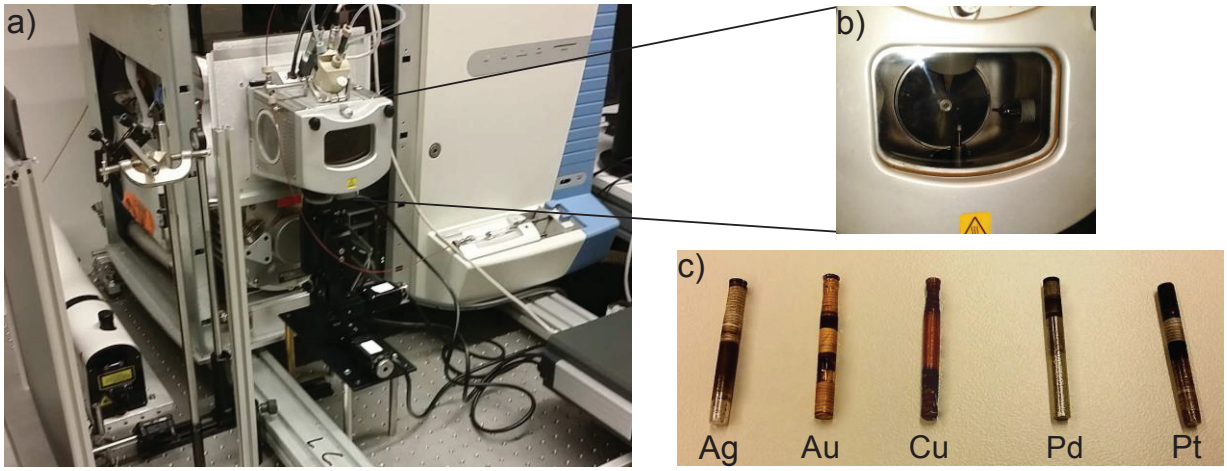

Figure 2. 16 a) The LAVESI setup. b) A look inside the ESI source and the metal rod placed in front of the entrance to the ion transfer capillary. c) Metal rods used for ablation. Damage from the laser and deposits of oxides made with reactions with atmosphere are clearly visible.

The same effect can be seen for other metals as well. It is worth noting that when the laser ablation is in effect no peaks corresponding to the thioglycolic acid can be seen in the mass spectrum. The observed species come completely from $M_nSR_m^-$ complexes and their fragments. The ligand is completely consumed by the reactions with the metal in the electrospray plume.

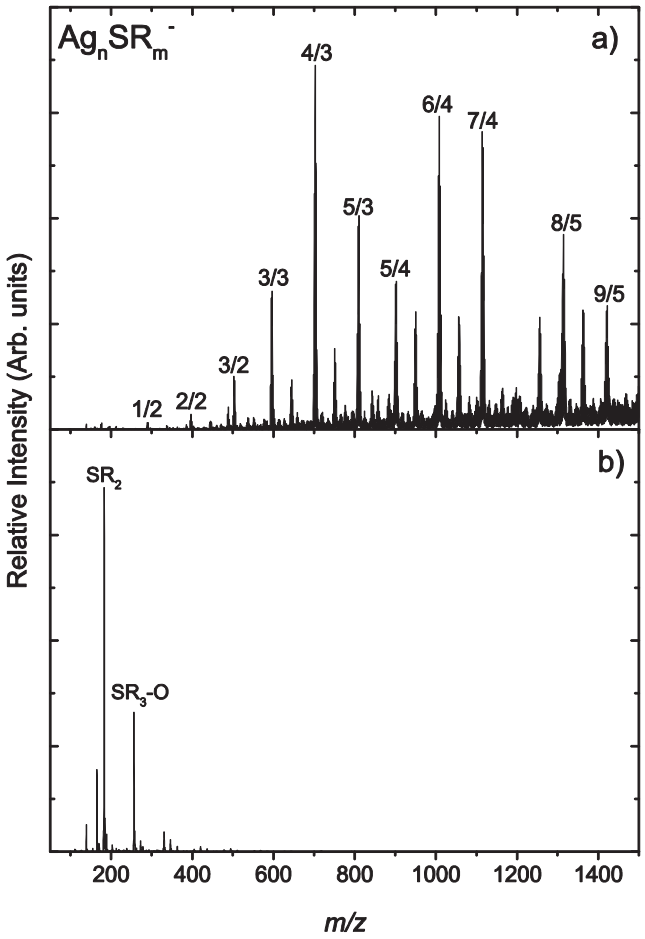

Figure 2. 17 Comparison of LAVESI mass spectrum a), ablating the silver rod and electrospraying thioglycolic acid, and standard ESI mass spectrum b) of thioglycolic acid.

Ligand concentration

Influence of the concentration of ligand sprayed is also important. The ligand used in experiments was thioglycolic acid, a small thiol molecule, suitable for these experiments because of the well-known affinity between sulphur and gold and silver atoms. Additionally its small size makes it easier to interpret the fragmentation spectra, and in the future, if necessary, conduct calculations. The fact that the ligand is a liquid at room temperature is also beneficial as it can be used in higher concentrations in the electrospray than solvated powder ligands. If pure water is electrosprayed, coupled with laser ablation, the mass spectrum obtained is very rich, dominated by a multitude of silver oxide and hydroxide species (Figure 2. 18). As we increase the concentration of thioglycolic acid in the electrospray, these species start to subside and instead we see $Ag_nSR_m^-$ starting to emerge, until, finally at ~1% (v/v) almost none of the peaks corresponding to the oxides and hydroxides can be seen in the mass spectrum, and it is

dominated by $Ag_nSR_m^-$ complexes. The ~2% thioglycolic acid concentration was deemed optimal for the experiments as it provided a very clean mass spectrum with abundance of $M_nSR_m^-$ complexes, and very few fragments. Further concentration increase did not result in significant improvement in mass spectrum quality and it presented increased risk of permanent contamination of the ion optics and ion trap of the instrument.

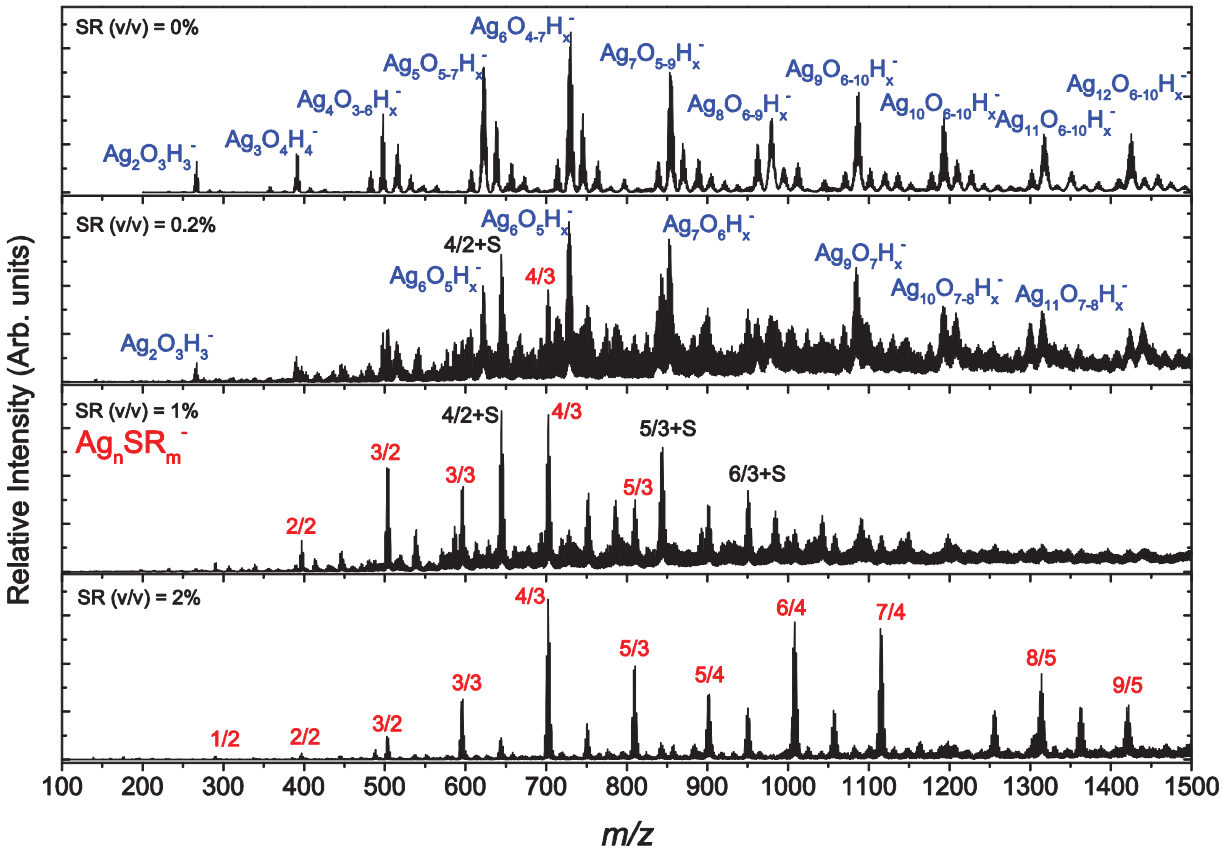

Figure 2. 18 LAVESI mass spectra obtained with different concentrations of thioglycolic acid. The concentration increases from top to bottom, the top mass spectrum being the one obtained by electrospraying pure water, and the bottom one being the one obtained by spraying 2% (v/v) thioglycolic acid. The blue formulas represent the silver oxide and hydroxide complexes, the red numbers represent the number of silver atoms and ligand molecules in the complex and the black formulas represent the $Ag_nSR_m+S^-$ species.

Laser power

Varying the laser power influences the distribution and the nature of the observed mass spectrum as well (Figure 2. 19). With low laser power, the mass spectrum is dominated by peaks of thioglycolic acid and its fragments. Other than the thioglycolic acid aggregates (SR_2^- and SR_4^-), two series of species corresponding to aggregates of thioglycolic acid and its fragments are observed too. The first one corresponds to general formula $[SR_3 + n(C_2H_2OS)]^-$ i.e. $[SR_3 + (C_2H_2OS)]^-$, $[SR_3 + 2(C_2H_2OS)]^-$, $[SR_3 + 3(C_2H_2OS)]^-$ and $[SR_3 + 4(C_2H_2OS)]^-$. The second series can be described by general formula $[SR_4 + n(C_2H_2OS)]^-$ i.e. $[SR_4 + (C_2H_2OS)]^-$, $[SR_4 + 2(C_2H_2OS)]^-$ and $[SR_4 + 3(C_2H_2OS)]^-$.

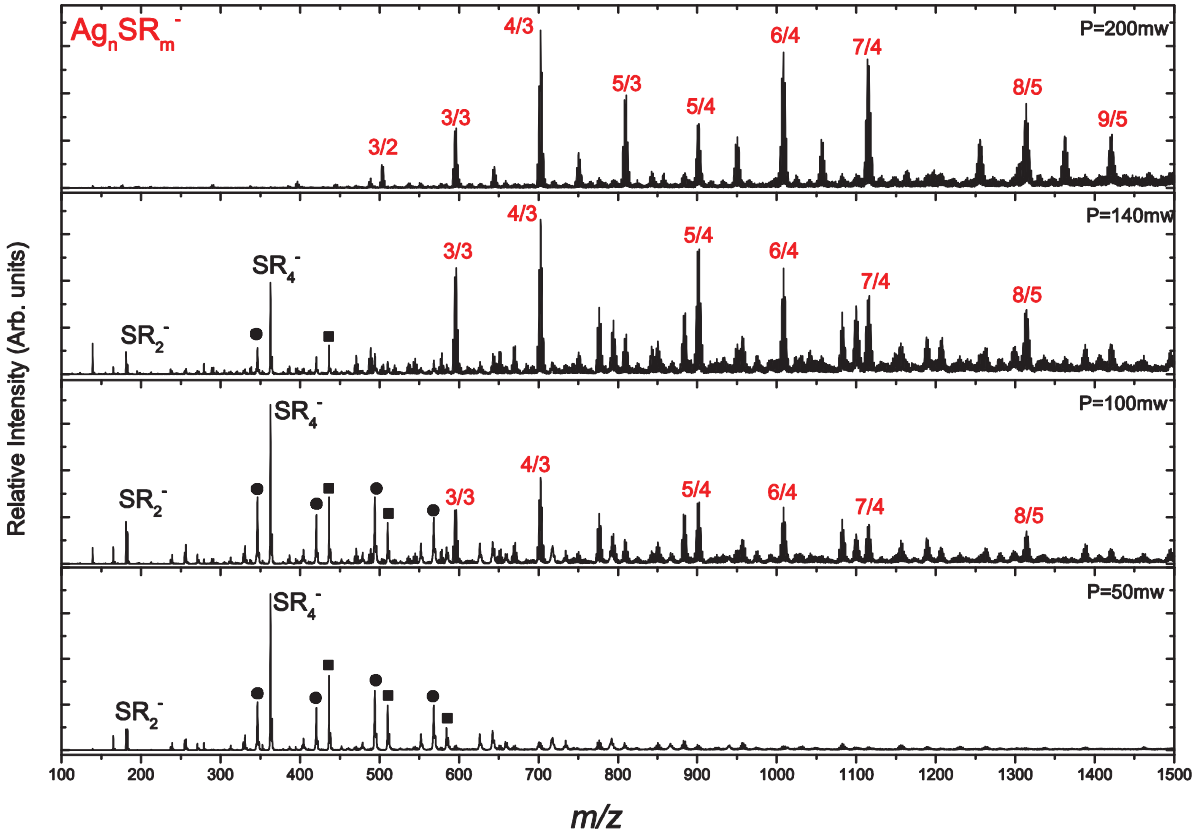

Figure 2. 19 Power dependence of the species observed in the mass spectrum of the LAVESI source. The experiments were conducted with variable laser power and 2% (v/v) thioglycolic acid. The black circles correspond to $[SR_3 + n(C_2H_2OS)]^-$, $1 \leq n \leq 4$ *respectively from left to right, and black squares correspond to* $[SR_4 + n(C_2H_2OS)]^-$, $1 \leq n \leq 3$ *respectively from left to right.*

The increase in laser power gives rise to the metal-ligand complexes and depletes the pure ligand and ligand fragment species from the spectrum, as more of the metal is available to react with ligand molecules in the electrospray plume.

Laser wavelength

LAVESI source hasn't shown any sensitivity in regards to the laser wavelength. As mentioned before, the laser in use is a nanosecond Nd3+:YAG. The synthesis was tried with two different harmonics of the laser to determine the wavelength influence on the created species (Figure 2. 20). The peak distribution shifts in favour of the lower masses and smaller species for the UV wavelengths. In terms of species observed, there is no difference between the wavelengths.

For the CID part of the MS^n, some additional energy is applied to the ions in order to achieve the collisions. This is done with resonance excitation RF voltage. Application of resonance excitation RF voltage to the endcap electrodes increases the axial motion of the ions in the in the trap and the ions gain kinetic energy. The amplitude of the resonance excitation RF voltage is sufficient to add kinetic energy to the ions so that, when they collide with helium buffer gas present in the mass trap, the ions dissociate

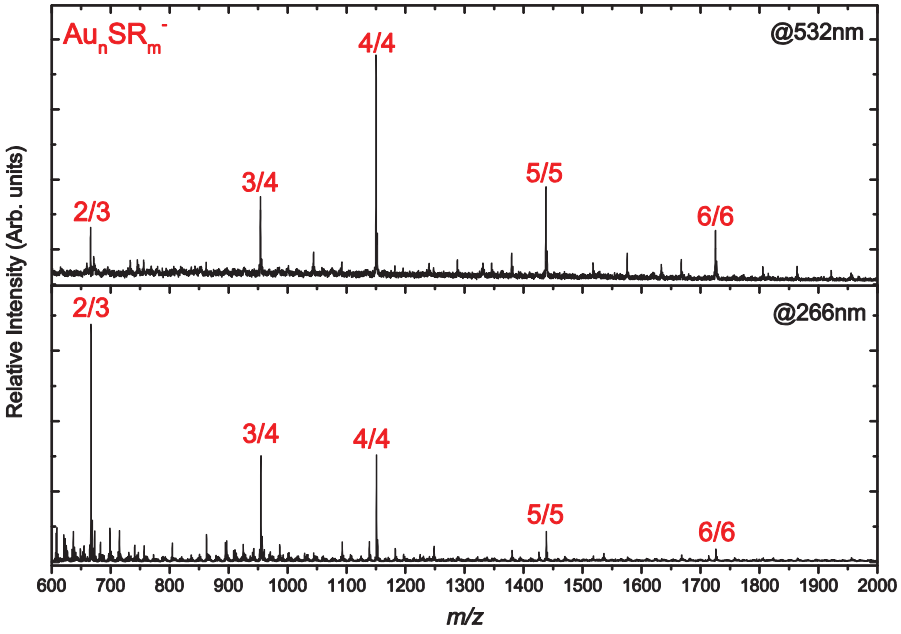

Figure 2. 20 Wavelength dependence of the species observed in the mass spectrum of the LAVESI source. The experiments were conducted with second (top) and fourth (bottom) harmonic of a Nd^{3+}:YAG laser and 2% (v/v) thioglycolic acid.

to form product ions. The measure of the amplitude of the resonance excitation RF voltage is the normalized collision energy (N.C.E.).

The N.C.E. scales the amplitude of the voltage to the parent mass, so that the appropriate amount of energy is always used to ensure the fragmentation of the selected ion. It is calculated by a formula:

$$A_{col} = E_n(m \cdot V_s + V_{int}) \tag{2.32}$$

Where $A_{col}$the amplitude of the voltage accelerating the collision gas is, E_n is the normalised collision energy, m is the isolated mass, V is tick amp slope and V_{int} is tick amp intercept which are parameters of amplitude of the resonance excitation RF voltage (so-called "tickle voltage")[127]. The N.C.E. is expressed in arbitrary units on a scale of 0-400. Mass analyser CID occurs automatically whenever the mass spectrometer is operated in either the MS/MS or MS^n scan modes (if an $N.C.E. > 0$ is assigned).

The CID can be effectuated upon ions for different durations of time. This is called the activation time, and it is the time in milliseconds that the resonance excitation RF voltage is applied. It can be chosen in a range of 0.03 to 10000 ms. The activation time default value is 30 ms. In general, shorter activation time results in less fragmentation and a longer activation time results in more fragmentation[127].

Figure 2. 21 shows two examples of CID on different species. Figure 2. 21a is a MS^2 spectrum of a gold-water complex. The parent ion at *m/z* 1003 which corresponds to $Au_5(H_2O)^+$ is isolated and, some collisional energy is applied to it. This causes the detachment of the water molecule and formation of Au_5^+. Figure 2. 21b shows an example of MS^2 and MS^3 experiments. In the first stage, the parent ion at

m/z 588 corresponding to $[Cu_5(SR)_3 - 3H]^-$ is isolated without any collision energy. Then, the collisional energy is added to induce fragmentation. At this stage we observe two fragmentation channels. The first one is the sequential loss of two CO_2 (44 Da) molecules followed by the loss of SCH_2 (46 Da). The second fragmentation channel, the less intense one, is the sequential loss of two $C_2O_2H_2$ (58 Da). Written by exact chemical formulas:

$$\begin{cases} [5Cu(C_2H_2O_2S)_3]^- \rightarrow [5Cu(C_2H_2O_2S)_2CH_2S]^- + CO_2 \\ [5Cu(C_2H_2O_2S)_2CH_2S]^- \rightarrow [5Cu(C_2H_2O_2S)(CH_2S)_2]^- + CO_2 \\ [5Cu(C_2H_2O_2S)(CH_2S)_2]^- \rightarrow [5Cu(CO_2)(CH_2S)_2]^- + CH_2S \end{cases} \quad (2.33)$$

$$\begin{cases} [5Cu(C_2H_2O_2S)_3]^- \rightarrow [5Cu(C_2H_2O_2S)_2S]^- + C_2H_2O_2 \\ [5Cu(C_2H_2O_2S)_2S]^- \rightarrow [5Cu(C_2H_2O_2S)S_2]^- + C_2H_2O_2 \end{cases} \quad (2.34)$$

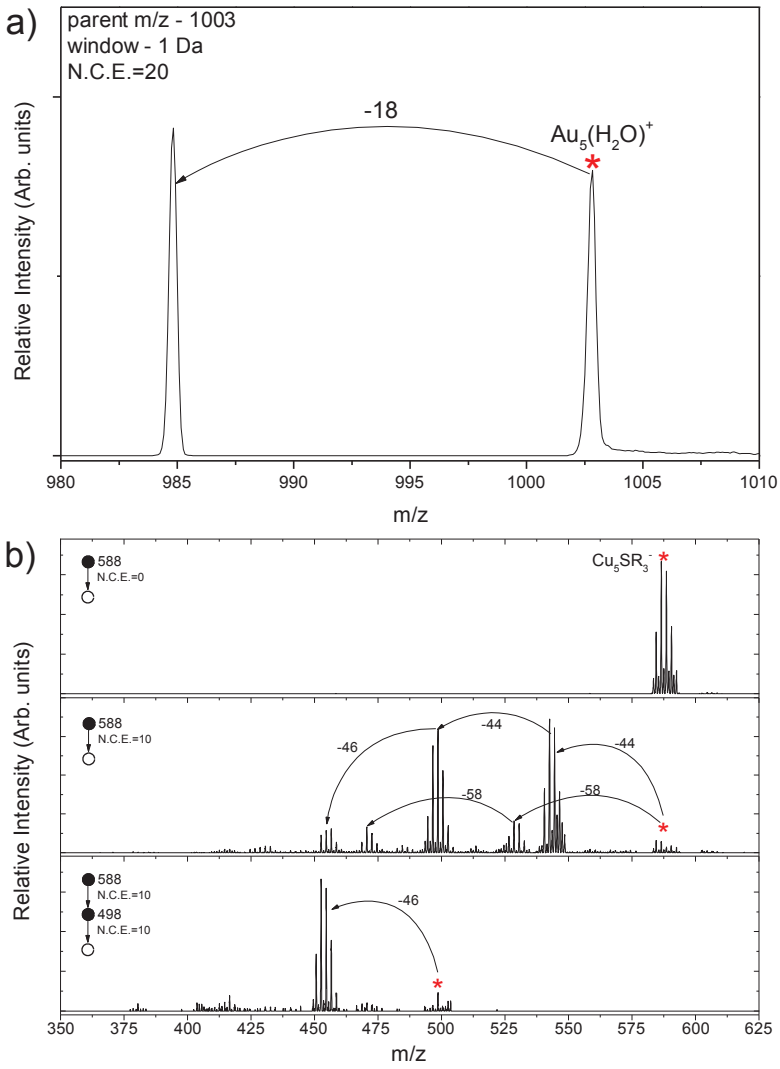

Figure 2. 21 Examples of the CID mass spectra. a) MS^2 mass spectrum of a gold-water complex. By applying the collisional excitation, the water molecule dissociates, leaving the pure gold pentamer. b) MS^2 and MS^3 spectra of a copper-thioglycolic acid complex. Simple isolation of the complex (b – top) is just a clean mass spectrum of the parent species. Adding collisional activation (b – middle) results in fragmentation of the parent species, with two distinct fragmentation channels. MS^3 of one of the fragment species provided a final product of the fragmentation.

2.4.3 Gas phase reaction setup

In order to study gas phase reactions on small metal complexes, we need to introduce the reactants into the ion trap. This way we can monitor the reactivity of all the species of the specific metal generated by LAVESI, or we can isolate individual species and monitor their reactions. In order to do this, we introduce the reactants directly into ion trap via the buffer gas inlet as shown in Figure 2. 22. Similar setups for gas phase reactions already exist, including the modified LTQ mass spectrometer for performing reactions of species, obtained in solution synthesis[129,130] or sputtering of metal targets[131], inside the ion trap. There are also setups coupling flow reactors with different cluster sources such as laser ablation[132,133] or dc discharge source[134]. Our setup for gas phase reactions consisted of a He/reagent gas mixture bought from Air Liquide (Bagneux, France). The bottle with the gas mixture was connected directly to the buffer gas line. This way, with a single regulation valve we can either send the pure buffer gas to the instrument to perform standard mass spectrometry, or we can send the He/rectant mixture to perform reactions in the ion trap. The reactant mixtures used were He/CO and He/NO. For the CO, we had two bottles of different concentrations, 5% and 0.1%. Experiments with NO were only done with 5% concentration.

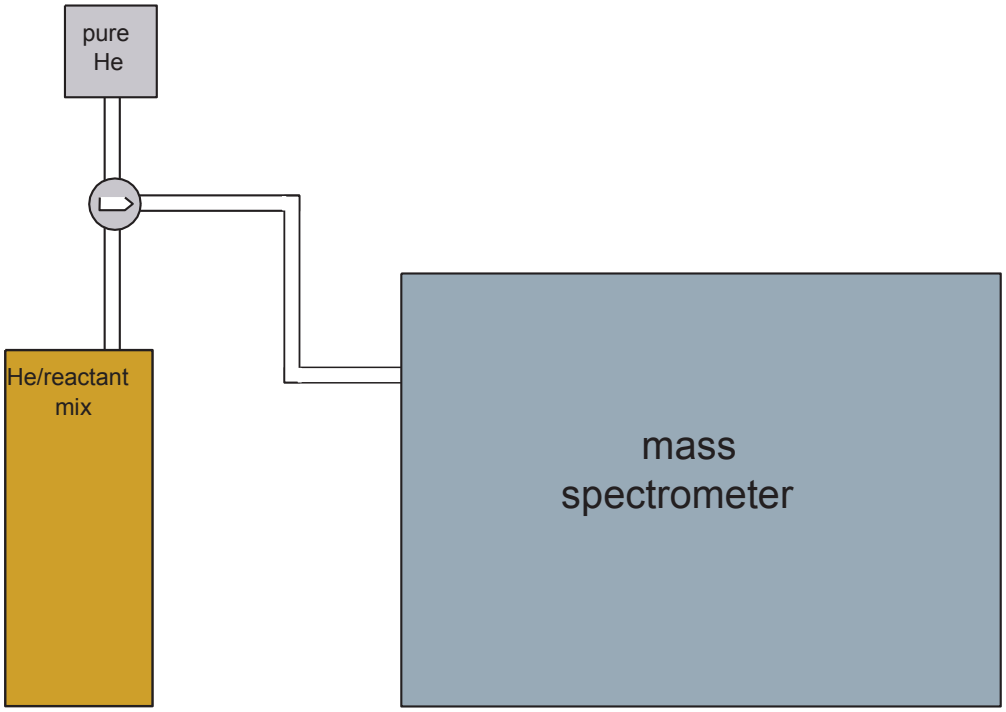

Figure 2. 22 Schematic of the experimental set-up for gas phase reactions.

Upon opening the valve to introduce the gas mixture in the ion trap, a period of ~20 minutes was required for the reactants to diffuse completely through the gas tubes and into the ion trap. Similarly, after the desired experiments with reactants were done, a period of around 20-30 minutes was required for the pure helium gas to flush the reactants completely out of the trap. Because the turbomolecular pump

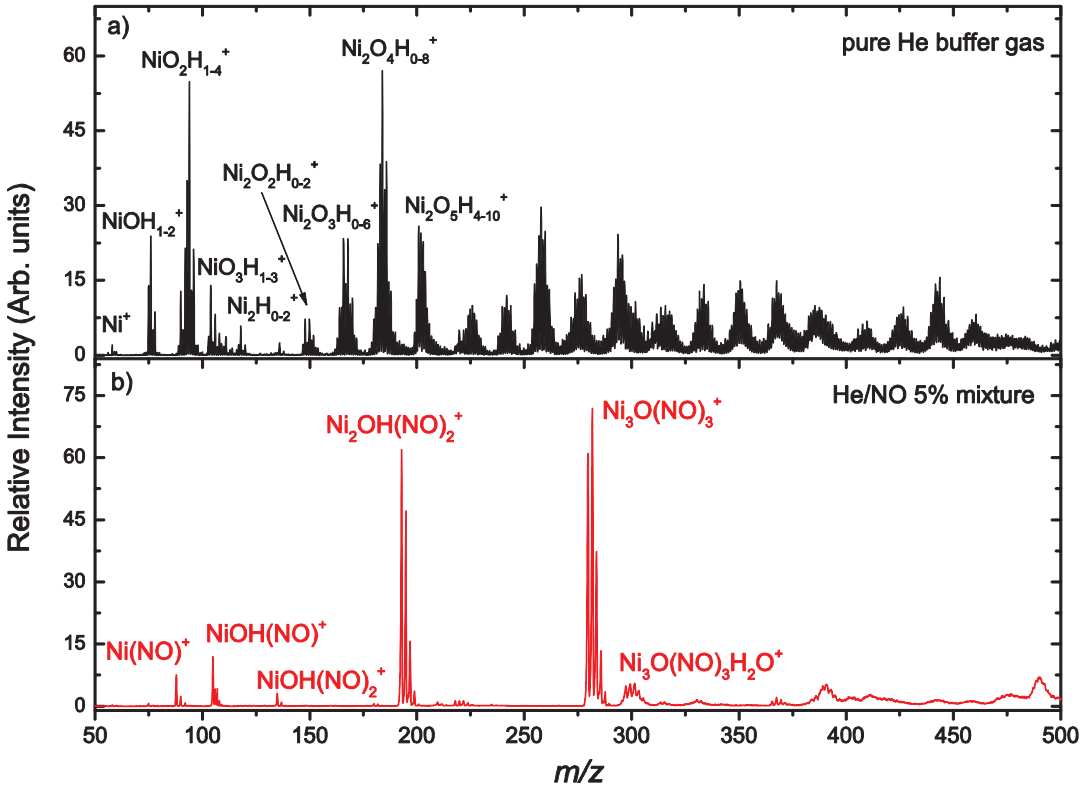

Figure 2. 23 Example reactions inside the ion trap. a) With pure He buffer gas. b) With He/NO 5% mixture.

pumps gases of different molecular weights with different efficiency pump, the actual concentration of the reactants in the trap are not the same as the mixture that we send in.

Helium gas is pumped with higher efficiency than the CO and the NO, which are pumped at ~77% of the rate of helium[135]. This means that effective concentrations of reactants in the ion trap are 6.835% and 0.13% when the bottle with 5% and 0.1% mixture are in use respectively. Figure 2. 23 shows how the mass spectrum changes upon introducing the reactants into the trap. The initial spectrum (Figure 2. 23a) is obtained by ablation of a nickel rod in the LAVESI source. The ablation in this case is done without the ESI syringe, with only ESI voltage, to promote the creation of pure metal clusters and reduce the amount of oxides, hydroxides and other products. Upon introducing the He/NO mixture, the composition of the mass spectrum changes completely (Figure 2. 23b). The pure nickel, as well as the oxides, hydroxides and other products disappear from the spectrum and are replaced by complexes with adsorbed NO. There are two peaks that dominate the spectrum. The species at *m/z* 193 corresponds to $Ni_2OH(NO)_2^+$, and the species at *m/z* 282 corresponds to $Ni_3O(NO)_3^+$. Further MS^2 and CID investigations show that these species are formed not only from one precursor, but that they are the final product of fragmentation of several different bigger species. This explains why in the mass spectrum with NO very few species above *m/z* 325 are observed even though there exist an abundance of possible precursors in that mass range.

2.4.3 Conclusion

To summarise, we have developed a new AP laser vaporisation source for producing bare and ligated metal clusters called LAVESI. It consists of laser vaporisation of a metal rod in the electrospray plume of a mass spectrometer. This way we are able to produce, depending on the chemical composition of the electrospray plume, pure metal clusters, ligated metal clusters and complexes and various other metal complexes (oxides, hydroxides, nitrides etc.). This source is used in conjunction with a modification to our linear trap mass spectrometer, in order to probe the reactivity of the newly synthesised species. The modification consists in adding a branching line to our buffer gas inlet in order to introduce reactant gases directly into the ion trap. This way reaction on ensembles of species created by LAVESI source can be studied, or reactions of individual species isolated in the trap, under various trapping times and collisional excitation conditions.

Bibliography

1. Enjalbal, C., Maux, D., Martinez, J., Combarieu, R. & Aubagnac, J.-L. Mass Spectrometry and Combinatorial Chemistry New Approaches for Direct Support-Bound Compound Identification. *Comb. Chem. High Throughput Screen.* **4,** 363–373 (2001).

2. Cui, W., Rohrs, H. W. & Gross, M. L. Top-down mass spectrometry: Recent developments, applications and perspectives. *Analyst* **136,** 3854 (2011).

3. Catherman, A. D., Skinner, O. S. & Kelleher, N. L. Top Down proteomics: Facts and perspectives. *Biochem. Biophys. Res. Commun.* **445,** 683–693 (2014).

4. Brodbelt, J. S. Photodissociation mass spectrometry: new tools for characterization of biological molecules. *Chem. Soc. Rev.* **43,** 2757–83 (2014).

5. Yu, C. & Hu, B. C18-coated stir bar sorptive extraction combined with high performance liquid chromatography–electrospray tandem mass spectrometry for the analysis of sulfonamides in milk and milk powder. *Talanta* **90,** 77–84 (2012).

6. Shen, Q., Jin, R., Xue, J., Lu, Y. & Dai, Z. Analysis of trace levels of sulfonamides in fish tissue using micro-scale pipette tip-matrix solid-phase dispersion and fast liquid chromatography tandem mass spectrometry. *Food Chem.* **194,** 508–515 (2016).

7. Won, S. Y. *et al.* Monitoring of 14 sulfonamide antibiotic residues in marine products using HPLC-PDA and LC-MS/MS. *Food Control* **22,** 1101–1107 (2011).

8. Becker, J. S. & Dietze, H.-J. Inorganic trace analysis by mass spectrometry. *Spectrochim. Acta Part B At. Spectrosc.* **53,** 1475–1506 (1998).

9. de Gouw, J. & Warneke, C. Measurements of volatile organic compounds in the earth's atmosphere using proton-transfer-reaction mass spectrometry. *Mass Spectrom. Rev.* **26,** 223–257 (2007).

10. Fenselau, C. *et al.* Mass spectrometry in the exploration of Mars. *J. Mass Spectrom.* **38,** 1–10 (2003).

11. Bieler, A. *et al.* Abundant molecular oxygen in the coma of comet 67P/Churyumov–Gerasimenko. *Nature* **526,** 678–681 (2015).

12. Thevis, M. *Mass Spectrometry in Sports Drug Testing*. (John Wiley & Sons, Inc., 2010).

13. Yuan, C., Chen, D. & Wang, S. Drug confirmation by mass spectrometry: Identification criteria and complicating factors. *Clin. Chim. Acta* **438,** 119–125 (2015).

14. Thomson, J. J. A New Method of Chemical Analysis. *Chem. News J. Ind. Sci.* **103,** 8 (1911).

15. Thomson, J. J. *Rays of Positive Electricity and Their Application to Chemical Analysis*. (Longmans, Green and Co. Ltd, 1913).

16. Meyerson, S. Reminiscences of the Early Days of Mass Spectrometry in the Petroleum Industry. **21,** 197–208 (1986).

17. Harvan, D. J. *et al.* Direct observation of the monomeric metaphosphate anion. *J. Am. Chem. Soc.* **101,** 7409 (1979).

18. Kroto, H. W., Heath, J. R., O'Brien, S. C., Curl, R. F. & Smalley, R. E. C 60: buckminsterfullerene. *Nature* **318,** 162 (1985).

19. Kroto, H. W. The stability of the fullerenes Cn, with n = 24, 28, 32, 36, 50, 60 and 70. *Nature* **329,** 529–531 (1987).

20. Stephens, W. E. A pulsed mass spectrometer with time dispersion. *Phys. Rev.* 691 (1946).

21. Paul, W. & Steinwedel, H. Ein Neues Massenspektrometer Ohne Magnetfeld. *Zeitschrift Fur Naturforsch. Sect. A-a J. Phys. Sci.* **8,** 448–450 (1953).

22. Comisarow, M. B. & Marshall, A. G. Fourier Transform Ion Cyclotron Resonance. *Chem. Phys. Lett.* **25,** 282–283 (1973).

23. Denison, D. R. Operating Parameters of a Quadrupole in a Grounded Cylindrical Housing. *J. Vac. Sci. Technol.* **8,** 266–269 (1971).

24. Frenkel, D. & Portugal, R. Algebraic methods to compute Mathieu functions. *J. Phys. A. Math. Gen.* **34,** 3541–3551 (2001).

25. Paul, W. in *Nobel Prize Lectures in Physics 1981-1990* 601–622 (World Scientific Publishing, 1993).

26. Fenn, J. B., Mann, M., Meng, C. K., Wong, S. F. & Whitehouse, C. M. Electrospray ionization-principles and practice. *Mass Spectrom. Rev.* **9,** 37–70 (1990).

27. Dole, M. *et al.* Molecular Beams of Macroions. *J Chem.Phys.* **49,** 2240–2249 (1968).

28. Yamashita, M. & Fenn, J. B. Electrospray ion source. Another variation on the free-jet theme. *J Phys.Chem.* **88,** 4451–4459 (1984).

29. Katta, V., Chowdhury, S. K. & Chait, B. T. Electrospray ionization: a new tool for the analysis of ionic transition-metal complexes. *J. Am. Chem. Soc.* **112,** 5348–5349 (1990).

30. Plattner, D. A. Electrospray mass spectrometry beyond analytical chemistry: Studies of organometallic catalysis in the gas phase. *Int. J. Mass Spectrom.* **207,** 125–144 (2001).

31. Kebarle, P. & Verkerk, U. H. Electrospray: From ions in solution to ions in the gas phase, what we know now. *Mass Spectrom. Rev.* **28,** 898–917 (2009).

32. Zeleny, J. The Electrical Discharge From Liquid Points, and a Hydrostatic Method of Measuring the Electric Intensity at their Surfaces. *Phys. Rev.* **III,** 69–91 (1914).

33. Zeleny, J. Instability of Electrified Liquid Surfaces. *Phys. Rev.* **10,** 1–6 (1917).

34. Rayleigh, Lord. XX. On the equilibrium of liquid conducting masses charged with electricity. *Philos. Mag. Ser. 5* **14,** 184–186 (1882).

35. Taylor, G. Disintegration of Water Drops in an Electric Field. *Proc. R. Soc. A Math. Phys. Eng. Sci.* **280,** 383–397 (1964).

36. Fernández de la Mora, J. The Fluid Dynamics of Taylor Cones. *Annu. Rev. Fluid Mech.* **39,** 217–243 (2007).

37. Luedtke, W. D. *et al.* Nanojets, electrospray, and ion field evaporation: Molecular dynamics simulations and laboratory experiments. *J. Phys. Chem. A* **112,** 9628–9649 (2008).

38. Cloupeau, M. & Prunet-Foch, B. Electrohydrodynamic spraying functioning modes: a critical review. *J. Aerosol Sci.* **25,** 1021–1036 (1994).

39. Tang, K. & Gomez, A. Generation of Monodisperse Water Droplets from Electrosprays in a Corona-Assisted Cone-Jet Mode. *Journal of Colloid and Interface Science* **175,** 326–332 (1995).

40. Iribarne, J. V & Thomson, B. A. On the evaporation of small ions from charged droplets. *J Chem.Phys.* **64,** 2287–2294 (1976).

41. Prudent, M. & Girault, H. H. Functional electrospray emitters. *Analyst* **134,** 2189 (2009).

42. Crotti, S., Seraglia, R. & Traldi, P. Some thoughts on electrospray ionization mechanisms. *Eur. J. Mass Spectrom. (Chichester, Eng).* **17,** 85–99 (2011).

43. Hotta, H. & Tsunoda, K. Electrospray Ionization Mass Spectrometry for the Quantification of Inorganic Cations and Anions. *Anal. Sci.* **31,** 7–14 (2015).

44. Tang, L. & Kebarle, P. Dependence of ion intensity in electrospray mass spectrometry on the concentration of the analytes in the electrosprayed solution. *Anal.Chem.* **65,** 3654–3668 (1993).

45. Breitbach, Z. S., Berthod, A., Huang, K. & Armstrong, D. W. Mass spectrometric detection of trace anions: The evolution of paired-ion electrospray ionization (PIESI). *Mass Spectrom. Rev.* **35,** 201–218 (2016).

46. Gibson, G. T. T., Mugo, S. M. & Oleschuk, R. D. Nanoelectrospray emitters: Trends and perspective. *Mass Spectrom. Rev.* **28,** 918–936 (2009).

47. Lebedev, A. T. Ambient ionization mass spectrometry. *Russ. Chem. Rev.* **84,** 665–692 (2015).

48. Yang, Q. *et al.* Paper spray ionization devices for direct, biomedical analysis using mass spectrometry. *Int. J. Mass Spectrom.* **312,** 201–207 (2012).

49. Soparawalla, S., Tadjimukhamedov, F. K., Wiley, J. S., Ouyang, Z. & Cooks, R. G. In situ analysis of agrochemical residues on fruit using ambient ionization on a handheld mass spectrometer. *Analyst* **136,** 4392 (2011).

50. Klampfl, C. W. & Himmelsbach, M. Direct ionization methods in mass spectrometry: An overview. *Anal. Chim. Acta* **890,** 44–59 (2015).

51. Chen, L. C. *et al.* Application of probe electrospray to direct ambient analysis of biological samples. *Rapid Commun. Mass Spectrom.* **22,** 2366–2374 (2008).

52. Dietz, T. G., Duncan, M. a., Powers, D. E. & Smalley, R. E. Laser production of supersonic metal cluster beams. *J. Chem. Phys.* **74,** 6511–6512 (1981).

53. Lubman, D. & Kronick, M. Mass spectrometry of aromatic molecules with resonance-enhanced multiphoton ionization. *Anal. Chem.* 660–665 (1982).

54. A, T. & Popov, B. Photodissociation of Salt Molecules into Ions. *Phys. Z. Sovjetunion* **2,** 299–318 (1932).

55. Beuhler, R. J., Flanigan, E., Greene, L. J. & Friedman, L. Proton Transfer Mass Spectrometry of Peptides. A Rapid Heating Technique for Underivatized Peptides Containing Arginine. *J. Am. Chem. Soc.* **96,** 3990–3999 (1974).

56. Flanigan, P. & Levis, R. Ambient femtosecond laser vaporization and nanosecond laser desorption electrospray ionization mass spectrometry. *Annu. Rev. Anal. Chem. (Palo Alto. Calif).* **7,** 229–56 (2014).

57. Demirev, P. *et al.* Matrix-assisted laser desorption with ultra-short laser pulses. *Rapid Commun. Mass Spectrom.* **6,** 187–191 (1992).

58. Wichmann, J. M., Lupulescu, C., Wöste, L. & Lindinger, A. Matrix-assisted laser desorption/ionization by using femtosecond laser pulses in the near-infrared wavelength regime. *Rapid Commun. Mass Spectrom.* **23,** 1105–1108 (2009).

59. Shiea, J. *et al.* Electrospray-assisted laser desorption/ionization mass spectrometry for direct ambient analysis of solids. *Rapid Commun. Mass Spectrom.* **19,** 3701–3704 (2005).

60. Huang, M., Hsu, H., Lee, J., Jeng, J. & Shiea, J. Direct Protein Detection from Biological Media through Electrospray-Assisted Laser Desorption Ionization / Mass Spectrometry research articles. *J. Proteome Res.* **5,** 1107–1116 (2006).

61. Huang, M. Z., Cheng, S. C., Cho, Y. T. & Shiea, J. Ambient ionization mass spectrometry: A tutorial. *Anal. Chim. Acta* **702,** 1–15 (2011).

62. Huang, M. Z. *et al.* Ambient molecular imaging of dry fungus surface by electrospray laser desorption ionization mass spectrometry. *Int. J. Mass Spectrom.* **325-327,** 172–182 (2012).

63. Shrestha, B. & Vertes, A. In Situ Metabolic Profiling of Single Cells by Laser Ablation Electrospray Ionization Mass Spectrometry. *Anal. Chem.* **81,** 8265–8271 (2009).

64. Shrestha, B., Patt, J. M. & Vertes, A. In situ cell-by-cell imaging and analysis of small cell populations by mass spectrometry. *Anal. Chem.* **83,** 2947–2955 (2011).

65. Shrestha, B., Nemes, P. & Vertes, A. Ablation and analysis of small cell populations and single cells by consecutive laser pulses. *Appl. Phys. A* **101,** 121–126 (2010).

66. Rezenom, Y. H., Dong, J. & Murray, K. K. Infrared laser-assisted desorption electrospray ionization mass spectrometry. *Analyst* **133,** 226–232 (2008).

67. Sampson, J. S. & Muddiman, D. C. Atmospheric pressure infrared (10.6um) laser desorption electrospray ionization (LDESI) coupled to a LTQ Fourier transform ion cyclotron resonance mass spectrometer. *Rapid Commun. Mass Spectrom.* **23,** 1989–1992 (2009).

68. Jorabchi, K. & Smith, L. M. Single droplet separations and surface partition coefficient measurements using laser ablation mass spectrometry. *Anal. Chem.* **81,** 9682–9688 (2009).

69. Karas, M., Bachmann, D., Bahr, U. & Hillenkamp, F. Matrix-assisted ultraviolet laser desorption of non-volatile compounds. *Int. J. Mass Spectrom. Ion Process.* **78,** 53–68 (1987).

70. Tanaka, K. *et al.* Protein and polymer analyses up to m/z 100 000 by laser ionization time-of-flight mass spectrometry. *Rapid Commun. Mass Spectrom.* **2,** 151–153 (1988).

71. Karas, M. & Hillenkamp, F. Laser desorption ionization of proteins with molecular masses exceeding 10,000 daltons. *Anal. Chem.* **60,** 2299–2301 (1988).

72. König, S., Kollas, O. & Dreisewerd, K. Generation of Highly Charged Peptide and Protein Ions by Atmospheric Pressure Matrix-Assisted Infrared Laser Desorption/Ionization Ion Trap Mass Spectrometry. *Anal. Chem.* **79,** 5484–5488 (2007).

73. Bondybey, V. E. Laser induced fluorescence of metal clusters produced by laser vaporization: Gas phase spectrum of Pb2. *J. Chem. Phys.* **74,** 6978 (1981).

74. Duncan, M. A. Invited Review Article: Laser vaporization cluster sources. *Rev. Sci. Instrum.* **83,** (2012).

75. Bloomfield, L. A., Geusic, M. E., Freeman, R. R. & Brown, W. L. Negative and positive cluster ions of carbon and silicon. *Chem. Phys. Lett.* **121,** 33–37 (1985).

76. Heath, J. R. *et al.* Semiconductor cluster beams: One and two color ionization studies of Six and Gex. *J. Chem. Phys.* **83,** 5520 (1985).

77. O'Brien, S. C. *et al.* Supersonic cluster beams of III–V semiconductors: GaxAsy. *J. Chem. Phys.* **84,** 4074 (1986).

78. Rohlfing, E. A., Cox, D. M. & Kaldor, A. Production and characterization of supersonic carbon cluster beams. *J. Chem. Phys.* **81,** 3322 (1984).

79. Geusic, M. E., Jarrold, M. F., McIlrath, T. J., Freeman, R. R. & Brown, W. L. Photodissociation of carbon cluster cations. *J. Chem. Phys.* **86,** 3862 (1987).

80. Heath, J. R. *et al.* The Formation of Long Carbon Chain Molecules during Laser Vaporization of Graphite. *J. Am. Chem. Soc.* **109,** 359–363 (1987).

81. Rohlfing, E. A., Cox, D. M., Petkovic-Luton, R. & Kaldor, A. Alloy cluster beams: nickel/chromium and nickel/aluminum. *J. Phys. Chem.* **88,** 6227–6231 (1984).

82. Wheeler, R. G. *et al.* Neutral gas-phase analogs of condensed-phase post-transition-metal cluster ions: laser vaporization and photoionization of tin-bismuth and lead-antimony alloys. *J. Am. Chem. Soc.* **108,** 8101–8102 (1986).

83. Wheeler, R. G., LaiHing, K., Wilson, W. L. & Duncan, M. A. Growth patterns in binary clusters of Group IV and V metals. *J. Chem. Phys.* **88,** 2831 (1988).

84. Guo, B. C., Kerns, K. P. & Castleman, A. W. Ti8C12+-Metallo-Carbohedrenes: A New Class of Molecular Clusters? *Science (80-.).* **255,** 1411–1413 (1992).

85. Pilgrim, J. S. & Duncan, M. A. Photodissociation of metallo-carbohedrene ('Met-Cars') cluster cations. *J. Am. Chem. Soc.* **115,** 4395–4396 (1993).

86. Pilgrim, J. S. & Duncan, M. A. Metallo-carbohedrenes: chromium, iron, and molybdenum analogs. *J. Am. Chem. Soc.* **115,** 6958–6961 (1993).

87. Pilgrim, J. S. & Duncan, M. A. Beyond metallo-carbohedrenes: growth and decomposition of metal-carbon nanocrystals. *J. Am. Chem. Soc.* **115,** 9724–9727 (1993).

88. Reddic, J. E. & Duncan, M. A. Composite samples and the generation of novel metal carbide clusters. *Chem. Phys. Lett.* **264,** 157–162 (1997).

89. Ticknor, B. W., Bandyopadhyay, B. & Duncan, M. A. Photodissociation of Noble Metal-Doped Carbon Clusters. *J. Phys. Chem. A* **112,** 12355–12366 (2008).

90. Deng, H. T., Kerns, K. P. & Castleman, A. W. Formation, Structures, and Reactivities of Niobium Oxide Cluster Ions. *J. Phys. Chem.* **100,** 13386–13392 (1996).

91. Kooi, S. E. & Castleman, A. W. Photofragmentation of Vanadium Oxide Cations. *J. Phys. Chem. A* **103,** 5671–5674 (1999).

92. Bell, R. C., Zemski, K. A., Justes, D. R. & Castleman, A. W. Formation, structure and bond dissociation thresholds of gas-phase vanadium oxide cluster ions. *J. Chem. Phys.* **114,** 798 (2001).

93. Foltin, M., Stueber, G. J. & Bernstein, E. R. On the growth dynamics of neutral vanadium oxide and titanium oxide clusters. *J. Chem. Phys.* **111,** 9577 (1999).

94. Molek, K. S., Jaeger, T. D. & Duncan, M. A. Photodissociation of vanadium, niobium, and tantalum oxide cluster cations. *J. Chem. Phys.* **123,** 144313 (2005).

95. Molek, K. S., Anfuso-Cleary, C. & Duncan, M. A. Photodissociation of Iron Oxide Cluster Cations †. *J. Phys. Chem. A* **112,** 9238–9247 (2008).

96. Beck, S. M. Studies of silicon cluster–metal atom compound formation in a supersonic molecular beam. *J. Chem. Phys.* **87,** 4233 (1987).

97. Hiura, H., Miyazaki, T. & Kanayama, T. Formation of Metal-Encapsulating Si Cage Clusters. *Phys. Rev. Lett.* **86,** 1733–1736 (2001).

98. Negishi, A. *et al.* Size-selective formation of tungsten cluster-containing silicon cages by the reactions of Wn+(n=1–5) with SiH4. *Chem. Phys. Lett.* **388,** 463–467 (2004).

99. Powers, D. E., Hansen, S. G., Geusic, M. E., Michalopoulos, D. L. & Smalley, R. E. Supersonic copper clusters. *J. Chem. Phys.* **78,** 2866–2881 (1983).

100. Bogaerts, A., Chen, Z., Gijbels, R. & Vertes, A. Laser ablation for analytical sampling: What can we learn from modeling? *Spectrochim. Acta - Part B At. Spectrosc.* **58,** 1867–1893 (2003).

101. Ready, J. F. *Effects of High Powered Laser Radiation*. (Academic Press Inc., 1971).

102. Yao, Y. L., Chen, H. & Zhang, W. Time scale effects in laser material removal: a review. *Int. J.*

Adv. Manuf. Technol. **26,** 598–608 (2005).

103. Autrique, D. *et al.* Revisiting the interplay between ablation, collisional, and radiative processes during ns-laser ablation. *Appl. Phys. Lett.* **103,** (2013).

104. Duncan, M. A. Spectroscopy of Metal Ion Complexes: Gas-Phase Models for Solvation. *Annu. Rev. Phys. Chem.* **48,** 69–93 (1997).

105. Duncan, M. A. Infrared spectroscopy to probe structure and dynamics in metal ion-molecule complexes. *Int. Rev. Phys. Chem.* **22,** 407–435 (2003).

106. Walker, N. R., Walters, R. S. & Duncan, M. A. Frontiers in the infrared spectroscopy of gas phase metal ion complexes. *New J. Chem.* **29,** 1495 (2005).

107. Duncan, M. A. Structures, energetics and spectroscopy of gas phase transition metal ion–benzene complexes. *Int. J. Mass Spectrom.* **272,** 99–118 (2008).

108. Walters, R. S., Pillai, E. D. & Duncan, M. A. Solvation Dynamics in Ni + (H 2 O) n Clusters Probed with Infrared Spectroscopy. *J. Am. Chem. Soc.* **127,** 16599–16610 (2005).

109. Carnegie, P. D., Bandyopadhyay, B. & Duncan, M. A. Infrared Spectroscopy of Cr + (H 2 O) and Cr 2+ (H 2 O): The Role of Charge in Cation Hydration. *J. Phys. Chem. A* **112,** 6237–6243 (2008).

110. Carnegie, P. D., McCoy, A. B. & Duncan, M. A. IR Spectroscopy and Theory of Cu + (H 2 O)Ar 2 and Cu + (D 2 O)Ar 2 in the O−H (O−D) Stretching Region: Fundamentals and Combination Bands. *J. Phys. Chem. A* **113,** 4849–4854 (2009).

111. Carnegie, P. D., Bandyopadhyay, B. & Duncan, M. A. Infrared spectroscopy of Sc+(H2O) and Sc2+(H2O) via argon complex predissociation: The charge dependence of cation hydration. *J. Chem. Phys.* **134,** 014302 (2011).

112. Ricks, A. M., Bakker, J. M., Douberly, G. E. & Duncan, M. A. Infrared Spectroscopy and Structures of Cobalt Carbonyl Cations, Co(CO) n + (n = 1−9) †. *J. Phys. Chem. A* **113,** 4701–4708 (2009).

113. Ricks, A. M., Reed, Z. D. & Duncan, M. A. Seven-Coordinate Homoleptic Metal Carbonyls in the Gas Phase. *J. Am. Chem. Soc.* **131,** 9176–9177 (2009).

114. Ricks, A. M., Reed, Z. E. & Duncan, M. A. Infrared spectroscopy of mass-selected metal carbonyl cations. *J. Mol. Spectrosc.* **266,** 63–74 (2011).

115. Yardley, J. T. *Introduction to Molecular Energy Transfer*. (Academic Press Inc., 1980).

116. Fojtik, A., Giersig, M. & Henglein, A. Formation of Nanometer-Size Silicon Particles in a Laser Plasma in SiH4. *Berichte der Bunsengesellschaft für Phys. Chemie* **97,** 252–255 (1993).

117. Neddersen, J., Chumanov, G. & Cotton, T. M. Laser Ablation of Metals: A New Method for Preparing SERS Active Colloids. *Appl. Spectrosc.* **47,** 1959–1964 (1993).

118. Sibbald, M. S., Chumanov, G. & Cotton, T. M. Reduction of Cytochrome c by Halide-Modified, Laser-Ablated Silver Colloids. *J. Phys. Chem.* **100,** 4672–4678 (1996).

119. Mafuné, F., Kohno, J., Takeda, Y., Kondow, T. & Sawabe, H. Structure and Stability of Silver Nanoparticles in Aqueous Solution Produced by Laser Ablation. *J. Phys. Chem. B* **104,** 8333–8337 (2000).

120. Mafuné, F., Kohno, J., Takeda, Y., Kondow, T. & Sawabe, H. Formation and Size Control of Silver Nanoparticles by Laser Ablation in Aqueous Solution. *J. Phys. Chem. B* **104,** 9111–9117 (2000).

121. Mafuné, F., Kohno, J., Takeda, Y., Kondow, T. & Sawabe, H. Formation of Gold Nanoparticles

by Laser Ablation in Aqueous Solution of Surfactant. *J. Phys. Chem. B* **105,** 5114–5120 (2001).

122. Amans, D. *et al.* Synthesis of oxide nanoparticles by pulsed laser ablation in liquids containing a complexing molecule: Impact on size distributions and prepared phases. *J. Phys. Chem. C* **115,** 5131–5139 (2011).

123. Yang, G. W. Laser ablation in liquids: Applications in the synthesis of nanocrystals. *Prog. Mater. Sci.* **52,** 648–698 (2007).

124. Pearce, S. R. J. *et al.* Production of nanocrystalline diamond by laser ablation at the solid/liquid interface. *Diam. Relat. Mater.* **13,** 661–665 (2004).

125. Amans, D. *et al.* Nanodiamond synthesis by pulsed laser ablation in liquids. *Diam. Relat. Mater.* **18,** 177–180 (2009).

126. Thermo Electron Corporation. LTQ XL Hardware Manual. (2006).

127. Thermo Electron Corporation. LTQ XL Instrument Glossary. (2006).

128. Thermo Electron Corporation. LTQ XL Getting Started Manual. (2006).

129. T. Waters, R. A. O'Hair, A. G. W. Catalytic gas phase oxidation of methanol to formaldehyde. *J. Am. Chem. Soc.* **125,** 3384–3396 (2003).

130. O'Hair, R. a J. The 3D quadrupole ion trap mass spectrometer as a complete chemical laboratory for fundamental gas-phase studies of metal mediated chemistry. *Chem. Commun. (Camb).* 1469–1481 (2006).

131. Bernhardt, T. M. Gas-phase kinetics and catalytic reactions of small silver and gold clusters. *Int. J. Mass Spectrom.* **243,** 1–29 (2005).

132. Bechtold, P. S., Parks, E. K., Weiller, H., Pobo, L. G. & Riley, S. J. Chemical Reactions of Small Gas Phase Metal Clusters. *Zeitschrift fur Phys. Chemie Neue Folge* **169,** 101–122 (1990).

133. Parks, E. K., Riley, S. J. & Thiel, P. A. in *The Chemical Physics of Atomic and Molecular Clusters* (ed. Scoles, G.) (Elsevier B.V., 1990).

134. Ervin, K. M. *Metal-ligand interactions: Gas-phase transition metal cluster carbonyls*. *International Reviews in Physical Chemistry* **20,** (2001).

135. Becker, W. The turbomolecular pump, its design, operation and theory; calculation of the pumping speed for various gases and their dependence on the forepump. *Vacuum* **16,** 625–632 (1966).

3. Wet chemistry synthesis

Owing to their extraordinary properties such as quantized charging and luminescence, thiolated Au clusters have become a very important group. Many experiments revealed that the chemical and physical properties of these clusters are governed by their size, due to the confinement effects[1–3]. The last decade has seen an explosion of interest in the use of coinage metals as catalysts in the synthesis of organic chemicals[4–6]. Ligated metal nanoclusters are also developed for a range of applications in biology, material sciences and physics[2]. However, isolating a given species in the condensed phase is complicated and the relationship between structure and chemical or physical properties is often not fully understood. With the development of electrospray ionization sources, mass spectrometry (ESI/MS) emerged as a key discovery tool to synthesize and examine ligand metal complexes[7–11]. Complexes are formed by electrospraying metal salts with organic and biomolecular ligands. Ligands with thiol groups are a good candidate for this due to the strong interactions between sulfur and gold and silver[1,12]. Their gas-phase structure[13–15], reactivity[16–19], optical properties… etc. are then examined by mass spectrometry. The characterization of synthesized solution by mass spectrometry was used over time to direct the solution phase synthesis of nanoclusters[8].

3.1 Synthesis in solution: $Au_{15}SG_{13}$

The monodisperse $Au_{15}SG_{13}$ was synthesized by dissolving and mixing glutathione and gold in the presence of reducing agents. The mixture is then left to react overnight. After this, the solution is concentrated and a series of dissolution-precipitation-centrifugation cycles is performed in order to remove the unreacted ligand. Following this, the unwanted, small Au-SG chains are removed through precipitation in water/acetic acid and centrifugation. The remaining supernatant is then goes through another cycle of dissolution-precipitation, before the final product can be dried as a yellow powder. Approximately 38 mg of $Au_{15}SG_{13}$ were obtained through this process out of the starting 235 mg of glutathione and 100 mg of chloroauric acid ($HAuCl_4$)[20].

For MS analysis the solution was diluted in water at a concentration of $1\,mg/ml$, and analyzed with ESI-MS. Gentle ESI conditions were used in order to minimize the fragmentation of the sample. Mass spectrum was obtained in negative mode, spray voltage used was -3kV, and capillary temperature was 100°C. Figure 3. 1 shows the mass spectrum of the solution. The peaks corresponding to charge states of $Au_{15}SG_{13}$ ranging from 4- to 8- dominate the mass spectrum. A close look at the isotopic distribution of one of the charge states shows good agreements with theoretical mass spectrum of the corresponding species (Figure 3. 1 inset). The described synthesis results in a nanocluster product of remarkable purity, with only minimum contribution of unwanted species. Signal-to-noise ratio is quite good, and only small amounts of $Au_{16}SG_{14}$ can be found in the solution.

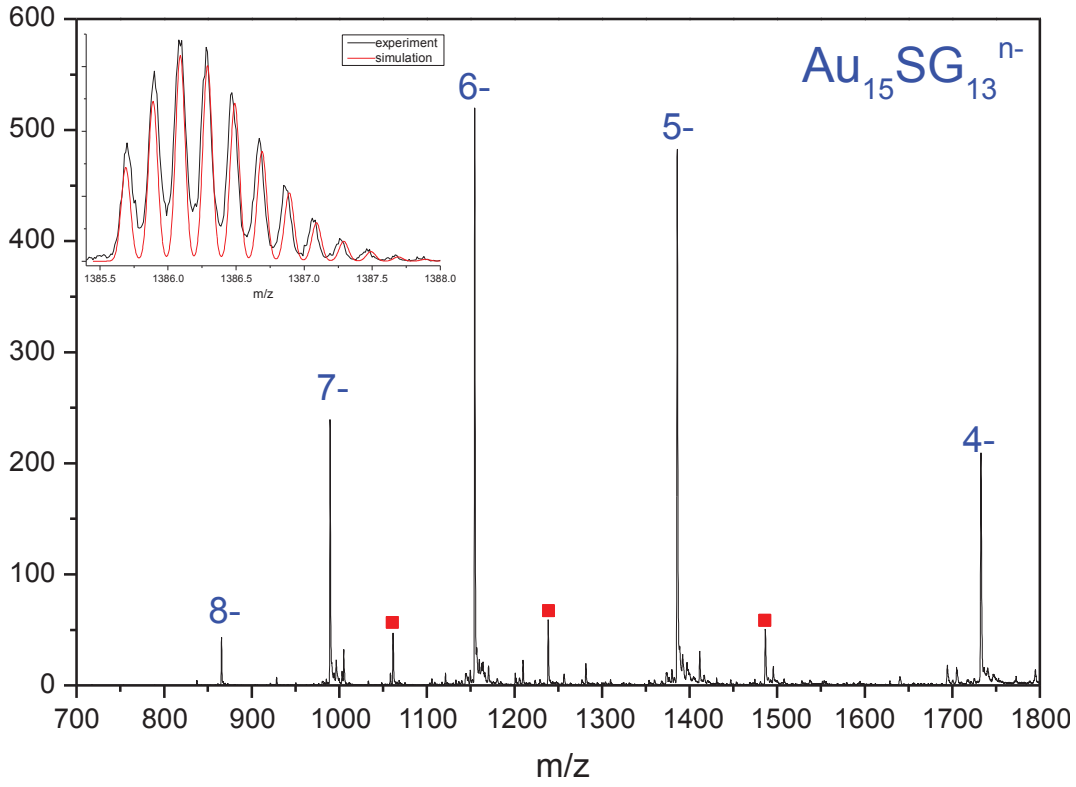

Figure 3. 1 ESI mass spectrum of $Au_{15}SG_{13}$ water solution. Blue numbers marks the charge states of $Au_{15}SG_{13}$. The red squares mark the 5-, 6-, 7- charge states of $Au_{16}SG_{14}$. Inset: close-up of the isotopic distribution of $Au_{15}SG_{13}^{5-}$, and comparison with a simulated mass spectrum.

3.2 Synthesis in electrospray: small clusters

Small clusters were synthesized by electrospraying the solution mixture of metal salt and ligand. The ligand used was thioglycolic acid ($H-SR = HSCH_2COOH$). The metal salts used in synthesis were silver nitrate ($AgNO_3$) and chloroauric acid ($HAuCl_4$). Both, salts and ligand, as well as ascorbic acid were purchased from Sigma Aldrich (St. Louis, MO, USA). For synthesis starting from metal salt aqueous solutions, the following conditions were used:

- Silver complexes were prepared by adding $20\mu L$ of a $25mM$ $AgNO_3$ solution to $10mL$ of a $50\mu M$ thioglycolic acid solution.
- Gold complexes were prepared by adding $20\mu L$ of a $25mM$ $HAuCl_4$ solution to $10mL$ of $50\mu M$ thioglycolic acid and $200\mu M$ of ascorbic acid solution. The pH was fixed to 7-8 with a buffer solution of NH_4OH.

The small stoichiometric species are also observed after electrospraying a solution containing a silver salt (Figure 3. 2)[21]. These species were previously attributed to chains and rings of Ag(I)-thiolate[22]. Peaks at higher masses, corresponding to larger complexes with silver in excess are not observed in Figure 3. 2. Since the largest mass observed is significantly lower than the detection limit of mass spectrometer (*m/z* 2000), the limited mass range of the detected species reflects the realistic size

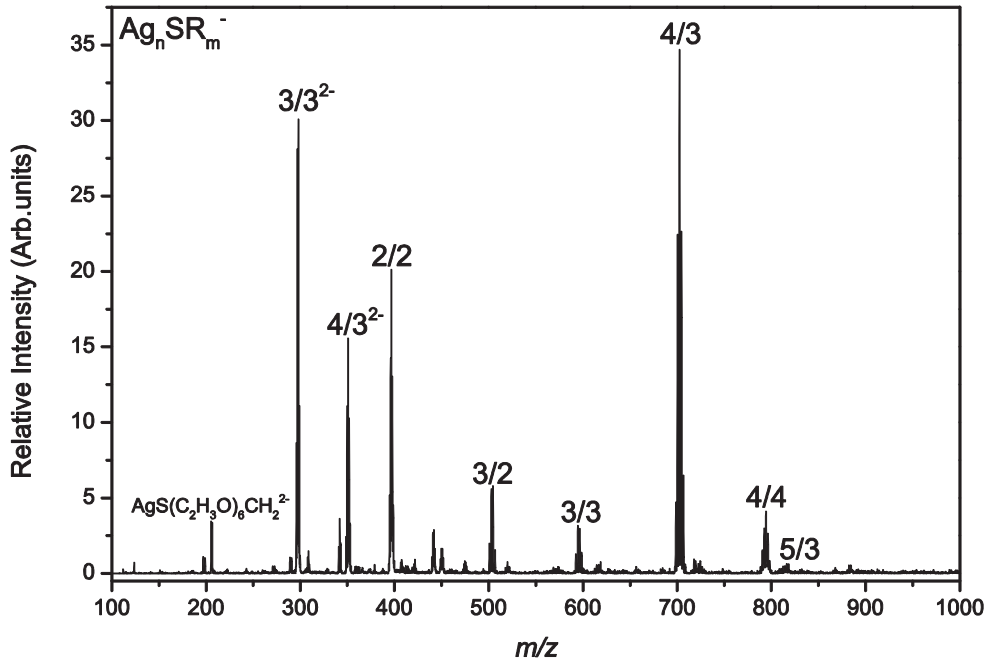

Figure 3. 2 ESI mass spectrum of small silver-thioglycolic acid complexes obtained through wet chemistry synthesis.

distribution due to the nature of the synthesis. This type of synthesis does not produce large complexes with a metal core surrounded by ligands as obtained from wet chemistry methods[23–26].

3.3 Collision induced dissociation of small clusters

Several different species are studied in the gas phase by sequences of collision induced dissociation (CID) of a silver–thioglycolic acid complex precursor (MS^n experiments). The different steps of ion selection and excitation are successively carried out in the high pressure cell. The peak corresponding to four silvers atoms and tree thioglycolic acids was selected (Figure 3. 3 - right). Isotopic distribution analysis shows that the peak at m/z 702.6 is due to $[4Ag(C_2H_2O_2S)_2C_2H_3O_2S]^-$, with a simplified notation $[Ag_4(SR)_3 - 2H]^-$. To record MS^2 spectra, a precursor ion was selected in the ion trap using an m/z window of 10 Th, it was then activated by collision and the resulting mass spectrum was recorded. The collision-induced dissociation (CID) was performed using helium gas at a normalized collision energy of 6 and 50 Arb. Units (1.5% and 12.5% respectively) for 30 ms. Figure 3. 3 (right – middle and bottom) shows the mass spectrum obtained after collisional activation of $[Ag_4(SR)_3 - 2H]^-$ (m/z 702.6). The analysis of mass spectra indicates two fragmentation channels. We observe two major peaks (m/z 658.5, and 614.5). Isotopic distribution analysis shows that these peaks correspond to successive losses of CO_2 (44 Da), a 2nd CO_2 and SCH_2 (46 Da) leading to a complex made of one thioglycolic acid and 4 silver atoms bonded to SCH_3. A possible pathway is first decarboxylation from the carboxylic group of a thioglycolic acid followed by a decarboxylation from a carboxylate. The later leads to the formation of CH_2S group, which is lost after further excitation. Second fragmentation

channel is observed through minor peaks at m/z 644.4 and 600.5. These correspond to successive losses of 58 Da and 44 Da. They are attributed to CO_2 and $C_2H_2O_2$ losses.

$$\begin{cases} [4Ag(C_2H_2O_2S)_2C_2H_3O_2S]^- \rightarrow [4Ag(C_2H_2O_2S)_2CH_3S]^- + CO_2 \\ [4Ag(C_2H_2O_2S)_2CH_3S]^- \rightarrow [4Ag(C_2H_2O_2S)(CH_3S)CH_2S]^- + CO_2 \\ [4Ag(C_2H_2O_2S)(CH_3S)CH_2S]^- \rightarrow [4Ag(C_2H_2O_2S)(CH_3S)]^- + CH_2S \end{cases} \quad (3.1)$$

$$\begin{cases} [4Ag(C_2H_2O_2S)_2C_2H_3O_2S]^- \rightarrow [4Ag(C_2H_2O_2S)_2SH]^- + C_2H_2O_2 \\ [4Ag(C_2H_2O_2S)_2SH]^- \rightarrow [4Ag(C_2H_2O_2S)CH_2SHS]^- + CO_2 \end{cases} \quad (3.2)$$

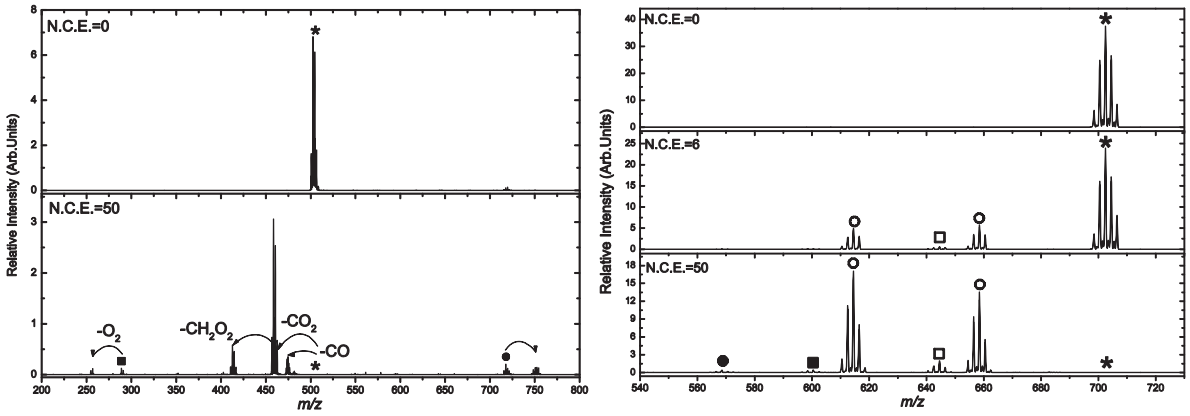

Figure 3. 3 CID fragmentation channels of selected small silver nanoclusters. Left – the peak at 502.7 Da corresponding to $[Ag_3(SR)_2 - 2H]^-$ (simplified notation) isolated with a m/z window of 10Th, with (bottom) and without (top) collisional activation energy (in arbitrary units). The star symbol marks the precursor ion, while the square and the circle mark the $[Ag(SR)_2]^-$ and $[Ag_5(SR)_2 - 3H]^-$ ions respectively. Right – the peak at 702.6 Da corresponding to $[Ag_4(SR)_3 - 2H]^-$ with three different values of collisional activation energy. The star symbol marks the precursor ion, and circle and square symbols mark the two different fragmentation channels, where the full shape marks the final product ion of the channel, and the empty ones mark the intermediary species.

By analysis of isotopic distribution we determine that the peaks at m/z 502.7 correspond to $[3Ag(C_2H_2O_2S)_2]^-$(simplified $[Ag_3(SR)_2 - 2H]^-$). Its collisional fragmentation spectrum shows multitude of species. We observe the already seen loss of CO_2, but there is also new species which correspond to losses of CO and CH_2O_2. Also we observe peaks at *m/z* 288.8 and 717.7. By isotopic structure analysis we determine the one at *m/z* 288.8 to be $[Ag(SR)_2]^-$ and the species at *m/z* 717.7 $[Ag_5(SR)_2 - 3H]^-$, whose existence indicates the presence of multicharged species in the isolated *m/z* range. These species then produce $[Ag_5(SR)_2 - 3H]^-$ through mfragmentation and loss of charge.

The peak at m/z 794.3 was determined to correspond to $[4Ag(C_2H_2O_2S)_3C_2H_3O_2S]^-$(simplified $[Ag_4(SR)_4 - H]^-$) (Figure 3. 4 – left). Under collisional activation the precursor ion disappears completely. The dominant peak becomes m/z 702.6 which is determined to correspond to $[Ag_4(SR)_3 - 2H]^-$. The small peak at m/z 746.5 indicated the possible fragmentation pathway by loss of SCH_2 and subsequent loss of CO_2.

$$\begin{cases} [4Ag(C_2H_3O_2S)_3C_2H_2O_2S]^- \rightarrow [4Ag(C_2H_3O_2S)_3CO_2]^- + SCH_2 \\ [4Ag(C_2H_3O_2S)_3CO_2]^- \rightarrow [4Ag(C_2H_2O_2S)_2C_2H_3O_2S]^- + CO_2 + H_2 \end{cases} \quad (3.3)$$

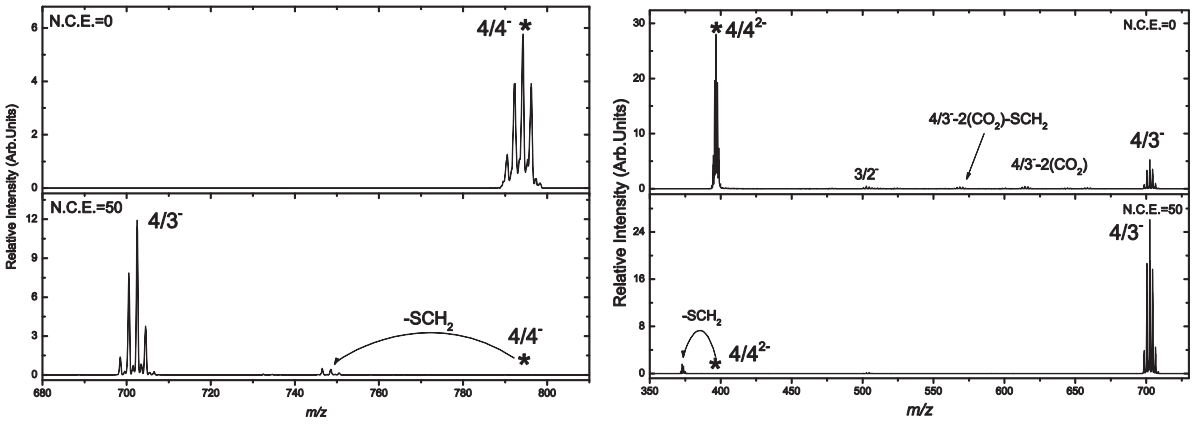

Figure 3. 4 CID mas spectra of 4/4 singly (left) and doubly (right) charged.

The doubly charged ion of the same species $[4Ag(C_2H_2O_2S)_2(C_2H_3O_2S)_2]^{2-}$(simplified $[Ag_4(SR)_4 - 2H]^{2-}$), at m/z 396.7, shows fragmentation even with collisional activation at 0 (Figure 3. 4 – right). The products of the fragmentation are singly charged ions, the $[Ag_4(SR)_3 - 2H]^-$ with its two fragments, which correspond to the same species identified in the main fragmentation channel of the $[Ag_4(SR)_3 - 2H]^-$. Upon the addition of collisional activation, a new fragmentation channel emerges. Is corresponds to the loss of SCH_2 from the precursor ion. At the same time, the low intensity intermediate peaks of the first fragmentation channel disappear, leaving only the peak at m/z 702.6, already identified as $[Ag_4(SR)_3 - 2H]^-$.

$$\begin{cases} [4Ag(C_2H_3O_2S)_2(C_2H_2O_2S)_2]^{2-} \xrightarrow{CID\ 0} [4Ag(C_2H_2O_2S)_2C_2H_3O_2S]^- + C_2H_3O_2S \\ [4Ag(C_2H_2O_2S)_2C_2H_3O_2S]^- \xrightarrow{CID\ 0} [4Ag(C_2H_2O_2S)_2(CH_3S)CH_2S]^- + 2CO_2 \end{cases} \quad (3.4)$$

$$\begin{cases} [4Ag(C_2H_3O_2S)_2(C_2H_2O_2S)_2]^{2-} \rightarrow [4Ag(C_2H_3O_2S)_2(C_2H_2O_2S)CO_2]^{2-} + CH_2S \\ [4Ag(C_2H_3O_2S)_2(C_2H_2O_2S)_2]^{2-} \rightarrow [4Ag(C_2H_2O_2S)_2C_2H_3O_2S]^- + C_2H_3O_2S \end{cases} \quad (3.5)$$

Figure 3. 5 shows a mass spectrum of gold-thioglycolic acid solution. Formation of ligated gold complexes is observed. The mass spectrum is dominated by species with N=M, which is in agreement with the formation of small chains with equal number of ligands and gold cations.

Due to difficulty of synthesis and susceptibility to oxidation upon exposure to air, it is a significant challenge to prepare stable ligated copper complexes, and therefore studies of Cu containing species are still at a preliminary stage compared to what has been achieved for both ligated Ag and Au clusters[27,28]. For this reason no results with copper based solution are shown here, as none of the attempted synthesis produced any detectable ligated copper complexes.

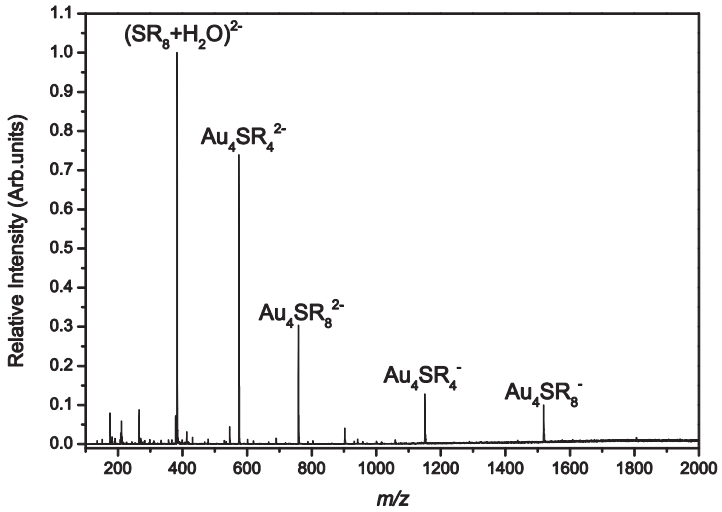

Figure 3. 5 ESI mass spectrum of small gold-thioglycolic acid complexes, obtained through wet chemistry synthesis.

3.4 Conclusion

We describe two different types of wet chemistry synthesis of metallic nanoclusters of gold and silver. The first synthesis is based on mixing the ligand and metal salt solution in the presence of reducing agents, and followed by a series dissolution-precipitation-centrifugation cycles in order to purify the solution. The result is remarkably monodisperse solution of ligated gold clusters $Au_{15}SG_{13}$.

The second synthesis consists of electrospraying the mix of metal salt and ligand solution in order to form the ligated metal complexes in the electrospray plume. Compared to the first one, there is a big increase in polydispersity of the products of this synthesis. A multitude of small stoichiometric species (singly and doubly charged) are produced, both with silver and with gold salts. MS^n experiments are used to probe their stability and fragmentation channels. This information is useful especially in context of comparison with the same species produced by other types of synthesis.

Bibliography

1. Jin, R. Quantum sized, thiolate-protected gold nanoclusters. *Nanoscale* **2,** 343–362 (2010).
2. Jin, R. Atomically precise metal nanoclusters: stable sizes and optical properties. *Nanoscale* **7,** 1549–65 (2015).
3. Bonačić-Koutecký, V. *et al.* Silver cluster–biomolecule hybrids: from basics towards sensors. *Phys. Chem. Chem. Phys.* **14,** 9282 (2012).
4. Stephen, A. & Hashmi, K. Homogeneous gold catalysis beyond assumptions and proposals-characterized intermediates. *Angew. Chemie - Int. Ed.* **49,** 5232–5241 (2010).
5. Hashmi, A. S. K. & Rudolph, M. Gold catalysis in total synthesis. *Chem.Soc.Rev.* **37,** 1766–1775 (2008).
6. Hashmi, A. S. K. in *Inorganic Chemistry* **48,** 143–164 (2012).
7. Ince, M. ., Perera, B. . & Van Stipdonk, M. . Production, dissociation, and gas phase stability of sodium fluoride cluster ions studied using electrospray ionization ion trap mass spectrometry. *Int. J. Mass Spectrom.* **207,** 41–55 (2001).
8. Khairallah, G. N. & O'Hair, R. A. J. Gas-phase synthesis of [Ag4H]+ and its mediation of the C-C coupling of allyl bromide. *Angew. Chemie - Int. Ed.* **44,** 728–731 (2005).
9. Li, H., Siu, K. W. M., Guevremont, R. & Le Blanc, J. C. Y. Complexes of Silver (1) with peptides and proteins as produced in electrospray mass spectrometry. *J. Am. Soc. Mass Spectrom.* **8,** 781–792 (1997).
10. Wang, G. & Cole, R. B. Solvation energy and gas-phase stability influences on alkali metal cluster ion formation in electrospray ionization mass spectrometry. *Anal. Chem.* **70,** 873–81 (1998).
11. Zhang, D. & Cooks, R. G. Doubly charged cluster ions [(NaCl)(m)(Na)2]2+: Magic numbers, dissociation, and structure. *Int. J. Mass Spectrom.* **195-196,** 667–684 (2000).
12. Häkkinen, H. The gold–sulfur interface at the nanoscale. *Nat. Chem.* **4,** 443–455 (2012).
13. Mitrić, R. *et al.* Gas-Phase Synthesis and Vibronic Action Spectroscopy of Ag 2 H +. *J. Phys. Chem. Lett.* **2,** 548–552 (2011).
14. Tabarin, T. *et al.* Absorption Enhancement and Conformational Control of Peptides by Small Silver Clusters. *Phys. Rev. Lett.* **101,** 213001 (2008).
15. Hamouda, R. *et al.* Glutathione capped gold AuN(SG)M clusters studied by isotope-resolved mass spectrometry. *Int. J. Mass Spectrom.* **335,** 1–6 (2013).
16. Khairallah, G. N. & O'Hair, R. a J. Gas phase synthesis and reactivity of Agn+ and Ag(n-1)H+ cluster cations. *Dalt. Trans.* 2702–2712 (2005).
17. Khairallah, G. N. & O'Hair, R. a J. Activation of the C-I and C-OH bonds of 2-iodoethanol by gas phase silver cluster cations yields subvalent silver-iodide and -hydroxide cluster cations. *Dalt. Trans.* **3,** 3149–3157 (2007).
18. Khairallah, G. N. & O'Hair, R. a J. Gas phase synthesis, structure and unimolecular reactivity of silver iodide cluster cations, AgnIm+ (n = 2–5, 0 < m < n). *Dalt. Trans.* 2956 (2008).
19. Wang, F. Q., Khairallah, G. N. & O'Hair, R. A. J. Role of cluster size and substrate in the gas phase C-C bond coupling reactions of allyl halides mediated by Agn+ and Agn−1H+ cluster cations. *Int. J. Mass Spectrom.* **283,** 17–25 (2009).
20. Russier-Antoine, I. *et al.* Non-linear optical properties of gold quantum clusters. The smaller the

better. *Nanoscale* **6,** 13572–8 (2014).

21. Bellina, B. *et al.* Formation and characterization of thioglycolic acid-silver cluster complexes. *Dalt. Trans.* **42,** 8328–8333 (2013).

22. Bell, R. a & Kramer, J. R. Structural chemistry and geochemistry of silver-sulfur compounds: Critical review. *Environ. Toxicol. Chem.* **18,** 9–22 (1999).

23. Bertorelle, F. *et al.* Synthesis, characterization and optical properties of low nuclearity liganded silver clusters: Ag31(SG)19 and Ag15(SG)11. *Nanoscale* **5,** 5637–5643 (2013).

24. Guo, J. *et al.* Mass spectrometric identification of silver nanoparticles: the case of Ag32(SG)19. *Anal. Chem.* **84,** 5304–8 (2012).

25. Kumar, S., Bolan, M. D. & Bigioni, T. P. Glutathione-stabilized magic-number silver cluster compounds. *J. Am. Chem. Soc.* **132,** 13141–13143 (2010).

26. Desireddy, A. *et al.* Ultrastable silver nanoparticles. *Nature* **501,** 399–402 (2013).

27. Ganguly, A., Chakraborty, I., Udayabhaskararao, T. & Pradeep, T. A copper cluster protected with phenylethanethiol. *J. Nanoparticle Res.* **15,** (2013).

28. Wei, W., Lu, Y., Chen, W. & Chen, S. One-pot synthesis, photoluminescence, and electrocatalytic properties of subnanometer-sized copper clusters. *J. Am. Chem. Soc.* **133,** 2060–2063 (2011).

4. Synthesis and characterisation of bare and ligated-metal species by Laser Vaporization Electrospray Ionization (LAVESI)

Due to their interesting physical and chemical properties and potential of use in nanotechnology, transitional metal complexes have seen a surge of interest in research in recent years[1–4]. Vaporization of metal rods coupled to fast cooling has been successfully used to produce bare clusters of any metal on a wide range of sizes[5–7]. Here, we will describe results of a new method for the production of pure and hybrid metal complexes based on laser vaporization electrospray ionization (LAVESI) mass spectrometry. Metal species generated by vaporization of the rod react with molecular species present in the spray to form hybrid complexes. First results are obtained with silver, gold and copper reacting with atmospheric constituents and thioglycolic acid. In absence of ligands in the spray plume some new insights into the stoichiometry and stability of metal oxides can be glimpsed. The results show that the presence of the ligand in the plume has a significant effect on the species observed. When compared with results obtained with H_2O and D_2O in the ESI syringe, and the empty ESI syringe, we see that the presence of ligand prevents the nucleation and oxidation of metal complexes in the plume, instead creating the ligated metal complexes $M_NSR_M^-$, (where M is silver and/or gold, and SR is thioglycolic acid) that were, in the case of silver thiolate complexes attributed with the chain-like structure[8].

4.1 Formation and properties of metal oxides

As LAVESI source is an API type of source, immediately upon vaporisation the created metal species are subject to reactions with atmospheric gases. This leads to formation of many metal oxides, hydroxides, hydrates and nitrides. The abundance of products and their varied stoichiometries are caused by the plasma plume formed from laser-metal interaction. It creates a plethora of ionised and neutral species[9] which readily react with vaporised metal outside of the plume as well as the atmospheric constituents. They are then transferred into the entry capillary of our mass spectrometer, and conducted into the ion trap where they can be at will mass selected and probed with collisional activation. Upon applying the in-source collisional activation we can see the change in the distribution of the peaks. Detailed analysis using MS^2 and MS^3 experiments helps us obtain information about the observed species. The experiments described here were conducted on gold and silver, both in positive and negative mode, so that we are able to compare the behaviour of both anions and cations of these metals. The analysis of copper oxides was hindered by overabundance of species in the mass spectrum, where several species would contribute to the signal at the same *m/z* making it impossible to unambiguously assign peaks. At the ESI level, we study the effect of H_2O and D_2O in the ESI syringe, and we also conducted experiments with the syringe mechanism turned off, where only ESI voltage was applied. Even though they are in the same column in the periodic system, due to relativistic effects, silver and

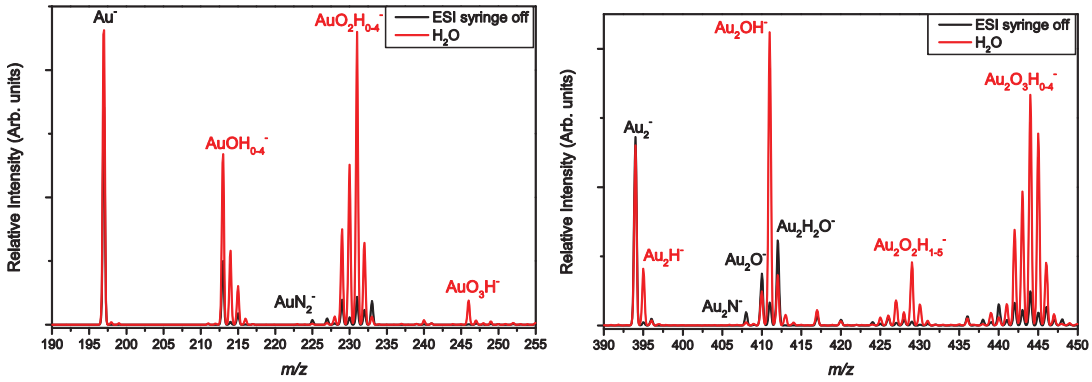

Figure 4. 1 Example of comparison of mass spectra obtained with different electrospray plume compositions, with electrospray syringe empty and turned off, and with pure water. (left) gold monomer and its products and (right) gold dimer and its products in negative mode.

gold bond in different ways. This has become known as "gold anomaly". The main relativistic effect in gold is the bringing the s and d orbitals closer together creating hybridisation of these states, which has consequences on their structural and chemical properties[10–14]. In terms of structure of the metal clusters, experiments and theory have shown the gold clusters to retain planar structure for clusters up to 12 atoms for anions, up to 10 atoms for neutral clusters and up to 8 atoms for cations[12,14–17]. Silver cluster anions start to show 3D structures already at 6 atoms size[14,18].

As will be discussed further in the chapter, the presence of chemicals in the electrospray plume has an effect on the abundances of observed pure metal complexes and products. The experiments were made with water (H_2O) or heavy water (D_2O) in the ESI syringe. Figure 4. 1 shows the mass spectrum of small gold species in negative mode. Introducing water in the electrospray plume aids in the bonding of oxygen and hydrogen to gold complexes. It also makes the bonding with nitrogen less favourable. The comparison of the effects of water and heavy water on the observed species is shown in Figure 4. 2. If the syringe contains D_2O the shift in the peaks can be seen due to the bonding of deuterium instead of hydrogen. We notice also that the relative intensities of products are comparable between the two cases. Since reactions with atmospheric vapour still continue in the case when we electrospray D_2O, there are species in the mass spectrum which contain the hydrogen atoms and not deuterium, though they are significantly lower in intensity. This tells us that the reactions with the plume constituents are favourable to the atmospheric ones. This deuterium labelling also allows us to more precisely identify the peaks seen in the mass spectrum, and remove the ambiguity between species containing OH_x and NH_{x+2}. As seen in Figure 4. 4, Figure 4. 7, Figure 4. 10 and Figure 4. 13 the presence of either water or heavy water always increases the total abundance of the products at the expense of the pure species. In some of the cases, difference between the product abundance with water and heavy water can be seen as well. For example, for silver, in positive mode (Figure 4. 4), the highest amounts of products are found when spraying H_2O.

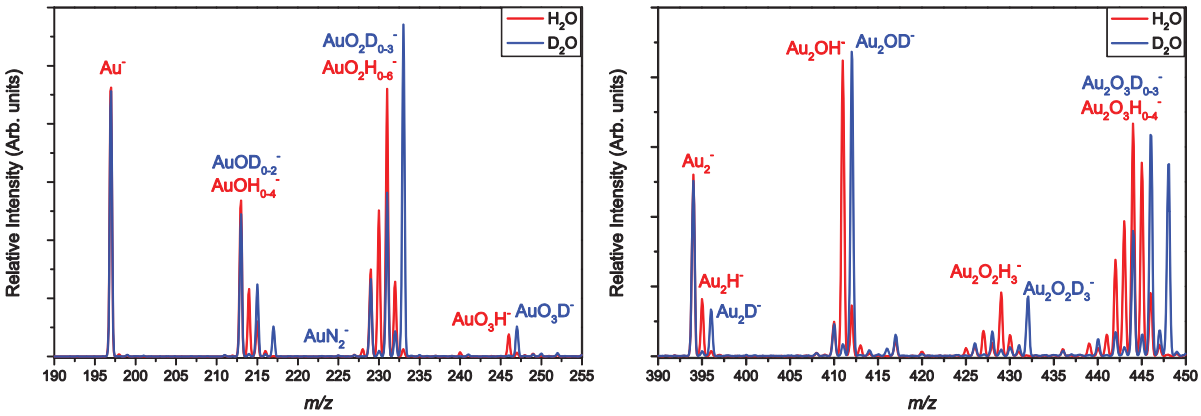

Figure 4. 2 Example of comparison of mass spectra obtained with different electrospray plume compositions for water and heavy water. (left) gold monomer and its products and (right) gold dimer and its products in negative mode.

In negative mode (Figure 4. 10), the differences in the intensities are very small between the case of D_2O and experiments without syringe, but again, with H_2O, the abundance of product is highest. If we look at the intensities of pure metal complexes in relation to the composition of the electrospray plume, we find the exact opposite. For experiments when syringe is turned off the abundance of pure complexes is highest, and with D_2O or H_2O their intensity is lowest.

4.1.1. Analysis of results obtained in positive mode

Mass spectrum obtained by vaporisation of a silver rod in positive mode, shows abundance of small pure metal species Ag_n^+, and their products with oxygen, nitrogen and hydrogen (Figure 4. 3). The pure clusters dominate in intensity for $n \leq 3$, while for $n \geq 4$, the intensity of the products becomes stronger. The relative abundance of the products depends heavily on the composition of the electrospray plume (Figure 4. 4). When the syringe mechanism is turned off, and only the ESI voltage and sheath gas are active, the mass spectrum is dominated by Ag_n^+ and Ag_nN^+ for $n \leq 3$ and $n \geq 4$ respectively. Previous studies have investigated the oxidation mechanism, stability and structure of Ag_n^+, Ag_nO^+ and $Ag_nO_2^+$[19]. The relative abundance of pure complexes and oxides produced by thermal evaporation was shown to be $Ag_nO_2^+ < Ag_nO^+ < Ag_n^+$ [20]. Figure 4. 3 shows our results to be in agreement with this, with addition of Ag_nN^+species, so that the total intensities relationship is $Ag_nO_2^+ < Ag_nO^+ < Ag_nN^+ < Ag_n^+$ with the last relation depending on the number of silver atoms, as stated above. Probing the clusters stability with collisional activation (Figure 4. 3) shows decrease in the product complex abundance, and at the highest collisional energy, leaves a mass spectrum dominated by Ag^+, Ag_2^+, Ag_3^+. Plotting the total change in relative intensities shows how the abundance of the products decreases and the abundance of bare metal cluster increases as a function of collisional energy (Figure 4. 4). This could lead us to conclude that the favourable fragmentation channel is the loss of oxygen and nitrogen, thus leaving the pure metal complexes. Combined with Figure 4. 3 though, we can see that the increase in abundance of pure complexes is the biggest for the Ag^+, Ag_2^+ and Ag_3^+.

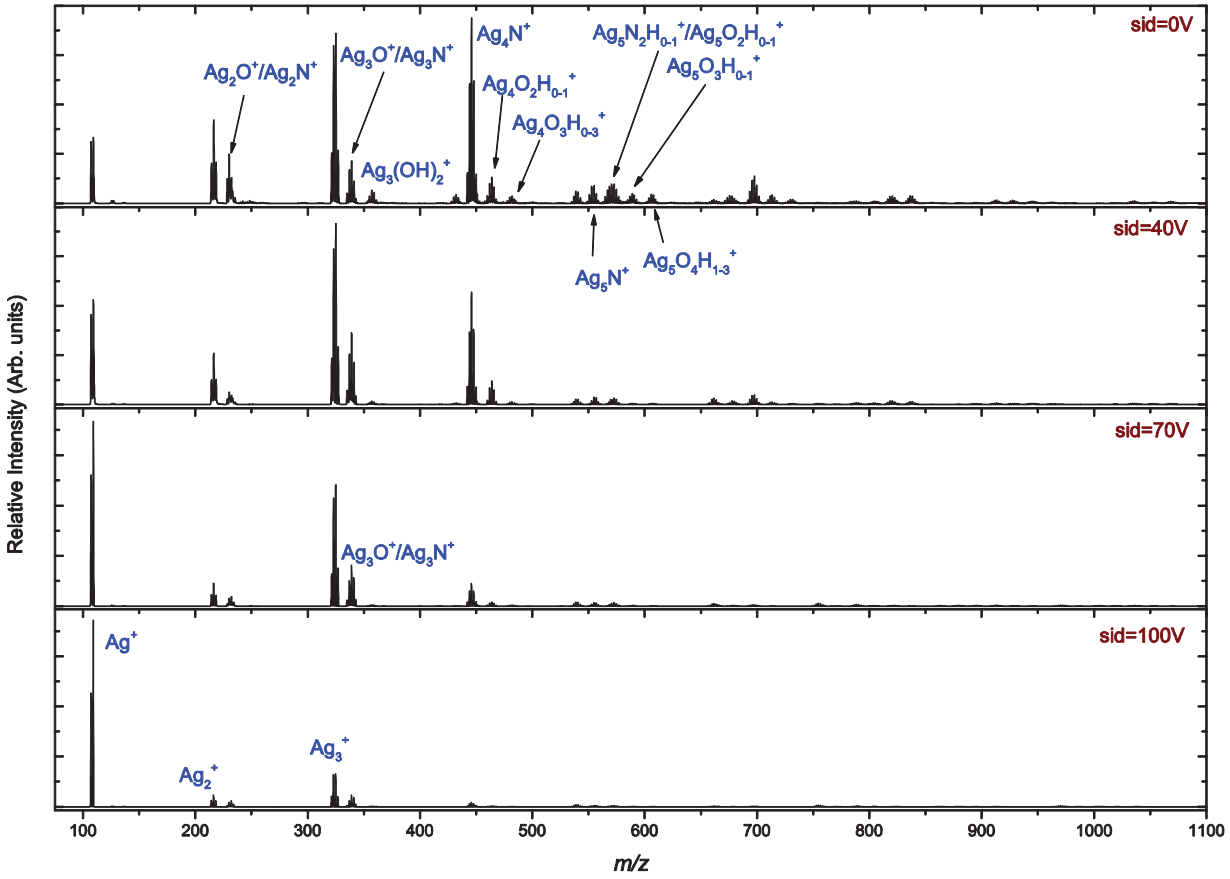

Figure 4. 3 Mass spectra obtained by vaporisation of silver rod, with different in-source activation energies, in positive mode. The formulas mark the groups of peaks corresponding to the silver oxides and nitrides with different number of adsorbed hydrogen atoms.

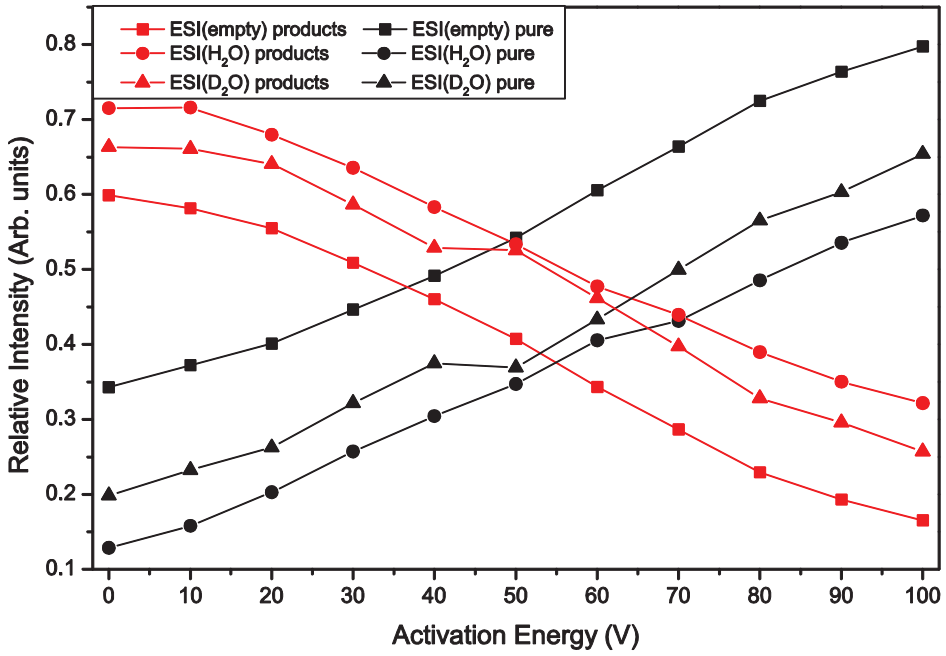

Figure 4. 4 Total relative intensities of pure silver complexes and their products, as a function of activation energy in positive mode.

This means that in addition to the loss of oxygen and nitrogen from the complexes, the bigger species fragment by losing silver and silver oxide or nitride. To further clarify this point we turn to the MS^2 experiments.

The MS^2 mass spectra allow us to examine more closely the fragmentation channels of specific species. For every experiment, the mass isolation interval was selected either to encompass the whole isotopic distribution of the selected species or, in cases when species in the isolation interval were not monodisperse, the isolation interval was selected to be $\sim 1\ Th$, to minimise the influence of the adjacent species. For better clarity, we plot the results of the multiple monoisotopic isolations in the same plot to get a compound mass spectrum representing the full isotopic distribution of the species in question. The experiments were done on Ag_n^+ and their products where $n \leq 5$, because for larger sizes, the number of species which contribute to the signal at same *m/z* becomes too big to confidently distinguish the species. Figure 4. 5 shows the MS^2 spectra of several cations of interest. The selected ion at *m/z* 230 (Figure 4. 5a – top) corresponds to superposition of ions Ag_2N^+ and Ag_2OH^+. The fragmentation channel is the loss of N to produce the silver dimer, as is clear from the CID of single isotopic peak (Figure 4. 5a – top, red line). The attempt to fragment the Ag_2OH^+complex reveals it to be more stable as it does not fragment even under strong collisional activation. By applying the same method on the next species at *m/z* 248, we can identify it as $Ag_2N_2H_4{}^+$ rather than $Ag_2O_2{}^+$, because the CID of the monoisotope shows the resulting fragment to be Ag_2N^+ and not an oxide (Figure 4. 5a – bottom). Smaller peaks between the ones belonging to the $Ag_2N_2H_4{}^+$ are due to $Ag_2O(OH)^+$, and through the loss of oxygen atom they produce the peaks at *m/z* 230.75 and 232.75. The full isotopic distribution of this species in not visible in this spectrum as it is cut off by the isolation window, but the isolation of individual peaks confirms its presence. The products of Ag_3^+ show similar behaviour. The first product at *m/z* 338 is identified as the superposition of $Ag_3N^+, Ag_3O^+, Ag_3(H_2O)^+$ and probably $Ag_3NH^+$and Ag_3OH^+ (Figure 4. 5b, c). The monoisotopic CID shows the main fragmentation coming from the Ag_3N^+ and $Ag_3(H_2O)^+$, not the Ag_3O^+. The isolation and fragmentation of the species at *m/z* 357 reveals it to be a superposition of $Ag_3NO^+$and $Ag_3(OH)_2{}^+$ (Figure 4. 5c – bottom). This conclusion was reached by observing its main fragmentation product, at *m/z* 338 which is a superposition of multiple species ($Ag_3N^+, Ag_3O^+, Ag_3(H_2O)^+$). This species however exhibits another fragmentation channel, by loss of $Ag(OH)$ and AgN, producing the $Ag_2N^+$and $Ag_2(OH)^+$(Figure 4. 5c – bottom). Due to electronic shell closing, $Ag_3^+$and Ag_4N^+ are very stable and appear as a products of several fragmentations (Figure 4. 5b-f). The Ag_4^+ for example appears as a product not only of higher Ag_4^+ products (Figure 4. 5d), but also of larger species with more silver atoms (Figure 4. 5e, f). Analogous to silver dimer products, the species at *m/z* 464 corresponds to superposition of $Ag_4O_2{}^+$ and $Ag_4N_2H_4{}^+$, with latter being the dominant species to produce the fragments seen in the spectrum (Figure 4. 5d). The species at *m/z* 554 corresponding to the Ag_5N^+ has, as its dominant fragmentation channel the loss of Ag (Figure 4. 5e) indicating that the structure of Ag_4N^+ is stable, and that the additional silver atom is loosely bound, and

is therefore easier to break off. This conclusion is supported by CID of a single isotopic peak of that species which confirms the loss of Ag as the fragmentation channel (Figure 4. 5e – red line). The Ag_5^+ species seen in the CID spectrum most probably comes from one of the adjacent oxide species, as does the peak at *m/z* 338 (already identified as superposition of $Ag_3N^+, Ag_3O^+$and $Ag_3(H_2O)^+$). An interesting species at *m/z* 570, which is a superposition of $Ag_5O_2H_2^+$ and $Ag_5N_2H_4^+$ seems to illustrate nicely the different fragmentation channels of $Ag_nO_mH_l^+$ and $Ag_nN_mH_l^+$ (Figure 4. 5f). As seen from the spectrum and confirmed by MS^3 experiment (not shown here), the fragments containing nitrogen are formed from $Ag_5N_2H_4^+$ through loss of Ag and $AgNH_2$. The $Ag_5O_2H_2^+$ loses sequentially a molecule of water and possibly an oxygen atom to make Ag_5O^+ and Ag_5^+. The Ag_n^+ fragments seen in the spectrum can originate from both precursors as we have already seen in the CID experiments with smaller masses that the Ag_n^+ can be formed from species with oxygen and nitrogen. The MS^2 spectra reveal the Ag_nN^+ are found in greater abundance than the Ag_nO^+, and they fragment more readily to produce the Ag_n^+ species.

Gold cations show the familiar mass spectrum of alternating even-odd intensities (Figure 4. 6). Products abundancies are much lower compared to pure complexes than what we see for silver. No pure oxides (Au_nO_m) are observed in the mass spectrum in positive mode. Other than the pure gold cations we observe $Au_n(H_2O)_m^+$ and $Au_nN_2^+$. Applying the in-source collisional causes the decline in total intensity of the products, and increase in pure gold clusters (Figure 4. 7). The in total intensities is not as pronounced as in the case of silver cations (Figure 4. 4), but the overall trends are the same. The MS^2 experiments shown in Figure 4. 8 show that the products loose the adsorbed water molecules with ease, leaving the pure gold cluster. Figure 4. 8a shows the CID of $Au_3(H_2O)^+$and $Au_3(H_2O)_2^+$ and the sequential loss of water molecule from the complex. The same is observed for $Au_5(H_2O)^+$. For the smaller gold species the intensity of the products is too low to effectively isolate and fragment the species. In Figure 4. 8b we show the MS^2 spectra of $Au_7(OH)_2^+$, without (top) and with (bottom) collision energy. Even without the collisional energy the parent complex is unstable and it dissociates $2OH^{\cdot}$. With added activation we see the emergence of Au_7O^+ which points to reactions with the fragments in the trap.

4.1.2 Analysis of results obtained in negative mode

In negative mode, the mass spectrum of ablated silver does not show the known characteristic isotopic patterns of Ag_n. Instead the peaks show rich isotopic distribution that we identify as superposition of multiple species. The analysis of the isotopic peaks reveals that these species can be described with a general formula $Ag_nO_mH_{0-l}^-$. This makes the MS^n experiments extremely hard to interpret, as it is often impossible to know which of the parent species isolated within the interval is responsible for which fragment.

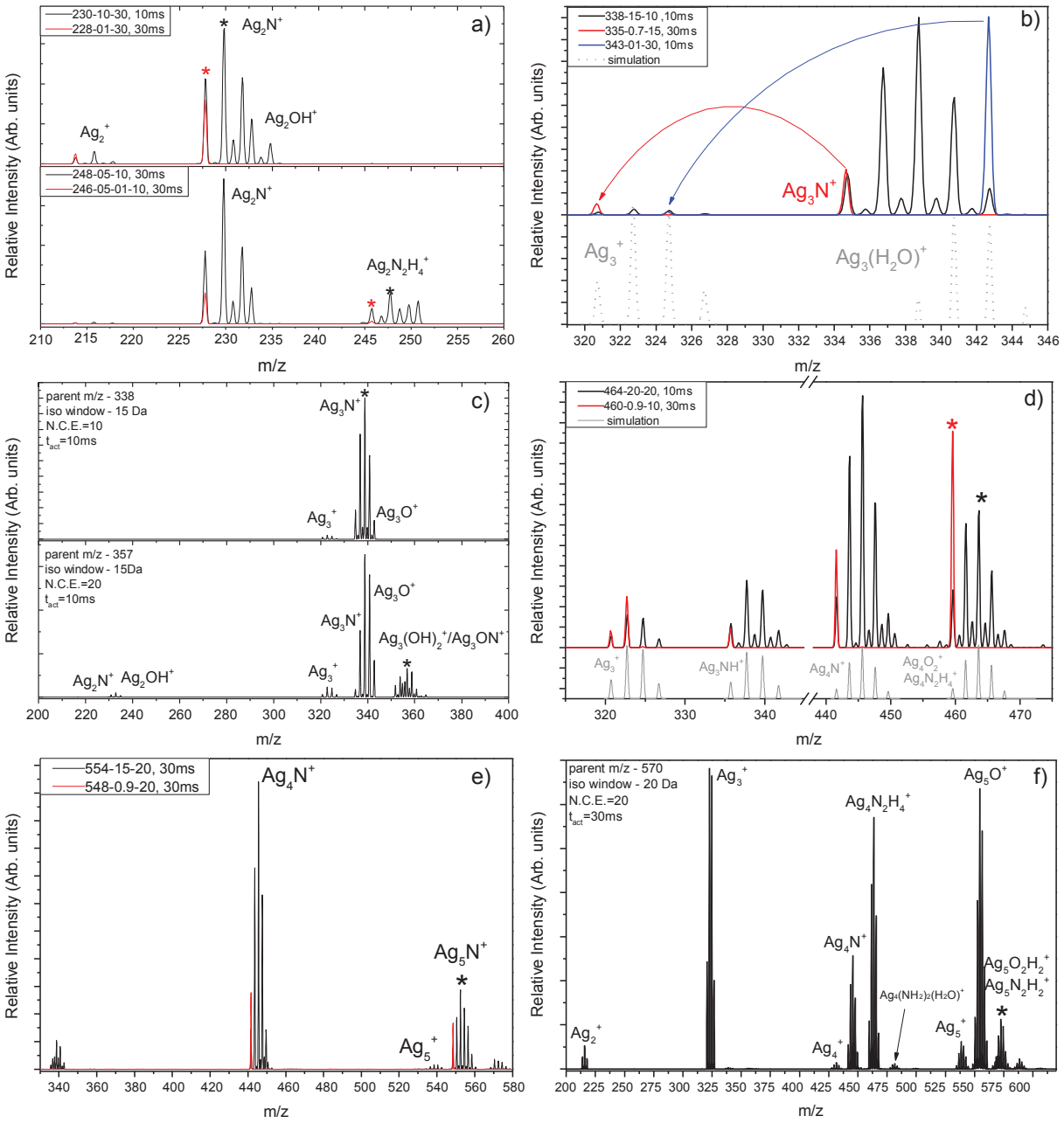

Figure 4. 5 MS^2 spectra of selected silver complexes in positive mode. Black lines mark the MS signal of isolated species and their fragmentation products, red and blue lines mark the single isotopes that are isolated and their products and grey lines are used to show the simulated mass spectrum of species of interest. Star symbols (in any colour) mark the centre of isolation interval. The legend (in a), b), d) and e)) is in the form of A-B-C, t_{act}, where A is the m/z of the centre of isolation interval, B is the width of isolation interval, C is the normalised collision energy (expressed in arbitrary units) and t_{act} is the trapping time in milliseconds.

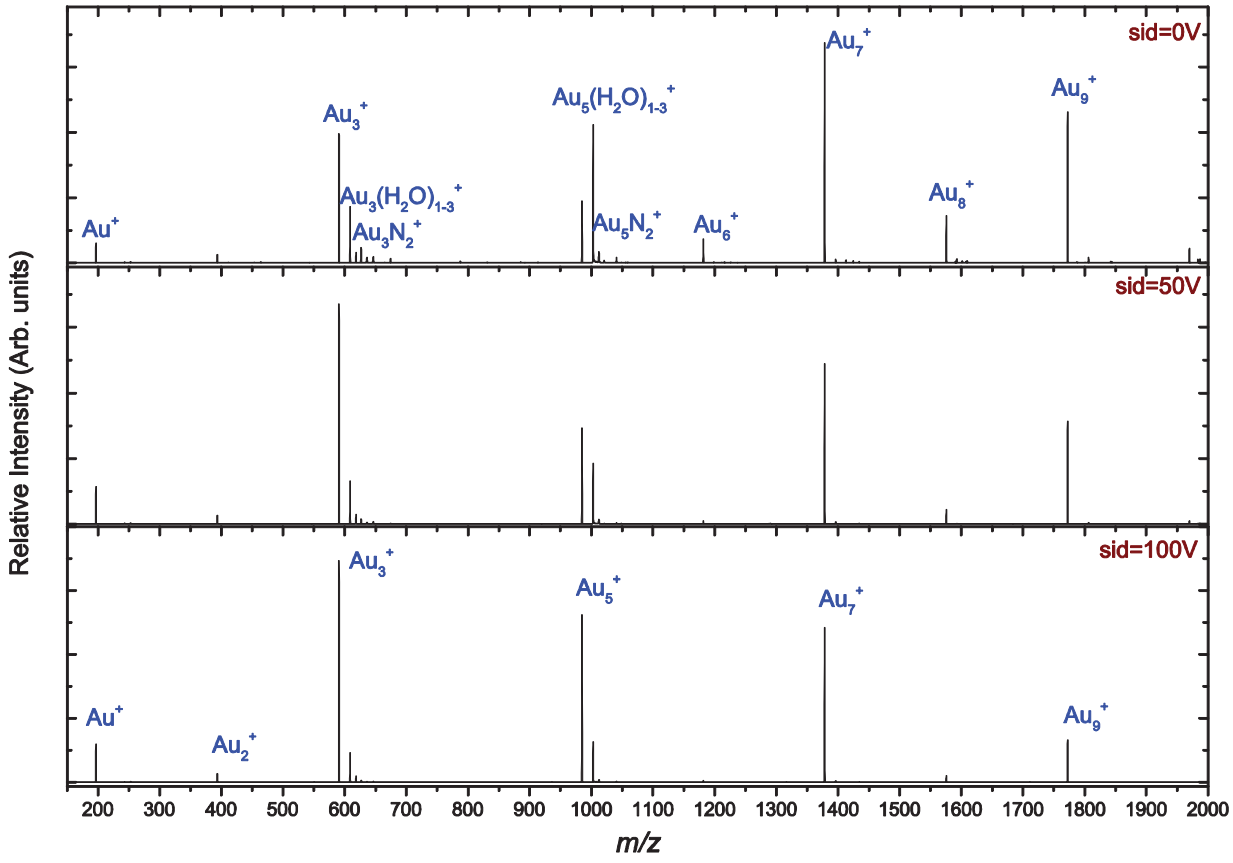

Figure 4. 6 Mass spectra obtained by vaporisation of gold rod, with different in-source activation energies, in positive mode. The formulas mark the groups of peaks corresponding to the silver oxides and nitrides with different number of adsorbed hydrogen atoms.

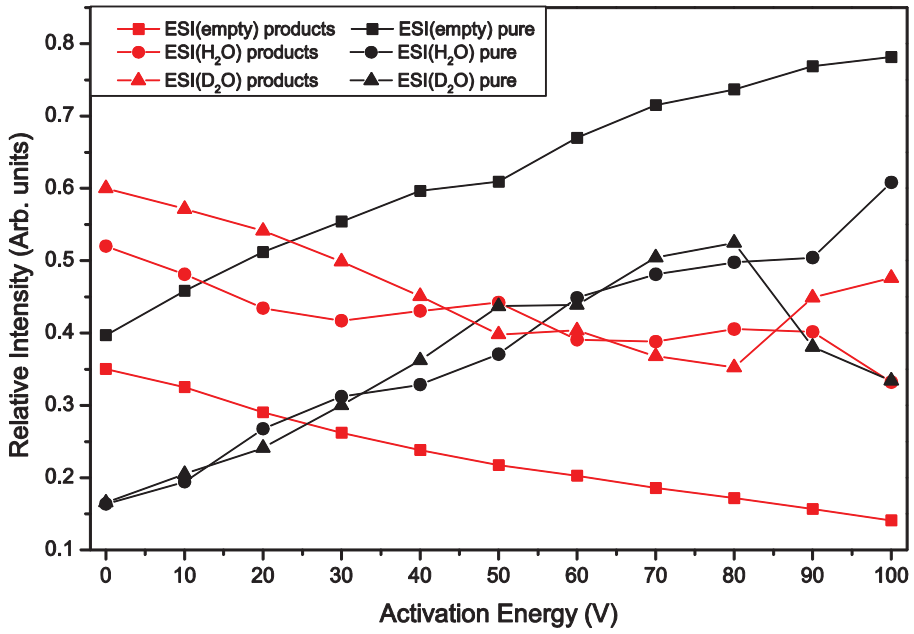

Figure 4. 7 Relative intensities of bare metal and metal complexes obtained through ablation of the gold rod as a function of collisional activation energy in positive mode.

Additionally, the strategy employed for cations, i.e. the isolation of single peaks corresponding to monoisotopes is drastically less useful here, as the peaks at extreme ends of the distribution, which we can attribute to only one species, are of very low intensity, and the peaks near the centre are due to superposition of multiple species.

The abundance of pure silver complexes seen in positive mode is absent here. Figure 4. 9 (top) shows that in full MS only Ag^-, Ag_2^- and Ag_3^- are present in the spectrum, and always in intensities lower than their products. Similar to the positive mode, we see a shift towards smaller *m/z*. The stoichiometries of the most intense product in each family of products for a given number of silver atoms are given in Figure 4. 10 (right).

As the size of the complex increases the relative number of oxygen atoms decreases. Figure 4. 9 shows how the distribution of peaks in mass spectrum changes with the activation energy. The increase in abundance of silver monomer as well as its oxides with increasing collisional energy points to fragmentation of the bigger, less stable species. The total increase in intensity is seen for the oxide, hydroxide and nitride species, and not for bare clusters, indicating anions favour the fragmentation channels with loss of Ag_nO_m. Figure 4. 10 shows higher intensities of products for experiments done with H_2O or D_2O in the ESI syringe, indicating their presence in the electrospray plume aids in the reactions, reducing the relative abundance of pure metal clusters. The fragmentation channels favoured by these are shown in Figure 4. 11. The dominant fragmentation channels are the loss of Ag, AgO, AgO_2 with possibly a number of hydrogen atoms.

The CID channels of species at *m/z* 267, are shown in Figure 4. 11. The species is identified as superposition $Ag_2O_3H_{1-5}^-$. The minor fragmentation channel is the loss of O_2H_{0-4}, producing $Ag_2H_2O^-$, which reacts with other ions in the trap to produce $Ag_2NOH_{1-3}^-$. The main fragmentation channel is the loss of $AgOH_{0-4}$. For the bigger species (Figure 4. 11b, c), the loss of OH_{0-4} is more significant channel and in intensity is comparable with the loss of AgH_{0-x}, $AgOH_{0-x}$ and AgO_2H_{0-x}. The loss of O_2H_{0-4} from the parent species is less significant. For the species at *m/z* 391, which corresponds to $Ag_3O_4H_{2-5}^-$, we see as major products$Ag_3O_3H_{0-3}^-$ and $Ag_2O_3H_{0-4}^-$ (Figure 4. 11b – top). A minor peak corresponding to $Ag_3O_2H_{0-3}^-$ is also present in the spectrum, but is of very low intensity. The isolation and CID of $Ag_3O_3H_{0-3}^-$ at *m/z* 373 (Figure 4. 11b – bottom) results in the same products. This time, the parent species combines with fragments in the trap, possibly water molecules to produce $Ag_3O_4H_{2-5}^-$. In CID it loses AgH_{0-2} to produce $Ag_2O_3H_{0-4}^-$. The recombination with fragments in the trap seem to also be favourable for the species at *m/z* 498, corresponding to $Ag_4O_4H_{2-4}^-$ (Figure 4. 11c). Its reactions in the trap result in $Ag_4O_5H_{2-3}^-$. The fragmentation gives an abundance of products, by loss of OH_{0-2}, O_2H_{0-4}, AgH_{0-2}, $AgOH_{0-3}$, AgO_2H_{0-2} and Ag_2OH_{0-2}, to produce the $Ag_4O_3H_{0-4}^-$, $Ag_4O_2H_{0-4}^-$, $Ag_3O_4H_{0-4}^-$, $Ag_3O_3H_{0-3}^-$, $Ag_3O_2H_{2-4}^-$ and $Ag_2O_3H_{0-4}^-$ respectively.

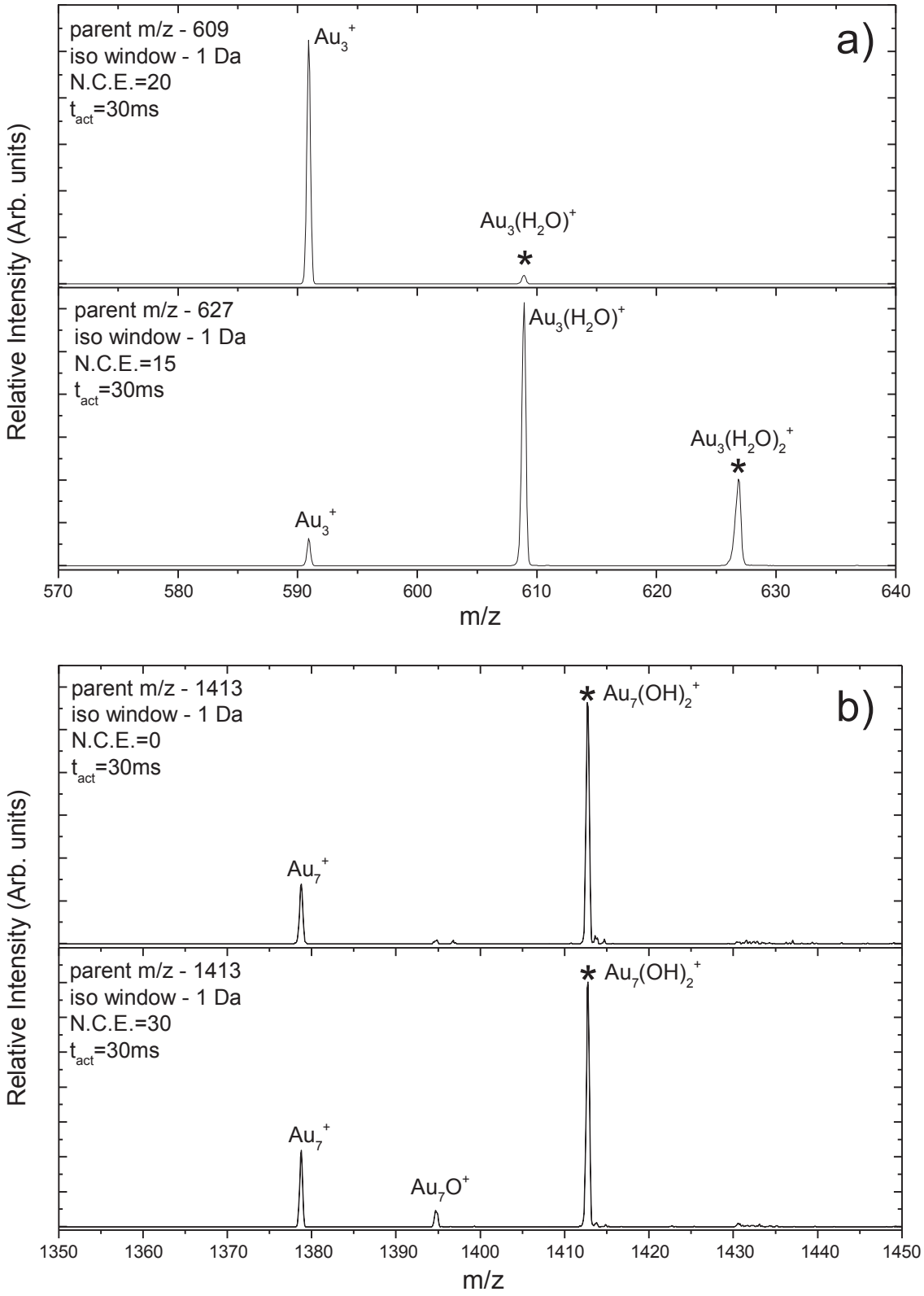

Figure 4. 8 MS^2 mass spectra of gold complexes in positive mode. Star symbols mark the centre of isolation interval. N.C.E. stands for normalised collision energy and is expressed in arbitrary units.

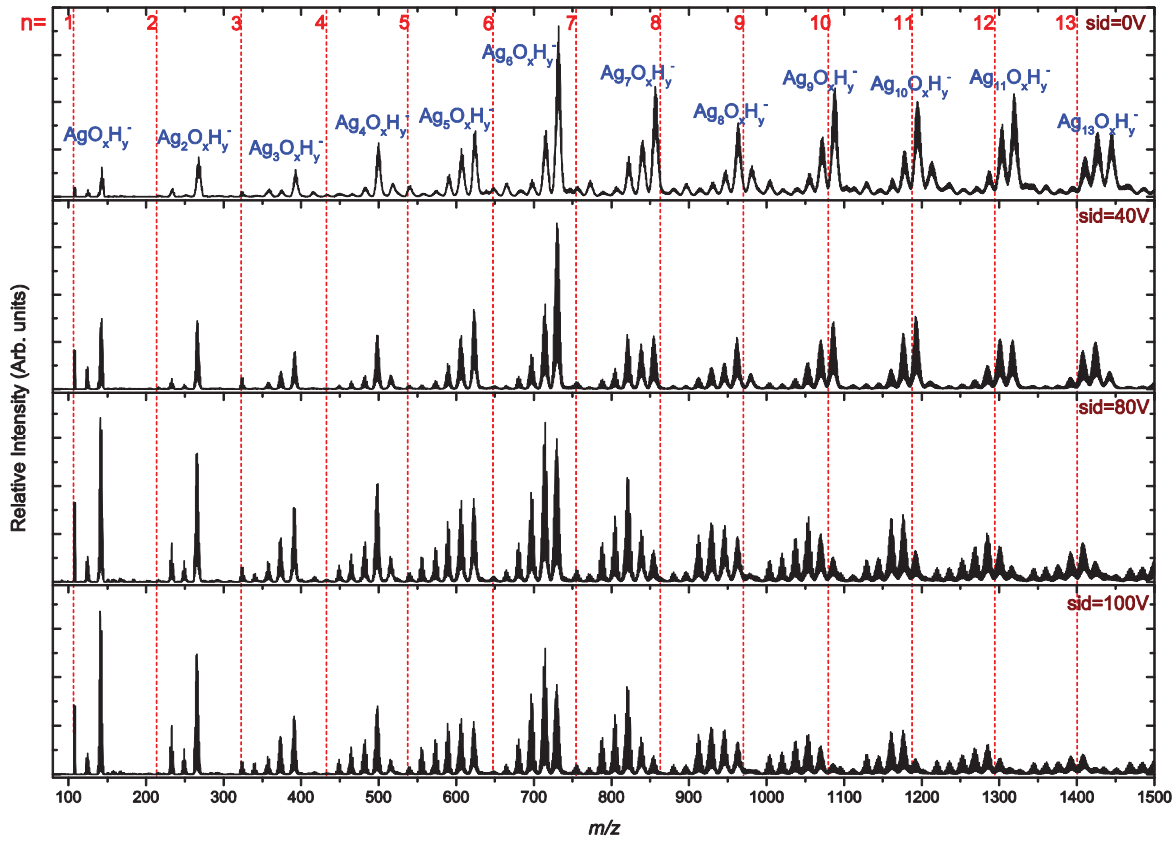

Figure 4. 9 Mass spectra obtained by vaporisation of silver rod, with different in-source activation energies, in negative mode. The red dashed lines show the m/z of the bare silver cluster with n atoms. The formulas mark the groups of peaks corresponding to the silver oxides, hydroxides and hydrates.

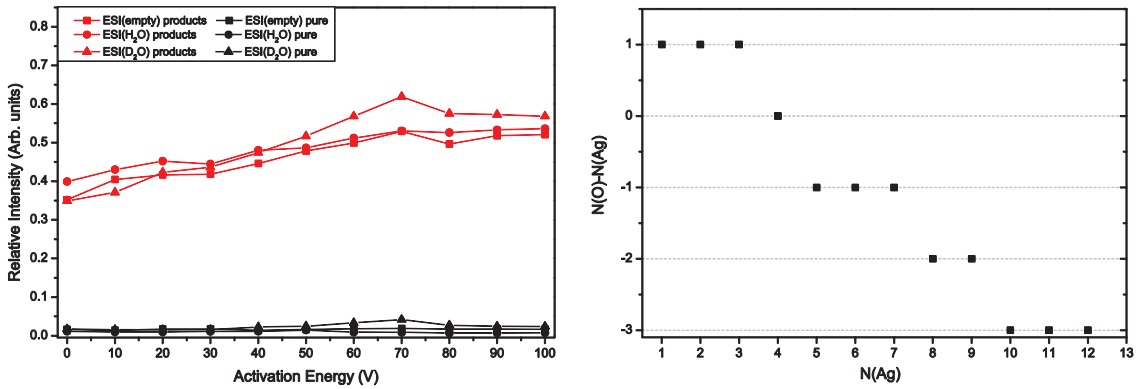

Figure 4. 10 (left) Total relative intensities of pure silver complexes and their products, as a function of activation energy in negative mode. (right) Stoichiometries of the most intense group of products observed for a given number of silver atoms in full mass spectrum. The y axis shows the relative number of oxygen to silver atoms in the complex, and the x axis shows the number of silver atoms.

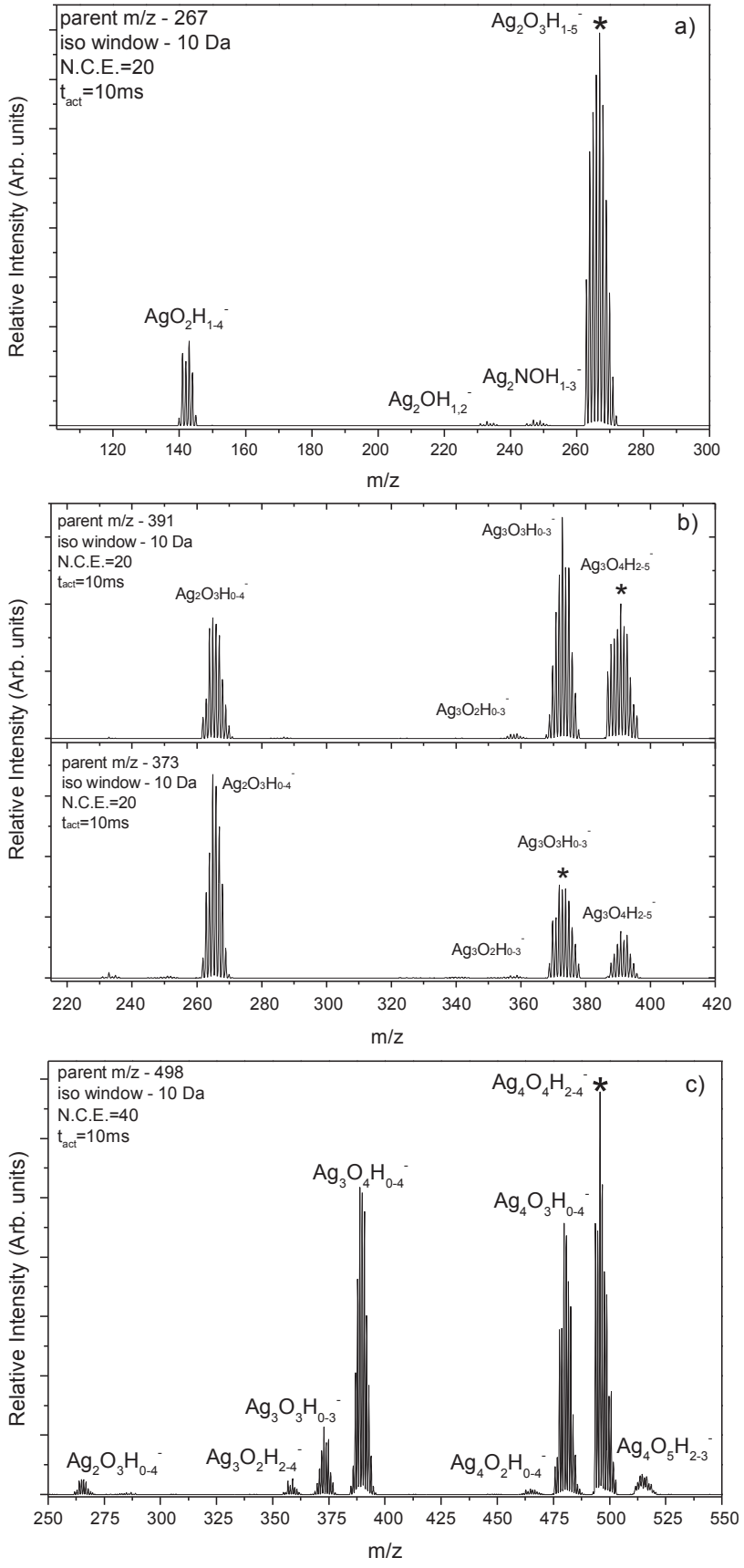

Figure 4. 11 MS^2 spectra of selected silver complexes in negative mode. Star symbols mark the centre of isolation interval. N.C.E. stands for normalised collision energy and is expressed in arbitrary units. The $Ag_nO_mH_{0-l}^-$ form for the formulas was used since the observed peaks are superposition of multiple species with variable number of hydrogen atoms.

The gold anions also exhibit the alternating stability pattern as seen in the mass spectrum in Figure 4. 12. The distribution of peak intensities shifts towards small masses with addition of in-source collisional activation. The overall tendencies of the pure and product complexes mirror each other when observed as a function of collisional activation energy (Figure 4. 13). The overall tendencies are the same as with gold and silver cations, but they differ from silver anions. The effect of the water plume on products formation is once again clearly visible. The trends of intensities of pure and product complexes are not as pronounced as in positive mode. The MS^2 experiments (Figure 4. 14) however reveal the loss of Au_2 and AuOH as either favoured or equivalent fragmentation channels to the loss of O and $OH^{\cdot}$. Some background reactions with water molecules same stoichiometries. Small species, $Ag_2O_3H_{1-5}^-$ and $Au_2O_3H_{0-2}^-$ show a similar fragmentation channel, which is the loss of same stoichiometries. Small species, $Ag_2O_3H_{1-5}^-$ and $Au_2O_3H_{0-2}^-$ show a similar fragmentation channel, which is the loss of oxygen, loss of dioxygen and loss of MOH_n. There are also differences in the fragmentation as well as stoichiometries of the most intense species in the mass spectrum. For gold anions, both with in-source activation and in MS^2 experiments, pure gold complexes can be obtained as a product of fragmentation, which is never the case for silver anions. In positive mode we do not find any analogous fragmentation patterns between silver and gold. The mass spectrum of positive gold shows the favoured products to be $Au_n(H_2O)_m^+$ and $Au_nN_2^+$ species. For the negative gold complexes, we see greater variability of species, similar to the negative silver, which can be described by general formula $Au_nO_mH_{0-l}^-$. Examination of the mass spectrum under increasing activation energy shows that these species fragment easily, leaving a spectrum with abundance of pure clusters. Combination of in-source activation and CID through MS^2 (Figure 4. 12 and Figure 4. 14) experiments shows that $AuOH_n$ is a strong fragmentation channel (Figure 4. 14b). The loss of Au, Au_2, O, $OH$and H_2O can also be seen.

The CID of *m/z* 444 corresponding to the $Au_2O_3H_{0-2}^-$ shows products corresponding to the $Au_2(H_2O)^-$ and $Au(H_2O)_2^-$ (Figure 4. 14a – top). The $Au_2(H_2O)^-$ is difficult to isolate without influence of any of the neighbours, so the species at *m/z* 411 is assigned to $Au_2(OH)^-$ as the most intense peak, but other complexes may contribute to the mass spectrum (Figure 4. 14a – bottom). It loses the OH to produce the gold dimer, and also, in a slightly less intense fragmentation channels produces the gold monomer, the $Au(H_2O)^-$ and $Au(H_2O)_2^-$. It is possible that the latter two are formed through reactions with residual fragments in the trap. The species at *m/z* 657 corresponds to $Au_3O_4H_{0-2}^-$. In fragmentation it loses O and O_2, as well as $AuOH_x$. For the species at *m/z* 805, corresponding to $Au_4(OH)^-$, fragmentation and subsequent reaction with residual fragments in the trap can be seen. The parent fragments to Au_4^- and Au_3^-. The latter one then adsorbs a molecule of water to make $Au_3(H_2O)^-$. The smallest fragment seen in this spectrum is the $Au_2(OH)^-$. Since the Au_2^- is not present in the spectrum, it is not clear whether this species is formed directly from the parent by loss of Au_2, or from gold dimer (which is formed by fragmentation of the parent) which adsorbs a hydroxide group.

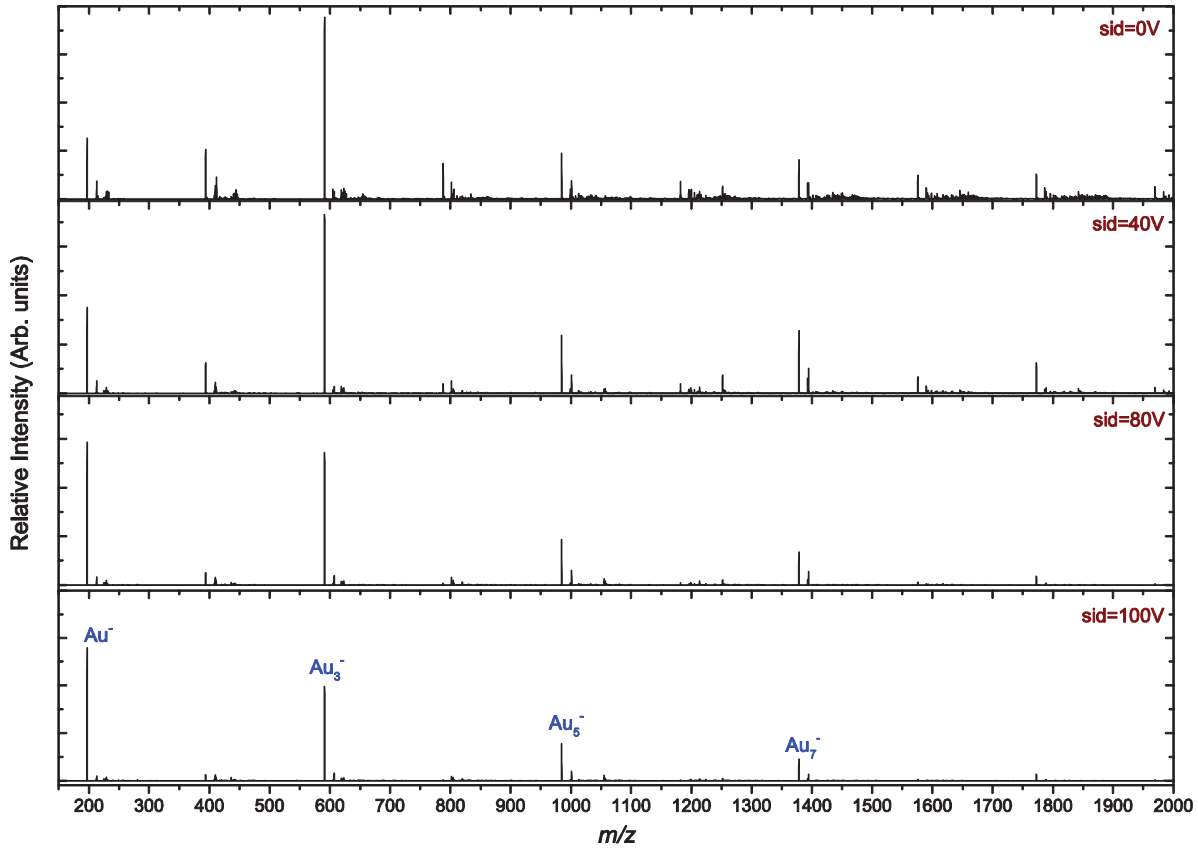

Figure 4. 12 Mass spectra obtained by vaporisation of gold rod, with different in-source activation energies, in negative mode.

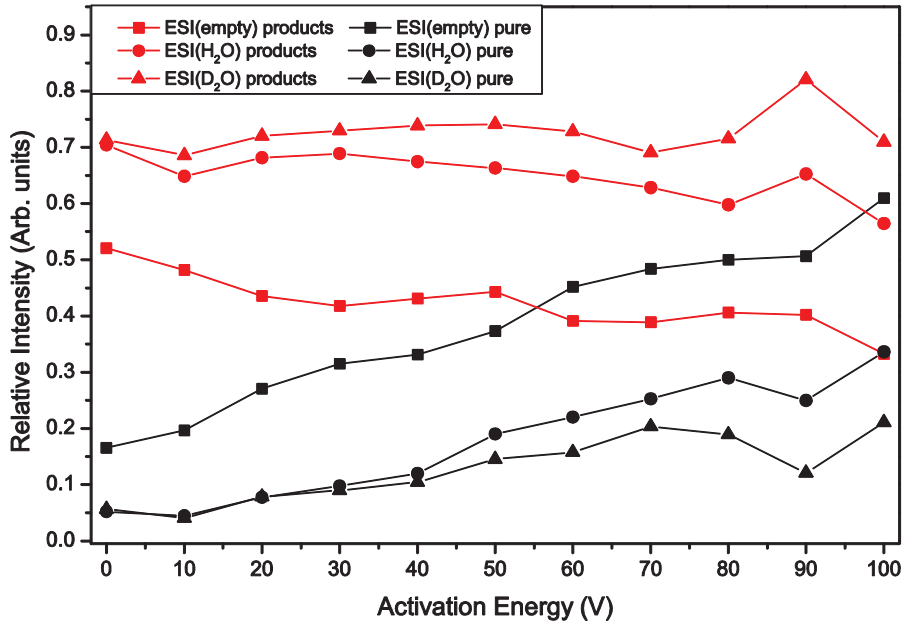

Figure 4. 13 Relative intensities of bare metal and metal complexes obtained through ablation of the gold rod as a function of collisional activation energy in negative mode.

4.1.3 Conclusions on metal oxides

LAVESI source is used to produce a variety of species of metal clusters, metal oxides, hydroxides, nitrides, and other products. Using linear ion trap mass spectrometer we are able to examine their stoichiometries and stability, both for cations and anions.

In the mass spectrum of cationic silver, species of smaller masses dominate the spectrum. Very prominent are the Ag_nN^+ species, and some silver oxides and hydroxides are also observed. In the case of gold cations, pure metal clusters Au_n^+ dominate the spectrum. Besides them, peaks of $Au_n(H_2O)_n^+$ and $Au_nN_2^+$ are very intense as well. The CID and in-source fragmentation spectra of the silver cations show the loss of N, O, $AgNH_x$ and $AgOH_x$ as the main fragmentation channels. contrary to this, the fragmentation channels of gold cations never contain gold atoms. The dominant channels are the sequential loss of $n(H_2O)$ and N_2, which dissociate from the complex to leave pure Au_n^+ as a product.

In case of anions, the mass spectrum of gold is dominated by the pure gold clusters. Various oxides, hydroxides, and nitrides can be seen as well, but their intensity is much lower than that of the pure clusters. The mass spectrum of silver anions is very different though. Almost no pure clusters can be seen except for the Ag^-, Ag_2^- and Ag_3^-. Instead, the silver oxide and hydroxide species are the ones with highest intensity. Despite the difference in the distribution of species in the mass spectrum, the CID analysis reveals some analogous fragmentation channels between gold and silver anions, namely the loss of MOH_n for the $M_2O_3H_x^-$ species. One major difference still exists in the fragmentation patterns between the two metals, for gold with in-source activation and in MS^2 experiments, we are obtain pure gold clusters through fragmentation, which is never the case for silver.

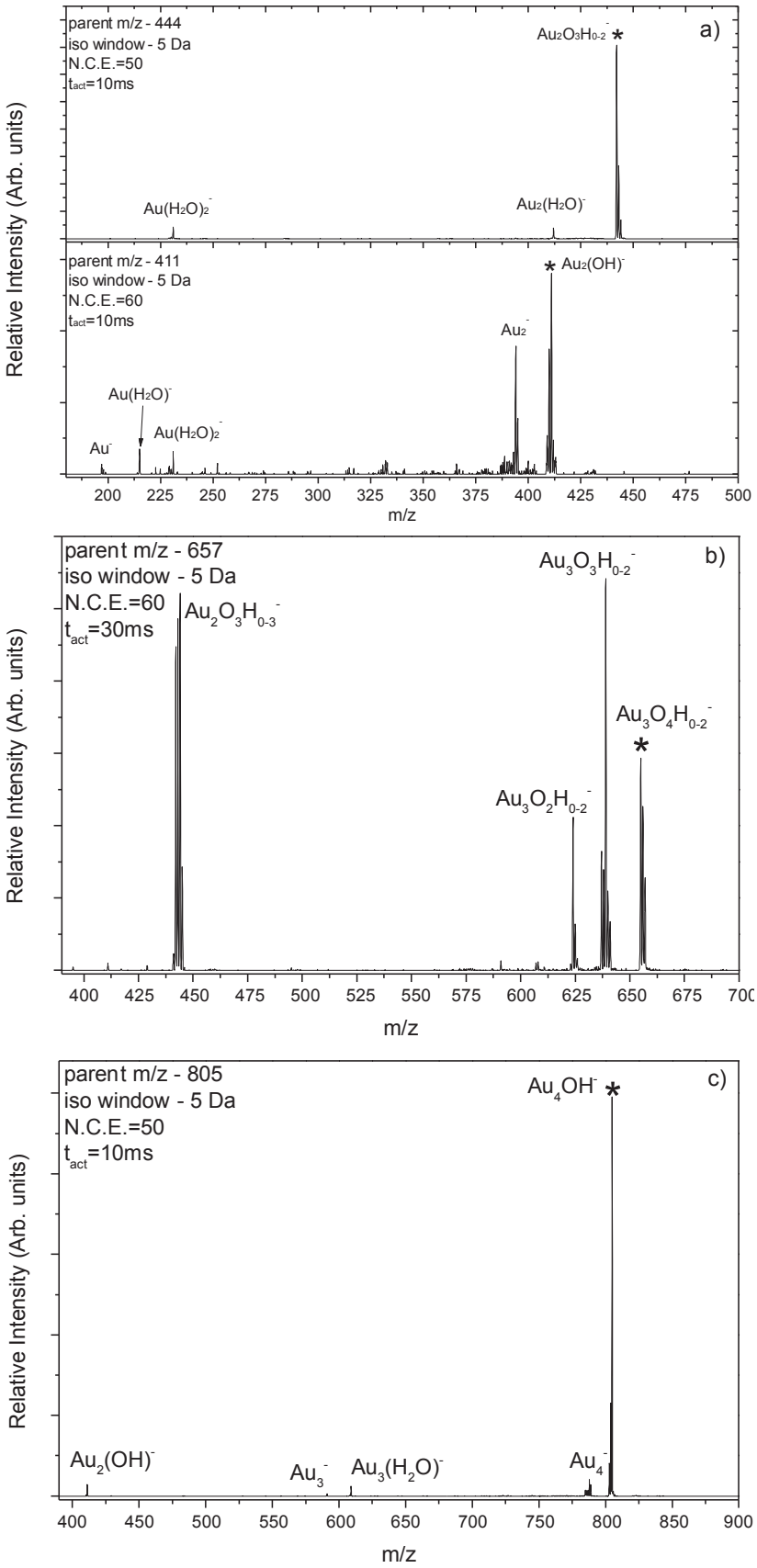

Figure 4. 14 MS^2 spectra of gold complexes in negative mode. Star symbols mark the centre of isolation interval. N.C.E. stands for normalised collision energy and is expressed in arbitrary units. The $Au_nO_mH_{0-l}^-$ form for the formulas was used since the observed peaks are superposition of multiple species with variable number of hydrogen atoms.

4.2 Ligated metal complexes

One of the main strengths of LAVESI source is the versatility in varying the composition of the ESI plume. So far the results have been shown that have been obtained with only ESI voltage applied (no plume), and with either water or heavy water in the ESI plume. We will now take a look at what happens when we electrospray small organic molecules and couple it with laser vaporization of silver, gold and copper rods.

4.2.1 Ligated silver complexes

Figure 4. 15a shows a mass spectrum recorded in the negative mode using the thioglycolic acid (marked SR in further text, where SR=SCH_2COOH, 91 Da) solution without laser vaporization of metal. Main peaks correspond to dimers and trimers of singly deprotonated thioglycolic acid. Figure 4. 15b shows a typical mass spectrum obtained by spraying the thioglycolic acid solution and vaporization of a silver rod. Dominant peaks corresponds to Ag_NSR_M complexes. Complexes are negatively charged due to the deprotonation of one thioglycolic acid. No multiply charged complexes are observed. Comparison of experimental and theoretical isotopic distributions shows that observed silver complexes correspond to the following generic formula $[Ag_N(SR)_M\text{-}(N\text{-}M+1)H]^-$, i.e. $[Ag(SR)_2]^-$, $[Ag_2(SR)_2\text{-}H]^-$, $[Ag_3(SR)_2\text{-}2H]^-$, $[Ag_3(SR)_3\text{-}H]^-$, $[Ag_4(SR)_3\text{-}2H]^-$, $[Ag_5(SR)_3\text{-}3H]^-$, $[Ag_5(SR)_4\text{-}2H]^-$, $[Ag_6(SR)_4\text{-}3H]^-$, $[Ag_7(SR)_4\text{-}4H]^-$, $[Ag_8(SR)_5\text{-}4H]^-$, $[Ag_9(SR)_5\text{-}5H]^-$, $[Ag_{10}(SR)_6\text{-}5H]^-$, $[Ag_{11}(SR)_6\text{-}6H]^-$… These species contains M thiolate groups. The additional N-M+1 deprotonations are due to carboxylate groups. One deprotonation accounts for the global charge of the system. We can then assume that each of the N remaining thiolate and carboxylate removes one valence electron from the N silver atoms. This indicates that the Ag can be viewed as Ag(I) in all the species observed here, therefore they can be categorized into Ag(I)-thiolate complexes. The peaks labeled with a star correspond to complexes with an additional sulfur atom attached. These complexes may come from in source dissociation of $[Ag_N(SR)_M\text{-}(N\text{-}M+1)H]^-$ species through a loss of $C_2O_2H_2$ (Figure 4. 16).

Previous combinations of electrospray ionization sources and lasers were used for ablation or desorption of organic and bio-molecules from substrates, which allowed to separate ablation and ionization processes[21–24]. Here, the laser is used to vaporize a metal rod resulting in metal atoms and/or metal clusters. Chemical reaction of the vaporized metal with the acid contained in the spray leads to the formation of ligated clusters. The droplets of solvent act as micro-reactors for chemical reactions. This reaction occurs on a time scale that is driven by solvent evaporation. The micrometer size of the droplet leads to a probability of encounter for the reactants close to 1. For comparison, Figure 4. 15c shows a mass spectrum recorded using only water as the solution for the spray. It shows oxidized silver clusters. Comparison between Figure 4. 15b and c illustrates how the ligands contained in the spray prevent the clusters oxidation. The observed size range is limited by the mass range of the mass spectrometer (*m/z* 2000) and we do not observe large complexes with a metal core surrounded by ligands as obtained from

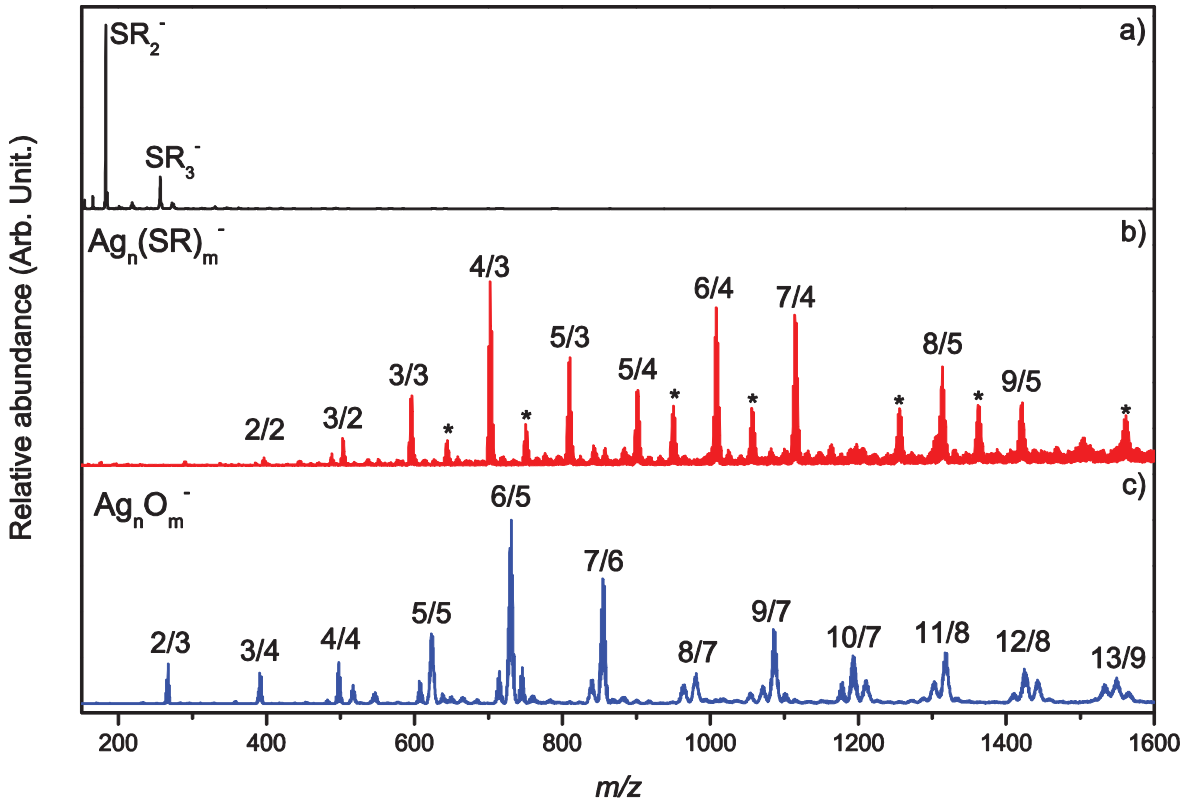

Figure 4. 15 a) Mass spectrum recorded using the thioglycolic acid solution without metal vaporisation. b) LAVESI mass spectrum obtained by vaporisation of a silver rod and spray of a thioglycolic acid solution with capillary temperature at 100°C. The clusters are labelled by N/M where N is the number of silver atoms and M is the number of ligands. The exact formula for these clusters is $[Ag_N(SR)_M - (N - M + 1)H]^-$. c) LAVESI mass spectrum obtained by vaporisation of a silver rod and spray of a thioglycolic acid solution with capillary temperature at 100°C. Peaks correspond to $[Ag_xO_yH_z]^-$.

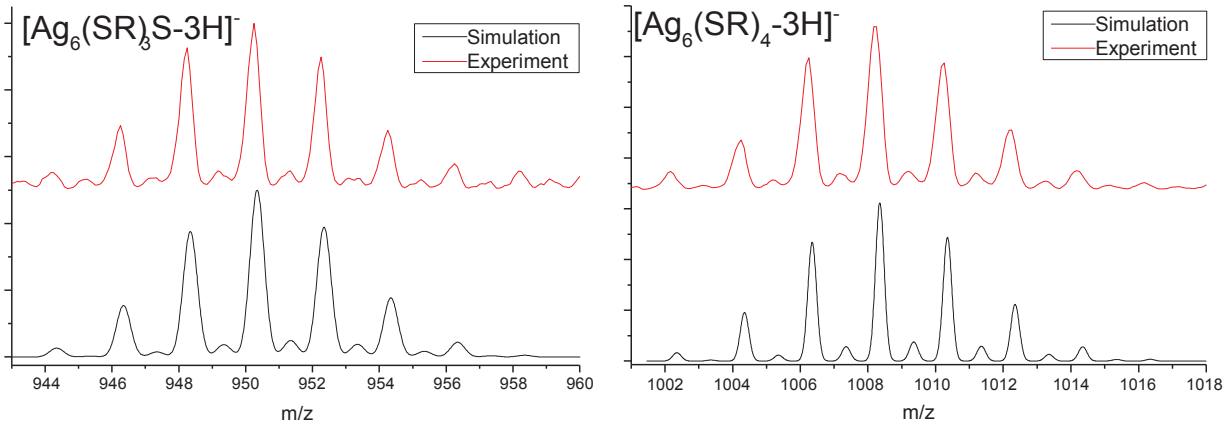

Figure 4. 16 Example of isotopic distribution comparison of experimental and simulated species for silver-thioglycolic acid complexes.

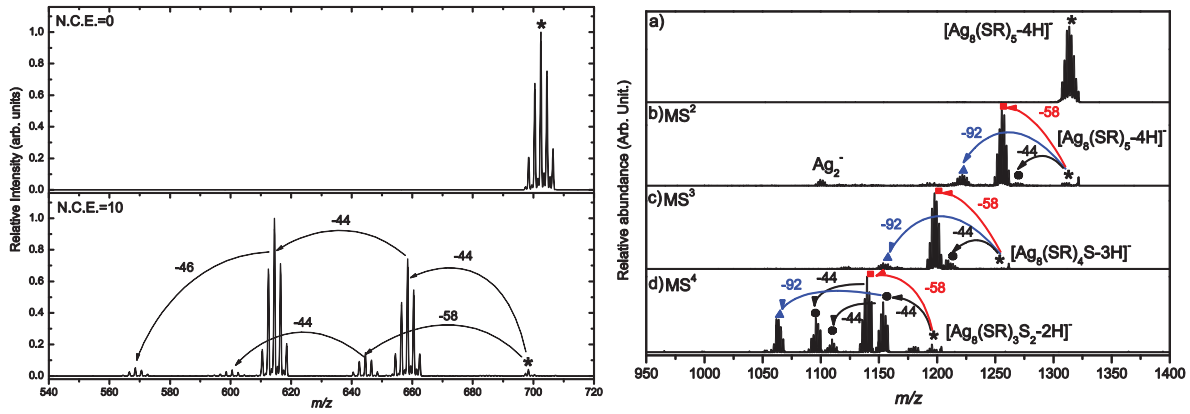

Figure 4. 17 The MS^n spectra of selected LAVESI species. (left) MS^2 spectrum of $[Ag_4(SR)_3 - 2H]^-$, with and without the collisional activation. (right) MS^2 to MS^4 spectrum starting with $[Ag_8(SR)_5 - 4H]^-$. The precursor for each subsequent step is selected as a product of the loss of $C_2H_2O_2$ marked by red squares. Black circles mark the loss of CO_2, and blue triangles mark the loss of one thioglycolic acid.

wet chemistry[25–28]. However, observation of metal clusters without spraying any ligand (Figure 4. 15c) demonstrates that clusters can be formed directly within the plasma plume generated on the surface of the rod without chemical reaction with ligands contained in the spray.

The different species studied in this contribution were synthesized by LAVESI in the gas phase by sequences of collision induced dissociation (CID) of a silver–thioglycolic acid complex precursor (MS^n experiments). The different steps of ion selection and excitation are successively carried out in the high pressure cell. The peak corresponding to four silvers atoms and tree thioglycolic acids was selected (Figure 4. 17 (left)). Isotopic distribution analysis shows that the peak at *m/z* 702.6 is due to $[4Ag(C_2H_2O_2S)_2C_2H_3O_2S]^-$, with a simplified notation $[Ag_4(SR)_3\text{-}2H]^-$.

Figure 4. 17 (left) shows the mass spectrum obtained after collisional activation of $[Ag_4(SR)_3\text{-}2H]^-$ (*m/z* 702.6). Two major peaks (*m/z* 658.5, and 614.5) are observed in the spectrum. Isotopic distribution analysis shows that these peaks correspond to successive losses of CO_2 (44 Da), a 2nd CO_2 and SCH_2 (46 Da) leading to a complex made of one thioglycolic acid and 4 silver atoms bonded to SCH_3. A possible pathway is first decarboxylation from the carboxylic group of a thioglycolic acid followed by a decarboxylation from a carboxylate. The later leads to the formation of CH_2S group, which is lost after further excitation.

$$\begin{cases} [4Ag(C_2H_2O_2S)_2C_2H_3O_2S]^- \rightarrow [4Ag(C_2H_2O_2S)_2CH_3S]^- + CO_2 \\ [4Ag(C_2H_2O_2S)_2CH_3S]^- \rightarrow [4Ag(C_2H_2O_2S)(CH_3S)CH_2S]^- + CO_2 \\ [4Ag(C_2H_2O_2S)(CH_3S)CH_2S]^- \rightarrow [4Ag(C_2H_2O_2S)(CH_3S)]^- + CH_2S \end{cases} \quad (4.1)$$

Minor peaks are observed at *m/z* 644.4 and 600.5 corresponding to successive losses of 58 Da and 44 Da. They are attributed to $C_2O_2H_2$ and CO_2 losses.

$$\begin{cases} [4Ag(C_2H_2O_2S)_2C_2H_3O_2S]^- \rightarrow [4Ag(C_2H_2O_2S)_2SH]^- + C_2H_2O_2 \\ [4Ag(C_2H_2O_2S)_2SH]^- \rightarrow [4Ag(C_2H_2O_2S)CH_2SHS]^- + CO_2 \end{cases} \quad (4.2)$$

Collision induced dissociation spectra recorded for $[Ag_4(SR)_3\text{-}2H]$- complexes (*m/z* 702.6) obtained through the two different formation pathways (vaporization of metal rod with the LAVESI source and from silver salt with the ESI source – previous chapter) result in CO_2, and $2CO_2$ neutral losses (Figure 4. 17 (left) and Figure 3. 2 (right)). The CID spectra are identical suggesting that both methods of formation lead to similar complexes.

In Figure 4. 17 (right), the peak corresponding to eight silver atoms and five thioglycolic acids was selected. Isotopic distribution analysis shows that the peak at *m/z* 1314 corresponds to $[8Ag(C_2H_2O_2S)_4C_2H_3O_2S]^-$ ($[Ag_8(SR)_5\text{-}4H]$). Figure 4. 17 (b-c) show the mass spectrum obtained after collisional activation of $[Ag_8(SR)_5\text{-}4H]$ – (*m/z* 1314). A major peak (*m/z* 1256) is observed in the spectrum. Isotopic distribution analysis shows that this peak corresponds to the loss of 58 Da and which is attributed to $C_2O_2H_2$, which is due to the internal fragmentation of the ligands. It results from a cleavage of the S-C bond. A sulfur atom is retained on the complex which illustrates the strength of the Ag-S bonding as compared to Ag-carboxylate[29]. Minor peaks are observed at *m/z* 1268, 1222 and 1100 and correspond to successive losses of 44 Da, 92 Da and 214 Da. They are attributed to CO_2, $C_2H_4O_2S$ and Ag_2 losses.

$$\begin{cases} [8Ag(C_2H_2O_2S)_4C_2H_3O_2S]^- \rightarrow [8Ag(C_2H_2O_2S)_4HS]^- + C_2H_2O_2 \\ [8Ag(C_2H_2O_2S)_4C_2H_3O_2S]^- \rightarrow [8Ag(C_2H_2O_2S)_4CH_3S]^- + CO_2 \\ [8Ag(C_2H_2O_2S)_4C_2H_3O_2S]^- \rightarrow [8Ag(C_2H_2O_2S)_3C_2HO_2S]^- + C_2H_4O_2S \end{cases} \quad (4.3)$$

MS^3 and MS^4 spectra obtained after collisional activation of $[Ag_8(SR)_4S\text{-}3H]^-$ (*m/z* 1256) and $[Ag_8(SR)_3S_2\text{-}2H]^-$ (*m/z* 1198) respectively (Figure 4. 17c and d) show that the loss of $C_2O_2H_2$ is still the dominant process. Decarboxylation in this case is a minor pathway. The loss of thioglycolic acid ($C_2H_4O_2S$) is also observed. This shows that the reactivity of the complex depends on the number of metal atoms.

4.2.2 Ligated gold complexes

Figure 4. 18 shows a mass spectrum obtained after vaporization of a gold rod. Formation of ligated gold complexes is observed. Small sizes have a stoichiometry similar to the one that we obtained by electrospraying a gold salt solution (Figure 3. 4). For gold, larger sizes are obtained using the LAVESI source. The mass spectrum is dominated by species with N=M, which is in agreement with the formation of small chains with equal number of ligands and gold cations. This is different from silver, for which chains with metal cation in excess were observed[27]. Due to difficulty of synthesis and susceptibility to oxidation upon exposure to air, it is a significant challenge to prepare stable ligated copper complexes, and therefore studies of copper containing species are still at a preliminary stage compared to what has been achieved for both ligated Ag and Au clusters[30,31]. ESI –MS and MALDI-TOF-MS was already used to analyze low mass Cu-thiolate fragments generated from Cu nanoparticles [31,32].

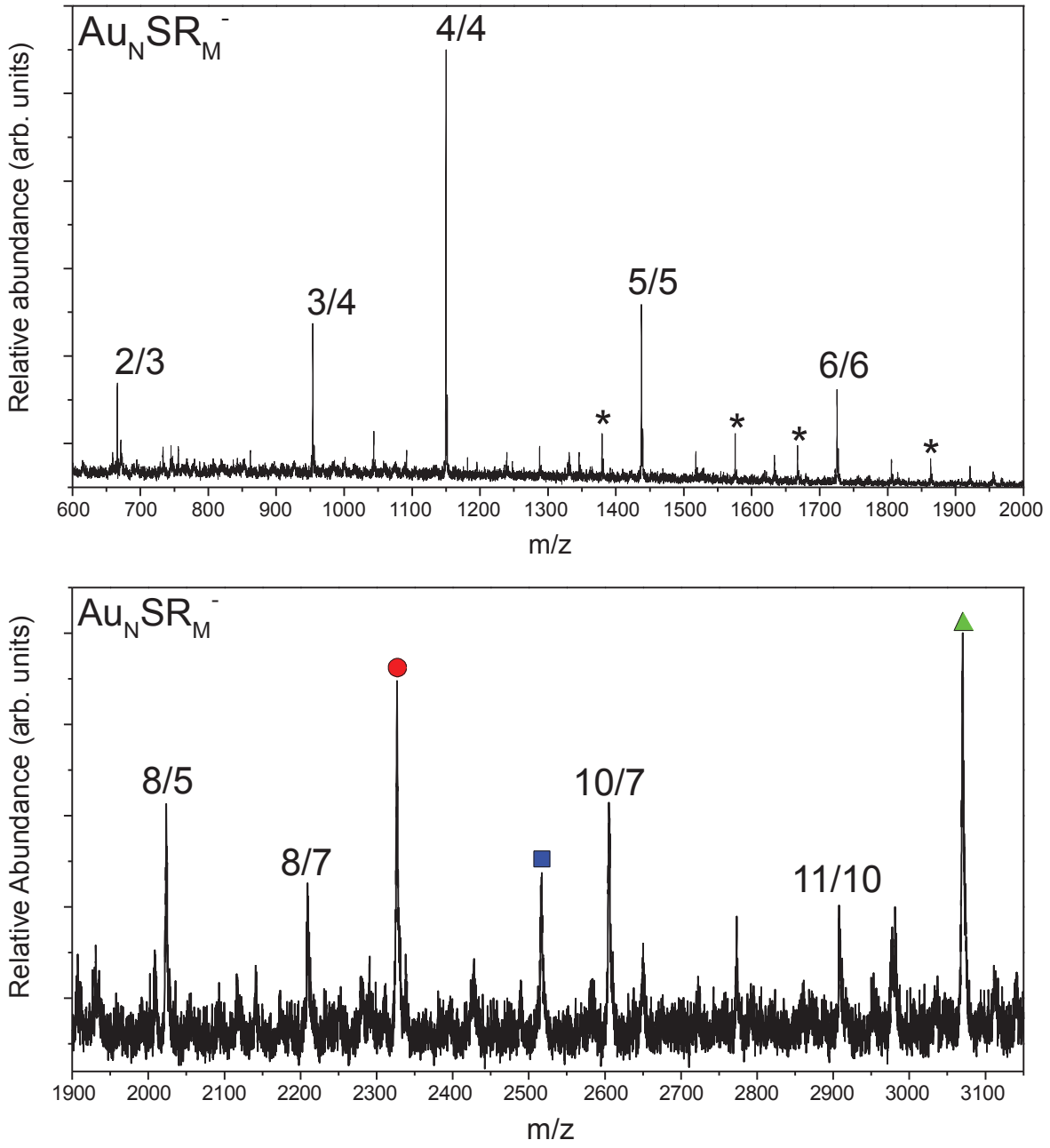

Figure 4. 18 LAVESI mass spectrum obtained by vaporisation of a gold rod and spray of thioglycolic acid. Mass ranges are separated to medium mass range (50-2000 Da) (top) and high mass range (2000-4000 Da) (bottom) due to the technical constraints of the instrument. The clusters are labelled by N/M where N is the number of gold atoms and M is the number of ligands. The exact formulas of all the species observed are given in Table 4. 3. The red circle, blue square and green triangle represent the $[Au_9(SR)_7\text{-}3H+S]^-$, $[Au_{10}(SR)_6+2H]^-$ *and* $[Au_{12}(SR)_8\text{-}3H\text{-}O]^-$ *respectively.*

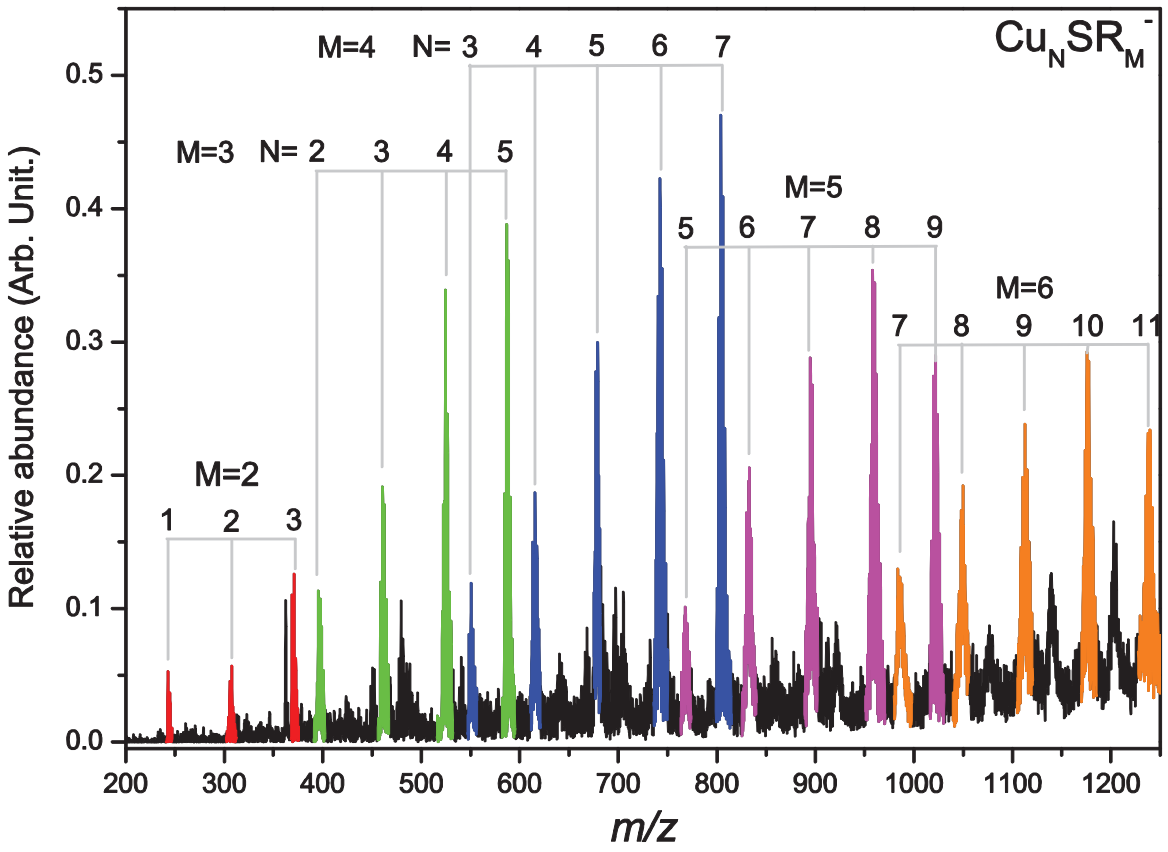

Figure 4. 19 LAVESI mass spectrum obtained by vaporisation of a copper rod at a capillary temperature of 50°C. The exact formulas for the species are given in the Table 4. 4.

4.2.3 Ligated copper complexes

Figure 4. 19 shows a representative mass spectrum obtained by vaporizing a Cu rod. Most intense peaks are assigned to $Cu_{1\text{-}3}(SR)_2$, $Cu_{2\text{-}5}(SR)_3$, $Cu_{3\text{-}7}(SR)_4$, $Cu_{5\text{-}9}(SR)_5$, $Cu_{7\text{-}10}(SR)_6$, and $Cu_{7\text{-}13}(SR)_7$ complexes. Examples of isotopic distributions recorded using the high resolution zoom scan mode of the mass spectrometer are shown in Figure 4. 20. Unlike silver and gold species, complexes containing a higher number of ligands than the number of metal atoms are observed. Experimental isotopic distribution recorded for $Cu(SR)_2^-$ is given in Figure 4. 20a. It corresponds to $[Cu(SR)_2\text{-}2H]^-$. Assuming a charge of ~-1 on each sulfur atom and on two deprotonated carboxylate groups, the total charge on the metal atom would be ~+III. Another possibility is the formation of a disulfide bridge mediated by copper[33]. In this case Cu is in the oxidation state +I. Experimental isotopic distribution recorded for $Cu_2(SR)_2^-$ is given in Figure 4. 20b. The comparison of the experimental data with calculated distributions establishes that the exact species that we observed here are a combination of two ions: $[Cu_2(SR)_2\text{-}2H]^-$ and $[Cu_2(SR)_2\text{-}H]^-$. Figure 4. 20c shows the isotopic distribution of $[Cu_3(SR)_2\text{-}2H]^-$, and Figure 4. 20d shows an isotopic distribution corresponding to the superposition of $[Cu_4(SR)_2\text{-}2H]^-$ and $[Cu_4(SR)_2\text{-}3H]^-$. Observation of multiple species at the same *m/z* is independent of the species stoichiometries and is due to the different combinations of copper oxidation states in the complex. The different complex sizes and

exact chemical formula observed in Figure 4. 19 are summarized in Table 4. 1. All of the observed species with exact chemical formula and corresponding mass range of the isotopic distribution for all three of the metals are listed in Table 4. 2 (silver), Table 4. 3 (gold), and Table 4. 4 (copper). While in silver and gold mass spectra, the observed species can be simply rationalized as Ag(I)-thiolate and Au(I)-thiolate complexes, in the case of copper the different possible oxidation numbers of copper lead to a richer chemistry and more complex mass spectra. In most cases, contribution of Cu ions with oxidation states (I) and (II) are observed. For two sizes ($[Cu(SR)_2\text{-}2H\ ]^-$, $[Cu_2(SR)_3\text{-}3H]^-$), Table 4. 1 suggests the contribution of the Cu (III) ion.

Table 4. 1 Comparison of ligated silver and copper complexes obtained with LAVESI.

N(Metal)	M(SR)	Formula for silver clusters	Formula for copper clusters
1	2	$Ag(SR)_2$	$Cu(SR)_2$-2H
2	2	$Ag_2(SR)_2$-H	$Cu_2(SR)_2$-2H and $Cu_2(SR)_2$-H
2	3		$Cu_2(SR)_3$-3H and $Cu_2(SR)_3$-2H
3	2	$Ag_3(SR)_2$-2H	$Cu_3(SR)_2$-2H
3	3	$Ag_3(SR)_3$-H	$Cu_3(SR)_3$-3H
4	3	$Ag_4(SR)_3$-2H	$Cu_4(SR)_3$-3H and $Cu_4(SR)_3$-2H
4	4		$Cu_4(SR)_4$-3H and $Cu_4(SR)_4$-2H
5	3	$Ag_5(SR)_3$-3H	$Cu_5(SR)_3$-3H
5	4	$Ag_5(SR)_4$-2H	$Cu_5(SR)_4$-3H and $Cu_5(SR)_4$-2H
6	4	$Ag_6(SR)_4$-3H	$Cu_6(SR)_4$-3H and $Cu_6(SR)_4$-2H
6	5		$Cu_6(SR)_5$-3H
7	4	$Ag_7(SR)_4$-4H	$Cu_7(SR)_4$-4H
7	5		$Cu_7(SR)_5$-4H
8	5	$Ag_8(SR)_5$-4H	$Cu_8(SR)_5$-5H and $Cu_8(SR)_5$-4H
9	5	$Ag_9(SR)_5$-5H	$Cu_9(SR)_5$-5H

Table 4. 2 List of formulas and mass ranges for silver species obtained with LAVESI source. All clusters are singly negatively charged.

Formula for silver clusters	Mass range (Da)
$Ag(SR)_2$	288.9-292.9
$Ag_2(SR)_2$-H	394.6-400.7
$Ag_3(SR)_2$-2H	500.5-508.5
$Ag_3(SR)_3$-H	592.5-600.5
$Ag_4(SR)_3$-2H	698.3-708.3
$Ag_5(SR)_3$-3H	804.1-814.3
$Ag_5(SR)_4$-2H	896.1-906.1
$Ag_6(SR)_4$-3H	1002.1-1014.1
$Ag_7(SR)_4$-4H	1107.9-121.9
$Ag_8(SR)_5$-4H	1305.9-1321.9
$Ag_9(SR)_5$-5H	1413.7-1429.7

Table 4. 3 List of formulas and mass ranges for gold species obtained with LAVESI source. All clusters are singly negatively charged.

Formula for gold clusters	Mass range (Da)
$Au_2(SR)_3$-H	666.1-668.1
$Au_3(SR)_4$-H	953.9-955.9
$Au_4(SR)_4$-2H	1150.0-1153.8
$Au_5(SR)_5$-2H	1437.8-1439.8
$Au_6(SR)_6$-2H	1725.6-1729.7
$Au_8(SR)_5$-7H	2022.2-2026.0
$Au_8(SR)_7$-3H	2007.6-2214.1
$Au_{10}(SR)_7$-H	2602.6-2610.0
$Au_{11}(SR)_{10}$-5H	3067.1-3075.6

Table 4. 4 List of formulas and mass ranges for copper species obtained with LAVESI source. All clusters are singly negatively charged.

Formula for copper clusters	Mass range (Da)
$Cu(SR)_2$-2H	242.8-246.8
$Cu_2(SR)_2$-2H and $Cu_2(SR)_2$-H	305.8-311.6
$Cu_2(SR)_3$-3H and $Cu_2(SR)_3$-2H	395.6-402.5
$Cu_3(SR)_2$-2H	368.7-374.5
$Cu_3(SR)_3$-3H	458.6-464.7
$Cu_4(SR)_3$-3H and $Cu_4(SR)_3$-2H	521.5-530.4
$Cu_4(SR)_4$-3H and $Cu_4(SR)_4$-2H	612.4-621.3
$Cu_5(SR)_3$-3H	584.4-592.3
$Cu_5(SR)_4$-3H and $Cu_5(SR)_4$-2H	675.3-686.3
$Cu_6(SR)_4$-3H and $Cu_6(SR)_4$-2H	738.2-750.1
$Cu_6(SR)_5$-3H	829.0-838.9
$Cu_7(SR)_4$-4H	800.1-812.2
$Cu_7(SR)_5$-4H	892.0-904.0
$Cu_8(SR)_5$-5H and $Cu_8(SR)_5$-4H	953.0-976.8
$Cu_9(SR)_5$-5H	1016.0-1029.6

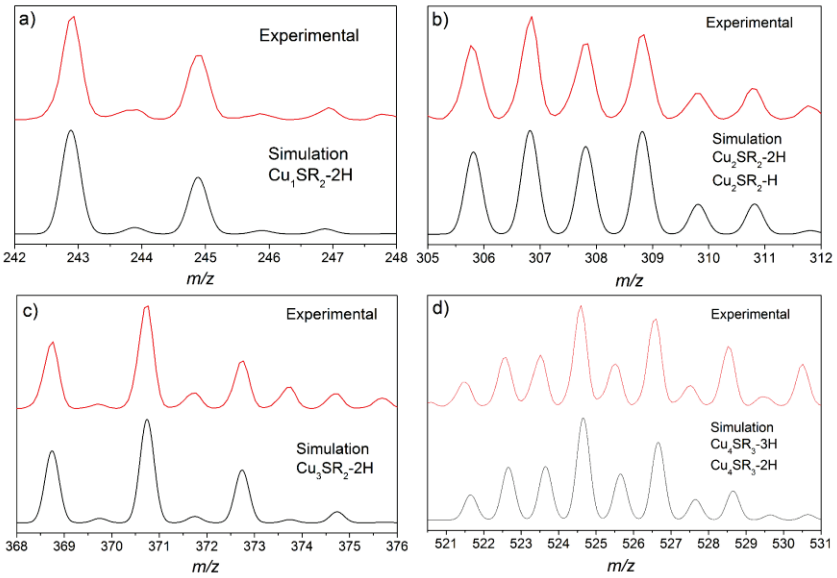

Figure 4. 20 Isotopic distributions for several ligated copper complexes created by LAVESI. Coppers characteristic isotopic pattern helps us identify the observed signal in some cases as superposition of two species.

4.2.4 Ligated bimetallic complexes

In order to produce the bimetallic clusters, an alloy rod was used in the LAVESI source. The rod was a silver *wt* 50%, gold *wt* 50% mixture. Figure 4. 21 shows mass spectrum rich with new species. Easily identifiable are the monometallic species of gold and silver with thioglycolic acid, already seen in LAVESI experiments with a rod of one metal. For the species with total number of metal atoms $1 \leq x + y \leq 5$ complexes with same or greater number of ligand molecules than metal atoms can be found in the spectrum. For number of metal atoms $x + y \geq 4$, though we see that number of ligand molecules never surpasses the number of metals, and in case of $x + y = 6$, metal is in greater abundance. A list of all of the observed species along with exact chemical formulas and *m/z* ranges can be found in Table 4. 5. All of the observed bimetallic species save four correspond to the same general formula $[(Au_x Ag_y SR_z) - ((x + y) - z + 1)H]^-$, which is the same generic formula that can be used to describe the observed silver clusters. This would indicate that these complexes follow the "chain-like" structure already attributed to small silver complexes[8].

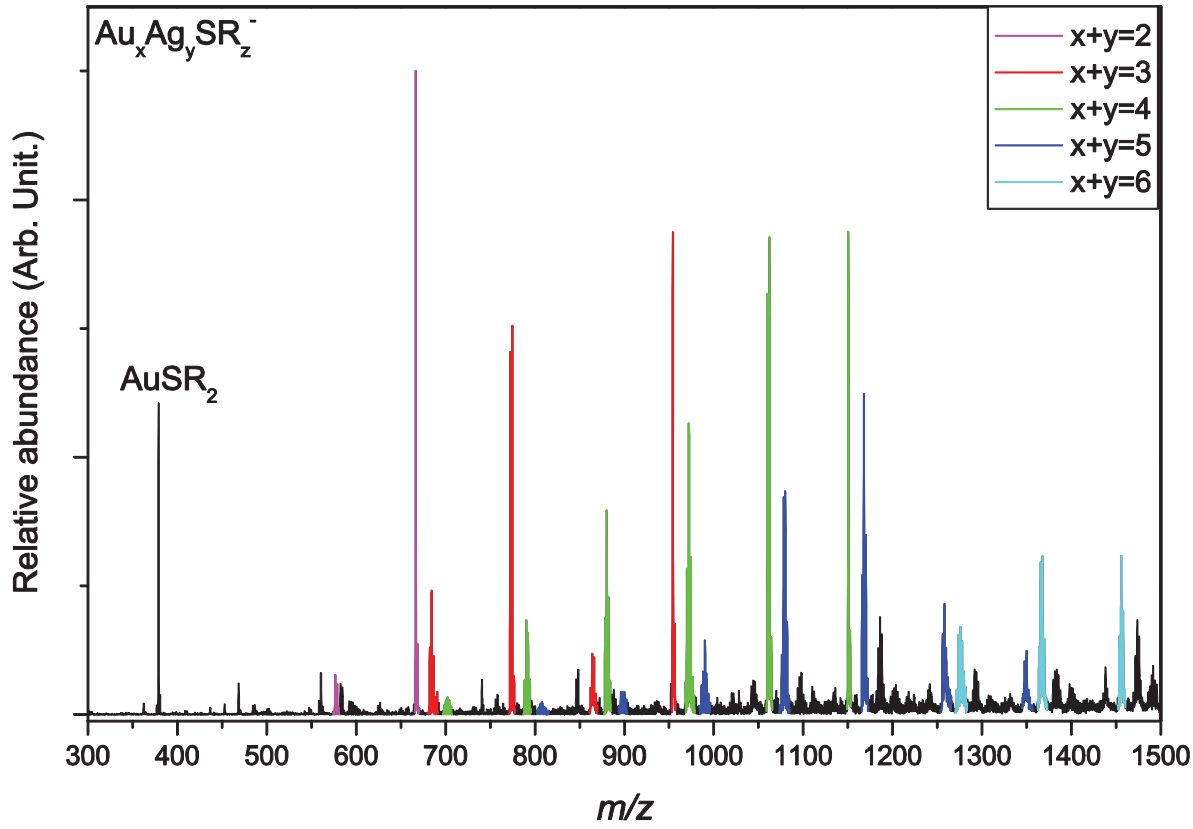

Figure 4. 21 LAVESI mass spectrum obtained through vaporisation of gold-silver alloy rod (1/1 ratio) and electrospraying thioglycolic acid. The coloured peaks represent the groups of the same total number of the metal atoms in the complex. The numbers correspond to the number of gold, silver and ligand respectively which make up the complex.

Table 4. 5 List of formulas and mass ranges for bimetallic species obtained with LAVESI source. All clusters are singly negatively charged.

Formula for bimetallic clusters	Mass range (Da)
$Au(SR)_2$	378.2-379.4
$AuAg(SR)_2$-H	483.9-489.2
AuAg(SR)3	575.8-581.3
$Au_2(SR)_3$	665.6-669.4
$AuAg_2(SR)_3$-H	681.6-689.1
$Au_2Ag(SR)_3$-H	771.6-777.2
$Au_2Ag(SR)_4$	863.0-869.2
$Au_3(SR)_4$	953.5-957.3
$Au_2Ag_2(SR)_3$-2H	877.6-885.1
$Au_2Ag_2(SR)_4$-H	969.2-977.1
$Au_3Ag(SR)_4$-H	1059.4-1065.2
$Au_4(SR)_4$-H	1149.2-1153.3
$Au_2Ag_3(SR)_4$-2H	1075.5-1085.0
$Au_3Ag_2(SR)_4$-2H	1165.4-1173.0
$Au_3Ag_2(SR)_5$-3H	1255.4-1262.4
$Au_4Ag(SR)_5$-H	1346.5-1352.4
$Au_2Ag_4(SR)_5$-4H	1271.3-1280.9
$Au_3Ag_3(SR)_5$-2H	1363.0-1372.4
$Au_4Ag_2(SR)_5$-2H	1452.5-1458.5

4.2.5 Conclusions on ligated complexes

In conclusion, we successfully combined ESI and laser vaporization to produce ligated-metal species. First results show the possibility of producing complexes with various metals, and metal alloys. We observe a variety of new species, in particular sizes and stoichiometries, which were not obtained from electrospraying a metal salt solution. Previous results on the formation of bare metal clusters by vaporization of metal rods[6] suggest that the LAVESI source could be used to produce hybrid clusters of almost any type of metal. LAVESI opens new perspectives to study the structure and chemical properties of ligated metal species by mass spectrometry as exemplified for silver and gold clusters with an extended range size as compared to previous reports and with the observation of completely new species for copper.

4.3 Conclusion

We have shown the mass spectra of the species obtained with the new LAVESI method. The method consists of coupling the laser vaporisation of a metal rod with electrospray ionisation of a solution. This way, the vaporised metal complexes react with the constituents in the electrospray plume and form new species. In cases when only electrospray voltage is applied and nothing is sprayed, metals react with atmospheric constituents to form diverse species $M_n N_m H_l{}^q$ and $M_n O_m H_l{}^q$, in both positive and negative modes. Also, pure metal clusters are detected. Electrospraying H_2O or D_2O increases the abundance of these products and decreases the intensities of pure metal clusters. Introducing a small thiol molecule in the ESI plume however completely changes the observed species. All of the previously observed complexes of pure metals and their products disappear and are replaced by ligated metal complexes $M_N SR_M^-$. The presence of the ligand in the electrospray prevents nucleation and oxidation of metal, instead replacing it with reactions with the ligand. Multiple new species are observed for thioglycolic acid and silver, gold, copper and silver/gold alloy.

Bibliography

1. Stephen, A. & Hashmi, K. Homogeneous gold catalysis beyond assumptions and proposals-characterized intermediates. *Angew. Chemie - Int. Ed.* **49,** 5232–5241 (2010).
2. Hashmi, A. S. K. & Rudolph, M. Gold catalysis in total synthesis. *Chem.Soc.Rev.* **37,** 1766–1775 (2008).
3. Hashmi, A. S. K. in *Inorganic Chemistry* **48,** 143–164 (2012).
4. Jin, R. Atomically precise metal nanoclusters: stable sizes and optical properties. *Nanoscale* **7,** 1549–65 (2015).
5. Heath, J. R. *et al.* The Formation of Long Carbon Chain Molecules during Laser Vaporization of Graphite. *J. Am. Chem. Soc.* **109,** 359–363 (1987).
6. De Heer, W. A. The physics of simple metal clusters: Experimental aspects and simple models. *Rev. Mod. Phys.* **65,** 611–676 (1993).
7. Ayers, T. M., Fye, J. L., Li, Q. & Duncan, M. A. Synthesis and Isolation of Titanium Metal Cluster Complexes and Ligand-Coated Nanoparticles with a Laser Vaporization Flowtube Reactor. *J. Clust. Sci.* **14,** 97–113 (2003).
8. Bell, R. a & Kramer, J. R. Structural chemistry and geochemistry of silver-sulfur compounds: Critical review. *Environ. Toxicol. Chem.* **18,** 9–22 (1999).
9. Bogaerts, A., Chen, Z., Gijbels, R. & Vertes, A. Laser ablation for analytical sampling: What can we learn from modeling? *Spectrochim. Acta - Part B At. Spectrosc.* **58,** 1867–1893 (2003).
10. Schwarz, H. Relativistic Effects in Gas-Phase Ion Chemistry: An Experimentalist's View. *Angew. Chemie Int. Ed.* **42,** 4442–4454 (2003).
11. Pyykko, P. Relativistic effects in structural chemistry. *Chem. Rev.* **88,** 563–594 (1988).
12. Häkkinen, H., Moseler, M. & Landman, U. Bonding in Cu, Ag, and Au Clusters: Relativistic Effects, Trends, and Surprises. *Phys. Rev. Lett.* **89,** 033401 (2002).
13. Lee, H. M., Ge, M., Sahu, B. R. & Tarakeshwar, P. Geometrical and electronic structures of gold, silver, and gold-silver binary clusters: Origins of ductility of gold and gold-silver alloy formation. *J.* ... 9994–10005 (2003).
14. Bernhardt, T. M. Gas-phase kinetics and catalytic reactions of small silver and gold clusters. *Int. J. Mass Spectrom.* **243,** 1–29 (2005).
15. Furche, F. *et al.* The structures of small gold cluster anions as determined by a combination of ion mobility measurements and density functional calculations. *J. Chem. Phys.* **117,** 6982 (2002).
16. Bonacic-Koutecky, V. *et al.* Density functional study of structural and electronic properties of bimetallic silver-gold clusters: Comparison with pure gold and silver clusters. *J. Chem. Phys.* **117,** 3120–3131 (2002).
17. Gilb, S., Weis, P., Furche, F., Ahlrichs, R. & Kappes, M. M. Structures of small gold cluster cations (Au[sub n][sup +], n<14): Ion mobility measurements versus density functional calculations. *J. Chem. Phys.* **116,** 4094 (2002).
18. Bonacic-Koutecky, V., Veyret, V. & Mitric, R. Ab initio study of the absorption spectra of Agn (n=5-8) clusters. *J. Chem. Phys.* **115,** 10450–10460 (2001).
19. Schmidt, M., Cahuzac, P., Bréchignac, C. & Cheng, H. P. The stability of free and oxidized silver clusters. *J. Chem. Phys.* **118,** 10956–10962 (2003).
20. Schmidt, M., Masson, A., Cheng, H.-P. & Bréchignac, C. Physisorption and Chemisorption on

Silver Clusters. *ChemPhysChem* **16,** 855–865 (2015).

21. Shiea, J. *et al.* Electrospray-assisted laser desorption/ionization mass spectrometry for direct ambient analysis of solids. *Rapid Commun. Mass Spectrom.* **19,** 3701–3704 (2005).

22. Nemes, P. & Vertes, A. Laser ablation electrospray ionization for atmospheric pressure, in vivo, and imaging mass spectrometry. *Anal. Chem.* **79,** 8098–8106 (2007).

23. Sampson, J. S., Hawkridge, A. M. & Muddiman, D. C. Generation and Detection of Multiply-Charged Peptides and Proteins by Matrix-Assisted Laser Desorption Electrospray Ionization (MALDESI) Fourier Transform Ion Cyclotron Resonance Mass Spectrometry. *J. Am. Soc. Mass Spectrom.* **17,** 1712–1716 (2006).

24. Flanigan, P. & Levis, R. Ambient femtosecond laser vaporization and nanosecond laser desorption electrospray ionization mass spectrometry. *Annu. Rev. Anal. Chem. (Palo Alto. Calif).* **7,** 229–56 (2014).

25. Bertorelle, F. *et al.* Synthesis, characterization and optical properties of low nuclearity liganded silver clusters: Ag31(SG)19 and Ag15(SG)11. *Nanoscale* **5,** 5637–5643 (2013).

26. Guo, J. *et al.* Mass spectrometric identification of silver nanoparticles: the case of Ag32(SG)19. *Anal. Chem.* **84,** 5304–8 (2012).

27. Kumar, S., Bolan, M. D. & Bigioni, T. P. Glutathione-stabilized magic-number silver cluster compounds. *J. Am. Chem. Soc.* **132,** 13141–13143 (2010).

28. Desireddy, A. *et al.* Ultrastable silver nanoparticles. *Nature* **501,** 399–402 (2013).

29. Li, H., Siu, K. W. M., Guevremont, R. & Le Blanc, J. C. Y. Complexes of Silver (1) with peptides and proteins as produced in electrospray mass spectrometry. *J. Am. Soc. Mass Spectrom.* **8,** 781–792 (1997).

30. Ganguly, A., Chakraborty, I., Udayabhaskararao, T. & Pradeep, T. A copper cluster protected with phenylethanethiol. *J. Nanoparticle Res.* **15,** (2013).

31. Wei, W., Lu, Y., Chen, W. & Chen, S. One-pot synthesis, photoluminescence, and electrocatalytic properties of subnanometer-sized copper clusters. *J. Am. Chem. Soc.* **133,** 2060–2063 (2011).

32. Jia, X., Yang, X., Li, J., Li, D. & Wang, E. Stable Cu nanoclusters: from an aggregation-induced emission mechanism to biosensing and catalytic applications. *Chem. Commun. (Camb).* **50,** 237–9 (2014).

33. Rokob, T. A. *et al.* On the Mechanism of the Copper-Mediated C–S Bond Formation in the Intramolecular Disproportionation of Imine Disulfides. *Inorg. Chem.* **50,** 9968–9979 (2011).

5. Gas phase reactions

Reactions of the bare metal clusters and metal complexes were done in the gas phase. The goal of the experiments was to achieve a catalytic cycle in the process of CO, NO, or alcohol oxidation, as those are the reactions either commonly used in industrial chemistry, or especially interesting for green chemistry applications.

In doing the reactions we focused on examining the smallest complexes, typically 1-5 atoms of metal, and their corresponding products. This was done because of ease of understanding the reactions observed, as it is simpler to do it on smaller systems, both for figuring out the reaction steps and for theoretical calculations. The problem of scalability is not considered for the time being.

All of the experiments are done with the setup described in the previous chapter, the reactant gas pressure and concentration are always the same, as well as the dimensions of the rod and laser power. The capillary temperature varies 25-150°C, and other ESI and ion optics conditions are optimised for each type of metal individually. The optimization is carried out with pure helium (He) as buffer gas, prior to introducing the reaction gas mixture. All of the mass spectra are recorded after ~20 minutes after the He/reactant mixture valve has been opened, to allow the pressure to equalise in all parts of the setup, and the reactant to fully diffuse into the trap.

5.1 Metals with CO

Carbon monoxide (CO) is a very important atmospheric constituent. Due to its health effects, it is considered as a pollutant in the atmosphere, it is dangerous for humans in concentrations above the 9 ppmv concentration. It can mostly be found in troposphere, which is the lowest layer of the atmosphere which makes it an important environmental factor. Since it is a product of internal combustion engine, as well as several industrial processes, a low-cost, ambient temperature and pressure CO oxidation or removal is of particular interest. In addition, because of effects of CO poisoning of catalysts in hydrogen fuel cells[1]. Another aspect of importance of reactions with CO is that they are suitable for probing the process of heterogeneous catalysis in general[2–4]. The studies carried out in the gas phase allow us to monitor the reaction on highly monodisperse species of small metal clusters, which can give us also an insight into their basic chemical properties. The reactions with CO were done at two different concentrations CO in He.

Reactions such as CO oxidation by molecular oxygen are very important in heterogeneous catalysis as a model surface reaction. Studies with metal clusters and CO have already been done in the gas phase. A very detailed account on transition metal carbonyl reactivity was published by Ervin in 2001 where they describe the reactions of multiple transitional metal cluster anions, with CO, under flow reactor conditions, with emphasis on the metals of nickel and copper groups[5]. Main contribution to CO – transitional metal bonding is the σ donation, π back-donation, which makes it very favourable for metals

with unfilled d shell which means that for the copper group metals, the CO is weakly bound[6]. According to this, the bond strength between the metal and CO depends on the balance between CO to metal electron donation and metal to CO electron back-donation, and thus the stronger bonding is expected for cations compared to neutral or anion species[7]. In case of silver anions, the bonding is unfavourable due to its low energy d orbital which makes the, π back-donation difficult. This could explain why so far silver anion reactions with CO have not been detected either in flow reactor or ion trap conditions[5,6]. Gold anion clusters on the other hand react with CO. Due to relativistic effects, the s-d orbitals distance is reduced, facilitating π back-donation. The formation of carbonyl complexes for all $Au_n^-, n > 1$ has been reported in variety of experimental conditions[8–13]. Cations of both gold and silver react with CO. $Ag^+$and Ag_2^+both adsorb CO molecules. The Ag_2^+also dissociates in the presence of CO to form $Ag(CO)_n{}^+$ complexes[6]. The catalytic activity of gold towards CO has been observed in several instances[14–16], as well as the reactions preference over gold oxidation via N_2O[17].

With small anionic and neutral clusters of palladium, a very strong size dependence in reactivity was observed[18]. Palladium cationic clusters show very high reactivity with CO. This is observed over a wide range of temperatures, from 100K to 300K[19]. In addition, IR spectroscopic studies on nickel group metals have investigated the binding sites of the first CO molecule on metal clusters with 3-25 atoms and found that platinum and nickel adsorb only in top site, while palladium exhibits a variety of binding sites.

In general for the small copper and nickel group metal clusters, of 3-7 atoms, the binding energies of a single CO molecule seems to be around 0.6-0.9 eV which is very close to the values for binding on extended surfaces (-0.5 - -0.6 eV)[20]. The nature of the CO – surface binding greatly depends on the metal, as well as the surface structure and reaction conditions. Insights into molecular or dissociative adsorption of CO on various metal gained through vibrational spectroscopy show that the copper and nickel group metals favour the molecular adsorption at ~300K for neutral and cationic clusters, and additionally anionic for Pd, Pt and Au. The exception is copper which favours the dissociative adsorption[20].

Several studies both theoretical and experimental have been made so far to study the influence of hydrogen adduct on the metal cluster. The calculations show that the Au_nH clusters become more catalytically active in comparison to Au_n and with lower activation energy for CO oxidation reaction[21]. Similarly, the preadsorption of H_2O on the Au_2^+ enhances the CO and O_2 adsorption. Also molecular hydrogen can overcome the inertness of gold cluster cations towards molecular oxygen[22]. For gold anions, the $Au_2H^-$is a minor contaminant. The study of this species has shed light on some previous anomalous Au-Au distances found in nanowires, implying the existence of an "invisible" hydrogen impurity[23]. The preadsorption of H2 and H2O has also been discussed as a suitable means of lowering the binding energy of CO to the Au_nAg_m cluster, due to charge donation[22,24].

5.1.1 Reactions at low CO concentration

The experiments with low CO concentration were done with a 0.1% He/CO mixture. The low concentration is suitable because it interferes less with the optimal buffer gas pressure in the ion trap. This reduces the degradation of resolution seen in the experiments with high concentration. Also, it allows us to see the intermediate products of reactions.

Figure 5. 1 shows the reactions of Au^+, Au_2^+, Au_3^+ and Au_4^+. The $Au^+$and Au_3^+ exhibit only simple reactions, i.e. sequential adsorption of several CO molecules. For the monomer, long trapping time is required to detect any products (Figure 5. 1a). The only products we can see are $Au(CO)^+$ and $Au(CO)_2^+$. The first two CO molecules are bound strongly to the monomer, and after that, the binding energy of subsequent ligand drops significantly[25]. The species observed are similar for Au_3^+ (Figure 5. 1c). The intensity of the products in comparison with the parent ion is very low. In addition to simple adsorption of one, two and three molecules of CO, we can see the $Au_3(CO)_3O^+$ species. It is unclear whether this species is created by fragmentation of from bigger species, or by dissociative adsorption of oxygen to $Au_3(CO)_3^+$ (Figure 5. 1c). The Au_2^+ and Au_4^+ show different behaviour than the other two species (Figure 5. 1b and d). The Au_2^+ is seen to dissociate in presence of CO. The observed species are $Au(CO)^+$ and $Au(CO)_2^+$. From the mass spectra alone it is not possible to determine whether the dissociation proceeds before the reactions, and it is gold monomer which reacts with CO, or if some product of Au_2^+ and CO is unstable and fragments into smaller species. Further discussion and analysis of this effect as well as comparison with Au_2H^+ reactivity and stability can be found in Section 5.1.3. In the mass spectrum of Au_4^+ we can see the products of the CO adsorption, the $Au_4(CO)^+$ $Au_4(CO)_2^+$, $Au_4(CO)_3^+$and $Au_4(CO)_4^+$. In addition to this there are $Au_3(CO)^+$, $Au_3(CO)_2^+$ and $Au_3(CO)_3^+$ present in the mass spectrum. This would indicate that in the presence of CO the Au_4^+ dissociates to the more stable Au_3^+ which then reacts with the reactant gas, or that some of the $Au_4(CO)_n^+$ products fragment, losing one gold atom to produce these species.

In Figure 5. 2 mass spectra of gold species with 5-9 atoms are shown. With low concentration CO in the ion trap, all of these species show some reactivity towards CO. The lowest relative intensity of the products compared to parent species is seen for Au_8^+. The products can be described by a general formula $Au_n(\mathrm{CO})_\mathrm{m}^+$, $5 \leq n \leq 9$, $1 \leq \mathrm{m} \leq 4$. Additionally, for $Au_7^+$and Au_8^+, $Au_7(\mathrm{CO})_5^+$and $Au_8(\mathrm{CO})_5^+$ are observed.

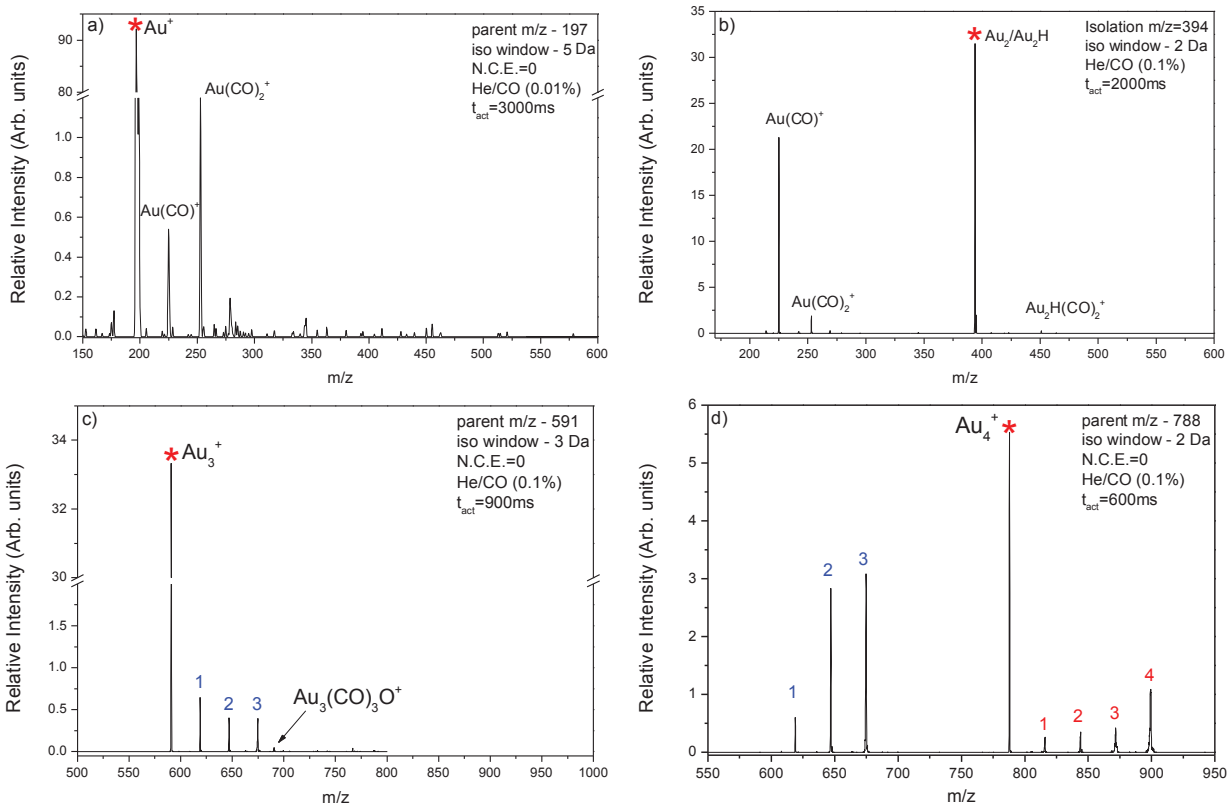

Figure 5. 1 Reactions of small $Au_n^+, n = 1 - 4$ clusters with low concentration CO. The red star marks the parent ion, the formulas in black mark the assignment of the adjacent peak. Due to the low intensity of the products, the y axis in a) and c) is split, so to make the peaks more visible. The isolation times are selected so that the reaction products are of sufficient intensity to be visible. In c) and d) the blue numbers marks the number of CO molecules adsorbed to gold trimer cluster. These complexes can be written as $Au_3(CO)_n^+$. The red numbers in d) mark the number of adsorbed CO molecules to gold tetramer, corresponding to the general formula $Au_4(CO)_n^+$.

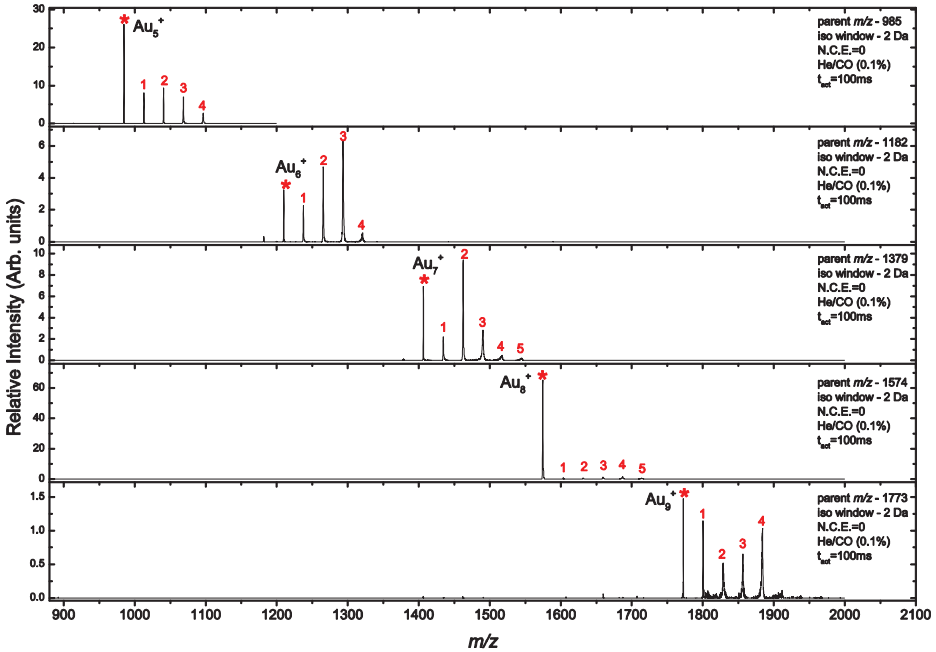

Figure 5. 2 Reaction with low concentration CO for Au_n^+ where $5 \leq n \leq 9$. The red star marks the parent ion, the red numbers mark the number of adsorbed CO molecules on the gold cluster.

In general, even though they do exhibit reactivity towards CO, the copper-group metals are not highly reactive towards it, and nickel group metals are known to be more reactive towards CO[5]. As can be seen inFigure 5. 3, analogous to gold, the $Pt^+$and Pt_3^+ adsorb a number of CO molecules, though, consistent with higher reactivity, for platinum more new species are observed than with gold monomer. The observed species are $Pt(CO)^+$, $Pt(CO)_2^+$ and $Pt(CO)_3^+$. PtN^+ and $PtN(CO)_3^+$ are also present in the spectrum. The intensity of the products for Pt^+ is very weak, regardless of the long trapping time (Figure 5. 3a). The reactivity of Pt_3^+ seems to be significantly higher than its gold counterpart (Figure 5. 3c). Many products can be seen in the spectrum as the result of CO adsorption to the cluster. All of these new complexes can be described by formula $Pt_3(CO)_n^+$. We observe species with $1 \leq n \leq 7$. As was the case with the gold dimer, the Pt_2^+species shows instability in the presence of CO. we can see the dissociation clearly, though, not the reaction products of the monomer. As with gold, more detailed look at this species in higher CO concentration can be found in Section 5.1.3. The Pt_4^+cluster seems to be much more reactive than the two previous ones, and also than the Au_4^+cluster. In Figure 5. 3d we can see with $t_{act} = 300ms$ same as other three species that the relative abundance of the products far surpasses that of the parent ion. The parent ion is almost completely consumed in reactions, and product species dominate the spectrum. The most intense of these is the $Pt_4(CO)_8^+$, which is also the biggest species detected, and was found to be the saturation limit for Pt_4^+ in the flow reactor conditions[5]. Same as Au_4^+, Pt_4^+ also dissociates, in the presence of CO, to produce Pt_3^+. The only detected product of Pt_3^+ that can be seen here is $Pt_3(CO)_6^+$. This situation is again analogous to gold, for which we also see the products of adsorption on trimer after the tetramer fragmentation.

Out of the copper group metals, silver is the least reactive with CO. In Figure 5. 4a we see that in pure helium the silver monomer is, as expected inert. Some minor aggregates with H_2O and $OH^\cdot$ are present, but their intensity is far below that of the precursor ion. In the presence of CO (Figure 5. 4b), the precursors intensity is reduced due to less efficient trapping. Also, new products, with CO can be seen. Unlike with gold, the silver-CO complexes observed here are never just $Ag(CO)_n^+$, but contain either oxygen, hydroxide or hydrogen.

5.1.2 Reactions at high CO concentration

As explained before (Chapter 2.4) our experiments uses two different He/CO mixtures for reactions in the ion trap. The high concentration bottle is 5% (v/v) mix of helium and CO. The concentration of CO in this case is high enough to disturb the normal operation of the ion trap, as it reduces the ability of helium buffer gas to effectively thermalize and stabilize the ions in the trap. Effectively, this causes a significant decrease in resolution of our mass spectra. Because we observe numerous species containing different number of hydrogen atoms, it is for this reason that we are not always able to precisely determine the number of hydrogen atoms present. In these cases, a question mark is used in place of the number of hydrogen atoms, indicating they are present in the complex, but in unknown quantity.

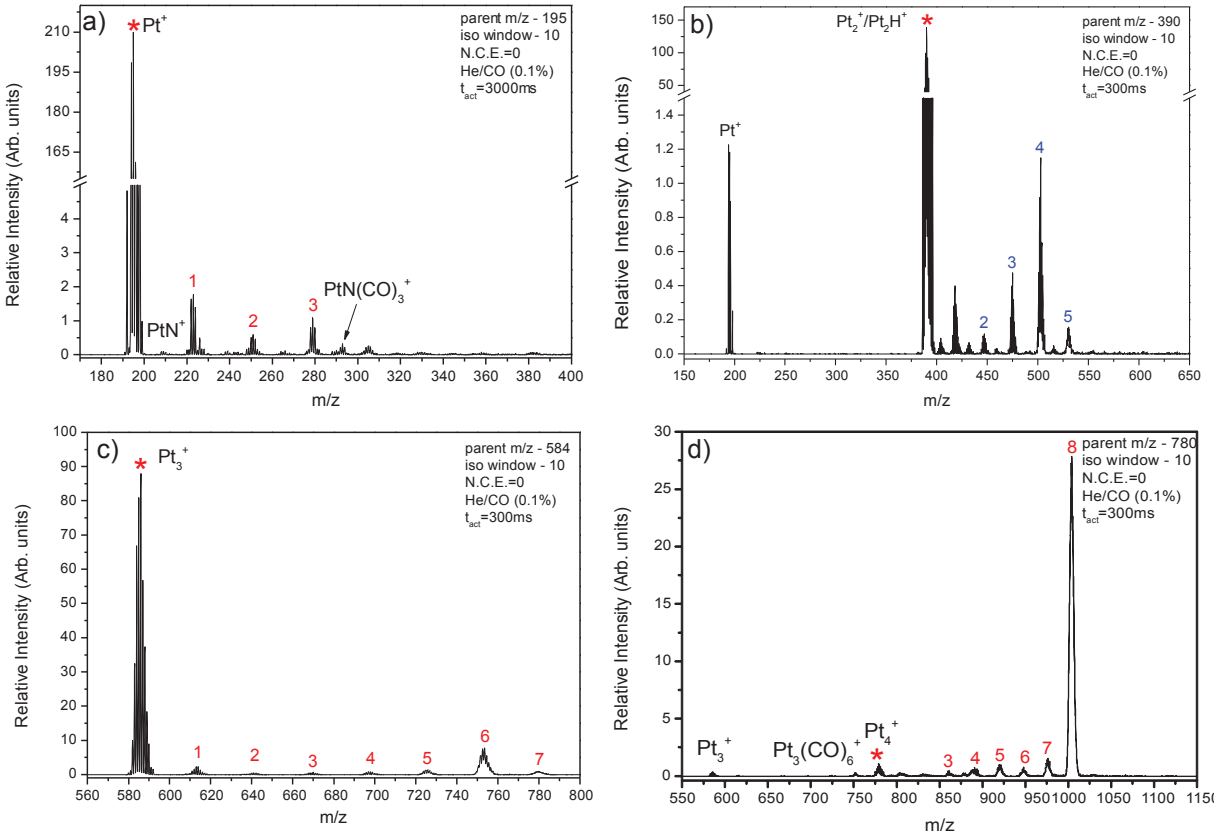

Figure 5. 3 Reaction with low concentration CO for Pt^+, Pt_2^+, Pt_3^+ and Pt_4^+. The red star marks the parent ion, the red numbers mark the number of adsorbed CO molecules to platinum cluster.

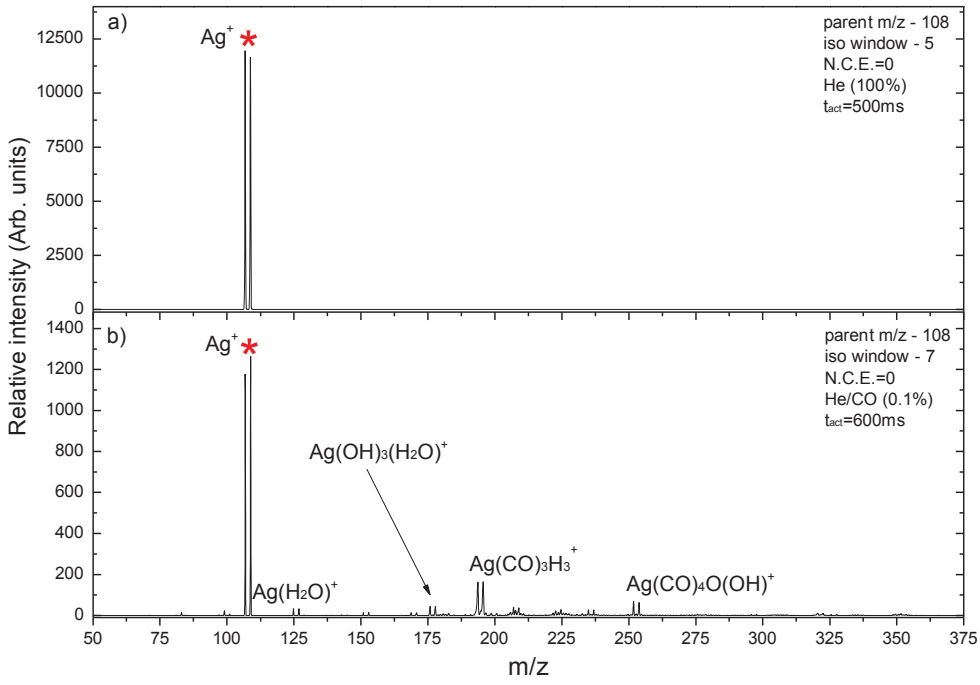

Figure 5. 4 Reactions of silver at low CO concentrations. a) silver monomer in pure helium buffer gas. b) silver monomer in He/CO 0.1% mixture.

As seen in the previous section, gold cations show reactivity with CO. The reactions observed are not just with pure gold complexes, but Au_nH^+ and Au_nN^+ as well, and they show very different reactivity.

As with the low concentration, the small, pure gold clusters the $Au^+$and Au_3^+ exhibit sequential adsorption of several CO molecules. With high concentration though we see the species with more CO molecules adsorbed to the metal cluster. In addition, the new species contain several hydrogen atom, something not seen in products obtained with low concentration. In case of gold monomer, for shorter trapping times ($t_{act} = 100ms$), the observed products are $Au(CO)^+$, $Au(CO)_2^+$, $Au(CO)_6H_{2/4}^+$ and $Au(CO)_7H_?^+$. For longer trapping times ($t_{act} = 500ms$) we can see some new peaks arising notably $Au(CO)_3H_{2/4/6}^+$ and $Au(CO)_{10}H_{3/5}^+$ and larger species as well (Figure 5. 5 – left). At the same time the $Au(CO)^+$ and $Au(CO)_2^+$ disappear, which leads to conclusion that the subsequent larger species are formed by reactions of the smaller precursors. Due to high concentration of CO in the trap (5% of the buffer gas) for longer trapping times we can assume the saturation limits for the adsorption of the CO on the gold complex is achieved. This is in agreement with experiments carried out with lower CO concentration (0.1% of the buffer gas), where we only see the $Au(CO)^+$ and $Au(CO)_2^+$ as products. This means that the hydrogen atoms that we see in larger species are added after the initial adsorption of one and two CO molecules, and aid in stabilising the complex. This could also explain significantly higher saturation rates observed in our experiment in comparison with previous gas phase studies of cationic gold clusters[26]. The peaks broadening in the case of higher concentration are caused by the non-nominal pressure in the trap due to introducing He/CO mixture instead of pure He. Also, the elongation of the peaks towards smaller *m/z* indicates that the detected species are metastable (Figure 5. 5 – right), which is in agreement with previous results assigning weaker binding energies to the $Au(CO)_n^+$ species for $n \geq 3$.

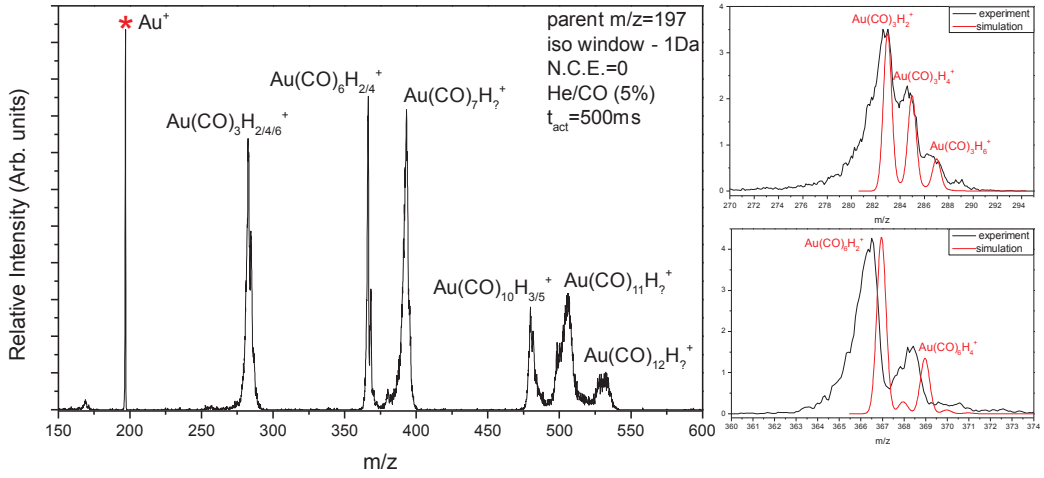

Figure 5. 5 (left) MS^2 spectrum of gold monomer with high concentration of CO in the ion trap. (right – top) Zoom in on $Au(CO)_3^+$ peak. (right – bottom) Zoom in on $Au(CO)_6^+$ peak. Because gold is monoisotopic the structure of the peaks cannot be explained by isotopic distribution of the constituting elements. The comparison with the calculated mass spectrum reveals them to be the result of the different number of hydrogen atoms present in the complex.

The Au_3^+ shows somewhat different behaviour. As products of its reactions we can see not only the adsorption of carbon monoxide and hydrogen, but some bonding of $H_2O(OH)$ as well. For higher CO concentration, the Au_3^+ seems to achieve saturation for fewer number of CO molecules than the gold monomer even when given more time to react inside the trap. The largest product species observed is $Au_3(CO)_8H_?^+$ (Figure 5. 6). The species observed in reactions with low CO concentration are depleted in favor of producing the bigger species. Same as with Au^+ hydrogen atoms stabilize the complexes. Reaction kinetics suggest that initially, for shorter trapping times, the reactions occur slowly. For trapping longer than 50 ms we see a drastic depletion in the precursor ion and increase in intensity of the products. The most abundant product is $Au_3(CO)_3^+$. The maximum of the peak at *m/z* 674 corresponds to exactly that formula without the added hydrogen atoms. The broadening of the peak to the right though suggests the existence of additional 1-3 hydrogen atoms. Under collisional activation the Au_3^+ does not show any fragmentation until 12 N.C.E. As can be seen in Figure 5. 6 (right – bottom), the fragmentation of $Au_3(CO)_3^+$ and $Au_3(CO)_8H_x^+$, together with the rise of $Au(CO)_n^+$ and $Au_2(CO)_2^+$starts already at 10 N.C.E., indicated that the small species are produced not just by reactions of the fragmented monomer, but they might be formed from $Au_3(CO)_3^+$ and $Au_3(CO)_8H_x^+$ by loss of $Au_2(CO)_n$.The main fragments are gold monomer and dimer. The fragmentation mass spectrum is dominated by products of the monomer. As in the case with direct isolation of the monomer, the smaller species are first to emerge, subsequently producing the bigger ones.

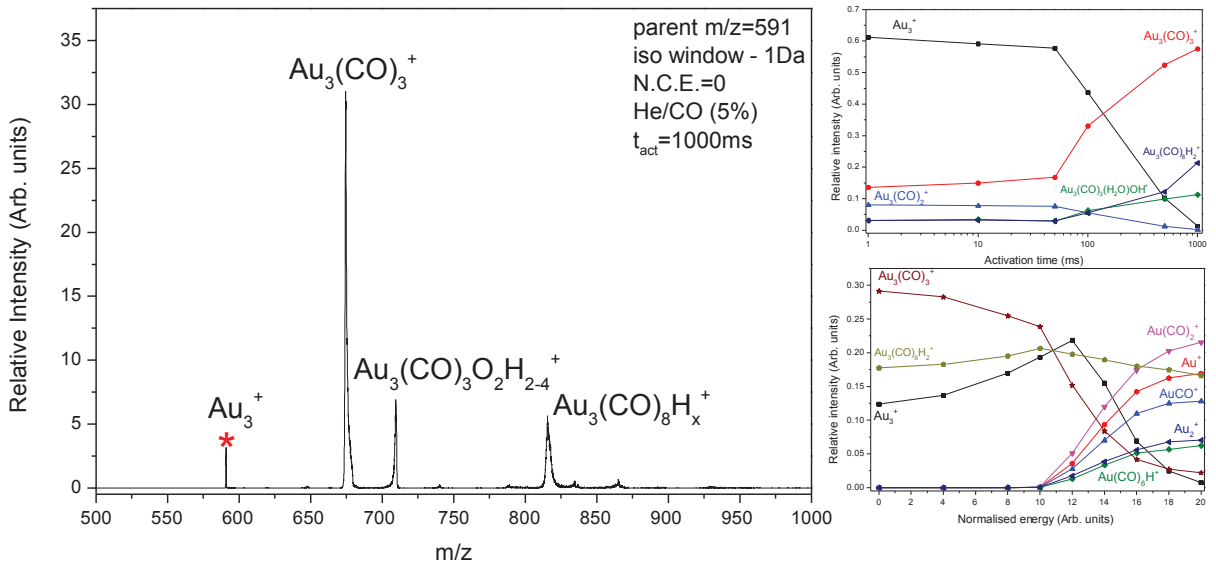

Figure 5. 6 (left)MS² spectrum of the gas phase reaction of Au_3^+ with CO, for two different concentrations of CO. (right - top) Reaction kinetics for the Au_3^+ for 5% He/CO. (right – bottom) Relative intensities as a function of collisional energy for 5% He/CO.

As was already seen in the experiments with low concentration, Au_4^+undergoes dissociation as well as reactions after the CO has been introduced in the trap. For high concentration of CO, in the MS^2 spectrum, we can see the fragment products $Au_3(CO)_3{}^+$ and $Au_3N(CO)_3{}^+$, as well as Au_4CO^+, $Au_4(CO)_3{}^+$, $Au_4(CO)_4{}^+$and $Au_4(CO)_5{}^+$ (Figure 5. 7). The existence of smaller species in the spectrum in absence of collisional activation indicates that, the Au_4^+ becomes unstable in the presence of CO. This results in formation of the products of $Au_3(CO)_n{}^+$. Comparison of the Figure 5. 6 and Figure 5. 7 shows that the $Au_3(CO)_n{}^+$ are analogous to the ones obtained in reactions of Au_3^+, for both high and low concentration CO. This could indicate that Au_4^+ fragments by loss of neutral gold atom, and the products are formed through successive adsorption of CO after the fragmentation.

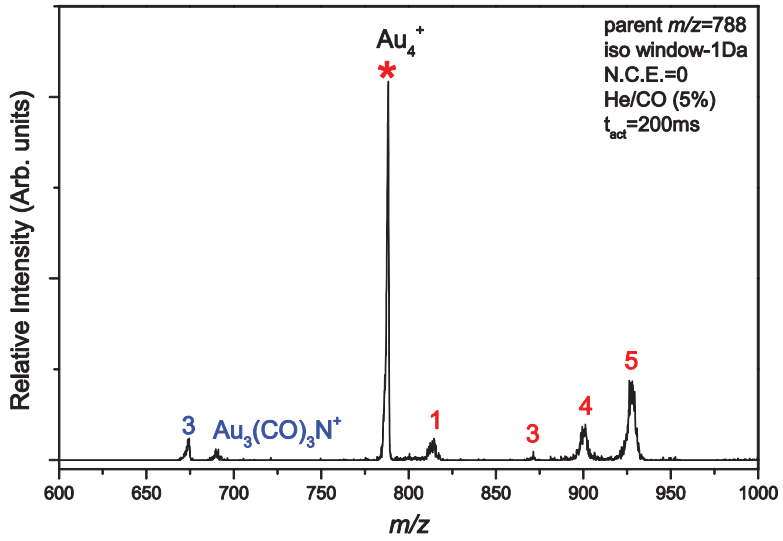

Figure 5. 7 (left) MS^2 spectrum of m/z 788 which corresponds to Au_4^+ (marked with a red star) for two different concentrations of He/CO. The red numbers correspond to complexes $Au_4(CO)_n^+$, and the blue numbers correspond to complexes $Au_3(CO)_n^+$.

As already seen in experiments with low CO concentration, platinum shows many similar properties to gold. This is confirmed in studying the reactions with CO. Platinum clusters show very high reactivity with CO (Figure 5. 8). The saturation rates of platinum clusters observed in our experiment exceed those previously reported in flow reactor conditions[5]. Except in the case of dimer, platinum clusters do not show dissociation in high concentration CO. Their reactivity is higher than those of gold and silver clusters, as is typical for the nickel-group metals[5]. For platinum, higher number of added CO molecules are observed, and with shorter isolation times than those applied for gold and silver.

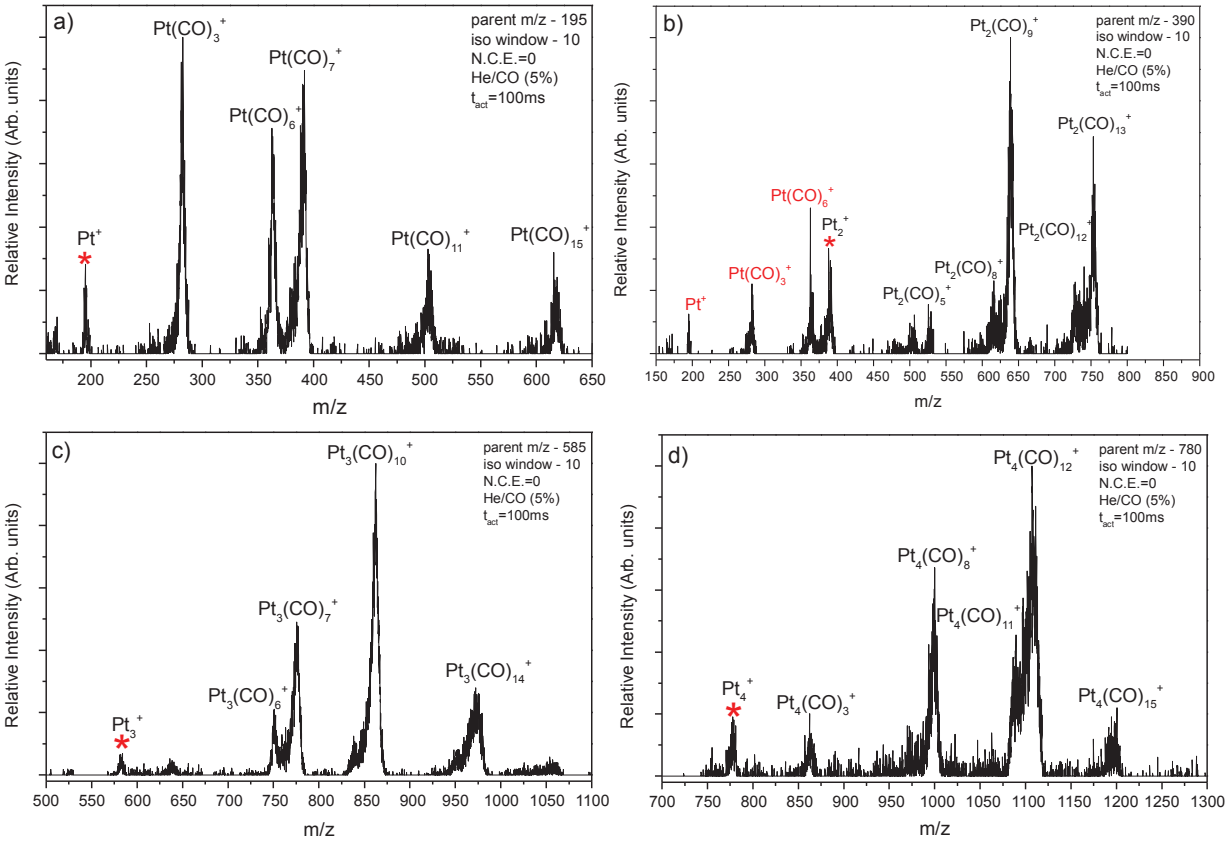

Figure 5. 8 Reaction with high concentration CO for a) Pt^+, b) Pt_2^+, c) Pt_3^+ and d) Pt_4^+. The red star marks the parent ion. Formulas in black correspond to the assignment of adjacent peaks.

In silver monomer reactions we see a similar effect as with gold. The products of reactions with high CO concentration are $Ag(CO)_nH_m^+$complexes. As already seen in experiments with low CO concentration, the complexes with silver show tendency to react with the background fragments in the trap. In Figure 5. 9 we again see the effect of addition of even number of hydrogen atoms to the metal-CO complex, an effect not seen in experiments with low CO concentration. The exact number can only be determined for the $Ag(CO)_5H_{2,4}^+$, but comparison with simulated mass spectrum of other species confirms they contain an even number of hydrogen atoms. Also an interesting feature is the apparent symmetry of the peaks observed in the mass spectrum, where, for the first group, the first peak is the most intense one, and for the second group, the highest *m/z* peak is the most intense one. This could point to the stability and the intermediate nature of some of the species, where, $Ag(CO)_5H_{2,4}^+$ could be more stable species, and species with additional CO molecules are less stable, so they fragment, while the high intensity of $Ag(CO)_{12}H_n^+$ could point to affinity of the silver monomer for high CO saturation levels in these conditions.

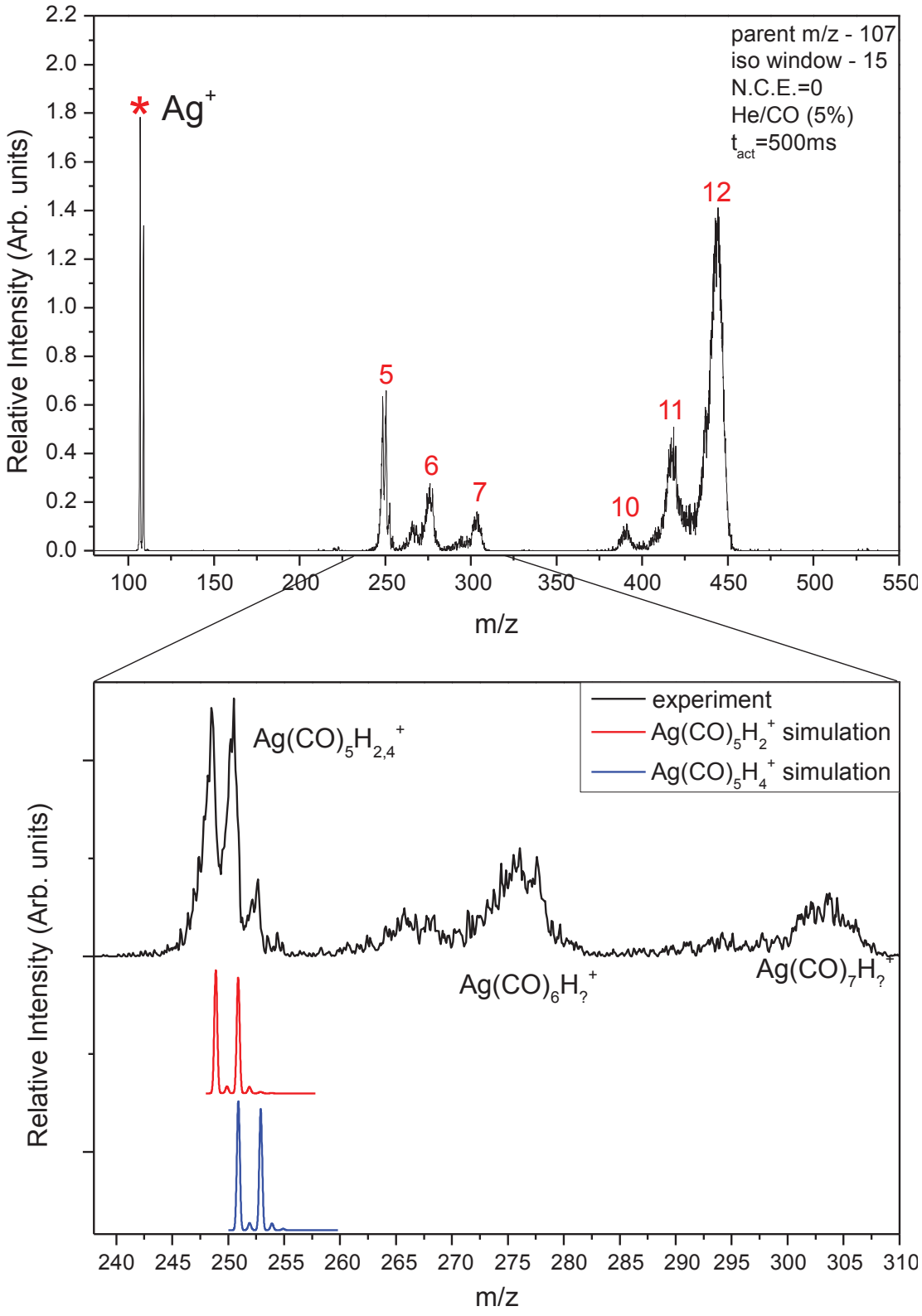

Figure 5. 9 Mass spectra of silver monomer reactions with CO. The red number above the peaks mark the number of CO molecules adsorbed to the cluster. The exact number of hydrogen atoms can only be resolved for the $Ag(CO)_5H^+_{2,4}$.

5.1.3 Hydrogen stabilised metallic dimers

5.1.3.1 Gold and platinum dimer reactivity

Gold dimer and Au_2H^+ are good example of reactivity modified by hydrogen adsorption. By doing tandem MS on both species with narrow mass selection window ($\Delta m \leq 1Da$), we were able to distinguish the reactivity of both species. Both species are stable in the presence of pure buffer gas. The mass spectrum shows no bonding of water molecules or oxidation. After introducing the CO in the trap, the gold dimer becomes unstable and dissociates, at the same time reacting with the CO (Figure 5. 10). The products observed are $Au(CO)^+$, $Au(CO)_2{}^+$ and $Au(CO)_6{}^+$. Some $Au_2(CO)_6{}^+$ is also formed, as well as some Au_2N^+. The $Au_mN_n^+$ complexes are not uncommon, and can be seen in the LAVESI mass spectrum of gold, prior to the introduction of CO, as they are formed in the source part of mass spectrometer. The reaction kinetics show the $Au(CO)^+$ is formed on a time scale faster than 0.1ms. The onset of $Au(CO)_2{}^+$ comes after 10 ms (Figure 5. 10 – right) trapping time, and its increase is followed by the decrease in abundance of $Au(CO)^+$ indicating that the bigger complex is formed from the smaller one by addition of a CO molecule. The complexes with more CO, $Au(CO)_6{}^+$ and $Au_2(CO)_6{}^+$ remain of low intensity even with longer trapping times, and only show slight rising trends. Unlike Au_2^+, the Au_2H^+ doesn't dissociate in the presence of CO in the trap. New species are formed by addition of CO on the precursor complex. They correspond to the generic formula, $Au_2H(CO)_n{}^+$, where $n = 1, 2, 6, 7$ (Figure 5. 11). The hydrogen atom seems to stabilize the complex and prevent dissociation. Furthermore, this species shows lower reactivity than Au_2^+. Figure 5. 11 shows that it takes trapping times of more than 50ms to observe some increase in abundance of the complexes with adsorbed CO and relative intensity of the products remains low even for trapping times longer than 1s.

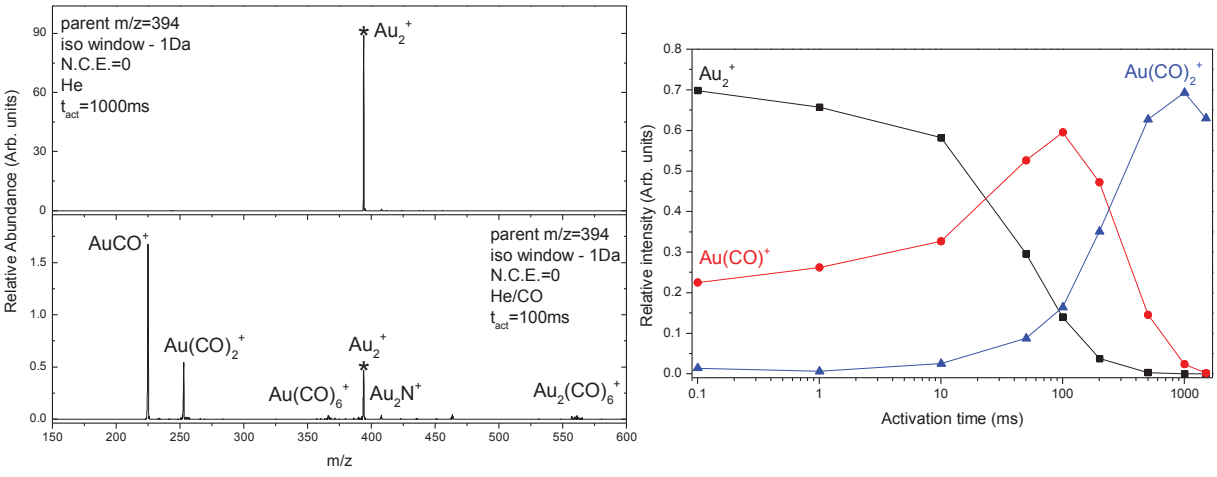

Figure 5. 10 Gas phase reactivity of gold dimer. (left) Mass spectrum of isolated gold dimer in pure He (top) and in He/CO mixture (bottom). The star symbol marks the precursor ion. (right) Reaction kinetics for 5% He/CO.

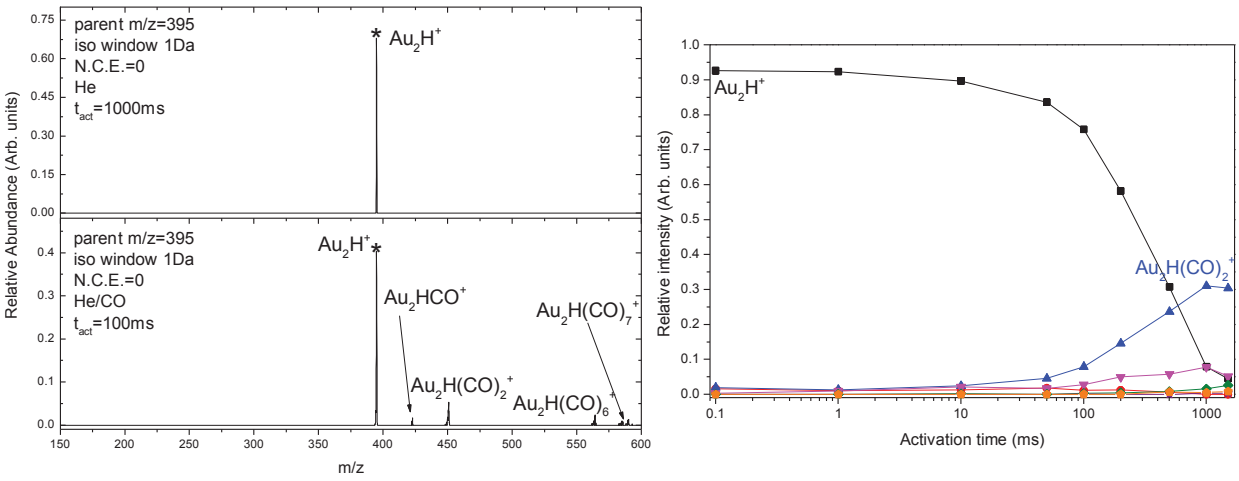

Figure 5. 11 Gas phase reactivity of Au_2H^+. (left) Mass spectrum of isolated gold dimer in pure He (top) and in He/CO mixture (bottom). The star symbol marks the precursor ion. (right) Reaction kinetics for 5% He/CO.

Platinum species show behaviour analogous to gold. In this case though, it is more difficult to distinguish the Pt_2^+ and Pt_2H^+ species because of rich isotopic distribution of platinum. This makes isolating a single peak corresponding to just one species difficult. Both species, Pt_2^+ and Pt_2H^+ are present in the mass spectrum with pure helium. When CO is introduced, we observe some new peaks. In this case, a precursor ion at *m/z* 390 is selected, encompassing both ions. There are two groups of new peaks emerging, both for experiments with low and high CO concentration. First one is the species formed by addition of CO to platinum monomer. We are able to identify these partially by their isotopic distribution, and partially by comparison with Pt^+ spectrum (Figure 5. 8). The other group is the addition of CO molecules onto the Pt_2^+. In experiments with high CO concentration, addition of up to 13 molecules of CO to Pt_2^+ is observed.

5.1.3.3 Ag_2^+ and Ag_2H^+ reactivity

Similar to platinum, the MS studies of silver clusters are made more difficult by the fact that silver in not a monoisotopic element. Still, since it has only two stable isotopes in approximately same abundances, and separated by 2 Da, it is not very difficult to identify and isolate separately $Ag_2^+$and Ag_2H^+. In figure Figure 5. 12 it is shown that both species are formed in the LAVESI source and exist in the mass spectrum prior to introducing the CO. In these conditions both ions are stable and inert, and no reactions of background fragments can be seen in the mass spectrum. Figure 5. 13a shows how, in the presence of CO Ag_2^+ dissociates to form Ag^+. It also forms a hydroxide complex Ag_2OH^+. The Ag_2H^+ is more stable, it doesn't go through dissociation, and in reactions with CO, it adsorbs more molecules than Ag_2^+ (Figure 5. 13b). Mass spectrum of Ag_2^+ shows many intermediate species which would mean that either the bigger complexes are less stable, so they fragment to smaller ones, or that the timescale for saturation of the complex with CO is longer, so the intermediate species are not yet depleted.

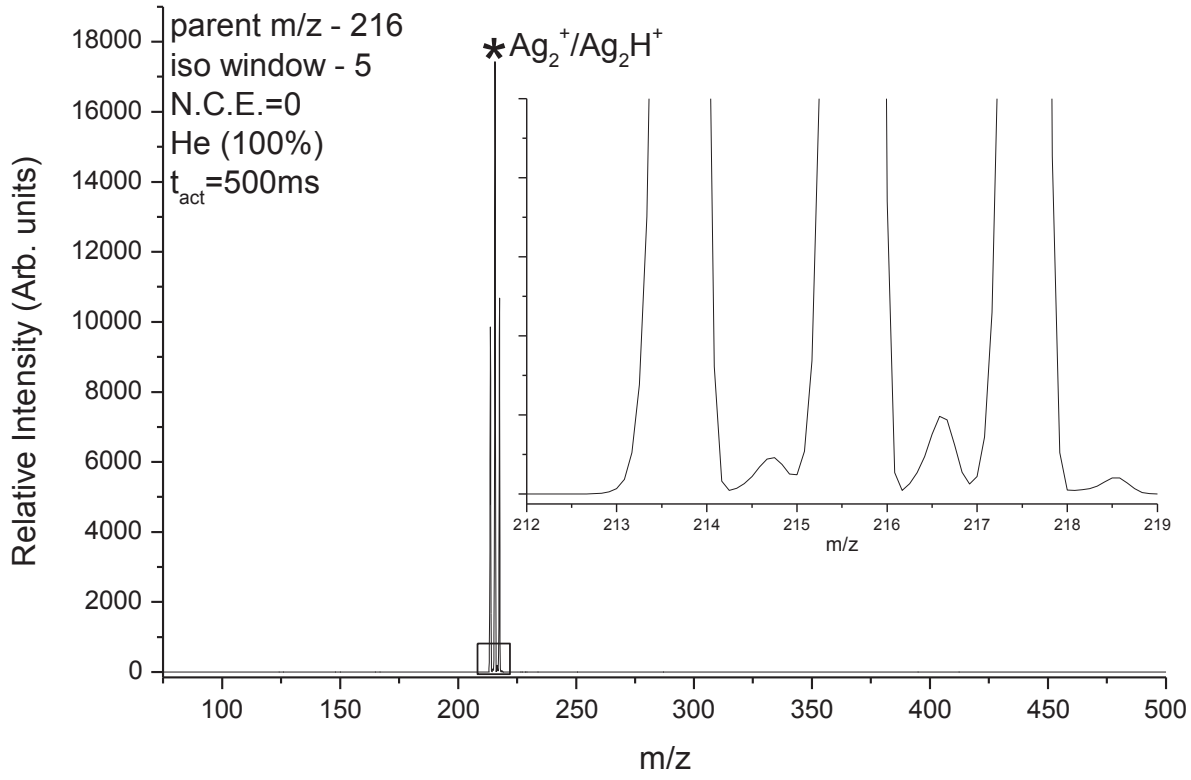

Figure 5. 12 Mass spectrum of Ag_2^+ and Ag_2H^+ in pure helium. Inset shows enlarged area in the rectangle. The peaks in between the Ag_2^+ correspond to Ag_2H^+.

5.1.3.4 Pd_2^+ and Pd_2H^+ reactivity

Palladium dimer behaves similar to silver. Despite the large number of isotopes of the element, we manage to isolate monoisomer peaks to correctly assign the origins of individual species (Figure 5. 14). In (Figure 5. 14 – bottom panel) we can see the effects of CO on Pd_2^+ and Pd_2H^+. Once again, the species without hydrogen dissociates, analogous with silver, except for Pd^+ we do not see any $Pd(CO)_n^+$ species. Instead $Pd_2(CO)_2^+$, $Pd_2(CO)_3^+$ and $Pd_2(CO)_4^+$ are observed. His neighbour, the Pd_2H^+ also reacts, and the products of these reactions are $Pd_2H(CO)^+$, $Pd_2H(CO)_2^+$ and $Pd_2H(CO)_4^+$. The intensity of the reaction products in this case is very low. Unlike for the other metals mentioned above, the results shown in Figure 5. 14 were obtained in low CO concentration conditions. The reason for this is that due to the complex isotopic structure of palladium, the degradation of resolution in the high CO concentration has made it impossible to confidently separate the effects of the Pd_2^+ and Pd_2H^+.

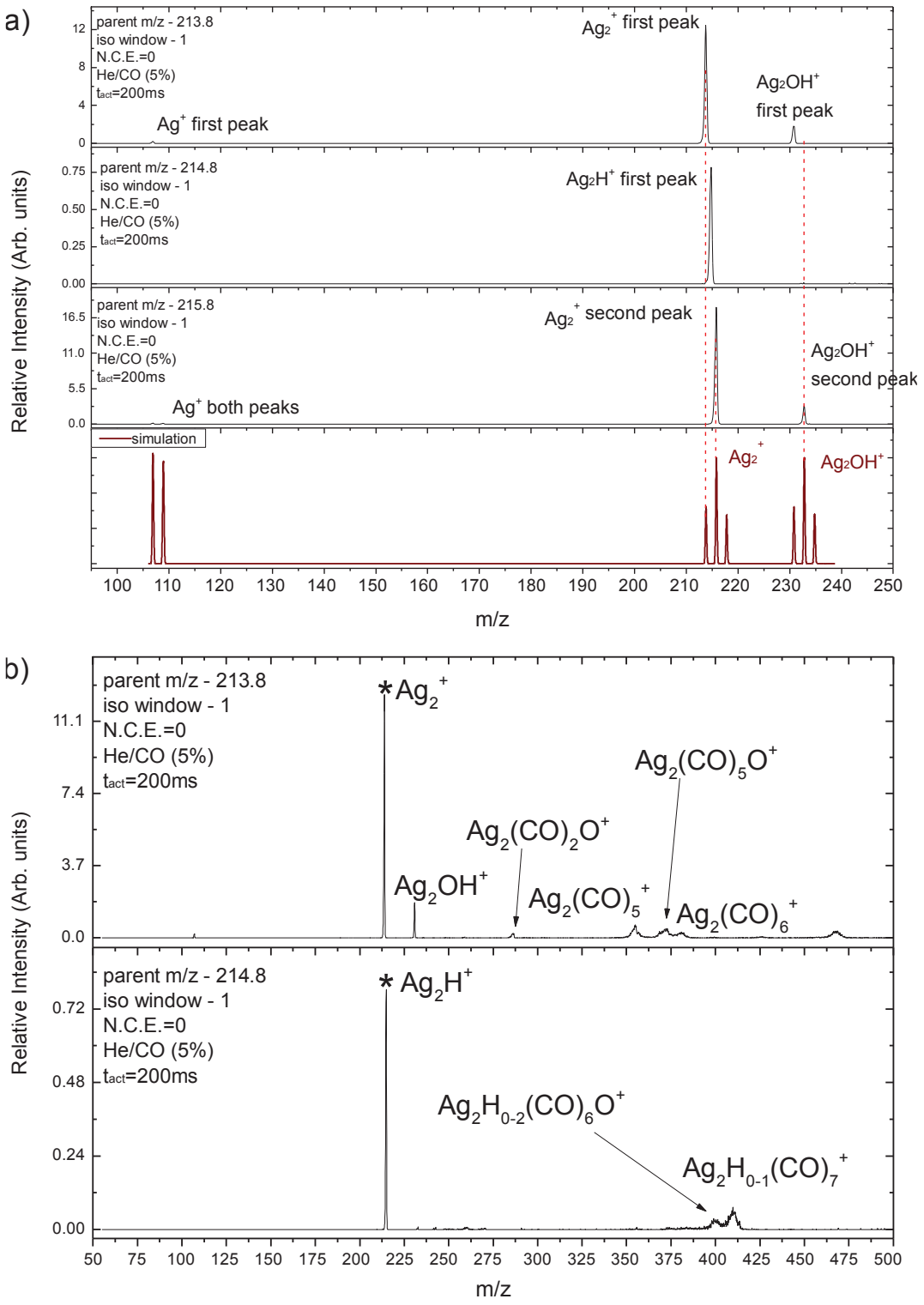

Figure 5. 13 Gas phase reactivity comparison of Ag_2^+ and Ag_2H^+. a) Isotopic MS^2 of selected peaks of both species and comparison with simulated mass spectrum. b) Mass spectra of reactions of each of the species with CO.

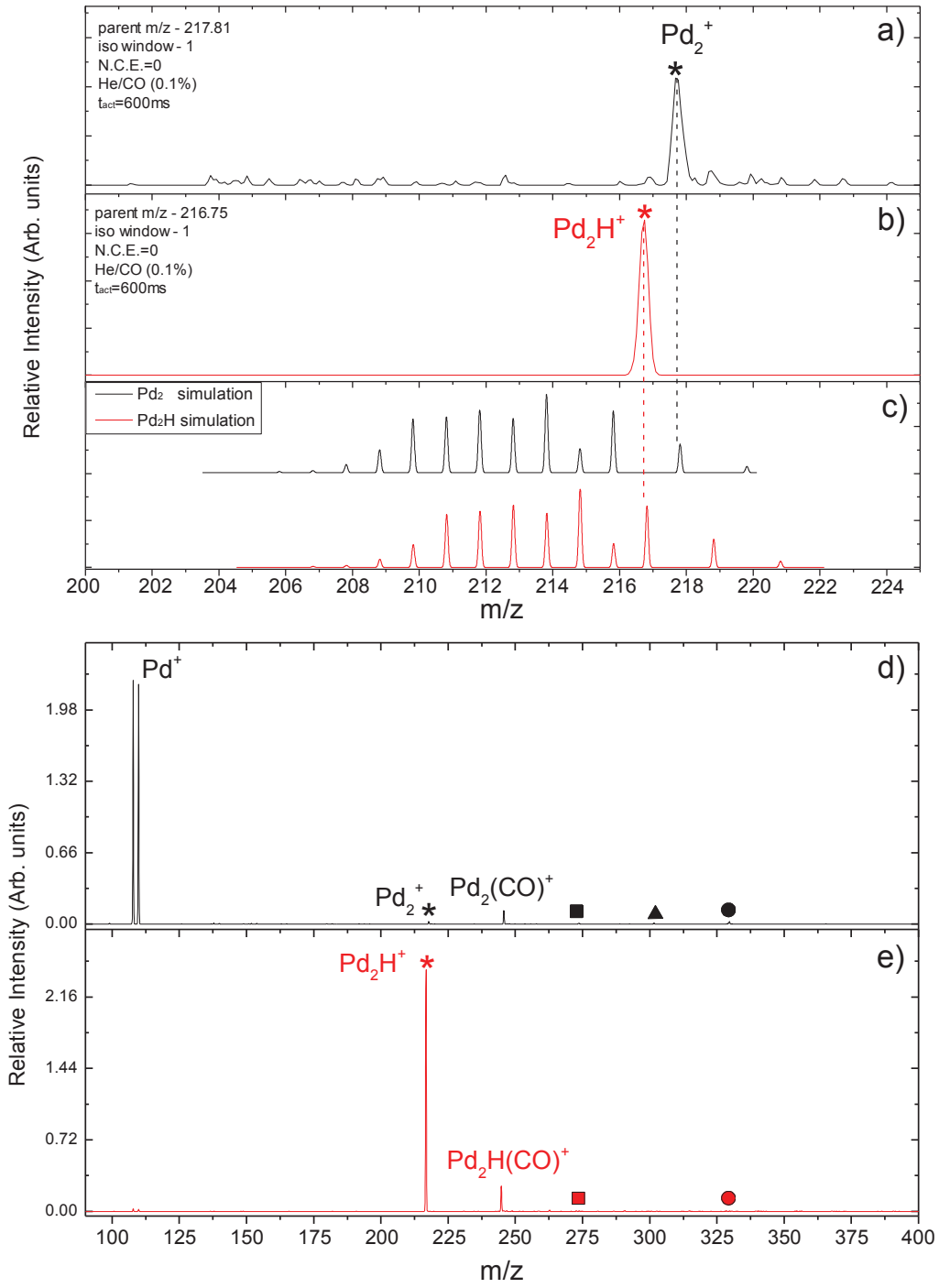

Figure 5. 14 Reactions spectra of palladium dimer. a) and b) monoisotopic peaks of Pd_2^+ and Pd_2H^+ respectively and c) comparison with simulated mass spectrum. d) mass spectrum of reactions of Pd_2^+ with CO. The black square, triangle and circle represent $Pd_2(CO)_2^+$, $Pd_2(CO)_3^+$ and $Pd_2(CO)_4^+$ respectively. e) mass spectrum of reactions of Pd_2H^+ with CO. The red square and circle represent $Pd_2H(CO)_2^+$ and $Pd_2H(CO)_4^+$ respectively. The experimental conditions of d) and e) are the same as a) and b).

5.2 Theory

In order to better understand the nature of the complexes and the processes behind their behaviour, DFT calculation were done on the system. The calculations were done by Dr. Pierre Mignon from the Theoretical physical chemistry team headed by Dr. Abdul Rahman Allouche, at Institut Lumière Matière in Lyon.

5.2.1 Au^+ structures and reactions

The calculations were done on Au^+ in order to explain the addition of hydrogen on $Au(CO)_n^+$ complexes, as seen for example in $Au(CO)_3H_{2/4/6}^+$ species (Figure 5. 5). Initial calculations are done on $Au(CO)_n^+$ for $n \leq 8$ to determine the geometries of the complexes and after that the positions and role of hydrogen are examined. The functionals used were B3LYP and RI-B2P LYP with a basis set def2-TZVPP for hydrogen and CO and def2-ECP-TZVVP for gold atoms. The results show that the first 4 CO molecules are bound strongly to the gold, and after that the bonding becomes weaker. Figure 5. 15 (top) shows how, with the addition of 5th CO, the initially tightly bound structure rearranges itself as $[Au(CO)_3(CO)_2]^+$ where 3 of the COs are bound strongly to the gold with bond lengths ~2.1Å, while the remaining two CO molecules bind loosely with ~3.3Å bond lengths. Examining all of the calculated structures for $Au(CO)_n^+$ we can see that the complexes for $n > 4$ can be described as $Au(CO)_2^+$ and $Au(CO)_3^+$ with certain number of loosely bond CO molecules on them. The very low energy differences between the structures for $n > 2$ tell us that the structure rearrangement seen for $n > 4$ are entirely possible and easily done from the energetic point of view. The fact that the addition of CO is energetically favourable does not explain the observed species in the mass spectrum in Figure 5. 5.

The hydrogens bond to the complex as radical, not as H_2 molecules. The exact mechanism of this bonding remains, because of time constraints, unknown, but some indications of a chemical reaction process exist. The calculations done on $Au(CO)_2H_2^+$ show hydrogen atom can coordinate to gold. The addition of next CO molecule then is not on the gold but on the hydrogen. The complex undergoes the rearrangement again, releasing the COH_2 in the process and regenerating $Au(CO)_2^+$ from the start of the cycle. The formation of the observed $Au(CO)_3H_6^+$ would come from a gold atom coordinated by three of the COH_2 groups produced in this cycle (Figure 5. 16).

N(CO)	complex structure	energy
3	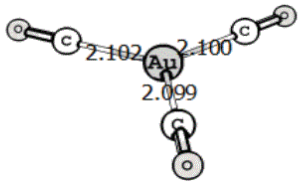	-4.310 eV
4	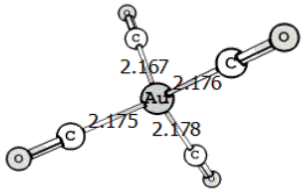	-4.424 eV
5	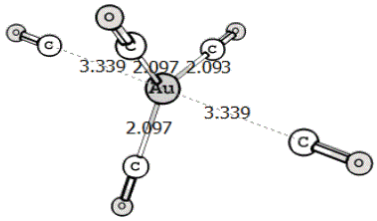	-4.546 eV

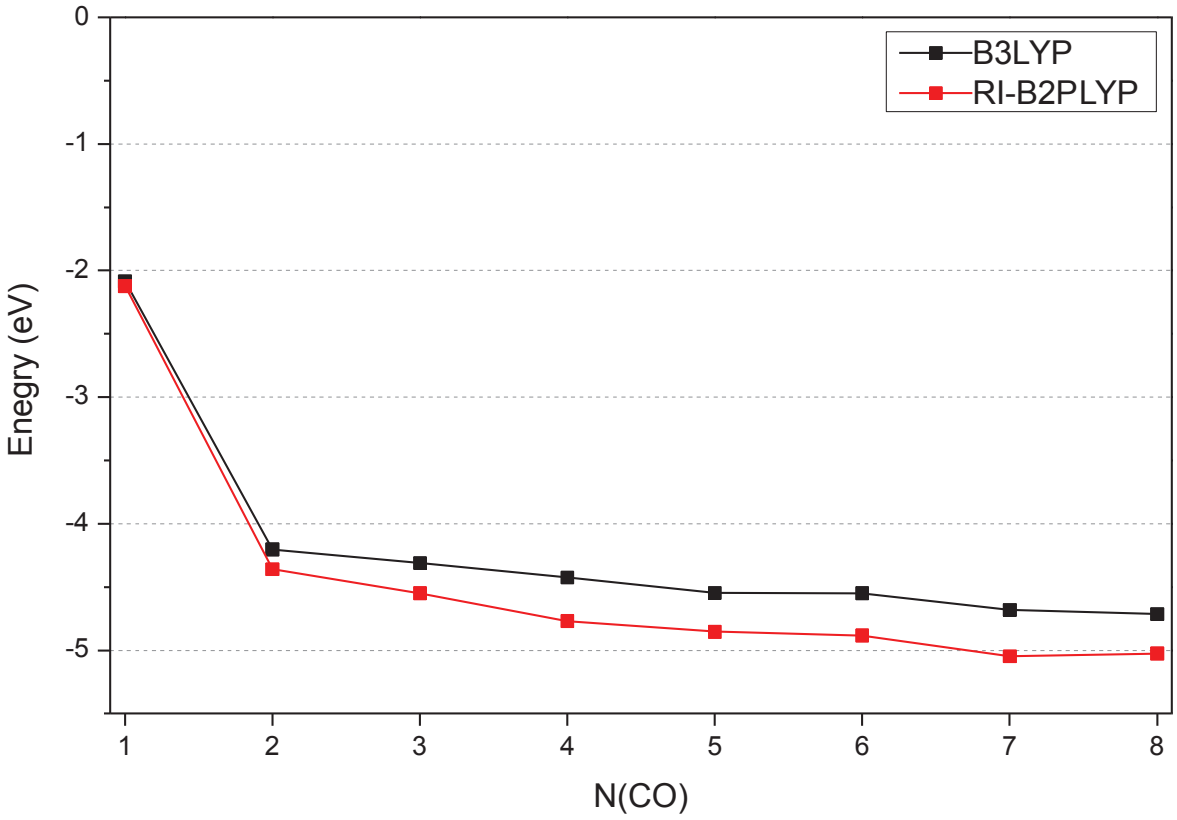

Figure 5. 15 (top) DFT structures of $Au(CO)_3^+$, $Au(CO)_4^+$ and $Au(CO)_5^+$. (bottom) Lowest energies of structures as a function of number of CO in the complex, for two different functionals.

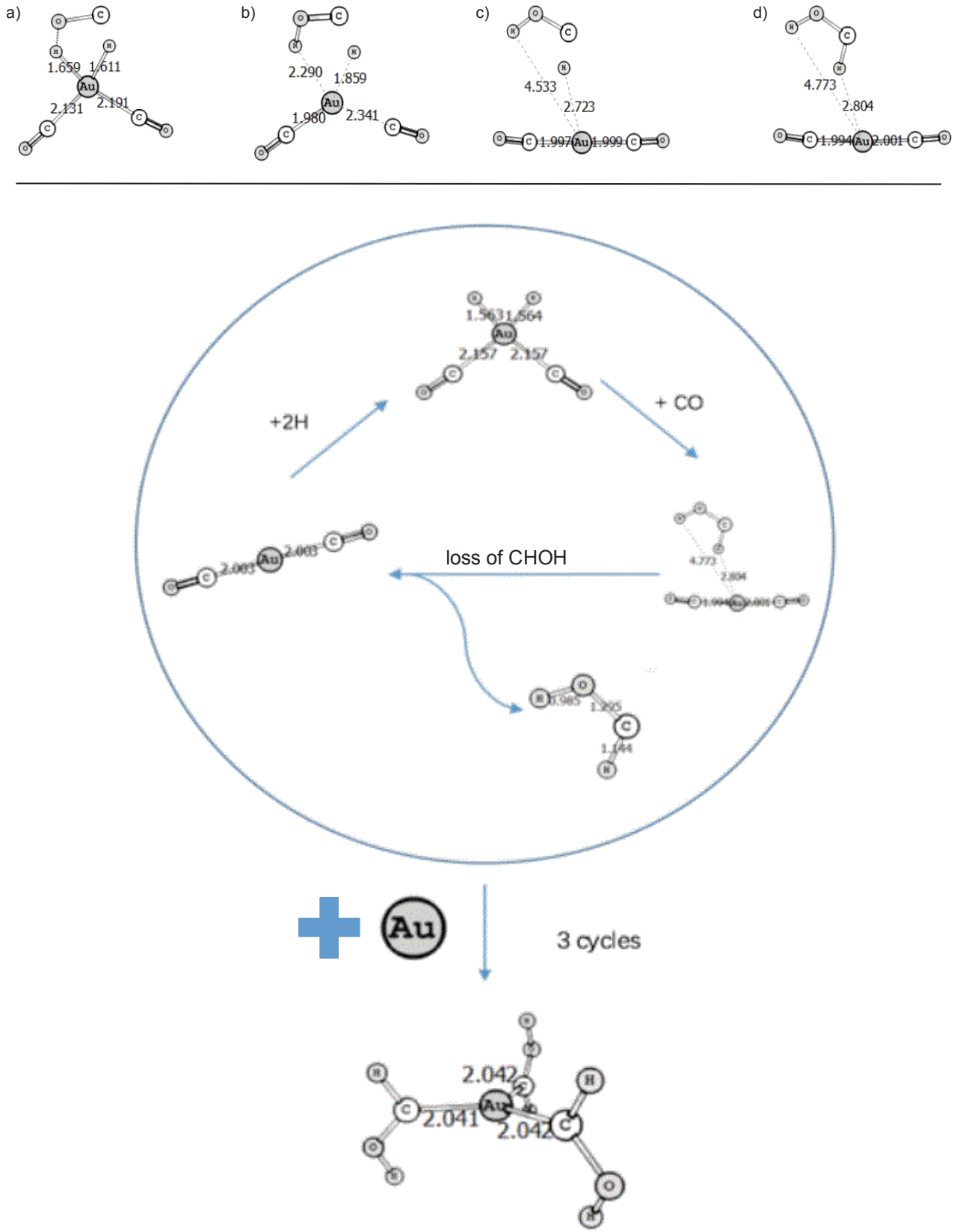

Figure 5. 16 The chemical cycle of forming $Au(CO)_3H_6^+$. (top) a)-d) the stages in the production oh CHOH group on $Au(CO)_2^+$. (bottom) the CHOH groups from 3 cycles combine with a gold atom to produce $Au(CO)_3H_6^+$.

5.2.2 Au_2^+ and Au_2H^+ structures and reactions

The DFT calculations were done on Au_2^+ and Au_2H^+ using a B2PLYP functional with a def2-TZVPP basis set. The results show that addition of a CO molecule increases the Au-Au distance (Figure 5. 17). This effect increases drastically for 1-3 CO molecules, and with addition of subsequent CO the distance varies a little, but remains around 0.5A longer than for Au_2^+, which favours the dissociation of Au_2^+. For both species, 4th CO coordinated to the complex seems to be only loosely bound. From the energetical point of view, the addition of CO molecules to the Au_2^+ is favourable. The dissociation of the complex after the adsorption of second CO is easier than the release of CO. The effect of the Au-Au bond elongation is not observed in the calculation results of Au_2H^+. The additional hydrogen atom prevents the Au-Au bond elongation, preserving the system. The hydrogen in this complex carries negative charge and the whole positive charge comes from gold atoms. It stabilises the complex by keeping the two gold atoms close. The energy diagram for adsorption of CO to Au_2H^+ shows the dissociation of $Au_2H(CO)_{1,2}^+$ to be an unfavourable, energetically forbidden process, and coordination of additional CO is easier. For the subsequent species with higher numbers of CO, the energy level of the dissociated species is always harder than the addition of new CO (Figure 5. 18).

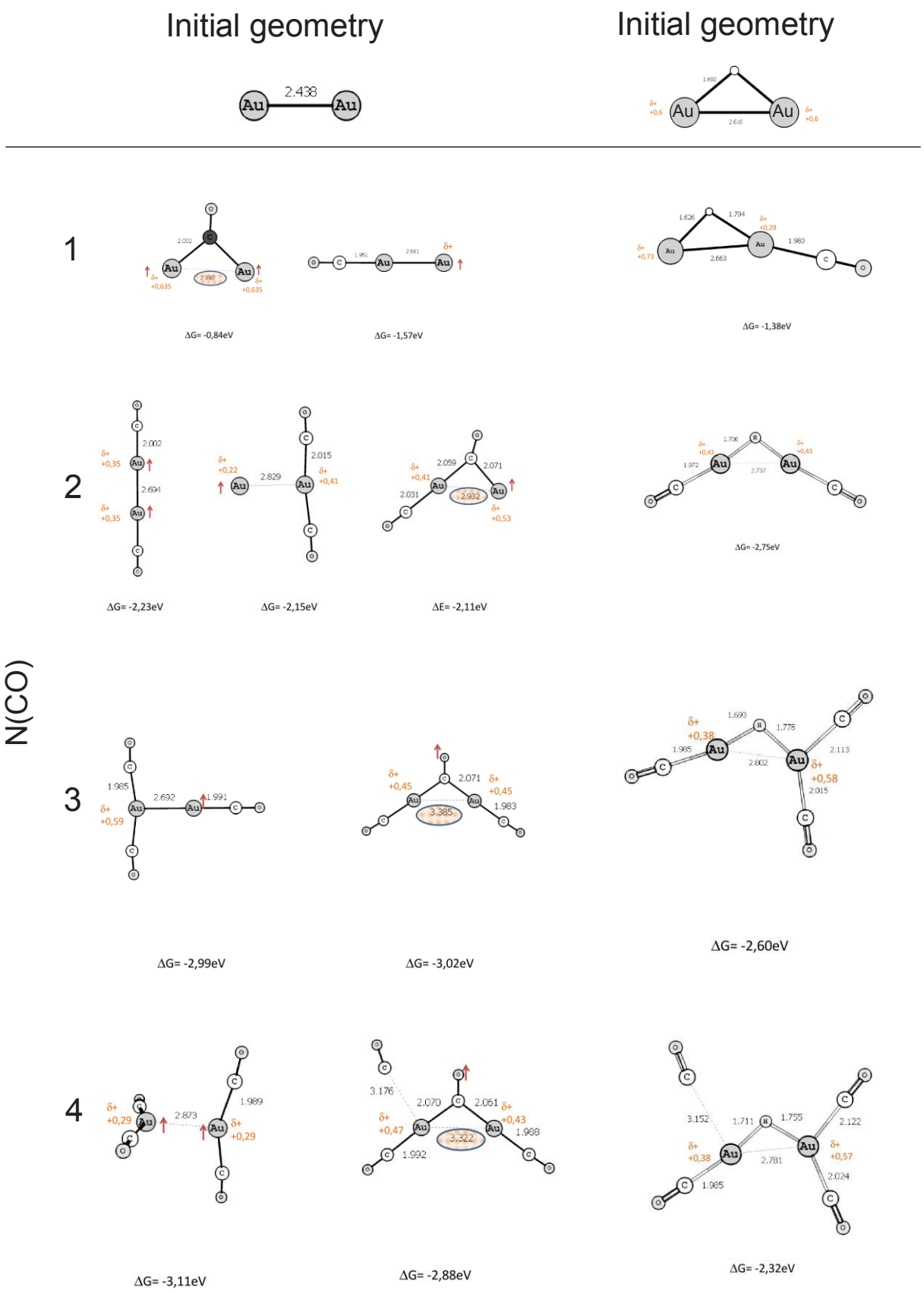

Figure 5. 17 DFT structures of 1-4 molecules of CO coordinated to Au_2^+ and Au_2H^+. For Au_2^+, the lowest energy structure and the structure with the biggest Au-Au distance is shown. The numbers in black mark the atomic distances in Å, and the orange numbers represent charge distribution.

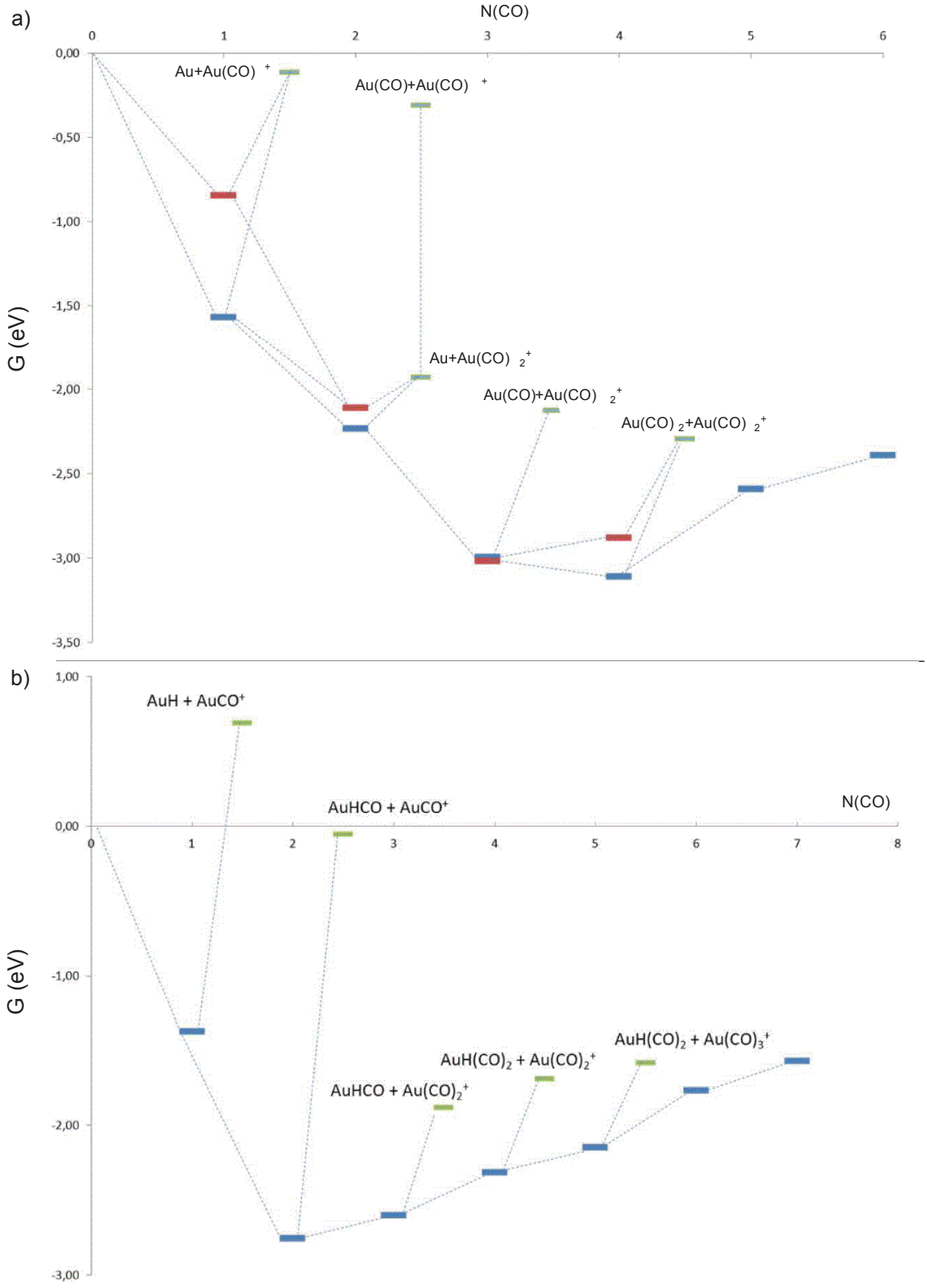

Figure 5. 18 Energy diagrams of a) $Au_2(CO)_n^+$ and b) $Au_2H(CO)_n^+$. The blue and red marks in a) represent the lowest energy structure and the structure with the greatest Au-Au distance. The green marks are the dissociated species. The formulas correspond to the dissociation products represented by the adjacent plot point.

5.3 Conclusions

The reactions with CO were done on gold, silver and platinum cation clusters. Two different concentrations of CO were used to investigate the influence on the reactivity of clusters. At low concentration CO (0.1% of the buffer gas pressure), the ion trap conditions are kept close to nominal, so the degradation of resolution is negligible. The adsorption of CO on the metal clusters is observed. In these conditions, the saturation rates of small gold and platinum clusters match those found in previous studies. Also, intermediate species can be seen in these conditions, in especially by tuning the trapping time. The products observed are the pure CO adsorption on the metal cluster in the case of gold and silver. Some residual water and OH bonding can be seen for silver cations. Reactions with palladium were not carried out with low concentration CO. In high concentration CO (5% of the buffer gas pressure), the amount of CO in the trap is high enough to cause some degradation of resolution. Additionally, the products observed are no longer the result of pure CO adsorption. The bonding of even number of hydrogen atoms is observed for gold and silver species. For platinum, due to the large number of isotopes and loss of resolution it is impossible to determine the exact numbers of hydrogen adducts. The DFT calculations carried out on the gold monomer suggest that the hydrogen is not molecular, but rather pairs of dissociated hydrogen. Due to high saturation with the reactant gas in the trap, many intermediate species cannot be detected in these conditions even with short reaction times. Also, we observe higher saturation rates of adsorption on the metal clusters, not previously reported.

For the dimers of gold, silver, platinum and palladium, and their neighbouring species, the M_2H^+, experiments and theoretical calculations show that the adsorption of the hydrogen on the metal dimer helps stabilise the complex. Platinum behaves in the same manner as gold, where the dimer dissociates easily and $M(CO)_n^+$ products are observed while the M_2H^+ doesn't dissociate and proceeds with CO adsorption. Palladium and silver show less dissociation and both species can adsorb a number of CO molecules. For the DFT study, Au_2^+ and Au_2H^+ were chosen for calculation. The analysis of the lowest energy structures for a number of coordinated CO molecules on the complex shows that without the hydrogen, dissociation of the complex becomes favourable after coordination of 2nd CO. The presence of the hydrogen atom makes the adsorption of CO energetically favourable. Dissociation in this case is forbidden for the first two coordinated CO molecules, and less likely for the subsequent ones. Metallic shell closings can be considered as a reason for the different reactivity and stability of these complexes, for the copper group metals. Both silver and gold have the same number of electrons in their final shell. The M_2^+ is an open shell system with only a single electron in the outer shell, while M_2H^+ is a closed shell. This gives it additional stability, as well as lower reactivity observed in reaction kinetics diagrams.

The Au_2H^+ complex is a closed shell system as compared to the gold cation dimer. In the most stable conformation gold atoms are bridged by a hydrogen atom. This means that each gold is involved in a covalent bonding with the other gold atom and with the hydrogen. A small amount of negative charge

is present on the H (-0.16 a.u.) while the gold are both positively charged (+0.58 a.u.). The hydrogen atom does act as a proton but accepts electron density from the gold dimer by forming covalent bonds with them and thus stabilizing the system. CO coordination to this complex allows a gain in free energy until the second CO coordination. Dissociation of these complexes in $AuH+AuCO^+$ or $AuHCO+AuCO^+$ would cost a significant amount of free energy from Au_2HCO^+ and $Au_2H(CO)_2^+$, respectively. As such these dissociation process are clearly unfavorable. From a free energy point of view, further CO coordination are comparable to this one. It has to be noticed that a fourth CO coordination to the $Au_2H(CO)_3^+$ complex spontaneously leads to a de-coordination of an initially bonded CO, thus leading to the same covalently bonded $Au_2H(CO)_3^+$ system. For each $Au_2H(CO)n^+$ complex with n=3,4,5 the dissociation of Au_2H is always the most unfavorable pathway.

Bibliography

1. Corti, C. W., Holliday, R. J. & Thompson, D. T. Commercial aspects of gold catalysis. *Appl. Catal. A Gen.* **291,** 253–261 (2005).

2. Yamamoto, S. Y., Surko, C. M., Maple, M. B. & Pina, R. K. Spatio-temporal dynamics of oscillatory heterogeneous catalysis: CO oxidation on platinum. *J. Chem. Phys.* **102,** 8614 (1995).

3. Ehsasi, M., Berdau, M., Karpowicz, A., Christmann, K. & Block, J. H. in 321–332 (1993). doi:10.1016/S0167-2991(08)64020-3

4. Guo, Z. *et al.* Recent advances in heterogeneous selective oxidation catalysis for sustainable chemistry. *Chem. Soc. Rev.* **43,** 3480–524 (2014).

5. Ervin, K. M. *Metal-ligand interactions: Gas-phase transition metal cluster carbonyls*. *International Reviews in Physical Chemistry* **20,** (2001).

6. Bernhardt, T. M. Gas-phase kinetics and catalytic reactions of small silver and gold clusters. *Int. J. Mass Spectrom.* **243,** 1–29 (2005).

7. Wu, X., Senapati, L., Nayak, S. K., Selloni, A. & Hajaligol, M. A density functional study of carbon monoxide adsorption on small cationic, neutral, and anionic gold clusters. *J. Chem. Phys.* **117,** 4010 (2002).

8. Lee, T. H. & Ervin, K. M. Reactions of Copper Group Cluster Anions with Oxygen and Carbon Monoxide. *J. Phys. Chem.* **98,** 10023–10031 (1994).

9. Hagen, J. *et al.* Coadsorption of CO and O2 on small free gold cluster anions at cryogenic temperatures: Model complexes for catalytic CO oxidation. *Phys. Chem. Chem. Phys.* **4,** 1707–1709 (2002).

10. Wallace, W. T. & Whetten, R. L. Carbon Monoxide Adsorption on Selected Gold Clusters: Highly Size-Dependent Activity and Saturation Compositions. *J. Phys. Chem. B* **104,** 10964–10968 (2000).

11. Balteanu, I. *et al.* Very low rate constants of bimolecular CO adsorption on anionic gold clusters: Implications for catalytic activity. *Phys. Chem. Chem. Phys.* **5,** 1213–1218 (2003).

12. Hagen, J., Socaciu, L. D., Heiz, U., Bernhardt, T. M. & Woste, L. Size dependent reaction kinetics of small gold clusters with carbon monoxide: Influence of internal degrees of freedom and carbonyl complex stability. *Eur. Phys. J. D - At. Mol. Opt. Phys.* **24,** 327–330 (2003).

13. Lüttgens, G., Pontius, N., Bechthold, P. S., Neeb, M. & Eberhardt, W. Photon-Induced Thermal Desorption of CO from Small Metal-Carbonyl Clusters. *Phys. Rev. Lett.* **88,** 076102 (2002).

14. Johnson, G. E., Reilly, N. M., Tyo, E. C. & Castleman, A. W. Gas-Phase Reactivity of Gold Oxide Cluster Cations with CO. *J. Phys. Chem. C* **112,** 9730–9736 (2008).

15. Kimble, M. L. & Castleman, A. W. Gas-phase studies of AunOm+ interacting with carbon monoxide. *Int. J. Mass Spectrom.* **233,** 99–101 (2004).

16. Bürgel, C. *et al.* Influence of Charge State on the Mechanism of CO Oxidation on Gold Clusters. *J. Am. Chem. Soc.* **130,** 1694–1698 (2008).

17. Popolan, D. M. & Bernhardt, T. M. Communication: CO oxidation by silver and gold cluster cations: Identification of different active oxygen species. *J. Chem. Phys.* **134,** 1–4 (2011).

18. Lang, S. M., Fleischer, I., Bernhardt, T. M., Barnett, R. N. & Landman, U. Low-Temperature CO Oxidation Catalyzed by Free Palladium Clusters: Similarities and Differences to Pd Surfaces and Supported Particles. *ACS Catal.* 2275–2289 (2015).

19. Lang, S. M., Schnabel, T. & Bernhardt, T. M. Reactions of carbon monoxide with free palladium oxide clusters: strongly size dependent competition between adsorption and combustion. *Phys. Chem. Chem. Phys.* **14,** 9364 (2012).

20. Fielicke, A., Gruene, P., Meijer, G. & Rayner, D. M. The adsorption of CO on transition metal clusters: A case study of cluster surface chemistry. *Surf. Sci.* **603,** 1427–1433 (2009).

21. Manzoor, D. & Pal, S. Hydrogen Atom Chemisorbed Gold Clusters as Highly Active Catalysts for Oxygen Activation and CO Oxidation. *J.Phys.Chem. C* **118,** 30067 (2014).

22. Lang, S. M., Bernhardt, T. M., Barnett, R. N., Yoon, B. & Landman, U. Hydrogen-promoted oxygen activation by free gold cluster cations. *J. Am. Chem. Soc.* **131,** 8939–8951 (2009).

23. Zhai, H.-J., Kiran, B. & Wang, L.-S. Observation of Au2H- impurity in pure gold clusters and implications for the anomalous Au-Au distances in gold nanowires. *J. Chem. Phys.* **121,** 8231–6 (2004).

24. Popolan, D. M., Nössler, M., Mitrić, R., Bernhardt, T. M. & Bonacić-Koutecký, V. Tuning cluster reactivity by charge state and composition: experimental and theoretical investigation of CO binding energies to Ag(n)Au(m)(+/-) (n + m = 3). *J. Phys. Chem. A* **115,** 951–959 (2011).

25. Velasquez, J., Njegic, B., Gordon, M. S. & Duncan, M. A. IR photodissociation spectroscopy and theory of Au+(CO) n complexes: Nonclassical carbonyls in the gas phase. *J. Phys. Chem. A* **112,** 1907–1913 (2008).

26. Fielicke, A. *et al.* Gold cluster carbonyls: Saturated adsorption of CO on gold cluster cations, vibrational spectroscopy, and implications for their structures. *J. Am. Chem. Soc.* **127,** 8416–8423 (2005).

6. Conclusion

Due to their remarkable chemical and optical properties metal nanoclusters present a very attractive domain of research. This work describes a development of a new experimental setup for bare and ligated metal cluster synthesis and study of their gas phase reactions. As the bare metallic nanoclusters can be very reactive or unstable, a protective shell of ligand molecules can be formed in order to stabilize the cluster and protect it from reactions with environment, in order to preserve its properties. Our experimental setup is based on coupling the laser vaporization with the electrospray ionization source of a mass spectrometer, and abbreviation LAVESI (Laser Vaporization Electrospray Ionization) is used. The idea is to couple the rich variety of metal species produced by the laser ablation with the ESI ability to ionize any soluble sample in order to produce metal nanoclusters protected by an organic ligand.

In order to validate the new setup, we compare the results obtained with the already known wet chemistry synthesis of ligated metal complexes. The ligated metal complexes are formed in the electrospray plume, when a mixture of metal salt and ligand solution is electrosprayed. This synthesis produces a variety of small stoichiometric species (singly and doubly charged), with silver and with gold salts and thioglycolic acid, a small thiol molecule, used as a ligand. This is useful especially in context of comparison with the same species produced by other types of synthesis.

The results of LAVESI source with gold, silver and copper rods and thioglycolic acid show the formation of metal-ligand complexes. The comparison with wet chemistry synthesis reveals the utility of the new source as new species are observed, which are not created in solution. In addition, while the attempts at creating ligated metal-thioglycolic acid complexes with copper and gold/silver alloy have so far been unsuccessful, LAVESI source is able to produce an abundance of these species. In experiments when only electrospray voltage is applied and nothing is sprayed, metals react with atmospheric constituents to form diverse species of oxides, hydroxides and nitrides, in both positive and negative modes. Presence of the ligand solution in the ESI plume completely eliminates the oxides, hydroxides and nitrides and shows how the ligated species are formed in the reactions in the droplets and how the ligand protects the metal complexes from oxidation.

Parallel to the development of the new cluster source, mass spectrometry was used to characterize another wet chemistry synthesis. The procedure is based on mixing the ligand and metal salt solution in the presence of reducing agents, and followed by a series of purification steps that results in a remarkably monodisperse solution of glutathione capped gold clusters ($Au_{15}SG_{13}$) which makes them ideal for non-linear optical studies.

Gas phase reactions with CO were done on gold, silver, platinum and palladium cation clusters obtained with LAVESI, with two different concentrations of CO in He buffer gas. CO adsorption reactions are observed, with different saturation limits depending on the concentration. For low CO concentration,

the saturation rates of small gold and platinum clusters match those found in previous studies. Intermediate species are observed as well in these conditions, especially by tuning the trapping time. In high concentration CO, the products observed are no longer the result of pure CO adsorption. The bonding of even number of hydrogen atoms is observed for gold and silver species. The preliminary DFT calculations carried out on the gold monomer suggest that this hydrogen is not molecular, but rather pairs of dissociated hydrogen atoms.

Very interesting results are obtained with dimers of gold, silver, platinum and palladium, and their neighbouring species, the M_2H^+. Experiments and theoretical DFT calculations show that the adsorption of the hydrogen on the metal dimer helps stabilise the complex and protects it from dissociation during reactions with CO. For the DFT study, Au_2^+ and Au_2H^+ were chosen for calculation. The analysis of the lowest energy structures for a number of coordinated CO molecules on the complex shows that without the hydrogen, dissociation of the complex becomes favourable after coordination of 2nd CO. Addition of CO to the complex increases the Au-Au distance, causing the dissociation. The presence of hydrogen atom makes the dissociation a very unfavourable process. Keeping in mind the already known chemical and catalytical activity of gold and platinum nanoclusters, shows the significance of this effect, as the hydrogen preadsorption can protect the catalyst from degradation during reactions. Additionally, platinum dimer behaves in the same manner as gold. Tetramers of gold and platinum show analogous effects as well. For palladium and silver, similar processes are observed, show less dissociation and both dimer and M_2H^+ can adsorb CO molecules.

The results obtained with reactions with CO present just the first step in the ultimate goal of finding new catalytic processes for CO oxidation. This presents perspectives for future work, where either bare or hydrogen protected clusters can be used to aid the oxidation of the adsorbed carbon monoxide. Having demonstrated the viability of the LAVESI source and the ability to produce novel ligated metal complexes, further work can be done with various metal-ligand combinations in order to synthesize new species.

Appendix 1

Non-linear optics

Introduction

The development of pulsed monochromatic maser and laser has made it possible to achieve focused laser beams with very high field intensities. This has made possible the study of second harmonic generation of intense laser beam when traveling through a crystal. This work was pioneered by the group of Peter A. Franken, in 1961[1], just after the discovery of laser. Around the same time the group of W. Kaiser and C. G. B. Garett experimentally demonstrated the multi-photon excitation[2]. It is worth noting that some nonlinear effects were known before that, without the use of a laser, such as the work of Gilbert Lewis in 1941[3] and Sergej Ivanovič Vavilov and W. L. Lewschin during 1920s[4,5]. However, only with the development of the laser did the systematic and detailed studies of these effects took place.

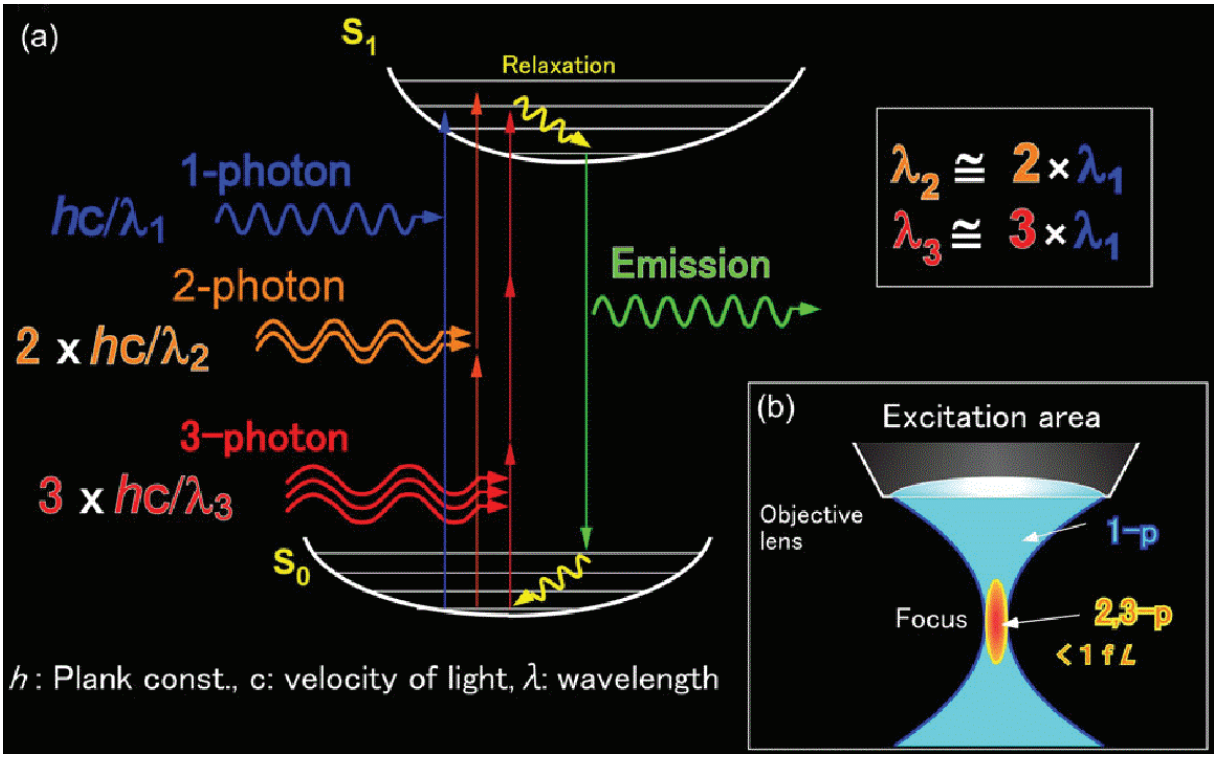

Figure A. 1 a) Schematic of single-photon, two-photon and three-photon excitation. The principle holds for multi-photon processes qs well. b) Fluorescing areas in single- and multi- photon excitation process used in microscopic imaging. Figure reprinted from Nemoto et al., Two-photon excitation fluorescence microscopy and its application in functional connectomics, Microscopy, 2015, 64, 1, 9-15, by permission of Oxford University Press.

Because of the great technological and scientific interest in nanoparticles, they have been the focus of intense research in many fields. Second order polarization (or second harmonic generation – SHG) is very non-centrosymmetrically dependent, that is it cannot be generated by centrosymmetric systems[6]. Many studies have been done in investigation of surfaces and interfaces of media possessing a centre of inversion. This is valid for nanoscale and non-nanoscale systems. In nanoscale systems, especially for

structures made of a few atoms only, the whole structure takes part in second harmonic generation, which has to be taken into account. In these cases, the main signal arises from the whole volume of the particle, so the absolute value of hyperpolarizability per volume $[\beta/V]$ should be used. Non-linear optical effects are, besides particle geometry, sensitive to the particle size as well, so for different systems different effects will occur.

Under proper experimental conditions, the process of SHG can be very efficient, so much so that all of the power of the incident beam is converted to the second harmonic radiation. In a single process two photons of the frequency ω are absorbed, and a photon of a frequency 2ω is created (Figure A. 1). Experimentally, the SHG is measured by a technique called hyper-Rayleigh scattering, first observed by Terhune, Maker and Savage in 1965[7]. For it, typically, a Ti:sapphire laser is used, at 800nm. The laser beam is focused on the sample and polarization filters can be used to select the polarisation plane of the incident wave. The detector is set at 90° relative to the incident beam. A series of lenses is used to collimate the scattered light, and a monochromator and filters are used to remove any contributions from the fundamental[8] (Figure A. 2). Particle concentration in the sample is very important as he signal scales with the particle number. Also, high density is conducive to multi-scattering events, which may distort the signal.

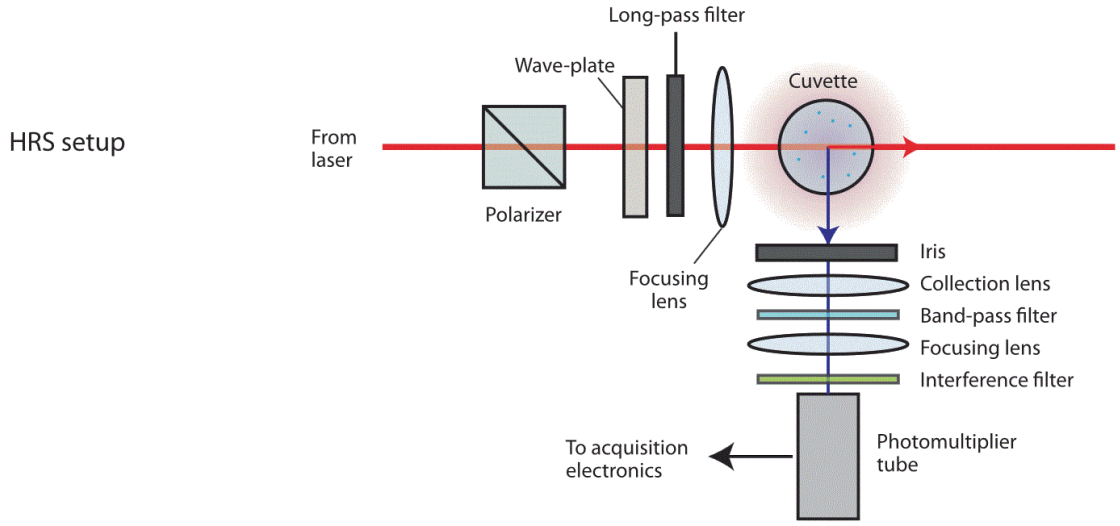

Figure A. 2 General schematic representation of experimental setup used for measuring hyper-Rayleigh scattering. Figure reprinted with permission from, reference [8].

The field of investigations of biological functions in the human body relies heavily on the advances of new imaging techniques. The non-linear optical effects present a good basis for such imaging techniques. Non-invasive imaging of brain functions of mice have been made possible recently by a technique called two photon excitation fluorescence microscopy (TPEFM)[9–16]. In the field of imaging, the multiphoton fluorescence has been introduced in 1990 by Watt W. Webb[17]. TPEFM is very advantageous compared to confocal microscopy due to the very limited and small region in which the excitation happens. When the focal point is moved horizontally this allows for the scanning of the tissue

in layers, providing a tomographic picture (Figure A. 1). Additionally the NIR wavelengths used for TPEFM are less absorbed and scattered in living tissue than visible light allowing for deeper imaging in tissue samples. Another advantage of TPEFM for biological applications is the lower absorption of the IR wavelengths by the living tissue, which leads to less thermal damage to the sample, so the imaging can be done for a longer time *in vivo*[16]. Theoretically, standard confocal microscopy should have a higher resolution than TPEFM, but in real world implementations there's always a trade-off between the resolution and signal strength.

The development of a monodisperse, wet chemistry synthesis of ligated Au nanoclusters and the investigation of its non-linear properties by hyper-Rayleigh scattering is described below. The developed new method for the glutathione stabilised monodisperse Au_{15} clusters are described, and they are studied together with Au_{25} nanoclusters obtained through current state-of-the-art methods. The study shows that the smaller nanoclusters exhibit much larger two-photon processes. The comparison of the results for small gold nanoclustes with previous studies of AU NPs reveals more than two orders of magnitude stronger effects for small nanoclusters, marking the outlines for the quantum cluster regime.

Bibliography

1. Franken, P. A., Hill, A. E., Peters, C. W. & Weinreich, G. Generation of optical harmonics. *Phys. Rev. Lett.* **7,** 118–119 (1961).

2. Kaiser, W. & Garrett, C. Two-Photon Excitation in CaF2:Eu2+. *Phys. Rev. Lett.* **7,** 229–231 (1961).

3. Lewis, G. N., Lipkin, D. & Magel, T. T. Reversible Photochemical Processes in Rigid Media. A Study of the Phosphorescent State. *J. Am. Chem. Soc.* **63,** 3005–3018 (1941).

4. Vavilov, S. I. *The Microstructure of Light*. (Izd-vo Akademii nauk SSSR, 1950).

5. Wawilow, S. J. & Lewschin, W. L. Die Beziehungen zwischen Fluoreszenz und Phosphoreszenz in festen und flüssigen Medien. *Zeitschrift für Phys.* **35,** 920–936 (1926).

6. Boyd, R. W. *Nonlinear Optics*. (Elsevier Inc., 2008).

7. Terhune, R. W., Maker, P. D. & Savage, C. M. Measurements of Nonlinear Light Scattering. *Phys. Rev. Lett.* **14,** 681–684 (1965).

8. Roke, S. & Gonella, G. Nonlinear Light Scattering and Spectroscopy of Particles and Droplets in Liquids. *Annu. Rev. Phys. Chem.* **63,** 353–378 (2012).

9. Masamizu, Y. *et al.* Two distinct layer-specific dynamics of cortical ensembles during learning of a motor task. *Nat. Neurosci.* **17,** 987–994 (2014).

10. Matsui, T. & Ohki, K. Target dependence of orientation and direction selectivity of corticocortical projection neurons in the mouse V1. *Front. Neural Circuits* **7,** (2013).

11. Grutzendler, J., Kasthuri, N. & Gan, W.-B. Long-term dendritic spine stability in the adult cortex. *Nature* **420,** 812–816 (2002).

12. Matsuzaki, M., Honkura, N., Ellis-Davies, G. C. R. & Kasai, H. Structural basis of long-term potentiation in single dendritic spines. *Nature* **429,** 761–766 (2004).

13. Nakashiba, T. *et al.* Young Dentate Granule Cells Mediate Pattern Separation, whereas Old Granule Cells Facilitate Pattern Completion. *Cell* **149,** 188–201 (2012).

14. Sawada, M. *et al.* Sensory Input Regulates Spatial and Subtype-Specific Patterns of Neuronal Turnover in the Adult Olfactory Bulb. *J. Neurosci.* **31,** 11587–11596 (2011).

15. Noguchi, J. *et al.* In vivo two-photon uncaging of glutamate revealing the structure-function relationships of dendritic spines in the neocortex of adult mice. *J. Physiol.* **589,** 2447–2457 (2011).

16. Nemoto, T., Kawakami, R., Hibi, T., Iijima, K. & Otomo, K. Two-photon excitation fluorescence microscopy and its application in functional connectomics. *Microscopy* **64,** 9–15 (2015).

17. Denk, W., Strickler, J. & Webb, W. Two-photon laser scanning fluorescence microscopy. *Science (80-.).* **248,** 73–76 (1990).

Nanoscale

RSCPublishing

ARTICLE

Non-linear optical properties of gold quantum clusters. The smaller the better.

Cite this: DOI: 10.1039/x0xx00000x

Isabelle Russier-Antoine, Franck Bertorelle, Marin Vojkovic, Driss Rayane, Estelle Salmon, Christian Jonin, Philippe Dugourd, Rodolphe Antoine* and Pierre-François Brevet

Received 00th January 2012,
Accepted 00th January 2012

DOI: 10.1039/x0xx00000x

www.rsc.org/

By developing a new method for synthesizing atomically monodisperse Au_{15} nanoclusters stabilized with glutathione molecules and using the current state-of-the-art methods for synthesizing monodisperse protected Au_{25} nanoclusters, we investigate their nonlinear optical (NLO) properties after two-photon absorption. The two-photon emission spectra and the first hyper-polarizabilities of these particles were obtained using, in particular, hyper-Rayleigh scattering technique. The influence on NLO of the excitation wavelength, the size as well as the nature of the ligands are also explored and discussed. Au_{15}, the *smallest* stable thiolated gold nanocluster, presents remarkable nonlinear properties with respect to two-photon processes. The TPA cross section at 780 nm for Au_{15} is ~ 65700 GM. This experimental cross-section value points to a quantum yield for two-photon emission of about $3x10^{-7}$ at 475 nm for Au_{15}. The first hyperpolarizability β for Au_{15} clusters (509×10^{-30} esu), as compared to Au_{25} clusters (128×10^{-30} esu) is larger considering the difference in the number of gold atoms. Also, the 10^{30}.β/atom values reported for Au_{15} and Au_{25} clusters are more than two orders of magnitude larger than the values reported for Au NPs in the size range 10-50 nm, outlining the quantum cluster regime.

Introduction

Due to discrete energy levels and molecular-like HOMO-LUMO transitions, ultrasmall clusters exhibit a spectacular optical behavior which is fundamentally different from that of larger plasmonic nanocrystals.[1] Recently, considerable progress has been achieved in the study of the linear and nonlinear optical properties of gold nanoparticles and clusters of varying size and shape.[2-4] The evolution of nonlinear optical properties, from gold atomic clusters to plasmonic nanocrystals has been addressed by Thomas and co-workers.[5] In particular they showed that the third-order optical nonlinearity in these ultrasmall gold clusters exhibits a significantly lower threshold for optical power limiting. On the other hand, the relatively strong emission under single-photon excitation for Au clusters leads to questions about the possibility of two-photon excited emission. For instance, by measuring two-photon fluorescence excited at 800 nm, Goodson et al.[6] have shown that two-photon absorption (TPA) cross-section increases as the size of small gold clusters increases from 1.1 to 4.0 nm. The TPA cross-section for Au_{25} is 427 000 GM, much larger compared to a typical value of approximately 1 000 GM at 800 nm for organic macromolecules. The large TPA cross sections open the way for applications of such small clusters in optical power limiting, nanolithography, and multiphoton biological imaging. Concerning biological imaging, recent developments in optical imaging techniques, in particular multi-photon excitation microscopy that allows studies of biological interactions at a deep cellular level, has motivated intensive research in developing multi-photon absorption fluorophores. For example, Polavarapu et al.[7] successfully demonstrated the applications of water soluble glutathione small gold clusters for both one and two-photon excitation live cell imaging.

Nonlinear optical (NLO) microscopies (two photon microscopy, TPM or second harmonic imaging microscopy, SHIM) received a tremendous interest for 3D imaging of biological tissues.[8] TPM and SHIM are based on fundamentally different NLO processes, two-photon excited fluorescence (TPEF) and second harmonic generation (SHG), respectively. Therefore, they provide complementary information and can be implemented simultaneously in the same microscope.[9] Whereas TPEF labels give information about molecular distribution, the coherent SHG signal is sensitive to the local non-centrosymmetric organization of the dye molecules and find promising applications for example for the measurement of membrane potential of the neuronal activity of the brain.[10, 11]

This journal is © The Royal Society of Chemistry 2014

While numerous works were devoted to measure the TPA cross-sections of low nuclearity Au clusters,[4] their non-linear susceptibilities were only scarcely explored. Third-order nonlinear optical susceptibilities of monolayer-protected Au_{25} were recently reported[5, 12] as well as the one for Au_{15} in contact with indium tin oxide films.[13] The first hyper-polarizabilities of silver quantum clusters of different sizes (Ag_{20}, Ag_{140} and Ag_{980}) have been recently measured using hyper-Rayleigh scattering technique.[14] In this paper, we aim at exploring NLO properties of ultra-small gold clusters protected by various functionalized thiols. Based on the current state-of-the-art methods for synthesizing atomically monodisperse protected Au_{25} nanoclusters,[15, 16] and reporting a new method for synthesizing atomically monodisperse Au_{15} nanoclusters stabilized with glutathione molecules, we report the TPE spectra and their first hyper-polarizabilities using hyper-Rayleigh scattering technique. The influence on NLO of the excitation wavelength (between 780 and 900 nm), the size (Au_{15} vs Au_{25}) and the nature of the ligands (glutathione vs cysteine) is also explored and discussed.

Results and discussion

Characterization and linear optical properties of as-prepared protected gold clusters. The gold clusters produced by synthesis described in supporting information (see methods section and fig. S1) were characterized by mass spectrometry and optical methods. The monodispersity in term of the size of the prepared gold clusters was verified by ESI-mass spectrometry. An ESI mass spectrum for the protected Au_{15} cluster from solution, and acquired under gentle ESI conditions is shown in Figure 1a). A charge state distribution was observed from $[M-4H^+]^{4-}$ through $[M-8H^+]^{8-}$. Deconvolution of charge states 4− through 8−, and using a multiplicative correlation algorithm,[17, 18] provided a mass of 6928 Da for the intact Au cluster, consistent with the calculated mass of $Au_{15}SG_{13}$ (see inset Fig. 1a). Also, PAGE for Au:SG clusters using Tsukuda synthesis[19, 20] and for our synthesis confirms the monodispersity in term of the size of the prepared $Au_{15}SG_{13}$ clusters (see inset Fig. 1b). Fig. 1b shows the UV-vis absorption spectra in solution of the synthesized $Au_{15}SG_{13}$ clusters. The main feature of the spectrum is a monotonic increase in the electron absorption as the laser wavelength decreases with an onset at ~500 nm and a shoulder observed at ~400 nm. The strong absorption arises from mixed intraband (sp←sp) and interband (sp←d) transitions.[21] Fig. 2c displays the photoemission and photoexcitation spectra of $Au_{15}SG_{13}$. An emission band centered at ~800 nm is observed and originates from radiative intraband transitions within the sp bands across the HOMO-LUMO gap.[19, 20] The excitation spectrum traces well the profiles of the corresponding absorption spectra (see Fig. 1b and 1c), indicating that the sp intraband excitations are responsible for the photoemission. For comparison, Figs. S2 and S3 show the optical absorption spectra of aqueous solutions of $Au_{25}SG_{18}$ and $Au_{25}Cys_{18}$ as well as the corresponding ESI

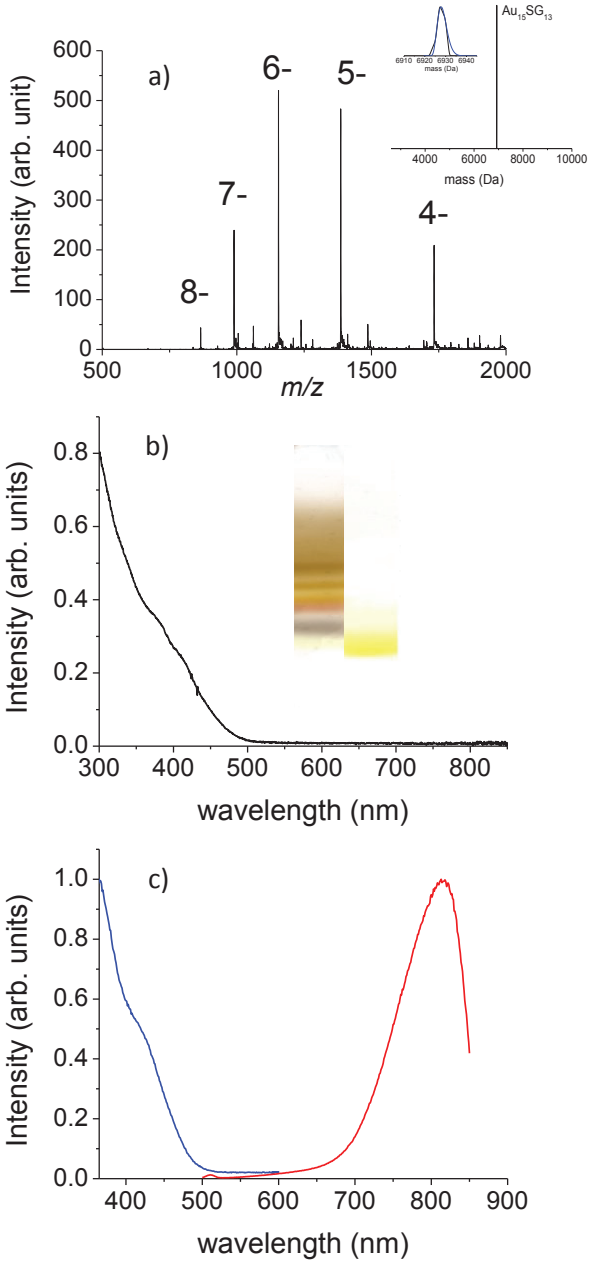

Figure 1 : (a) ESI mass spectrum for the protected Au15 cluster from water solution, and acquired under gentle ESI conditions. Inset. ESI deconvoluted spectrum of $Au_{15}SG_{13}$, based on the experimental ESI spectrum and using a multiplicative correlation algorithm. Comparison of the experimental and simulated deconvoluted spectra of $Au_{15}SG_{13}$. (b) (Black line) Absorption spectrum of $Au_{15}SG_{13}$. Inset: PAGE for Au:SG clusters using (left) Tsukuda synthesis (see ref. 19) and (right) our synthesis. (c) Photoexcitation (with an emission at 820 nm) and emission spectra (with an excitation at 435 nm) of $Au_{15}SG_{13}$.

spectra. The optical spectra are very similar to those reported in the literature.[15, 16, 19] The main features of the spectra are a monotonic decrease in the absorption as the laser wavelength increases and a broad band on the red side of the spectrum (around 650 nm). Both Au_{25} cluster (protected with glutathione and cysteine) solutions display the two features described

This journal is © The Royal Society of Chemistry 2014

above. The absorption band on the red side of the spectrum is due to the intraband transition (HOMO−LUMO) derived from sp orbitals of Au[21, 22] and is systematically observed for protected Au_{25} clusters.[15, 19, 23, 24] The excitation spectra trace well the profiles of the corresponding absorption spectra and an emission band centered at ~800-850 nm is also observed. Optical spectra in solution are very similar to those reported by Tsukuda and coworkers[19, 20] on separated band after PAGE separation.

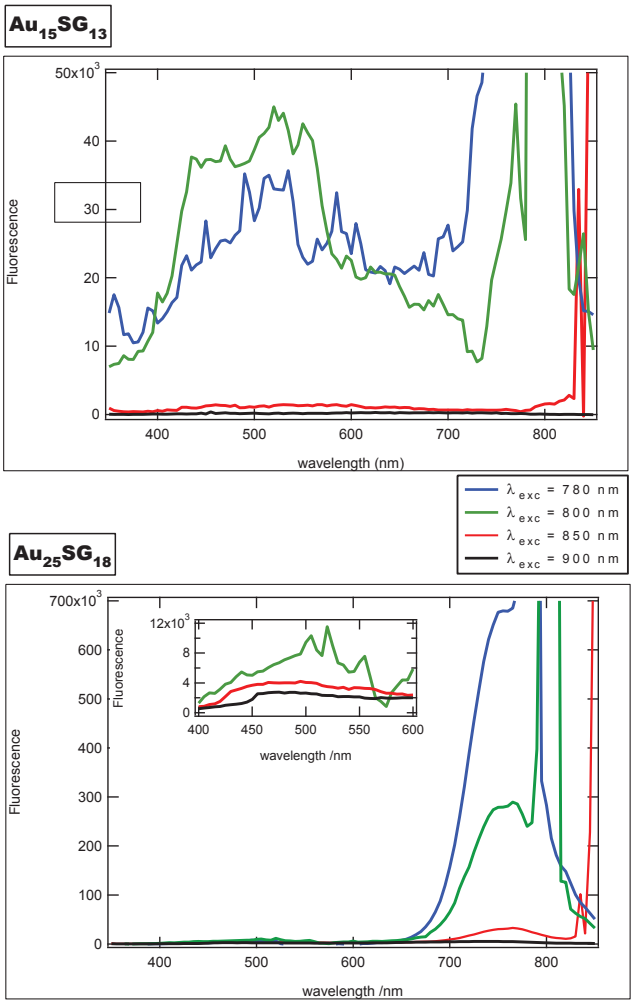

Figure 2: Two-photon emission spectra for $Au_{25}SG_{18}$, $Au_{15}SG_{13}$ as a function of wavelength for different excitation wavelengths (780, 800, 850 and 900 nm). The huge increases in the right part of the spectra are due to the excitation laser lines (780, 800, 850 and 900 nm).

Two-photon absorption and emission of as-prepared protected gold clusters. Two-photon excited fluorescence spectra with excitations ranging from 780 nm to 900 nm have been recorded for Au_{15} and Au_{25} gold clusters. Spectra are given in Fig. 2. A broad band in the visible range (between 400 and 600 nm) is observed and is more intense for Au_{15} clusters than for Au_{25} clusters. Fluorescence in the visible region was observed for gold nanoparticles and nanoclusters (in particular Au_{25}).[4, 6] Interestingly a well-defined intense band centered at ~750 nm appears for Au_{25} in the near IR region (between 700 nm and 800 nm) and is certainly due to the radiative intraband transitions within the sp bands across the HOMO-LUMO gap reported for protected Au_{25} clusters (see also Figs. S2 and S3).[19, 20] No absorption is observed in the red part of the spectrum for Au_{15} clusters (see Figure 1b) which is in agreement with a TPE spectrum dominated by a broad band between 400 nm and 600 nm.

We attempt to determine the two-photon cross-section at 475 nm of gold clusters. The number of fluorescence photons collected in an experiment is given by :[25]

$$F(t) = \frac{1}{2}\,\phi\eta_2 N(t) \qquad (1)$$

Where *N(t)* is the number of excited molecules, η_2 the quantum efficiency for fluorescence of the molecule and ϕ the collection efficiency of the experimental arrangement. The ½ factor accounts for the physical reduction by half of the number of photons owing to the two-photon excitation process.

For a pulsed excitation, the number of excited photons is :

$$N(t) = \sigma_2 C \frac{g_p \langle P(t)\rangle^2}{f\tau\pi\lambda/n} \qquad (2)$$

Where σ_2 is the two-photon absorption (TPA) cross-section, *C* the concentration, *f* the laser pulse frequency, τ the pulse duration, g_p its second-order coherence function, λ the excitation wavelength, *n* the optical index at that frequency and $\langle P(t)\rangle$ the incident power averaged over a duty cycle. Using Eqs.(1) and (2), it is experimentally simpler to compare the two-photon excited fluorescence of the sample and that of a known reference compound. Here, we have chosen fluorescein dye as an internal reference. From literature, we assume at the excitation wavelength of 780 nm : σ_2 (fluorescein) = 33.3 GM using a quantum yield of 0.9 and two photon absorption cross-section of 37 GM.[26] Fluorescein dye was used at the low concentration of 10 µM in order to obtain two-photon emission yields compatible with the Au_{15} and Au_{25} two-photon yields. In particular, no changes in the experimental settings were performed between the two measurements.

Experimentally, we find for the TPE fluorescence cross section at 475 nm: 0.022 GM for Au_{15} but only 0.0022 GM for Au_{25} clusters. As expected, for the same excitation wavelength, the TPE fluorescence cross section at 755 nm is only 0.82 GM whereas it is 4.99 GM for Au_{25}. Since this cross-section value is rather low, its power dependence with the square of the input laser intensity was checked. Fig. S4 in supporting information shows the fluorescence spectra obtained after excitation at 800 nm and at different pump-powers for Au_{15} and pump-power dependence of the fluorescence which gave a slope of ~2 suggesting also that it is indeed a two-photon excited emission. Interestingly, we also measured the TPA cross section at 780 nm for Au_{15} and we found σ (TPA, $Au_{15}SG_{13}$) = 65700 GM. Detailed TPA experimental arrangement, using a P-scan set-up

is given in supporting information (see Fig. S5). These experimental cross-section values point to a quantum yield (QY= $\sigma_{TPE}/\sigma_{TPA}$) for Au_{15} of about $3x10^{-7}$ at 475 nm, in very good agreement with what is expected for such compounds.[6]

Hyperpolarizability measurements. In these experiments where the HRS intensity is collected, the monochromaticity of the second harmonic light generated was always assessed to prevent any spurious contributions from fluorescence. To this end, the HRS intensity for different concentration was normalized against that of the bare solvent. At each concentration, a 20 nm narrow band spectrum around the HRS line was recorded, see Fig. 3. This experimental procedure is deemed necessary to ensure that the process indeed corresponds to the conversion of two photons at the fundamental frequency into one photon at the harmonic frequency. It is observed in particular that the HRS line is located on top of the strong fluorescence background. Two methods are known to remove this fluorescence background, a time-domain and a spectral-domain method. Here the spectral domain method was used owing to the experimental gated photon counting set-up used. The subtraction of the background was then performed by fitting the narrow band spectra with a Gaussian function for the HRS line superposed on a linear function of the wavelength accounting for the fluorescence background. This subtraction procedure is allowed since the two processes, fluorescence and HRS, are incoherent.

The HRS intensity is then given by :

$$\frac{I_{HRS}}{I_{HRS}^{w}} = \frac{\langle N_w\beta_w^2 + N\beta^2 \rangle}{\langle N_w\beta_w^2 \rangle} = 1 + b' N \langle \beta^2 \rangle \qquad (3)$$

where $b' = 1/N_w\langle\beta_w^2\rangle$ (4)

with the subscripts *w* standing for water, the reference solvent used in this experiment. The losses due to absorbance at the fundamental and the harmonic frequency were determined from the separate UV-visible absorption measurements and all data were corrected prior to the analysis. The HRS intensity recorded for different concentrations of $Au_{15}SG_{13}$ in aqueous solution is reported in Fig.3.

As seen in Eq.(3), it is necessary to know the hyperpolarizability of the bare solvent to determine the hyperpolarizability of the gold clusters. In the present report, we use the value of $0.087x10^{-30}$ esu for the first hyperpolarizability of the neat water solution. A discussion on this value may be found in a previous work.[27] The hyperpolarizability values obtained for the different solutions are reported in Table 1.

Interestingly $Au_{25}SG_{18}$ and $Au_{25}Cys_{18}$ have similar hyperpolarizability, meaning that the ligands size has only a weak effect on the SH generation. An absolute value of $(0.16 \pm 0.01) \times 10^{-30}$ esu for the first hyperpolarizability of nonaromatic amino acids was reported by Duboisset et al.[28] And by using a collagen like model, the microscopic hyperpolarizability along the peptide bond was evaluated at $(0.7 \pm 0.1) \times 10^{-30}$ esu. It is clear that the huge hyperpolarizabilities reported in this work cannot be accounted by the ligand shell alone (which only would give a contribution of several 10^{-30} esu for the first hyperpolarizability for a fully coherent superposition). The first hyperpolarizability for Au_{15} clusters, as compared to Au_{25} clusters is also larger considering the difference in the number of gold atoms. Structural theoretical investigations on $Au_{15}(SR)_{13}$ model features staple motifs protecting the Au_4 nucleus.[29, 30] On the other hand, the Au_{25} cluster features a centered icosahedral Au_{13} core capped by twelve gold atoms that are situated in six pairs around the three mutually perpendicular 2-fold axes of the icosahedron.[21] Both Au_{15} and Au_{25} structures are expected to have symmetric gold core structures, which preclude any intense SH generation. The nature of staple motifs protecting the gold core and in particular the structuration of Au-S bonds may be different between Au_{15} and Au_{25} clusters, and may account for enhanced SH signal for Au_{15}.

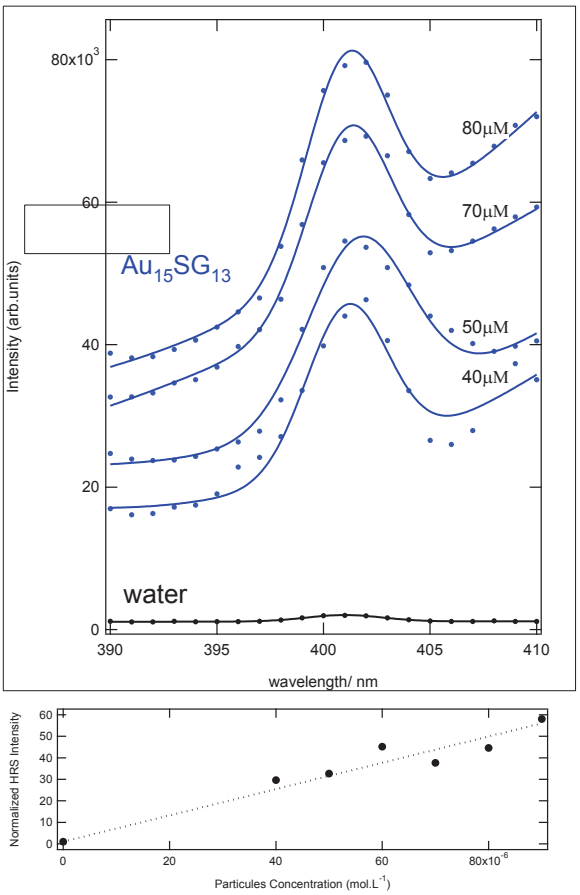

Figure 3: (top panel) HRS intensity versus wavelength for $Au_{15}SG_{13}$ solutions of different concentrations (blue circles). Lines : fit to a Gaussian function superposed on a linearly increasing function of the wavelength. (bottom panel) Plot of the HRS intensity of for $Au_{15}SG_{13}$ as a function of concentration. The continuous lines correspond to the linear adjustment to eq (3).

This journal is © The Royal Society of Chemistry 2014

Also, the 2-photon absorption leads a resonant excitation (around 400 nm). This resonant SH generation is in competition with a vibronic relaxation leading to two-photon emission. Differences in the dynamics of relaxation may also account for the difference of first hyperpolarizability reported for Au_{15} and Au_{25}. Finally, we would like to emphasize that the 10^{30}.β/atom values reported for Au_{15} and Au_{25} clusters are more than two order of magnitude larger than the values reported for Au NPs in the size range 10-50 nm (see Fig. 4 and Table S1 in supporting information). 10^{30}.β/atom values decrease drastically with increasing the number of gold atom and there is a saturation-type of behavior for large gold nanoparticles. The results can be explained by the evolution and involvement of interband transitions in smaller clusters, outlining transition of the cluster behavior to a gold nanoparticle behavior possessing strong surface plasmon absorption.

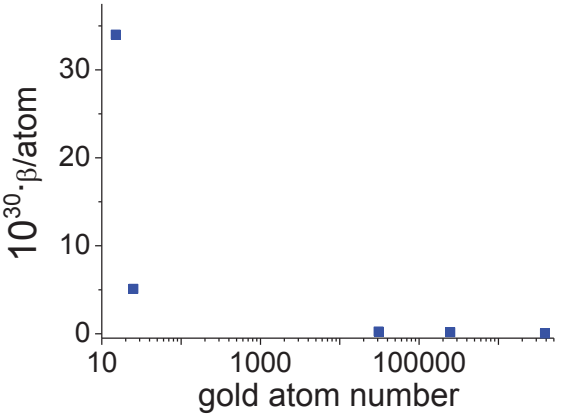

Figure 4: 10^{30}.β/atom as a function of the number of gold atom, obtained with 802 nm excitation.

Solution	10^{30}β (esu) (water=0.087.10^{-30}esu)	10^{30}.β/atom (water=0.087.10^{-30}esu)
$Au_{15}SG_{13}$	509(12)	34
$Au_{25}SG_{18}$	128(1)	5.1
$Au_{25}Cyst_{18}$	163(4)	6.5

Table 1 : Quadratic hyperpolarizabilities for the different solutions at 802 nm.

Conclusions

In summary, size-controlled synthesis of monodispersed gold nanoclusters offers the possibility to address non-linear optical properties of ultrasmall gold quantum clusters in solution. Both the size (Au_{15} and Au_{25}) and the nature of ligands (glutathione vs cysteine) were varied to fathom their influence on the nonlinear behavior of such low nuclearity gold clusters upon two-photon excitation. Au_{15}, the *smallest* stable thiolated gold nanocluster presents remarkable two-photon nonlinear properties. $Au_{15}SG_{13}$ appears to be a good candidate for nonlinear optical microscopies by either two photon microscopy or second harmonic imaging microscopy. The present experimental results provide unique benchmarks for theoretical modeling of NLO properties of such clusters, although the origin of enhanced NLO properties of Au_{15} clusters, as well as the interplay between the cluster core and the interface between ligand shell and the metallic part needs to be clarified. These NLO data are supposed to be highly sensitive to structure of gold clusters and we anticipate that our work could help to unambiguously assign structures for such low nuclearity gold clusters. Works under these lines are currently undertaken in our lab.

Materials and methods

Materials. All the chemicals were commercially available and were used without purification. HAuCl4•3H2O, trifluoroacetic acid (TFA), methanol (HPLC grade), acrylamide (98%), bis-acrylamide (98%), glycine, tris(hydroxymethylamine), cysteine and GSH (γ-Glu-Cys-Gly, MW 307) were purchased from Carl Roth. Sodium borohydride ($NaBH_4$) and tetramethylammonium borohydride ($(CH_3)_4BH_4$) were purchased from Sigma Aldrich. MilliQ water with a resistivity of 18.2 MΩ cm was used for all experiments.

Preparation of protected gold clusters. The detailed synthesis of $Au_{15}SG_{13}$ is available in the supporting information. Briefly, 234 mg of Glutathion (GSH) was dissolved in 35 ml of methanol and 4 ml of tributylamin in a 100 ml balloon. Then 15 ml of ether was added followed by 5ml of a water gold solution (100 mg of $HAuCl_4,3H_2O$). Solution was mixed at -10°C during 1 hour and gold salt was reduced by adding tetrabutylammonium borohydride. The solution was kept the night at ambient temperature before being concentrated to a volume of ≈5 ml in a rotary evaporator. The precipitation is induced by adding methanol (5ml) and ether (15ml). Then precipitated was washed to removed unreacted glutathione and unwanted Au_xSG_x.
Protected Au_{25} clusters were synthesizing as described by T. Pradeep and co-workers[15] for $Au_{25}SG_{18}$ and by J. Xie and co-workers[16] for $Au_{25}Cys_{18}$.

Polyacrylamide gel electrophoresis (PAGE). PAGE separation was carried out by using a vertical gel electrophoresis unit with a size of 0.2 cm × 20 cm × 20 cm. The separating and stacking gels were prepared by acrylamide monomers with the total contents of 35 and 7 wt% (acrylamide/bis-(acrylamide) 94:6), respectively. The eluting buffer consisted of 192 mM glycine and 25 mM tris(hydroxymethylamine). The as-prepared Au(SG) clusters were dissolved in a 15% (v/v) glycerol/water solution (6 mg in 100 µl). The samples solutions were loaded onto the stacking gel (10 µl per well) and eluted for 14 h at a constant voltage mode (150 V) to achieve sufficient separation.

Mass spectrometry. Solutions were diluted without gel separation at a concentration of ~1 mg/mL in H2O, electrosprayed at a flow rate of 10 µL/min and analyzed in negative mode with a linear quadruple ion trap mass spectrometer (LTQ, Thermo Fisher Scientific, San Jose, CA) with a spray voltage of −3 kV and a capillary temperature of 100 °C. Other instrument settings were adjusted for each species to optimize the distribution of charge states observed in the mass spectrum. Isotope-resolved mass spectrum were recorded using the ultra zoom scan mode of the instrument (mass resolution ~ 30 000, mass accuracy 0.2 Th).[31] Collision-induced dissociation (CID) was performed using helium gas at a normalized collision energy of 12% for 30 ms.

Absorption and emission measurements. UV−vis spectra in solution were recorded using an AvaSpec-2048 fiber optic spectrometer and an AvaLight-DH-S deuterium halogen light source. Fluorescence excitation and emission spectra were measured using a Fluoromax-4 Horiba fluorescence spectrophotometer.

HRS and TPE measurements. The light source for the present HRS and TPE experiments was a mode-locked femtosecond Ti:sapphire laser delivering at the fundamental wavelength of 800 nm pulses with a duration of about 140 femtoseconds at a repetition rate of 76 MHz. After passing through a low-pass filter to remove any unwanted harmonic light generated prior to the cell, the fundamental beam of about 300 mW was focused by a microscope objective into a 1 cm spectrophotometric cell containing the aqueous solution. The HRS (or TPE) light was collected at an angle of 90° from the incident direction by a 2.5 cm focal length lens. The second harmonic light was separated from its linear counterpart by a high-pass filter and a monochromator positioned on the second harmonic wavelength. The HRS light was then detected with a photomultiplier tube and the pulses produced counted with a photon counter. The fundamental beam was chopped at about 115 Hz to enable a gated photon counting mode allowing automatic subtraction of the noise level. For TPE signal, a short pass filter with a cut-off wavelength at 750 nm was placed before the monochromator to minimize the light scattering from the excitation beam.

Notes and references

Institut Lumière Matière, UMR5306 Université Lyon 1-CNRS,
Université de Lyon 69622 Villeurbanne cedex, France
Fax: +33 4 72 43 15 07; Tel: +33 4 72 43 10 85
rodolphe.antoine@univ-lyon1.fr

Electronic Supplementary Information (ESI) available: Detailed synthesis and purification for $Au_{15}SG_{13}$ clusters. MS and optical spectra for $Au_{25}SG_{18}$ and Au_{25} Cys_{18}. Hyperpolarizability data for gold NPs. Two-photon emission spectra at different pump powers for $Au_{15}SG_{13}$ clusters. Detailed TPA experimental arrangement. See DOI: 10.1039/b000000x/

1. R. C. Jin, *Nanoscale*, 2010, 2, 343-362.
2. P. K. Jain, X. H. Huang, I. H. El-Sayed and M. A. El-Sayed, *Acc. Chem. Res.*, 2008, 41, 1578-1586.
3. S. Link and M. A. El-Sayed, *Int. Rev. Phys. Chem.*, 2000.
4. S. H. Yau, O. Varnavski and T. Goodson, *Acc. Chem. Res.*, 2013, 46, 1506-1516.
5. R. Philip, P. Chantharasupawong, H. Qian, R. Jin and J. Thomas, *Nano Lett.*, 2012, 12, 4661-4667.
6. G. Ramakrishna, O. Varnavski, J. Kim, D. Lee and T. Goodson, *J. Am. Chem. Soc.*, 2008, 130, 5032-5033.
7. L. Polavarapu, M. Manna and Q.-H. Xu, *Nanoscale*, 2011, 3, 429-434.
8. P. N. Prasad, *Introduction to Biophotonics*, Wiley Interscience 2003.
9. L. Moreaux, O. Sandre, S. Charpak, M. Blanchard-Desce and J. Mertz, *Biophys. J.*, 2001, 80, 1568-1574.
10. D. A. Dombeck, M. Blanchard-Desce and W. W. Webb, *J. Neurosci.*, 2004, 24, 999-1003.
11. B. A. Nemet, V. Nikolenko and R. Yuste, *J Biomed Opt.* , 2004, 9, 873-881.
12. Y. Hamanaka, N. Okada, K. Fukagawa, A. Nakamura, Y. Tai and J. Murakami, *J. Phys. Chem. C*, 2012, 116, 10760-10765.
13. S. Kumar, E. S. Shibu, T. Pradeep and A. K. Sood, *Optics Expr.*, 2013, 21, 8483-8492.
14. S. A. Khan, D. Senapati, T. Senapati, P. Bonifassi, Z. Fan, A. K. Singh, A. Neeley, G. Hill and P. C. Ray, *Chem. Phys. Lett.*, 2011, 512, 92-95.
15. E. S. Shibu, M. A. H. Muhammed, T. Tsukuda and T. Pradeep, *J. Phys. Chem. C*, 2008, 112, 12168-12176.
16. Y. Yu, Z. Luo, Y. Yu, J. Y. Lee and J. Xie, *ACS Nano*, 2012, 6, 7920-7927.
17. J. J. Hagen and C. A. Monnig, *Anal. Chem.*, 1994, 66, 1877-1883.
18. F. Lux, A. Mignot, P. Mowat, C. Louis, S. Dufort, C. Bernhard, F. Denat, F. Boschetti, C. Brunet, R. Antoine, P. Dugourd, S. Laurent, L. V. Elst, R. Muller, L. Sancey, V. Josserand, J.-L. Coll, V. Stupar, E. Barbier, C. Rémy, A. Broisat, C. Ghezzi, G. Le Duc, S. Roux, P. Perriat and O. Tillement, *Angew. Chem. Int. Ed.*, 2011, 50, 12299-12303.
19. Y. Negishi, K. Nobusada and T. Tsukuda, *J. Am. Chem. Soc.*, 2005, 127, 5261-5270.
20. Y. Negishi, Y. Takasugi, S. Sato, H. Yao, K. Kimura and T. Tsukuda, *J. Am. Chem. Soc.*, 2004, 126, 6518-6519.
21. M. Zhu, C. M. Aikens, F. J. Hollander, G. C. Schatz and R. Jin, *J. Am. Chem. Soc.*, 2008, 130, 5883-5885.
22. J. Akola, M. Walter, R. L. Whetten, H. Hakkinen and H. Gronbeck, *J. Am. Chem. Soc.*, 2008, 130, 3756-+.
23. Y. Shichibu, Y. Negishi, T. Tsukuda and T. Teranishi, *J. Am. Chem. Soc.*, 2005, 127, 13464-13465.
24. H. Tsunoyama, H. Sakurai, Y. Negishi and T. Tsukuda, *J. Am. Chem. Soc.*, 2005, 127, 9374-9375.
25. C. Xu and W. W. Webb, *J. Opt. Soc.Am. B*, 1996, 13, 481-491.
26. M. A. Albota, C. Xu and W. W. Webb, *Appl. Opt.*, 1998, 37, 7352-7356.
27. J. Duboisset, G. Matar, I. Russier-Antoine, E. Benichou, G. Bachelier, C. Jonin, D. Ficheux, F. Besson and P. F. Brevet, *J. Phys. Chem. B*, 2010, 114, 13861-13865.
28. J. Duboisset, A. Deniset-Besseau, E. Benichou, I. Russier-Antoine, N. Lascoux, C. Jonin, F. Hache, M.-C. Schanne-Klein and P.-F. Brevet, *J. Phys. Chem. B*, 2013, 117, 9877-9881.
29. A. Tlahuice-Flores, M. Jose-Yacaman and R. L. Whetten, *Phys. Chem. Chem. Phys.*, 2013, 15, 19557-19560.

 This journal is © The Royal Society of Chemistry 2014

30. D. Jiang, S. H. Overbury and S. Dai, *J. Am. Chem. Soc.*, 2013, 135, 8786-8789.
31. F. Bertorelle, R. Hamouda, D. Rayane, M. Broyer, R. Antoine, P. Dugourd, L. Gell, A. Kulesza, R. Mitric and V. Bonacic-Koutecky, *Nanoscale*, 2013, 5, 5637-5643.

Appendix 2

List of publications

1. Daly, S; Girod, M; Vojkovic, M; Giuliani, A; Antoine, R; Nahon, L; O'Hair, R.A.J.; Dugourd, P. *"Single-Photon, Double Photodetachement of Nickel Phthalocyanine Tetrasulfonic Acid 4-Anions"*, 2016, The Journal of Physical Chemistry Letters.

2. Vojkovic, Marin; Rayane, Driss; Bertorelle, Franck; Antoine, R; Broyer, M; Dugourd, P. *"Synthesis of ligated-metal species by laser vaporization electrospray ionization (LAVESI)"*, 2015, International Journal of Mass Spectrometry, 387, SI, 45-50.

3. Girod, Marion; Sanader, Zeljka; Vojkovic, Marin; Antoine, R; MacAleese, L; Lemoine, J; Bonacic-Koutecky, V; Dugourd, P. *"UV Photodissociation of Proline-containing Peptide Ions: Insights from Molecular Dynamics"*, 2015, Journal of the American Society for Mass Spectrometry, 26, 3, 432-443.

4. Russier Antoine, I; Bertorelle, F; Vojkovic, M; Rayane, D; Salmon, E; Jonin, C; Dugourd, P; Antoine, R; Brevet, PF. "No*n-linear optical properties of gold quantum clusters. The smaller the better"*, 2014 Nanoscale, 6, 22, 13572-13578

5. Salamunićcar, G., Lončarić, S., Vinković, D., Vučina, D., Gomerčić, M., Pehnec, I., Vojković, M., Hercigonja, T. *"Test-field for evaluation of laboratory craters using a Crater Shape-based interpolation crater detection algorithm and comparison with Martian and Lunar impact craters"* 2012, Planetary and Space Science, 71, 106